MECHANICAL COMPRESSION OF COILED CARBON NANOTUBES

A Dissertation
Presented to
The Academic Faculty

by

Jabulani Randall Timothy Barber

In Partial Fulfillment
of the Requirements for the Degree
Inorganic Chemistry in the
School of Chemistry and Biochemistry

Georgia Institute of Technology
May 2009

MECHANICAL COMPRESSION OF COILED CARBON NANOTUBES

Approved by:

Dr. Lawrence A Bottomley, Advisor
School of Chemistry and Biochemistry
Georgia Institute of Technology

Dr. E. Kent Barefield
School of Chemistry and Biochemistry
Georgia Institute of Technology

Dr. Robert Whetten
School of Chemistry and Biochemistry
Georgia Institute of Technology

Dr. Aldo A. Ferri
School of Mechanical Engineering
Georgia Institute of Technology

Dr. Levent Degertekin
School of Mechanical Engineering
Georgia Institute of Technology

Dr. Satish Kumar
School of Polymer and Textile Engineering
Georgia Institute of Technology

Dr. Zhong L. Wang
School of Materials Science and Engineering
Georgia Institute of Technology

Date Approved: Feb. 24, 2009

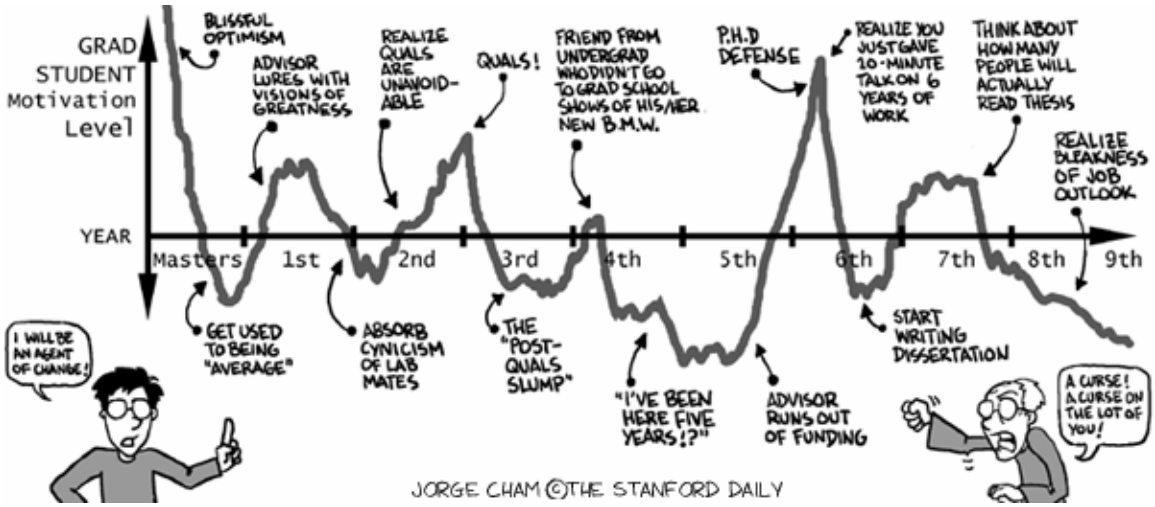

Image courtesy of "Piled Higher and Deeper" by Jorge Cham www.phdcomics.com

To everyone that gave words or thought of support, especially around year four,
Thank you.

To my family,
I love you more than words can ever express.

ACKNOWLEDGEMENTS

I would like to thank Advisor Professor Lawrence A. Bottomley for giving me the freedom and opportunity to learn from my mistakes. I would to also thank him for the near endless support and guidance that he has given me during my pursuit of that "invisible bar".

I would also like to thank my doctoral committee for guiding my scientific growth. A special thanks goes to fellow researcher and officemate Kane Barker, for tolerating my eccentricities and countless helpful discussions regarding atomic force microscopy. Mark Poggi for developing MPFS and laying the groundwork on which this dissertation stands. Gary Spinner and Charlie Hsu of the GT MiRC clean room for their efforts to maintain world class instrumentation. Yolande Berta for her open-mindedness in allowing me to modify the TEM sample holder. I would like to thank Professor Aldo Ferri and Professor Jonathan Colton for helping to broaden my understanding of beam mechanics.

I would also like to thank Cattien V. Nguyen of NASA Ames Research Center for welcoming me into his research group during my tenure as a McNair Scholar and continued research collaborations. Financial support from the NASA Graduate Student Researchers Program (NNA-04-CK71H) and FACES scholarship is gratefully acknowledged.

TABLE OF CONTENTS

LIST OF TABLES

LIST OF FIGURES

LIST OF SYMBOLS AND ABBREVIATIONS

$<A>^2$	mean-square amplitude
A	cross-sectional area
Å	Angstrom
A/D	analog to digital
a_1	width of carbon ring
AFM	atomic force microscope
C(t)	in-plane stiffness
CCNT	coiled carbon nanotube
CFM	chemical force microscopy
CNT	carbon nanotube
CVD	chemical vapor deposition
D	coil diameter
D	bar diameter
D(t)	Bending rigidity
d_0, *b*	outer diameter
DAQ	data acquisition card
d_i, *a*	inner diameter
d_{NT}	nanotube diameter
DSA	Dynamic signal analyzer
dtime	time stamp for waterfall data
E	Young's modulus
EDS	energy-dispersive x-ray spectrometry
EELS	Electron energy-loss spectrometry
EI	Flexural rigidity or bending modulus
eV	Electron volt

F	distributed load force
FEA	finite element analysis
FFM	Friction force microscopy
FFT	fast Fourier transform
freq	frequency range of data
G	shear modulus
Gpa	Gigapascal
HM	horizontal deflection data
HRTEM	high-resolution transmission electron microscope
Hz	Hertz
I	Inertia
K,k	spring constant
k_B	Boltzman's constant
kHz	Kilohertz
l,L	beam length
LFM	Lateral Force Microscopy
L_{NT}	nanotube length
M	Bending moment
MD	molecular dynamic
MEMS	micro-electromechanical systems
MPFS	multi parameter force spectroscopy
MWCNT	multi-walled carbon nanotube
N	active coils
N	Number of walls in nanotube
$N_{C,n}$	Number of helical coils
NI	National Instruments

Nm	Nanometer
N_W	shell number
OA	oscillation amplitude
α_H	helical angle
OLS	optical lever sensitivity
P	point load
P_{crit}	critical buckling load
PSD	Position sensitive detector
PSD	power spectral density
R,r	Radius
SAM	signal access module
SAM	self assembled monolayer
SEM	scanning electron microscope
SHO	simple harmonic oscillator
SPM	scanning probe microscopy
STEM	scanning transmission electron microscope
STM	scanning tunneling microscope
T	nanotube wall thickness
T	Temperature
T	Time
TEM	transmission electron microscope
™	Trademark
TPa	Terapascal
V	shear force
WDS	Wavelength-dispersive spectrometer
WF	Waterfall amplitude data matrix

A	Angle
α_0	compressive rigidity
B	Solution to boundary equation
Θ	beam deflection
Mm	Micrometer
N	Poisson's ratio
Ξ	Dimensionless coefficient for nanocoil
Π	Pi
P	Density
Σ	amplitude of vibration
σ_{CR}	critical buckling deflection
Ω	frequency of vibration

SUMMARY

Carbon nanotubes are molecular-scale tubes of graphitic carbon that possess many unique properties. They have high tensile strength and elastic modulus, are thermally and electrically conductive, and can be structurally modified using well established carbon chemistries. There is global interest in taking advantage of their unique combination of properties and using these interesting materials as components in nanoscale devices and composite materials.

The goal of this research was the correlation of the mechanical properties of coiled carbon nanotubes with their chemical structure. This research project began with the hypothesis that these nanostructures would respond to mechanical compression in a similar manner to macroscale springs. A novel experimental approach was developed to test this hypothesis. Individual nanocoils, grown by chemical vapor deposition, were attached to scanning probe tip using the arc discharge method. Using a scanning probe microscope the nanocoils are repeatedly brought into and out of contact with a chemically-modified substrate. Precise control over the length (or area) of contact with the substrate is achievable through simultaneous monitoring the cantilever deflection resonance, and correlating these with scanner movement. The mechanical response of nanocoils depended upon the extent of their compression. Nonlinear response of the nanocoil was observed consistent with compression, buckling, and slip-stick motion of the nanocoil. The chemical structure of the nanocoil and its orientation on the tip was determined using scanning and transmission electron microscopy.

The mechanical stiffness of eighteen different nanocoils was determined in three ways. In the first, the spring constant of each nanocoil was computed from the slope of the linear response region of the force-distance curve. The assumptions upon which this calculation is based are: 1) under compression, the cantilever-nanocoil system can be modeled as two-springs in series, and 2) the nanocoil behaves as an ideal spring as the

load from the cantilever is applied. Nanocoil spring constants determined in this fashion ranged from $6.5x10^{-3}$ to 5.16 TPa for the CCNTs understudy. In the second, the spring constant of the nanocoil was computed from measuring the critical force required to buckle the nanocoil. The critical force method measured the force at the point where the nanocoil-cantilever system diverges from a linear region in the force curve. Nanocoil spring constants determined in this fashion ranged from $1.3x10^{-5}$ to 10.4 TPa for the CCNTs understudy. In the third, the spring constant of each nanocoil was computed from the thermal resonance of the cantilever-nanocoil system. Prior to contact of the nanocoil with the substrate, the effective spring constant of the system is essentially that of the cantilever. At the point of contact and prior to buckling or slip-stick motion, the effective spring constant of the system is modeled as two springs in parallel. Nanocoil spring constants determined in this fashion ranged from $2.7x10^{-3}$ to 0.03 TPa for the CCNTs understudy.

Using the thermal resonance of the cantilever system a trend was observed relating nanocoil structure to the calculated modulus. Hollow, tube-like nanostructures had a higher measured modulus than solid or fibrous structures by several orders of magnitude. One can conclude that the structure of carbon nanocoils can be determined from using their mechanical properties. This correlation should significantly contribute to the knowledge of the scientific and engineering community. It will enable the integration of carbon nanocoils in microelectromechanical (MEMS) or nanoelectromechanical systems (NEMS) as resonators, vibration dampers, or any other application in which springs are used within complex devices.

CHAPTER 1

MECHANICAL PROPERTIES OF CARBON NANOTUBES

1.1 Research Motivation

Creating nanoscale devices is one of the great challenges of this millennium. The integration of newly discovered nanoscale phenomena into real world applications is a cross-disciplinary task, requiring the collaboration of engineers and scientists. Because of their unique mechanical and electronic properties [1] carbon nanotubes have received great interest in their application in devices and technologies.

Some of these devices are already coming into fruition. Carbon nanotube arrays are being used to make ultralight and flexible displays. Samsung, in collaboration with Unidym has created a prototype carbon nanotube-based color active matrix electrophoretic display (EPD) which uses the nanotubes as field emission source material [2]. The EPD claims to have improved brightness and energy conservation compared to conventional flat display technologies. Jensen et al. [3] have constructed a functional radio receiver from an individual carbon nanotube; where it serves as the antenna, band-pass filter, amplifier and demodulator. Although both of these examples are utilizing nanomaterials, they are being integrated into large scale platforms. Significant research continues to be needed for the integration of nanomaterials into nanoscale devices.

The goal for the work presented in this dissertation was the correlation of the mechanical properties of coiled carbon nanotubes with their chemical structure. This research project began with the hypothesis that helical nanostructures will have similar mechanical behavior to macroscale springs. A novel experimental approach was developed to test this hypothesis. A secondary objective was the creation of a predictive model for the compression of the nanocoils. The development of this model would

significantly contribute to the knowledge of the scientific and engineering community. It will enable the integration of carbon nanocoils in microelectromechanical (MEMS) or nanoelectromechanical systems (NEMS) as resonators, vibration dampers, or any other application in which springs are used within complex devices.

This chapter will serve as an introduction to carbon nanotube chemistry. The discovery of these structures and a look at some proposed and realized applications will be discussed therein. In addition to these topics, current experimental techniques used to measure the mechanical properties of carbon nanotubes will be discussed. Chapter 2 of this dissertation will serve as an introduction into the field of scanning probe and electron microscopies. These were the primary tools used in presented work. Chapter 3 will discuss the experimental design used within the study. Chapter 4 and 5 investigates the use of multi-parameter force spectroscopy (MPFS) to measure the response of the coiled nanotube under a compressive load. Chapter 6 presents the developed compression model.

1.2 Carbon Nanotube History

Carbon nanotubes were accidentally discovered by Iijima in 1991 during a study on manufacturing methods for fullerenes [4]. Unlike the spherical fullerenes, he found carbon tubes with nanometer scale widths and lengths in microns. These structures, termed carbon nanotubes (CNTs), were found to be cylindrical in shape with hexagonal carbon bonding similar to that of graphene. Figure 1.1 displays the atomic structures of a carbon nanotube and a C_{60} fullerene. This figure shows the nanotube with both an open and closed-end configuration. In the closed-end configuration, the nanotube is capped with a fullerene hemisphere. The sides of the nanotube have been described as a rolled

graphene sheet. Most nanotubes are synthesized with both ends capped and require post synthesis processes to form an open structure.

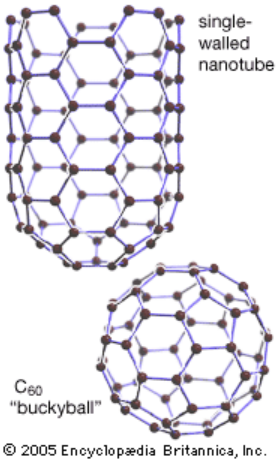

Figure 1.1. Model of single-walled carbon nanotube and fullerene structures. The nanotube displays both an open and closed cap structure. (By courtesy of Encyclopaedia Britannica, Inc., copyright 2005; used with permission)

Both the scientific and engineering communities have embraced carbon nanotubes due to their exceptional and unique properties [5]. CNTs can have metallic or semi-conducting electric properties, an outgrowth of their atomic structure [6]. The mechanical properties of CNTs have led to their proposed application in structural materials, due to their extremely high stiffness and strength. CNTs have been estimated to have 1 TPa modulus and a 10-12% strain to failure [7, 8]. Individual nanotubes have been observed to elastically bend through 360° without accumulated damage [9]. A nanotube under high strain is shown in Figure 1.2. The electric and mechanical properties of the carbon nanotube are due primarily to the hybridized bonds, which are similar to that of graphite. These properties, combined with the nanometer and micron

scale dimensions of the nanotube, have led to their proposed use in a variety of nanotechnology and nanoscience applications.

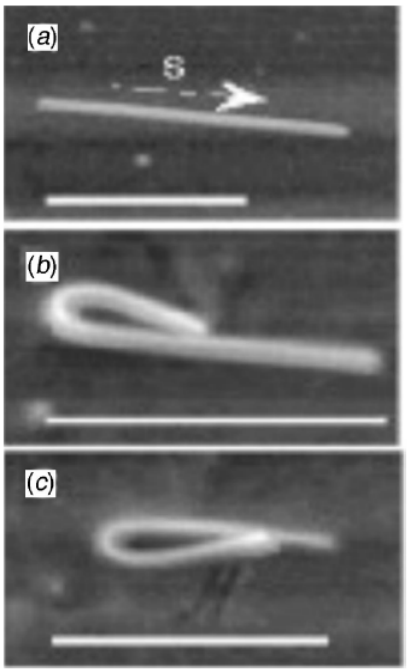

Figure 1.2. Bending and buckling of MWCNT through high applied strain: (a) original straight MWCNT, (b) the MWCNT is bent upwards onto itself, (c) the same tube is bend downward onto itself in opposite direction of (b). (Reprinted by permission from Macmillan Publishers Ltd: Nature [9], copyright 1997.)

1.3 Carbon Nanotube Structure

The structural units of the carbon nanotube are hexagonal carbon rings. The primary bond between the atoms consists of sp2 hybridization (one sigma and two pi-bonds) with trigonal planar symmetry, where each atom is bonded to its three closest neighboring atoms at approximately 120° in plane (Figure 1.3). The in-plane properties of the nanotube are derived from the strong sigma bonds. The weaker pi-bonds are delocalized within the hexagonal ring; centered symmetrically at a distance of 0.33Å from the central axis of the sigma bond. The pi-bond is responsible for both the

electrical conductivity and the out of plane properties, such as wall bending stiffness. There are numerous crystalline structures for carbon nanotubes. These are determined by the helicity (chirality) of the graphitic lattice and the diameter of the hexagonal carbon structures. The various nanotube structures are commonly classified using the White notation [10]. Simplified, this notation describes the way in which a graphene sheet is rolled to make a graphitic tube structure. The White notation contains a basal vector which is used to find the circumferential joining point to turn the sheet into a tube. The number of hexagonal rings used when following the *a* and *b* vectors to close the tube structure is written in the form (a,b), which also defines the helical angle (θ_H)of the nanotube (Figure 1.4). This nomenclature is similar to that often used to describe helical chain polymers with translational symmetry.

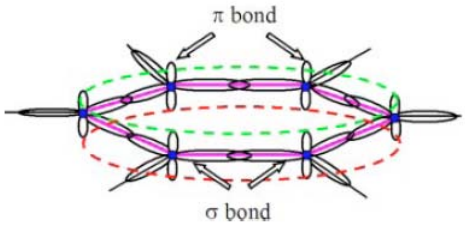

Figure 1.3. Hexagonal bonding structure for one graphite layer: the carbon nuclei are shown in filled circles, out-of-plane delocalized π-bonds are shown as dotted lines, σ-bonds connect the carbon nuclei in-plane.

Changes to the hexagonal lattice of the nanotube can lead to temporary or permanent changes in the tube radius or structure. Wang et al. [11], asserted that inclusion of heptagonal and pentagonal rings pairs into the hexagonal lattice is necessary to promote the formation of helical and zigzag structures. A helical carbon nanotube is shown in Figure 1.5A. The inclusion of a pentagonal ring into the hexagonal lattice

Figure 1.4. Notation for indexing nanotube structures. The definition of a roll-up vector is a linear combination of base vectors R_1 and R_2. ([10] Copyright 1993 by the American Physical Society.)

causes the inward curvature in the structure, leading to a surface with positive curvature [12, 13]. Inclusion of the larger pentagonal ring into the lattice causes the lattice to curve outward forming negative curvature (Figure 1.5B). These defects are known to exist in the fullerenes, giving rise to their curved shapes. Wang et al. also proposed that if there was no twist on the pentagonal-heptagonal (P-H) paired carbon rings along the growth axis of the tube, a planar-spiral structure would form. If, however the P-H pairs do twist along the growth axis, a helical structure would form. The helicity and twist angle are determined by the distance between the P-H pairs. They also proposed that a variety of structures can be formed by the inclusion of these bending defects in the hexagonal lattice. In practice, however, these defects occur during the growth of the carbon nanostructures, where the nucleation at the catalyst has a large impact on the inclusion, or prevention, of these defects during synthesis [14-20].

Up to this point, the discussion has focused on single-walled carbon nanotubes (SWCNTs). These structures consist of a single graphitic carbon layer that is exactly one carbon atom thick. The electric and mechanical properties discussed previously were

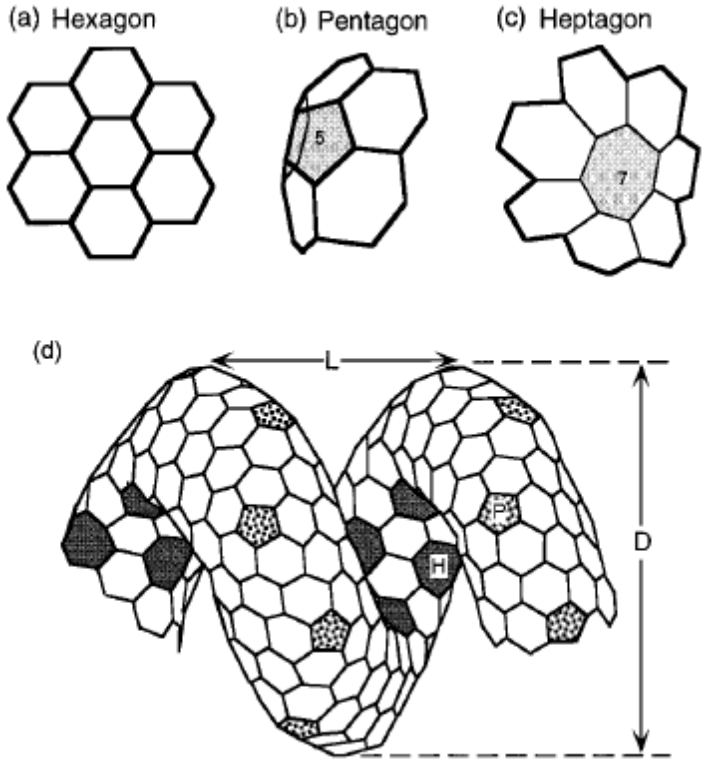

Figure 1.5. (a-c) Hexagonal, pentagonal and heptagonal carbon ring structures in the matrix of graphitic layer. (d) Helical carbon nanotube formation by twisting the orientations of the P-H pairs. (Adapted with permission from [11]. Copyright 2000 American Chemical Society.)

determined for this structural form of the carbon nanotube. The nanotubes found by Iijima in 1991 consisted of concentric tubular graphene sheets and named multi-walled carbon nanotubes (MWCNTs). The individual walls are not bonded to each other and only weakly interact through van der Waals forces. In this case, one can visualize a tube made by rolling sheets of graphite into a tube. The walls are separated by a spacing of 3.4Å, the distance between the individual sheets of graphite. Because they are not covalently bound together, the individual walls of the MWCNT can freely rotate and slide between each other with minimal resistance, again a property very similar to

graphitic sheets. Because of this freedom of motion, it is believed that tension and torsional loads will not transfer between the layers of the MWCNT. High resolution transition electron microscope (HRTEM) images of several MWCNTs are given in Figure 1.6. As with SWCNTs, MWCNTs are synthesized with a capped end that allows the transfer of a compressive load between the walls via van der Waals forces. In addition to compressive loading, applied loads may also be transferred throughout the MWCNT structure if global or local buckling occurs. Buckling is discussed in more detail in Chapter 6. The presence of multiple walls does not change the axial stiffness of the nanotube compared to SWCNTs, but will significantly increase the bending stiffness.

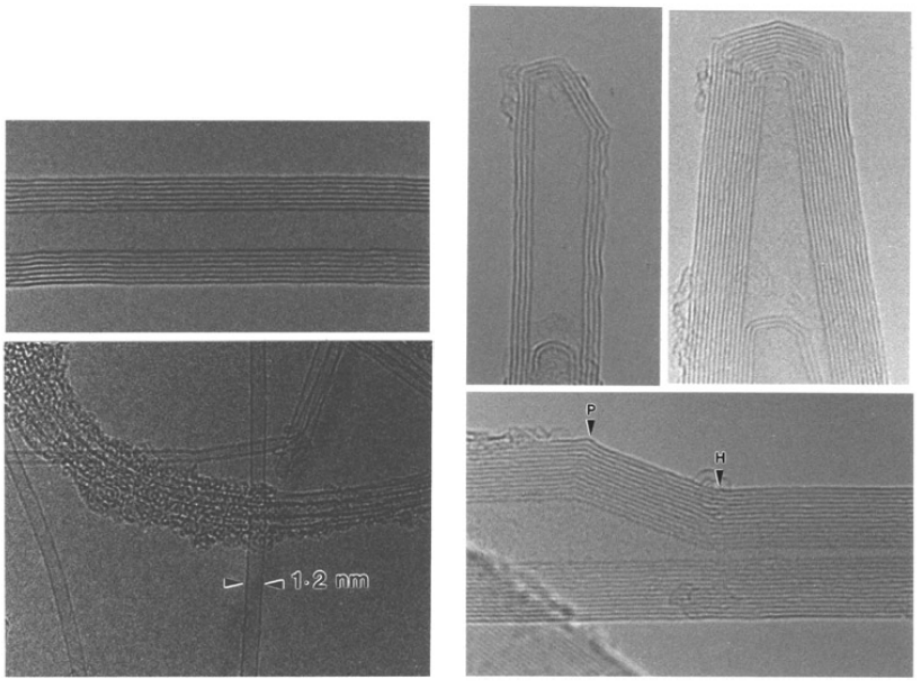

Figure 1.6. High resolution TEM images of various multi-walled carbon nanotubes. The image of a multishell nanotube showing the geometric changes due to the presence of five and seven membered rings (position indicated in the image by 'P' and 'H') in the lattice. Note that the defects in all the shells are well aligned. (From [21]. Reprinted with permission from AAAS)

1.4 Nanotube Synthesis Methods

Carbon nanotubes are synthesized through three primary techniques: arc discharge, chemical vapor deposition, and laser ablation. The arc discharge method involves sending a charge through two graphite rods placed a few millimeters apart creating plasma between the electrodes. The plasma vaporizes the carbon atoms; as they condense, they form a variety of carbon structures including fullerenes, nanotubes, and amorphous carbon. The quality of the nanotube sample is dependant on the stability of the plasma formed between the electrodes, current density, cooling, atmosphere, etc. [22]. This technique produces both SWCNT and MWCNT with a very low yield (25% of starting material [21, 22]). Nanotubes generated by this technique must be purified and separated from the other material generated during synthesis. In chemical vapor deposition (CVD) a hydrocarbon feedstock (commonly methane, ethane or ethylene) is passed over a substrate held at a temperature between 600-1000°C [23]. As the hydrocarbon feedstock decomposes, carbon atoms reform into either SWCNT or MWCNTs as they interact with the substrate surface [24]. Often, substrates used in the CVD synthesis technique are treated with specific catalyst materials to aid in the synthesis of nanotubes with a particular structure. CVD synthesis is capable of producing very high yields of nanotubes; however the defect concentration tends to be higher than other methods. Laser ablation, as the name implies, uses a laser to vaporize a graphite source material and the nanotubes are formed in a process similar to that of the arc discharge technique. This process produces SWCNT and the laser source can be tuned in order to control nanotube diameter [25].

1.5 Applications

The size and extraordinary properties of these molecules have made them prime candidates for replacing conventional materials or used in the development of new

technologies. There are numerous potential applications for carbon nanotubes in materials and micro-electromechanical systems (MEMS). The high stiffness, strength, and aspect ratio have led to applying carbon nanotubes (CNTs) in composite materials as fiber reinforcement [26]. Because of their small size, the nanotubes could be used along side with the liquid resin used in mold injection technologies, a common commercial technique for making plastic parts. Unfortunately, there are several obstacles that exist before such applications become commercially feasible. The first, and most significant, obstacle to implementing this technology is the cost of bulk material. In applications such as composites, where uniform material properties are required, the bulk nanotube material will often require a series of purification steps in order to achieve homogenous properties. Also, uniform dispersion of CNTs in composite materials remains a technical challenge [27-29]. Currently, there are several companies selling carbon nanotubes. These companies offer a range of carbon nanotube products for both industry and academic customers. Offerings include pure, functionalized, and length specific SWCNT or MWCNTs, as well as industrial grade supplies. Costs scale with sample purity.

A number of applications of carbon nanotubes in micro-electromechanical systems have also been proposed. Using their high aspect ratio dimensions, CNTs could

Figure 1.7. Illustration of telescoping walls of MWCNT. (Image courtesy of Lawrence Berkeley National Lab.)

be used as structural components in MEMS systems, dramatically reducing their size into nanoelectromechanical system scale. Another proposed use of MWCNTs is to use them as mechanical bearings, taking advantage of the free rotation the layers have with respect to each other [30]. In this application, the outermost shell would be mechanically clamped or pinned to a device followed by exposure of one or more inner shells (Figure 1.7). The interior tubes would be a free rotating axis while the remaining exterior shells can be used as structural components in MEMS systems. MWCNTs can also be used as gear-like structures. The nanotube would act as a shaft while gear-like teeth are imbedded in the outer wall of the structure [31], an example is given in Figure 1.8. In addition to device applications, other proposed applications for nanotubes include hydrogen fuel storage [32] and drug delivery [33]. The applications of carbon nanotubes are, for all intensive purposes, limited only by ones imagination and capability to construct such devices.

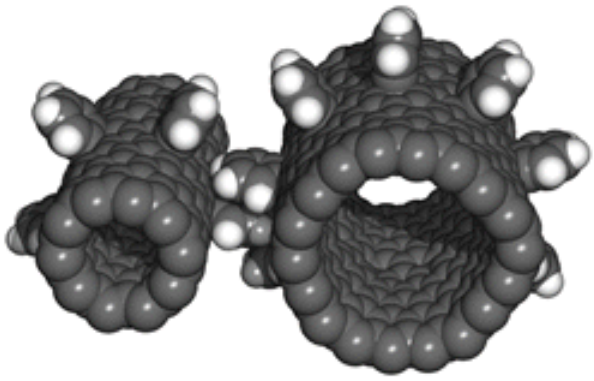

Figure 1.8. Carbon nanotube based gears utilizing embedded benzene molecules. (image courtesy NASA, Ames Research Center)

1.6 Measurements of CNT Mechanical Properties

Mechanical property measurements have been performed on either individual nanotubes or nanotube-containing composite materials. Nano-composite testing is simpler because the sample dimensions are compatible with conventional mechanical testing methods. Traditional mechanical testing becomes difficult to implement on nanoscale-sized samples. Simply put, picking up, pulling, bending, or twisting an individual nanotube is a nontrivial achievement. Although challenging, mechanical tests have been performed on individual single-walled and multi-walled nanotubes [9, 27, 34-53]. Ruoff et al. [47] have published a comprehensive review of nanotube mechanical experimentation.

1.6.1 Vibration Analysis

Due to their large aspect ratio and regular structure, nanotubes are often modeled as simple beams. Through monitoring the vibration of a nanotube, its Young's modulus (E) can be calculated. The first experimental measurement of the Young's modulus of multi-walled carbon nanotubes (MWCNTs) was performed by Treacy et al. [54]. In this work, the authors observed MWCNTs undergoing thermal vibration in a TEM image (Figure 1.9). The mean square vibration amplitude was determined to be proportional to the temperature within the instrument, confirming thermal excitation as the source for the nanotube vibration. The authors assumed equipartition of thermal energy among the vibrating modes and hollow cylinder geometry of the nanotubes. This allowed the Young's modulus to be calculated based on the observed vibration amplitude of the free end of the nanotube. Eleven nanotubes were examined, their moduli ranged from 0.40 to 4.75 TPa for the modulus with a mean of 1.8 TPa and an uncertainty of ± 1.4 TPa. Krishnan et al. [55] used this technique to determine the elastic modulus of SWCNTs.

These authors, examined 27 SWNTs and from these calculated the average modulus to be 1.3 (-0.4/+0.6) TPA from a study of 27 SWCNTs.

Advancing this technique, Poncharal et al. [56] used electromechanical excitation as a method to investigate the mechanical properties of MWCNTs from resonance frequency vibrations. This was accomplished though attaching a gold lead to a fiber composed of MWCNTs and electrically isolating them inside the TEM. A potential was applied to the sample through the wire to electromechanically excite the nanotubes. The authors found a relationship between the modulus and the nanotube diameter. For tubes with outer diameters less than 12 nm, the calculated Young's modulus was ~1TPa. For nanotubes with larger diameter, the modulus was calculated in the range of 0.1 and 1TPa. A TEM image of the electromechanical excitation of a MWCNT is given in Figure 1.10.

1.6.2 Nanomechanical Analysis

Nanoscale manipulation is the most direct means of experimentally determining the mechanical properties of carbon nanotubes. The atomic force microscope (AFM) has been an important tool in carrying out these measurements on nanotubes, as well as other nanomaterials. A limitation in using the AFM in this manner is that the nanotube must be laying on a surface. As a result, one must account for the tip interactions with both the nanotube as well as the substrate. For more complex mechanical tests, three-dimensional manipulation of the nanotube is required. The AFM is in the family of scanning probe microscopes and can be operated in several modes, including: lateral force, contact mode, or tapping mode operations. A more detailed description of this instrument is given in the following chapter.

Falvo et al. [9] used a nanomanipulator and a contact mode AFM cantilever probe tip to manipulate and bend MWCNTs deposited onto a mica substrate. The nanotubes had sufficient friction on the substrate to allow these operations to be performed.

Through manual manipulation of the nanotubes, the author was able to create large bends in the MWCNTs (Figure 1.2). During bending, buckling and rippling of the MWCNT surface was observed. The authors estimated that the MWCNTs could undergo a strain up to 16% without observable mechanical or structural defects.

The bending modulus of a MWCNT was directly measured using an AFM probe. This was accomplished by Wong et al. [57], using the lateral force mode of the AFM on immobilized nanotube samples on a MoS_2 substrate. The nanotubes were deposited at random on the substrate and pinned through the application of SiO pads using lithographic patterning (Figure 1.11a). Once secured, the substrate was imaged by the AFM until individual, secured nanotubes were located. MWCNT diameter and length were measured by sectional analysis of the image(s). The authors used the AFM probe tip to apply a lateral force at different locations along the length of the nanotube. A lateral deflection is observed on the cantilever beam as probe tip interacts with the nanotube (Figure 1.11d). This deflection is recorded with respect to scanner position. The friction with the substrate, rigidity of the cantilever beam, and lateral deflection are analyzed to determine the force acting on the nanotube. The bending modulus of the MWCNT is then calculated by fitting force versus deflection curve. The measured values of the bending modulus were 14.2±8.0 GPa, with a maximum measured value of 28.5GPa. These values are considerably lower than theoretical values for the MWCNTs. The authors postulate that the inclusion of defects within the MWCNT contributed to the difference between the observed and predicted values.

Salvetat et al. also measured the deflection of MWCNTs [52] and SWCNT ropes [58] under an applied load. In their method, the nanotube and nanoropes were deposited onto a membrane with 200 nm pores (Figure 1.12a). An AFM probe tip would be positioned at the midpoint of the carbon nanotube spanning the pore and used to apply a bending force, effectively performing a three-point bend (Figure 1.12b). Force versus

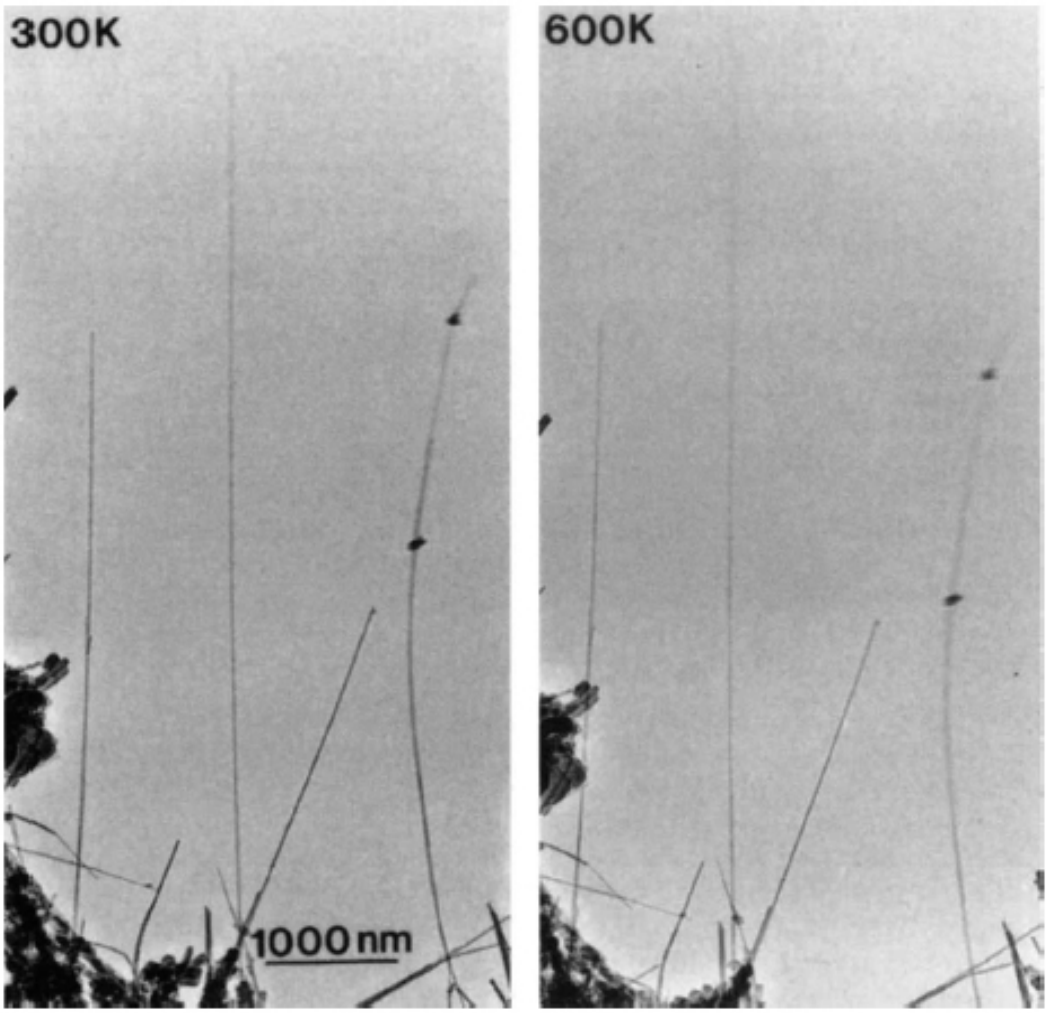

Figure 1.9. Bright Field TEM of free standing MWCNT fibers showing the blurring at the tips due increased thermal vibration. (Reprinted by permission from Macmillan Publishers Ltd: Nature [54], copyright 1996.)

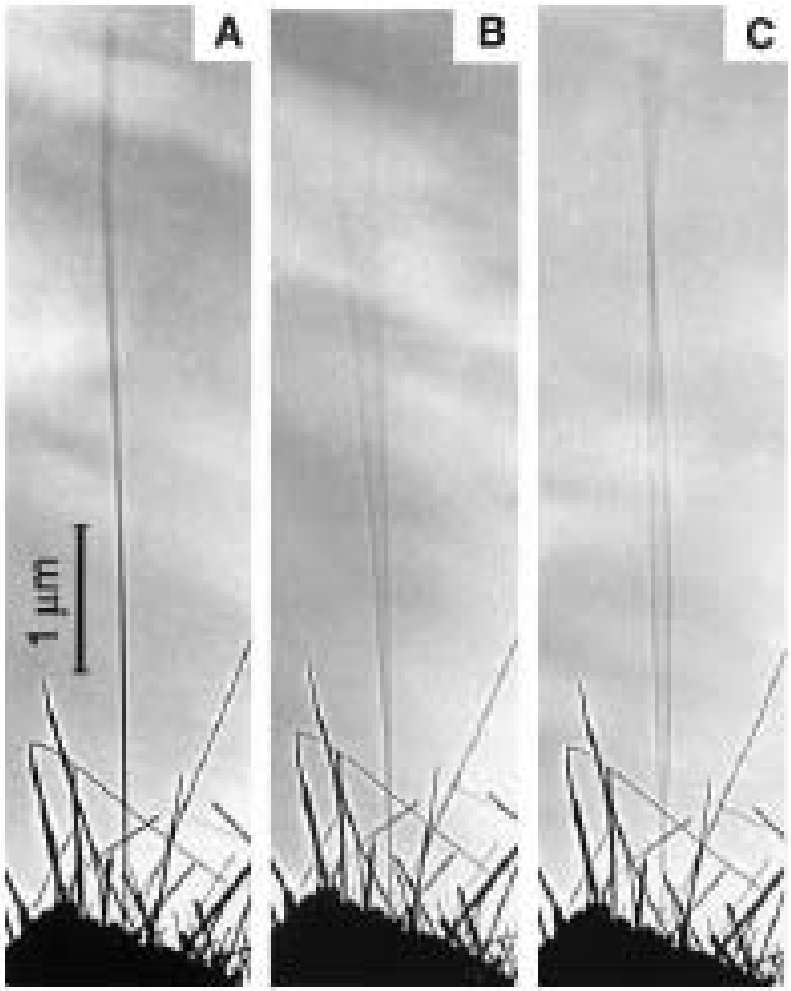

Figure 1.10. Nanotube response in applied resonant potentials: (A) no external excitation of the nanotube, (B) resonant excitation of the nanotube at its fundamental vibration (ω_1=530 kHz), (C) resonant excitation at the second harmonic (ω_2=3.01 MHz). The shape of the nanotube during excitation resembles that of a classical beam in primary and secondary vibration. (From [56]. Reprinted with permission from AAAS)

deflection data was captured during the deflection of the nanotube; this is used to calculate the elastic modulus of the individual nanotube or SWCNT rope bundle. Using the equation for mechanical deflection of a hollow cylinder, the elastic modulus can be calculated from the measured deflection and applied load force. The calculated elastic modulus for MWCNTs was between 10 and 60 GPa [52]. Both the elastic and shear modulus for the SWCNT rope was calculated. The elastic modulus of the SWCNTs were found to be near 1TPa while the shear modulus of the nanorope had a low shear modulus ($G \approx 1GPa$). The low shear modulus of the SWCNT ropes is hypothesized to be due to imperfections in the structure of individual tubes such as variations in tube diameter and/or vacancies in the tube lattice. These imperfections may increase the friction between the nanotubes within the rope inducing a large damping capacity [58].

Yu et al. [59] measured the axial tensile loading of multi-walled carbon nanotube. This was accomplished through the use of a custom stage capable of three-dimensional manipulation with the capability to pick-up, position, and clamp individual MWCNTs. This stage was designed to fit into an SEM, allowing the authors to perform the manipulations while imaging the nanotubes. To measure the tensile loading, an individual MWCNT was attached to the tip of an AFM probe through the use of the stage and localized electron beam induced deposition (EBID) of carbonaceous material [59]. The other end of the MWCNT was clamped to another AFM probe tip of lower stiffness (see Figure 1.13a). A tensile load was applied on the MWCNT, through a displacement of the more rigid cantilever through the use of a y-axis piezomotor. The applied force was measured by the deflection of the more pliant cantilever beam (Figure 1.13b). Using the stiffness of the pliant cantilever and the measured displacement, the force acting on the beam from the MWCNT is calculated. The maximum tensile load on the MWCNTs was measured as the load applied caused the tube to break. Once fractured, the nanotube was taken to a TEM to accurately determine the geometry and number of walls. The

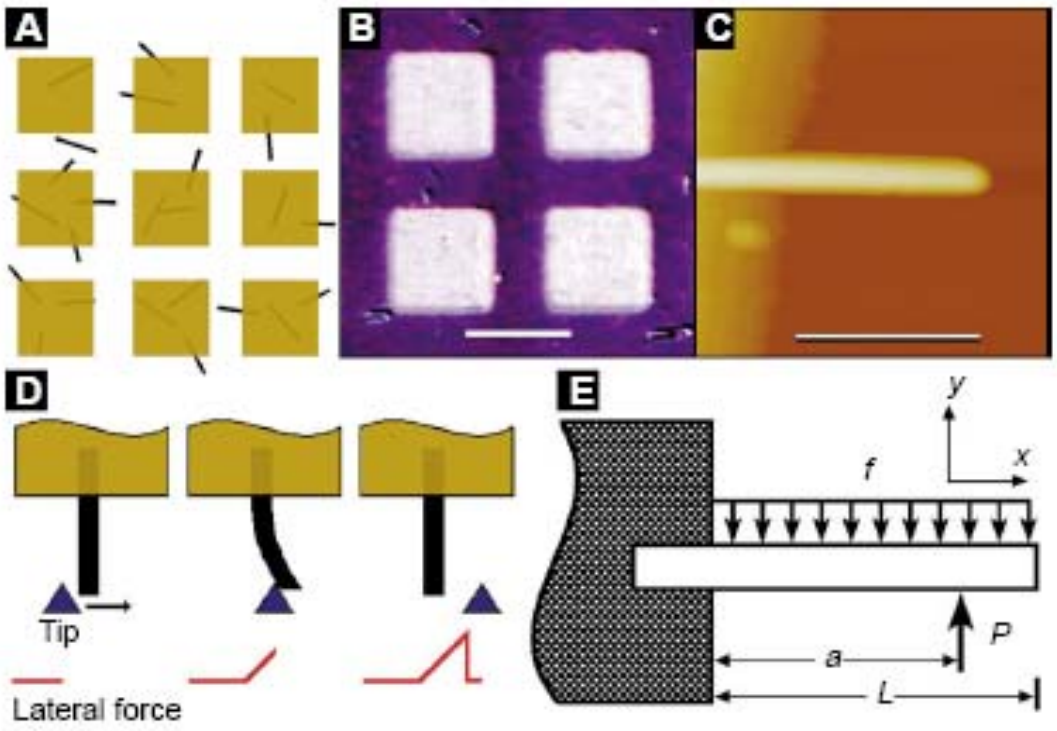

Figure 1.11. Overview of AFM measurement of bending modulus of MWCNT: (a) carbon nanotubes were deposited on a cleaved MoS_2 substrate, pinned in place by deposition of patterned SiO_2 pads, (b) optical micrograph of sample (scale bar is 8μm), (c) AFM image of 35.3 nm nanotube protruding from a SiO_2 pad, (d) schematic of beam bending by AFM probe tip (lateral force is indicated in red trace), (e) schematic of pinned beam of length L subjected to a point load P with a distributed load force of f. (From [57]. Reprinted with permission from AAAS)

measured tensile strength of the outermost layer of the MWCNTs was measured between 11 and 63 GPa; a value significantly lower than theoretical estimates for SWCNT tensile strength. Since the nanotubes were synthesized using the arc discharge method, the outer walls may have contained defects, thereby reducing its tensile strength. Using a similar attachment method, Chen et al. [46, 60] measured the tensile response of coiled carbon

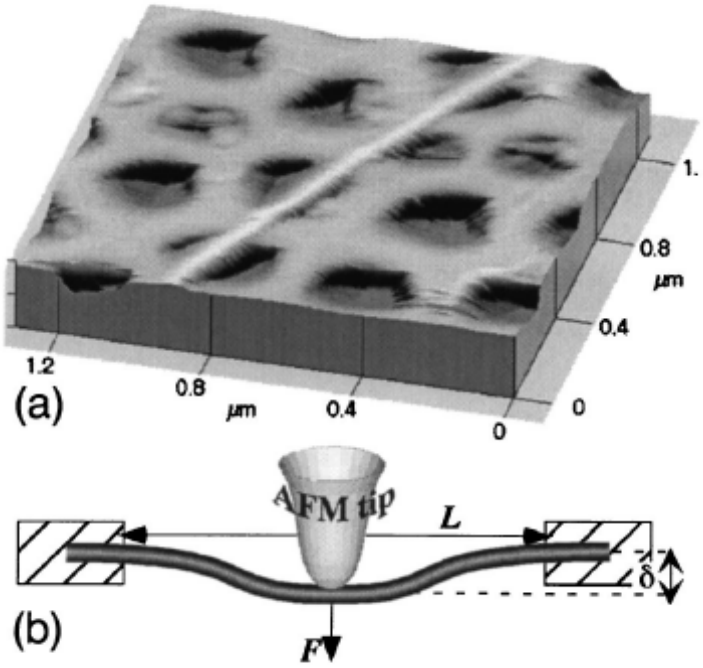

Figure 1.12. Three-point bending of carbon nanotubes.: (a) AFM image of SWCNT rope laying on a polished alumina membrane, (b) schematic of the AFM probe use to apply a bending force to the nanotube/nanorope. (Reprinted figure with permission from [58]. Copyright (1999) by the American Physical Society.)

nanotubes. This study demonstrated that the behavior of carbon nanocoils are analogous to elastic springs under tension (Figure 1.14). They found that the nanocoil could undergo an elongation of up to ~42% of the free length without measurable structural damage [46]. The nanocoil had a measured spring constant K of 0.12 N/m in a low strain regime. The spring constant was found to increase with the extent of elongation. The mechanical properties of the nanocoil were characterized on the basis of a nonlinear relationship between the spring constant K and shear modulus G, through the expression

$$K = \frac{G(d_o^4 - d_i^4)}{64R^3 N_c} \bullet \frac{1}{\xi} \qquad \text{Equation 1.1}$$

where d_0 is the outer diameter, d_i is the inner diameter, R is the radius of the coil, N is the number of coils, and ξ is a dimensionless coefficient for the geometry of the coil [46].

1.7 Summary of Material Properties

Table 1.1 summarize the values for Young's modulus, E, from various investigators using molecular mechanics simulations or experimental data. These published elastic modulus values for carbon nanotubes ranges from 0.76- 5.5 TPa. The table demonstrates that the mechanical properties of carbon nanotubes are highly dependant on the assumptions made by the investigators. For MWCNTs, a wall spacing of 3.4 Å is often used; derived from the spacing of the layers in graphite.

Table 1.1. Published values for the material properties of CNTs derived from molecular simulations.

Author(s)	Year	Modulus (TPa)	Thickness (Å)	N	Method	Trends
Robertson *et al*. [61]	1992	1.06	3.4		local density function	$1/r^2$
Yakobson *et al*. [62]+	1995	5.5	0.66		TB	
Yakobson et. al.[62]	1996	1.07	3.4	0.19	TB	
Cornwell *et al*. [63]+	1997	1	3.4		TB	$1/r^2$
Lu (MWCNT) [64]	1997	1.11	3.4		universal force	# of walls
Lu (SWCNT)[64]	1997	0.97	3.4		universal force	
Hernandez *et al*. [65]	1998	1.24*	3.4		density funct. theory (QM)	
Yao [66]	1998	1	3.4		universal force, tight binding	$1/r^2$
Ozaki *et al*.[67]	2000	0.98	3.4		O(N)	
Van Lier *et al*. [68]	2000	1.09	3.4	0.11	Hartree-Fock (QM)	
Zhou *et al*. [69]	2000	5.1	0.71		electronic band theory	$1/r^2$
Zhou	2001	0.76	3.4	0.32	LDF(QM)	
Belytschko *et al*. [70]	2002	0.94	3.4	0.29	modified Morse	
Troya *et al*. [71]+	2003	1.16	3.4		PM3 (QM)	
Troya *et al*.[71]+	2003	1.4	3.4		MSINDO (QM)	

* computed surface modulus of 0.42 TPa-nm
(QM) quantum mechanics method
+ study focusing on nonlinear responses (buckling or fracture)

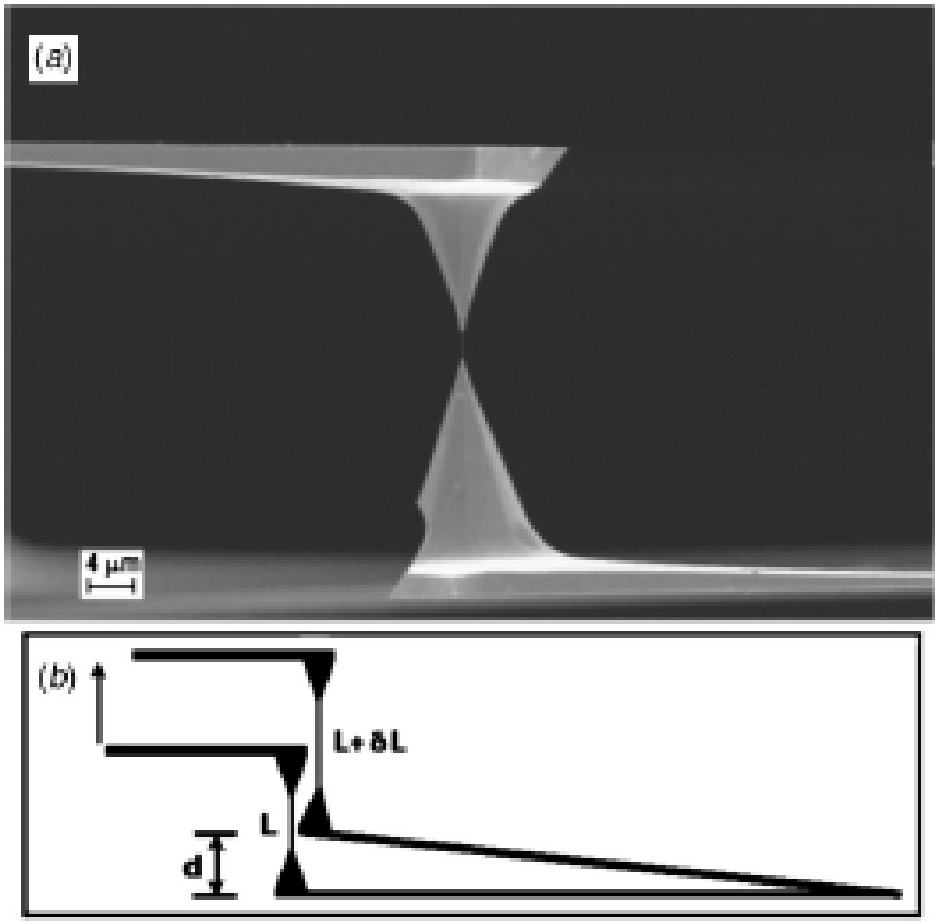

Figure 1.13 (a) individual MWCNT clamped between two AFM scanning probe tips. (b) schematic of tensile loading experiment. (From [8]. Reprinted with permission from AAAS.)

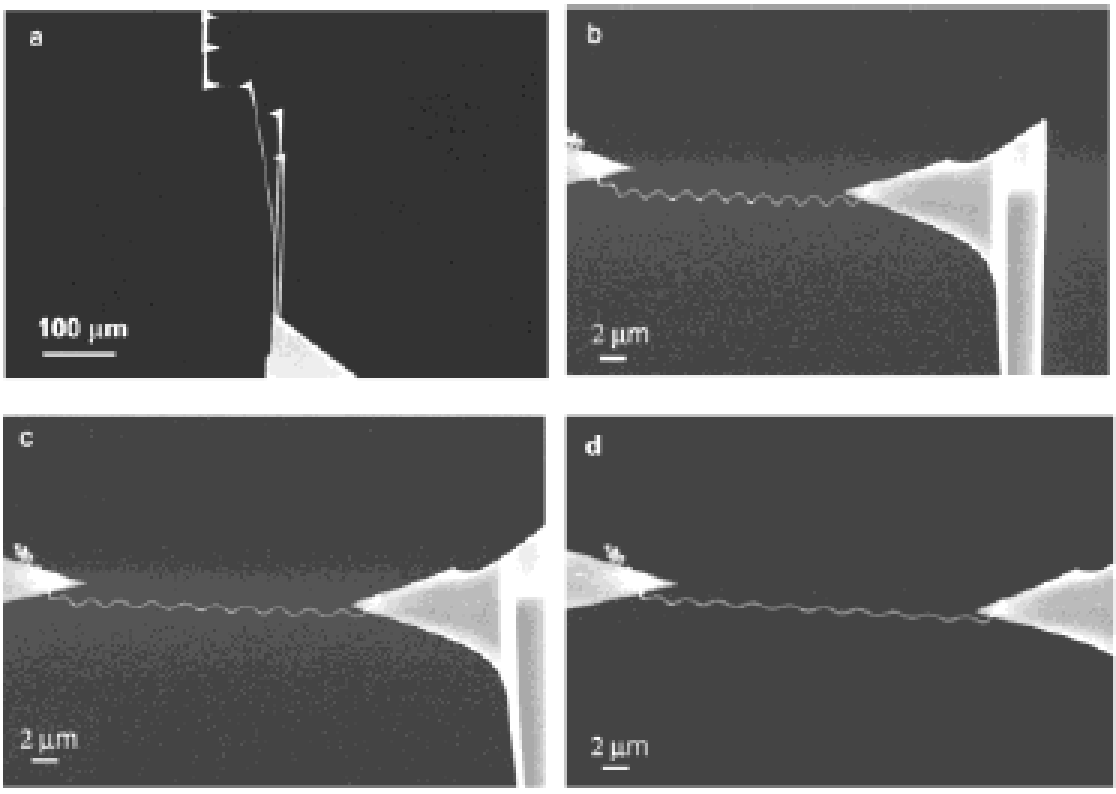

Figure 1.14. SEM images of the tensile loading of a carbon nanocoil. (a) A nanocoil clamped between two AFM cantilevers. (b) Relaxed nanocoil prior to loading. (c) Nanocoil at elongation of 20#. (d) Nanocoil at relative elongation of 33%. (Reprinted in part with permission from [46]. Copyright 2003 American Chemical Society.)

CHAPTER 2

SCANNING PROBE AND ELECTRON MICROSCOPY

2.1 Scanning Probe Microscopy

Scanning probe microscopy (SPM) encompasses a family of techniques that image surfaces using a physical probe. Scanning probe microscopes raster a probe across the specimen surface through the use of a piezoelectric actuator while recording the tip-sample interactions as a function of probe location. The field began with the invention of the scanning tunneling microscope (STM) in 1981 by Gerd Binning and Heinrich Roher [72], utilizing the quantum tunneling effect to interrogate the density of states on a sample surface. They were awarded the Nobel Prize in Physics for this invention in 1986. The STM is capable of generating atomic scale resolution of semiconducting and conducting surfaces. The atomic force microscope (AFM), invented in 1986 by Gerd Binning, Calvin V. Quate, and Christopher Gerber, interrogates the topography of many types of samples regardless of the sample conductivity [73]. The resolution of the scanning probe microscope varies between the different techniques; however it is highly influenced by the probe geometry and the resolution of a piezoelectric motor. A typical scanning probe microscope and controller are shown in Figure 2.1.

In many research groups, scanning probe microscopy is used in tandem with electron microscopy (discussed in the section 2.5), as both techniques are capable of resolutions near the atomic scale. Scanning probe microscopy offers several advantages over electron microscopy. The resolution of SPM microscopes is limited only by the size of the probe-sample interaction, rather than beam diffraction. The scanning probe microscope is capable of imaging in air at standard; pressures, under vacuum, or in liquid

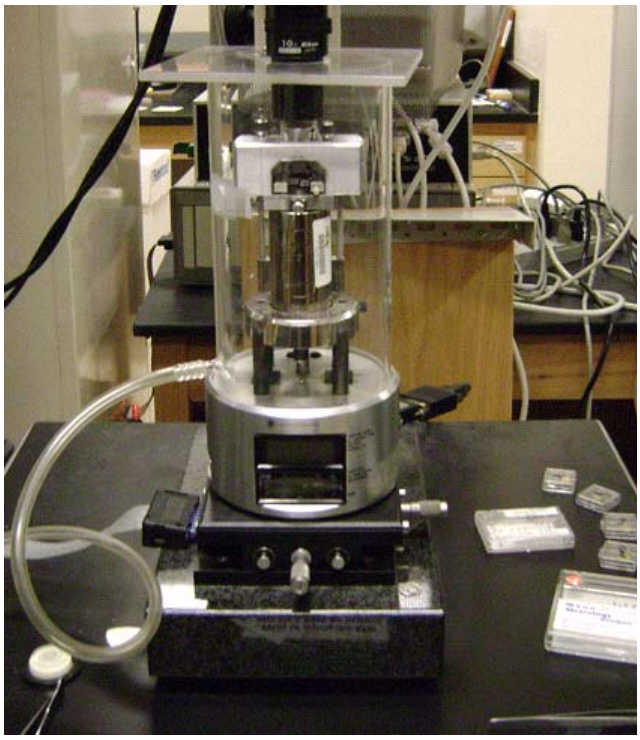

Figure 2.1. Veeco MultiMode IIIa Scanning Probe Microscope (SPM). The instrument is capable of atomic force microscopy (AFM) and scanning tunneling microscopy (STM) techniques.

[74-77] (using specialized specimen holders). Samples for electron microscopy must be held under a partial vacuum. This allows the use of scanning probe microscopes in the investigation of biological samples [78-81], thin film assembly in real time [82-85], or any number of other applications. In addition to sample topography, both the STM and AFM have been used to directly modify specimen surfaces. With the choice of a stiff probe, the AFM has been used to pattern a surface through the creation of nanoindentations [86-88], scratches [89, 90], or nanomanipulation of features on the sample surface. In 1989, Eigler and Schweizer [91], researchers at IBM's Zurich Research Laboratory, reported the manipulation of individual xenon atoms using an STM at ultra low temperatures into a highly ordered array (Figure 2.2).

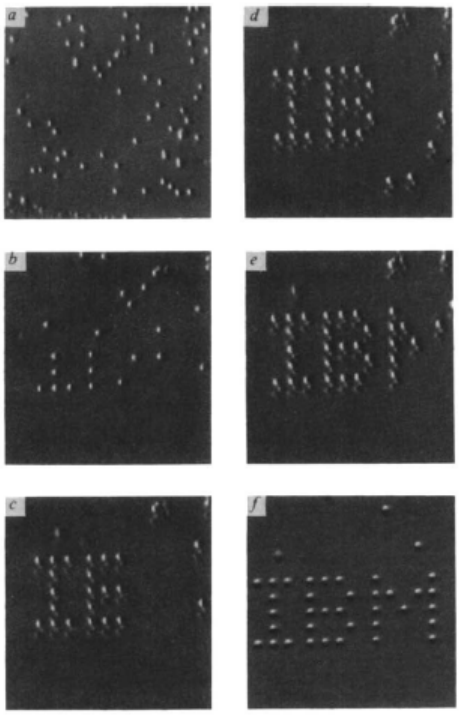

Figure 2.2. A sequence of STM images taken during the construction of a patterned array of xenon atoms on a nickel (110) surface. (Reprinted by permission from Macmillan Publishers Ltd: Nature [91], copyright 1990.)

Scanning probe microscopy is not without its own limitations. The image resolution is greatly limited by the tip size and geometry. The scan rate of scanning probe methods is slower than those of electron microscopy due to the raster time of the piezoelectric actuator. Some research groups are investigating methods of improving the speed and resolution of scanning probe techniques through modifications of the probe design. Onaran *et al* [92] integrated a probe tip onto a micromachined optoacoustic membrane creating a high speed atomic force probe capable of up to 60 kHz scan rate, an order of magnitude greater than conventional speeds. Some SPM techniques are limited in their ability to probe the interior features of specimens. The AFM is primarily used for topographic imaging; however phase imaging techniques can be used to interrogate interior sample features. The STM can tunnel several nanometers into a sample with the appropriate electron tunneling settings.

The AFM has developed into an invaluable analytical tool yielding information about the topography as well as chemical and physical properties of samples at the nanoscale. In order to obtain reliable information from the AFM, one must have knowledge of the components and the operating principles of the instrument.

2.2 Atomic Force Microscopy

The atomic force microscope (AFM) operates by measuring the interactions of a cantilever probe tip with the specimen surface as the two are moved relative to one another. Typically, the vertical deflection of the cantilever is measured during sample imaging. Torsional deflection of the cantilever beam can also be measured. The method of the raster varies from manufacturer to manufacturer. For example, Veeco Instrument Inc. (Plainview, NY) Nanoscope Models II and IIIa implement a piezoelectric actuator on which the sample rests, while the probe tip is held in a fixed position. Pacific Nanotechnologies (Santa Clara, CA) places the piezoelectric actuator on their cantilever, while the sample is in a fixed position. The advantage of this setup is that it allows for large samples and increased imaging speed. Originally, the cantilever probe deflection was directly recorded [73], through the mechanical connection of a stylus to the scanning probe. Modern instruments utilize a laser optic system to measure the deflection of the cantilever. A piezoelectric actuator or scanner is used for the precise control of the system in x, y, and z directions.

The basic setup of the atomic force microscope (AFM) is demonstrated in Figure 2.3. The AFM consists of the cantilever holder, laser optics, position sensitive detector (PSD), piezoelectric scanner, and computer controller. This setup is similar to that of the VeecoNanoscope IIIa (Veeco Instruments, Plainview, NY). The basic operation of the instrument consists of the following operations: 1) the sample is moved into close contact with the cantilever probe tip through the use of positioning screws for large scale

movements. Often an optical scope is used during this approach step. 2) The sample is brought into contact with the probe tip through Z-axis motion of the piezoelectric scanner (piezoscanner). The point of contact is determined from an initial deflection of the cantilever through a change in the reflected laser from the beam as measured on the PSD. 3) Once contact is achieved, the piezoscanner begins to raster the substrate under the tip in the X,Y-plane. As surface features interact with the tip, the contact forces cause deflections of the beam. The extent of the beam deflection follows Hooke's law. These are measured by changes in reflected laser optics incident on the PSD. The voltage change of the PSD is sent to the computer controller where it converts these voltage values to a distance value. This will correspond to the height of the feature deflecting the cantilever. 4) An image of the sample features are generated by correlating the collected PSD deflection signals with the x,-position of the tip on the sample.

2.2.1 AFM Components

The basic operation of the AFM is to measure sample surface features through the use of a probe. The means of accomplishing this vary between manufacturers as described previously. There are several common components. These include vibration isolation units, piezoelectric scanner(s), cantilever or other mechanical probes, detectors, and controller units.

2.2.2 Vibration Isolation

Although not specifically a component of an AFM, the use of a vibration isolation unit greatly reduces environmental mechanical and acoustic noise from interfering with image quality as the instrument operates by detecting the lateral or vertical deflections of

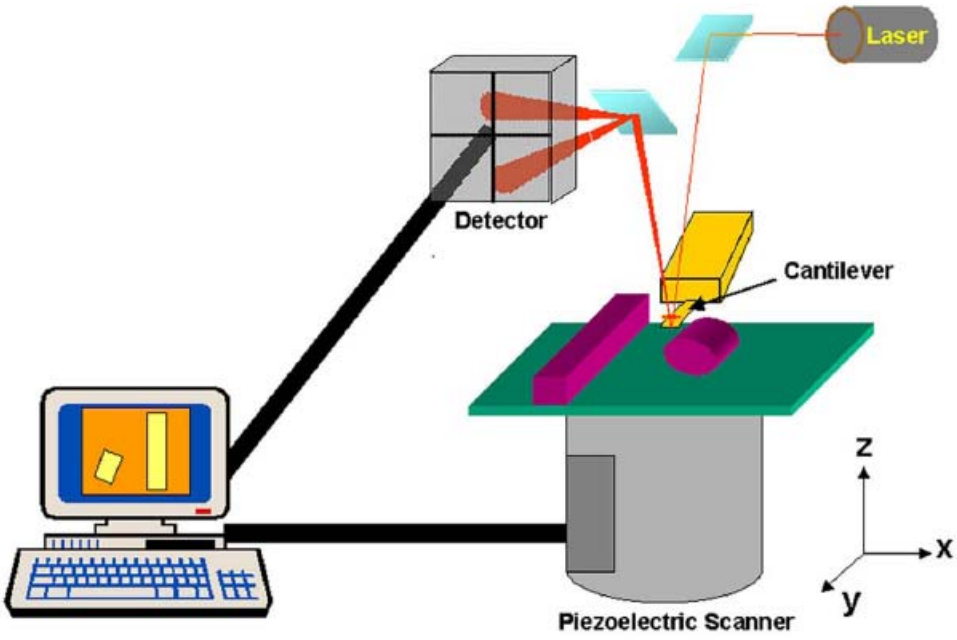

Figure 2.3 Schematic of basic setup and operation of AFM.

a cantilever. By mechanically isolating the cantilever beam, the sensitivity of the instrument is enhanced. In AFM operation, the mechanical isolation of the cantilever is analogous to the electrical shielding of the instrument wiring, and is completed through the use of rigid microspore designs as well as an external vibration isolation unit [93].

External vibration isolation units vary in design, cost and application. A simple unit can consist of using rubber stopper or pad between the instrument and the table (<$20) or a large concrete slab suspended by bungee chords (~$100); the latter is shown in Figure 2.4A More expensive units consist of pneumatically suspended tabletops (~$2,500) capable of isolating the instrument from a large range of environmental vibrations (Figure 2.4B). Without the use of vibration isolation units, using the instrument to visualize atomic-scale features is difficult, if not impossible.

2.2.3 Piezoelectric Scanner

Piezoelectric materials undergo a mechanical deformation in response to an applied electric field. A key component of the AFM is the piezoelectric scanner or motor, which consists of a column of piezoelectric material capable of precise displacements in the three dimensions when a controlled voltage is applied. The sensitivity and magnitude of the displacements of the piezoelectric scanner are determined from the column geometry. They are capable of operating at high resonant frequencies, allowing high scan rates in the instrument. Often manufacturers will sell different scanners with varying scan size values. Unfortunately, piezoelectric scanners (piezoscanner) exhibit both a linear and non-linear response to the applied voltage, and operation of the instrument should only be during the linear portion of the scanner motion (Figure 2.5). The response of piezoelectric materials, and thus the scanner, is sensitive to temperature fluctuations and are designed to be thermally insulated [94].

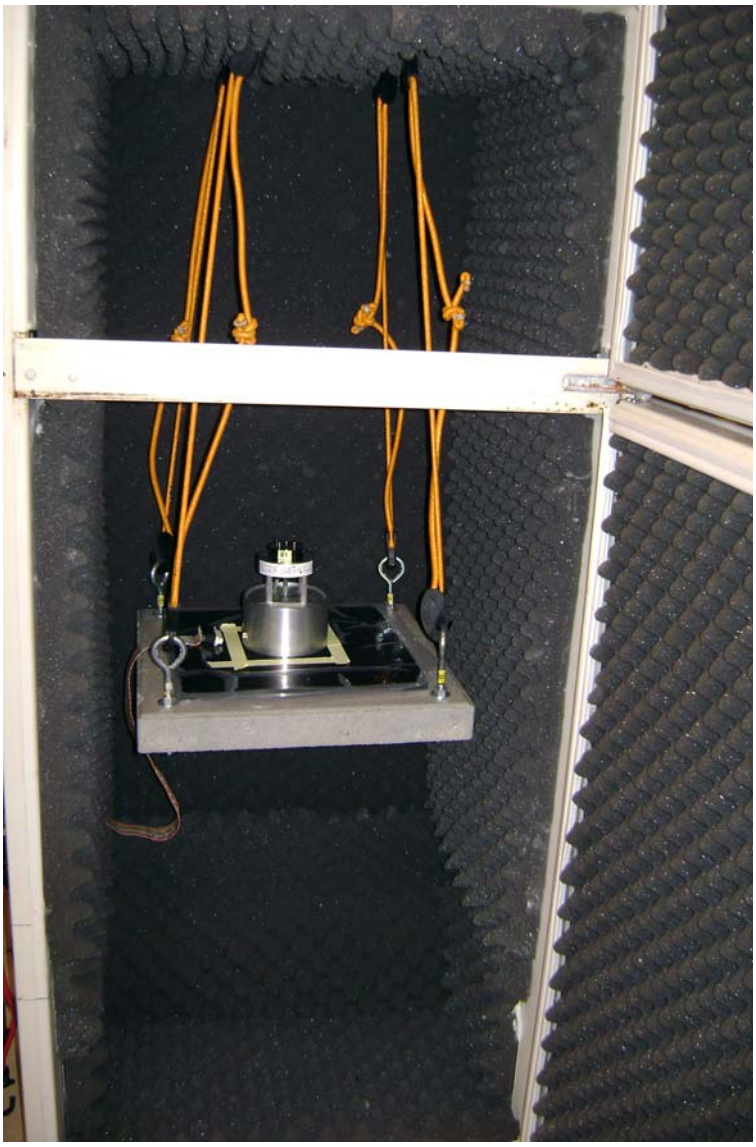

Figure 2.4. Image of bungee based vibration isolation system.

Because of the non-linear response of the piezoscanner frequent calibration required. The calibration allows the software to correct data collected during scanner operation in the non-linear voltage region. The scanner calibration procedure varies from between manufacturers, but is commonly performed using a standard surface grating created through a micromachining technique [95]. For best results, the scanner should be calibrated against a surface grating with features similar in size to those of the samples to be analyzed. Often a large scale (>10μm line spacing) and small scale (<1μm line spacing) grating are used to correct for the nonlinearities of the scanner.

In most cases the sample is mounted onto a metal specimen disc magnetically held in place on the piezoscanner. Tape or adhesive is often used to secure the specimen to the disc during imaging limiting the movement of the sample. When imaging a sample under fluid, a permanent adhesive (epoxy or glue) is often used. Careful consideration of the chemical inertness of the adhesive to the fluid must be determined to avoid failure or contamination from the adhesive.

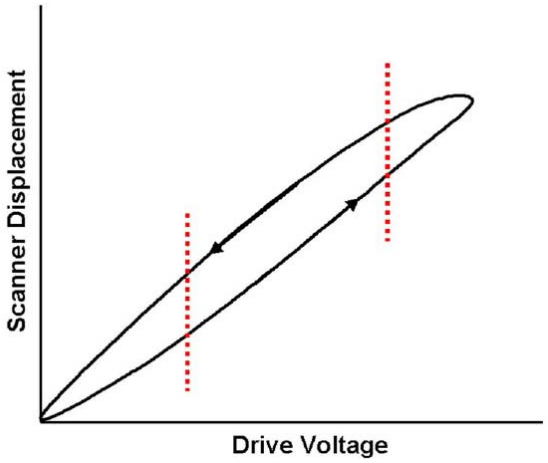

Figure 2.5. Image of the response of a piezoelectric scanner to an applied potential. The region in between the red lines represents the linear response.

2.2.4 Cantilever Probes

Cantilevers are commercially available from a variety of manufacturers. They are produced using microfabrication techniques (similar to those used in integrated circuit fabrication) from silicon or silicon nitride materials. Typically, the user chooses the cantilever based on its imaging application. Factors considered when choosing a cantilever include tip geometry, cantilever geometry, cantilever beam spring constant, resonance frequency, and cantilever material. To reduce interference from acoustic or building noise, the fundamental resonance frequency of the cantilever should be high. Both vibrational and thermal noise can reduce the sensitivity of the AFM and are both reduced through the use of shorter length cantilever beams. The cantilever tip geometry is of critical importance to the AFM image resolution. The tip sharpness, measured as a radius at the apex, is a key element in the capability of the AFM to resolve sample features.

Often the cantilevers are available with a metal coating on the topside of the beam (opposite the tip) to enhance the laser reflection from the beam material. There are two primary beam geometries for the cantilevers: triangular and rectangular. Triangular cantilevers are designed to reduce lateral (torsional) deflection of the beam. Rectangular beams are susceptible to torsional bending during contact imaging mode. Rectangular beam geometries are preferred for this reason for use in lateral force imaging.

Modification of the cantilever tips can be performed to enhance the performance of cantilever probes. The attachment of a carbon nanotube to the apex of a cantilever tip has become a popular enhancement due to the high aspect ratio of carbon nanotubes, smaller radius of curvature, and durability. The use of a nanotube modified tip enables greater capability to probe deep and narrow features; an ideal capability for profiling lithographic processes [96]. Several different attachment methods have been developed from electromechanical welding of the carbon nanotube to a metal coating of the

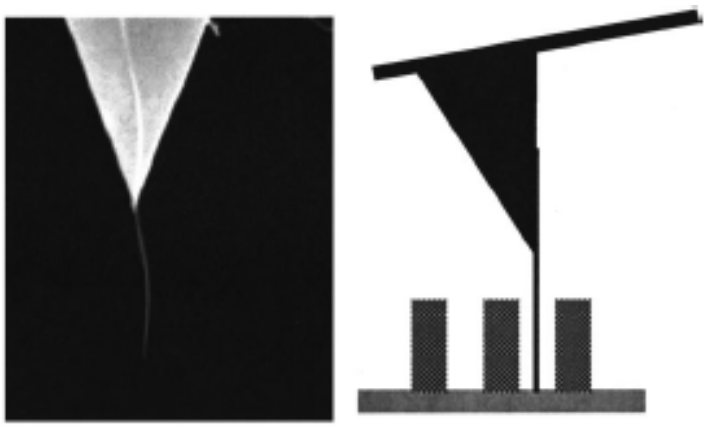

Figure 2.6. SEM image of a MWCNT modified scanning probe tip (left) and a schematic showing the ability of a CNT modified tip to trace the profile of trenches with deep narrow features (right). (Reprinted with permission from [96]. Copyright 2002, American Institute of Physics.)

cantilever tip [97] to the growth of the nanotube directly from the tip [98]. Tips can also be chemically functionalized to study chemically specific interactions between the tip and sample [99-104]. In this study, coiled carbon nanotubes are attached to the cantilever probe tips via the method developed by Stevens et al. [97].

2.2.5 Detectors

Commercial AFMs use laser optics to track the vibration and deflection of the cantilever beam. The instruments use optical detectors to measure changes in the beam as it interacts with the sample. The most popular laser detection system used in AFMs is the position sensitive detector (PSD). The PSD consists segmented photodiode transducers output a voltage commensurate with incident light intensity. Early generations of AFM PSDs consisted of a two-segment photodiode array capable of only measuring the vertical motion of the incident laser beam (vertical deflection of the cantilever beam). Later designs incorporated a four-segment or quadrant-photodiode array enabling capture of both the vertical and torsional deflection of the cantilever

beams. The torsional signal provides information about the frictional forces between the tip and sample. A schematic of the two-segment and quad-PSD are given in Figure 2.7. Cantilever deflection and torsion are determined from the detector. In the quad-PSD design, vertical deflection results in an intensity difference between quadrants A and C versus quadrants B and D. The cantilever torsion is determined by tracking the intensity changes of quadrants A and B against C and D.

Recently some groups have developed the means to directly measure the cantilever deflection. This has been accomplished through the integration of a silica piezoelectric detector (strain gauge) onto the cantilever[105-108]. Because it is a piezoelectric material, the resistance of the silica changes as the cantilever beam deflects. By monitoring the fluctuations of an electrical current through the silica, one can track the cantilever deflection. These cantilevers are useful for imaging samples that are light sensitive [109]. This research has also led to piezoelectric actuated cantilevers; allowing a significant reduction in the instrument size as the scanner is removed [105, 106, 110].

2.2.6 Controllers

The AFM controller is a critical instrument component that affects the precision, sensitivity, and performance of the microscope. The controller is responsible for collection and analog-to-digital (A/D) conversion of data from the detectors and the precise actuation of the piezoscanner. This component is also functions as a lock-in amplifier for the purposes of modulating the cantilever beam resonance for thermal tuning. The number of functions for the controller varies between manufacturers, but in general, serves as the interface device between the user and the instrument.

2.3 Imaging Modes

Atomic force microscope images can be acquired in various ways. Contact mode (also known as static mode) is a scanning technique where the sample and tip are kept in contact during image capture. Dynamic or intermittent-contact mode (also known as Tapping Mode™), involves the external oscillation of the cantilever beam allowing the tip to have minimal contact with the sample during image capture. Using either of these operating modes, the instrument can be used to interrogate van der Waals forces, capillary interactions, chemical bonding, electrostatic and magnetic forces, friction forces, etc [111] in addition to sample topography. Sample compliance can also be determined through the use of phase imaging and force volume imaging techniques.

2.3.1 Contact Mode Imaging

Constant-force imaging keeps the force exerted on the tip from the sample at a constant. The extent of deflection exerted on the cantilever beam through tip-surface interactions is used as the feedback signal for measuring the surface topography. This is achieved in a feedback loop that keeps a user generated set-point voltage from the photodiode signal at a constant value during the sample imaging. The effect of this is that the cantilever is held at a constant deflection during the sample raster process. The piezoscanner on the substrate compensates for topographical changes during the raster motion by changing the Z-axis position so that the net deflection on the cantilever is kept to the desired setpoint value. By tracking the changes that the piezoscanner undergoes, the controller computer can reconstruct the detail of the sample in a topographical image.

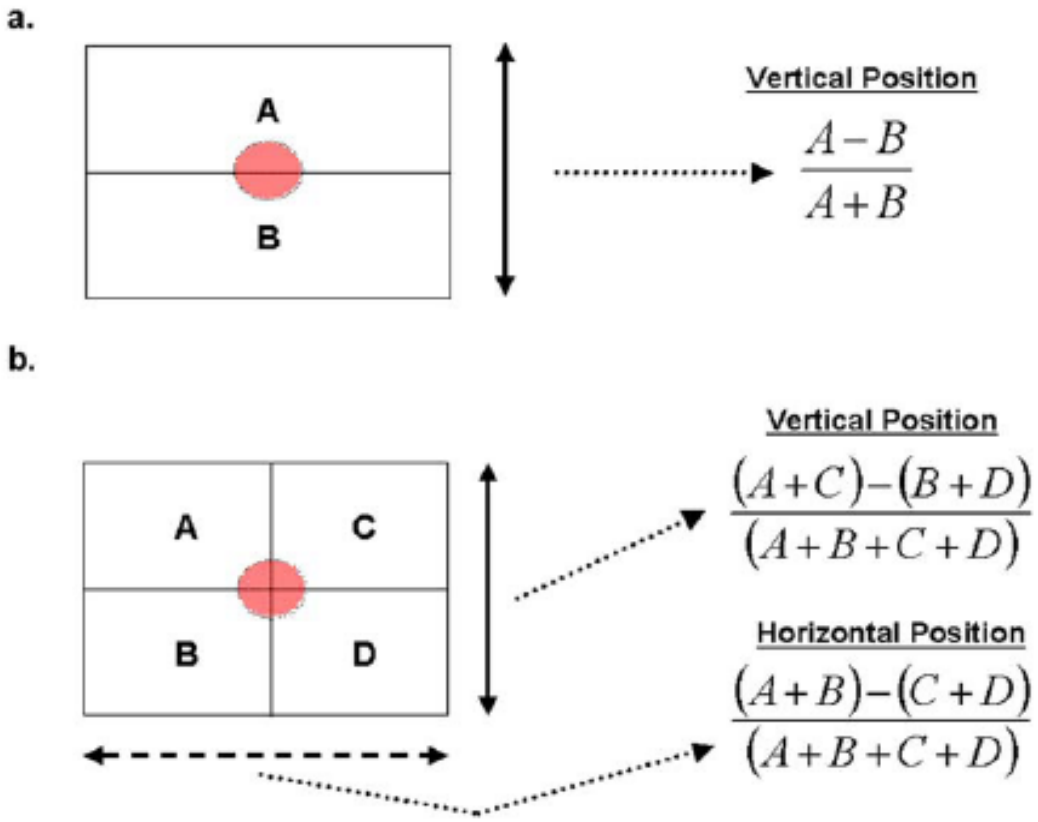

Figure 2.7. Schematic for two-segment (a) and four-segment (b) position sensitive detectors. The cantilever deflection and torsion are determined from the ratio of voltages on the detector quadrants defined on the given equations.

2.3.2 Torsional Mode Imaging

Torsional mode imaging is a secondary contact imaging method that measures the torsional (lateral) deflection of the cantilever beam as the tip interacts with the sample. As the tip is rastered across the substrate during most scans, the tip experiences lateral forces in addition to vertical forces. This operating mode is known as Friction Force Microscopy (FFM) or Lateral Force Microscopy (LFM) and measures frictional forces between the tip and the substrate. Cantilever torsion causes the cantilever beam to undergo torsional bending (twisting); this causes the reflected laser beam to move horizontally across the PSD (Figure 2.8 (top)). Applications of FFM include measuring the sample hydophobicity or hydrophilicity. For example, the friction profiles of an uncoated and octadecanethiolate(ODT)-coated Au(111) surface are shown in Figure 2.8 (bottom). The measured friction force of the tip on the modified Au(111) surface is less than that of the unmodified Au(111) [112]. Only AFM instruments with quadrant photodiode arrays are capable of this imaging mode. A specialized use of LFM is the Chemical Force Microscopy (CFM), where the tip is functionalized with a chemical species and scanned over the sample to detect adhesion differences between the tip and the species on the sample surface [113, 114].

2.3.3 Force Modulation Imaging (FM-AFM)

This technique is a secondary contact imaging method that measures substrate compliance (stiffness or elasticity) in addition to surface topography [115]. In this imaging mode, a secondary piezoelectric actuator oscillates the cantilever chip at a higher rate than the raster scan rate. This causes the force exerted by the tip to be modulated so that the average force on the sample is equivalent to contact mode imaging. The

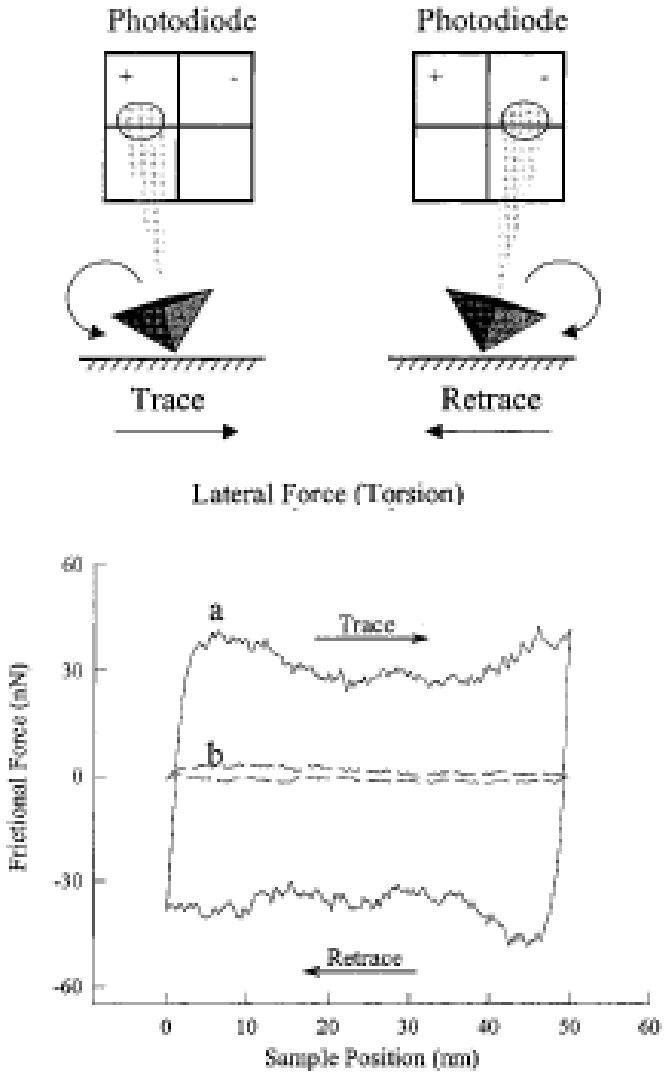

Figure 2.8. Friction force measurements with AFM. (Top) As the sample is scanned laterally, the cantilever experiences a torsion that deflects the laser beam laterally. (Bottom) Friction loops collected using an uncoated Si_3N_4 tip on (a) bare Au(111) surface and (b) octadecanethiolate (ODT)-modified Au(111) surfaces. The friction of the ODT/Au(111) surface is less than uncoated Au(111), indicative of the lubricating properties of the layer. Reprinted with permission from [112]. Copyright 1999 American Chemical Society.)

sample material resists the oscillation. Under the same applied tip load, a stiffer material will deform less than that of a softer material. In other words, a stiff material will resist the vertical oscillation of the cantilever causing the beam to deflect more than a softer material. This method measures the cantilever deflection as the oscillating beam is rastered across the sample. Sample compliance is measured through monitoring the variation in the deflection amplitude of the cantilever at the frequency of oscillation. The topographic information of the sample is collected simultaneously with the force modulation data.

2.3.4 Dynamic Mode

In dynamic (intermittent-contact) mode, the cantilever is externally oscillated. This is achieved through the use of a secondary piezoelectric actuator held in intimate contact with either the cantilever itself, or the cantilever holder. The piezoelectric actuator amplitude is driven by the controller module and typically applies an oscillation to the cantilever at a frequency near its natural resonance or harmonics. During imaging under this technique, the applied oscillation amplitude and frequency from the piezoelectric actuator serve as a reference. The measured oscillation amplitude, frequency, and phase of the cantilever are measured against this reference. During contact with the sample, the oscillation amplitude of the cantilever becomes dampened. This is due to a combination of van der Waals forces, electrostatic, and other forces acting on the tip as it approaches the surface of the sample [116]. The creation of a topographical image is similar to the feedback mechanism described in the contact mode imaging. Instead of holding the beam deflection constant, the damping factor of the cantilever is used as the feedback signal. The advantage of using intermittent contact

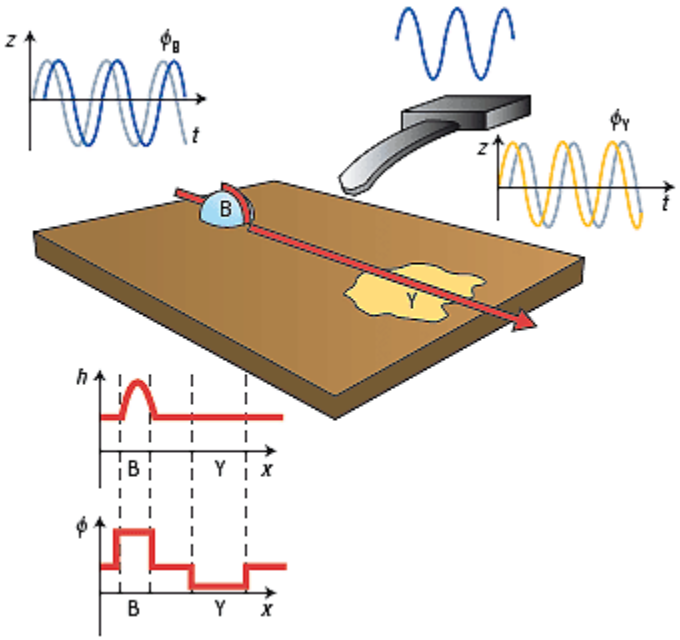

Figure 2.9. Schematic of phase imaging mode operation of AFM. The cantilever oscillation depends on the composition and topography of the sample. The phase shift signal occurs as the probe tip dissipates energy as it contacts the-surface. The illustration describes two local regions on a flat substrate (brown). The blue region (B) is made of different material, and protrudes from the substrate. The yellow region (Y) demonstrates a change in material properties within the substrate. The only the blue region will register in a topography image, while both the blue and yellow image will be measured during phase imaging. (Reprinted by permission from Macmillan Publishers Ltd: Nature Materials [117], copyright 2007.)

mode is that one can image more delicate samples (such as supported lipid bilayers) due to the decreased contact and forces acting between the tip and the sample [118].

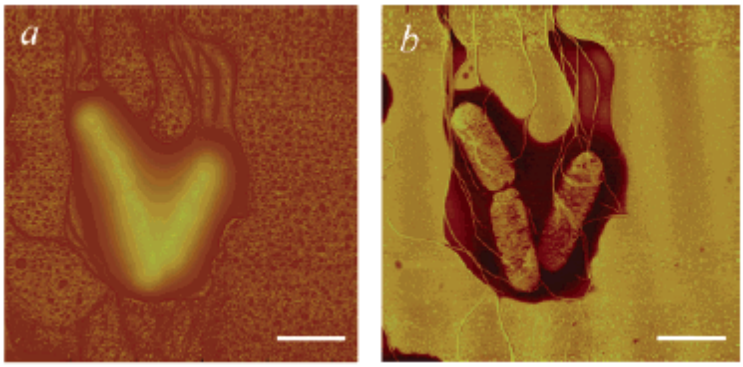

Figure 2.10. Contact mode imaging topography (A) and phase image (B) of three aggregated *Salmonella typhimurium* cells covered with an extracellular polymeric capsule. The phase image reveals the inner structure of the cell in addition to the continuity of the flagella. Scale bar corresponds to 2µm. (Adapted with permission from [119]. Copyright 2007 American Chemical Society.)

2.3.5 Phase Imaging

Phase imaging is a secondary dynamic mode technique that is capable of detecting variations in sample composition, adhesion, friction, elasticity. As previously described, during dynamic mode imaging, the cantilever is excited to its resonance oscillation through an external piezoelectric actuator (Figure 2.9). This amplitude is used as a feedback signal to measure the topographical features of the sample. During the feedback loop there is a lag between the input drive signal to the actuator and the beam oscillation measured by the PSD [117]. This phase lag is monitored simultaneously with the topography data. The sample stiffness and sample-tip interactions are the causes of the phase lag; similar to that of force modulation AFM. In addition to investigating the variations in material properties of the sample, phase imaging can also be used to

improve the contrast of a topography image. Figure 2.10 displays the use of phase imaging to interrogate the internal structures of *Salmonella typhimurium* cells covered with an extracellular polymeric capsule [119].

2.3.6 Non-contact imaging

Non-contact mode atomic force microscopy (NC-AFM) imaging obtains surface topography though measuring long-range molecular forces occurring as the cantilever is oscillated near the sample [101, 120]. This technique is also known as Dynamic Force, acoustic AC mode or wave mode AFM. In this mode, the instrument oscillates the cantilever near its resonant frequency. It then measures changes in the resonant frequency or vibration amplitude as the tip interacts with sample features. The sensitivity of this method can provide similar resolution to contact mode AFM. NC-AFM does not suffer from tip or sample degradation effects that are often observed during repeated scans with contact mode AFM.

2.4 Quantitative AFM Measurements

In addition to generating topography, friction, compliance, or any number of other images of the substrate, the AFM can also quantify the tip-sample interactions. This is commonly done through the use of force-distance curves or oscillation amplitude plots. These plots are obtained through disabling the x and y-motion of the piezoelectric scanner, allowing only the extension and retraction of the scanner in the z-direction. The instrument operator can control the scan rate, scan size, and scan start position to vary the contact force exerted between the tip and sample.

2.4.1 Force-Distance Curves

Force-distance curves (force curves) correlate the vertical deflection of the cantilever beam measured from the PSD against the vertical movement of the AFM scanner during a scan cycle. Force curves are commonly used to measure the vertical force that the tip applies to the substrate while a contact mode image is acquired. This allows the user to prevent excessive tip wear or sample damage during image acquisition, or to induce such damage. This technique can also be used in the quantitative analysis of sample viscosity as well as elasticity.

Several commonly encountered force-distance curve effects are displayed in Figure 2.11. An idealized force curve is presented in Figure 2.11a. This plot describes a scan cycle with no measurable tip-sample interactions. The plot consists of approach (blue) and retract (green) data collected during a single scan cycle. During the approach curve, there is no observable deflection (bending) of the cantilever beam until the space between the tip and sample is small (typically <1 nm). Under this distance, van der Waals interaction will begin to cause the tip to become attracted to the sample surface and a downward deflection will be measured in the beam, often called the "jump-to-contact" [86, 121, 122]. Since the scanner is still moving the substrate in the direction of approach, the beam will experience an upward deflection. This deflection will continue until the scanner motion is reversed or the cantilever breaks.

During the retract motion of the scanner the cantilever deflection returns to its original position, as long as no damage is experienced by the beam. Eventually, as the retract motion continues, the distance between the cantilever will be enough to remove the tip from contact with the surface. If an adhesive or attractive force is experienced by the tip, the downward deflection of the beam may continue past the jump-to-contact point. When the restoring forces of the cantilever exceed the attractive forces of the sample, the tip will release from the substrate and the cantilever will return to its original position (Figure 2.11b). Often, a hydration layer (water layer) will be present on either

the tip or sample, or both. This water layer can cause an attractive interaction between the tip and the sample that is not characteristic of the sample properties. To reduce the effects of the water layer, tips and samples can be stored in desiccators, or the AFM can be placed in a dry environment (N_2 box) or ultra high vacuum (UHV) during imaging [94].

The force curve depicted in Figure 2.11c describes the interaction between the tip and a long molecule on the surface. No significant effects are observed during the approach portion of the curve. During the retract portion of the curve the molecule undergoes unfolding followed by mechanical elongation beyond the jump-to-contact region. As the molecule unfolds, a more gradual deflection of the cantilever is observed relative to an explosive rupture or release event observed in Figure 2.11b.

The force-distance curve allows for quantitative analysis of the forces during the cycle as well as for the calibration of the instrument sensitivity. The mechanical load exerted by the cantilever is calculated by multiplying the total deflection of the cantilever by its spring constant. The optical lever sensitivity (OLS) is a measure of the commensurate movement of the laserspot on the PSD during cantilever deflection relative to the voltage applied to the scanner. This is a unique value to individual cantilevers. The units for the OLS are ΔV (PSD)/ ΔV (scanner). This value is used in several methods to determine the spring constant of the cantilever.

2.4.2 Oscillation Amplitude Plots

Oscillation amplitude (OA) plots are similar to force-distance curves. They are acquired during a single vertical scan cycle of the AFM scanner under dynamic mode operations. The curves are generated through monitoring the oscillation amplitude of the cantilever at a specific drive frequency during the approach and retract portion of the scan cycle. The oscillation amplitude plot can be captured simultaneously with, or

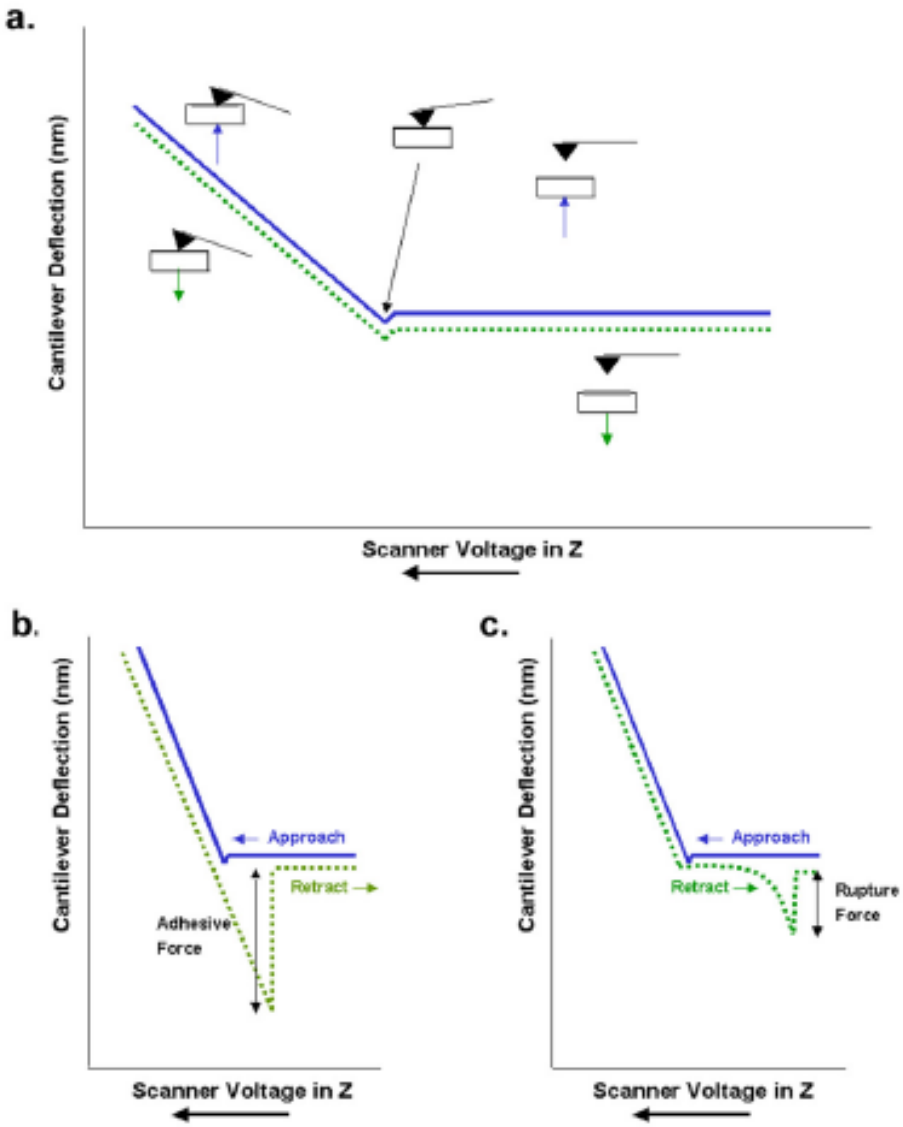

Figure 2.11. Force-distance curves describing beam deflection behavior with different surface interactions. The blue line represents the cantilever position as the scanner moves the substrate toward the probe tip (approach curve). The green line represents the cantilever position as the scanner moves away from the probe tip (retract curve). (a) Ideal force-distance response with no interfacial adhesion between probe and sample. (b) Typical force curve observed when adhesive interactions occur between tip and sample. (c) Force curve predicted when tension is placed on a molecule secured between the tip and substrate.

independently of, the force-distance curve. A typical oscillation amplitude plot is shown in Figure 2.12 along with a force curve that was simultaneously captured. During the extension of the scanner (green approach curve), the oscillation amplitude of the beam is unchanged until a small distance exists between the tip and the sample. At this point, as was the case with the force curves, van der Waals forces attract the tip to the sample surface causing a drop in the oscillation amplitude to occur. This occurs just prior to physical contact of the tip with the surface (jump-to-contact). As the scanner extension continues, the tip is in mechanical contact with the sample causing the oscillation amplitude to "bottom out" while the tip is pinned. This continues as the scanner motion is reversed, and until the adhesive (attractive) interaction of the tip with the sample is exceeded by the restoring force of the cantilever. When this occurs, the oscillation amplitude of the cantilever is almost instantaneously restored. A 'ringing' event is observed (far right portion of Figure 2.12b) as the cantilever tip ruptures from the surface and the cantilever returns from a state of mechanical tension returning to its fundamental resonance. The oscillation amplitude plot allows microscopists to precisely position the cantilever tip (through monitoring the amplitude drop prior to contact) into close proximity with the sample surface in order to minimize tip damage.

2.5 Electron Microscopy

There are a wide range of analytical techniques for the characterization of materials. The two commonly used for high resolution imaging of surfaces are atomic force microscopy (AFM) and scanning electron microscopy (SEM) [123-125]. These techniques share a number of similarities. The AFM rasters a physical probe across the sample and measure its interactions to form an image. The SEM scans a focused

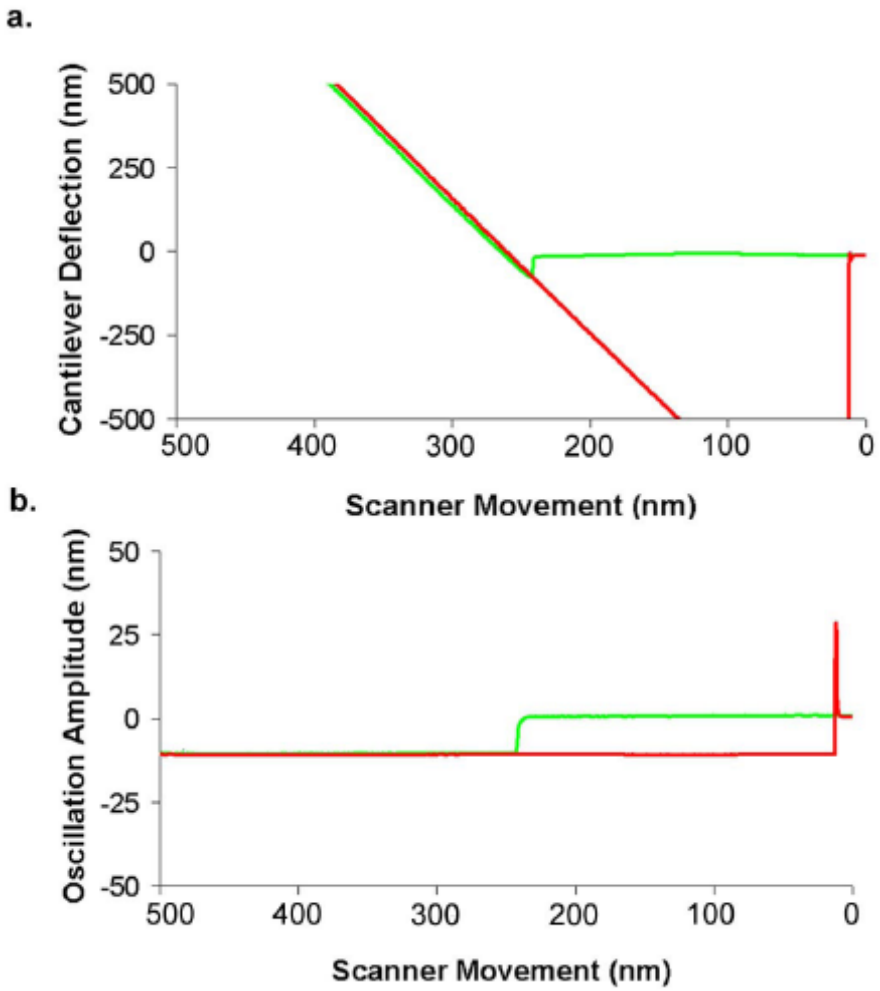

Figure 2.12. Force-distance curve (a) and oscillation amplitude plot (b) acquired during interaction of probe tip with a clean gold substrate. The green trace represents the approach curve, the red trace represents the retract curve.

electron beam across the sample surface. The AFM offers several advantages over the SEM in that it can be used on non-conducting samples, as well as in ambient or fluid environments. The AFM is also capable of providing topographical imaging of the sample. The SEM is not without its own advantages. It is capable of measuring the features of rough samples due to its large depth of field and lateral field of view. It is also capable of elemental analysis of the sample surface. When used as complements, these techniques provide a more complete representation of the surface, than if they were to be used independently.

2.5.1 Transmission Electron Microscopy

Electron microscopy is based on two fundamental discoveries: the wave-particle postulation formed by Luis de Broglie in 1924 [126], and that the magnetic field of a solenoid can bend electrons, discovered in 1926 by Hans Busch [127]. de Broglie was awarded the Physics Nobel Prize in 1929 for his discovery of the wave nature of electrons. These two discoveries led Ernst Ruska to the conclusion that it is possible to build a microscope which uses electrons instead of photons. This was realized in 1931 with the invention of the first electron microscope. Ruska was awarded the Physics Nobel Prize for this invention in 1986. His design, the basis for electron microscopes up to the 1970s, would later be known as the transmission electron microscope (TEM) [128]. A basic schematic of a TEM is shown in Figure 2.13.

The transmission electron microscope (TEM) has become an invaluable tool for the characterization of materials. It is the premier instrument for measuring microstructural properties. The basic operation of the instrument is analogous to a light microscope: a beam of electrons is passed through a thin sample where it diffracts after passing through the material. The diffracted electrons are collected and magnified through the use of a series of condenser and objective lenses. Either the diffraction

pattern of the beam, or the magnified image of the sample, can be viewed through the manipulation of these lenses. Although other techniques are also capable of measuring the crystalline structure of a material, such as x-ray diffraction [129], the use of electrons has several advantages over diffraction techniques. Unlike x-rays, electrons can be easily focused. This allows the creation of diffraction patterns from microscopic regions of the sample, used in the analysis of crystalline materials.

There are several imaging techniques that the TEM can perform beyond sample diffraction. The following is a discussion of some of the more common techniques. Diffraction contrast imaging [129] is used to image defects (dislocation, interfaces, second phase particles, etc) within a sample. As the electron beam diffracts through the sample, electrons with various intensities are generated. A diffraction contrast image is created by measuring the intensities of the diffracted beam. High resolution uses a high energy electron source causing a reduction of the transmitted beam diameter. In high-resolution transmission electron microscopy (HRTEM), the phase of the diffracted electron beam is preserved and can undergo constructive or destructive interference with the transmitted beam. Through the use of this technique, called "phase-contrast imaging", a column of atoms can be imaged. In addition to diffraction and spatial imaging, the HRTEM can also be used to obtain chemical information about the sample through energy-dispersive x-ray spectrometry (EDS) and electron energy-loss spectrometry (EELS). In EDS, an x-ray spectrum is acquired from small regions of the sample that are illuminated by focusing the electron beam. These x-rays are compared against the characteristic x-rays from chemical elements to determine the concentration of the elements within a sample [130]. In EELS the energy losses of the electrons after they travel through the sample are measured, where they have undergone plasmon excitations to core electron excitations [131, 132]. The chemical information of the sample is determined from the collected EELS spectra. There are several basic TEM imaging modes each is capable of providing different information about the sample. The

techniques mentioned above are the most common imaging modes. For a more in depth discussion of the operation of the TEM and material diffraction, the reader is referred to the book by Fultz and Howe [129].

2.5.2 Scanning Electron Microscopy

The first SEM was built in 1938 by von Ardenne by rastering the electron beam of a TEM to create what is now commonly known as a scanning transmission electron microscope (STEM) [133, 134]. In 1942, the first SEM for bulk samples was developed by Zworkin et al., containing many of basic principles of the modern SEM [134, 135] described in Figure 2.14. A number of improvements have been made on the instrument since this time, resulting in an increase in the instruments resolution from 50 nm in 1942 to ~0.7 nm today. Several other functional improvements were developed enabling the instrument determine the sample composition through measure of X-rays, backscattered electrons, cathodeluminescence, Auger electrons, and specimen current [136].

Because the SEM operates through electron beam travel and detection, the sample must be both conductive and able to withstand vacuum. A voltage is applied between the sample and a filament, resulting in electron emission from the filament. In order to achieve this, the sample chamber must be held in a vacuum environment ranging from 10^{-4} to 10^{-10} Torr. The electrons are guided to the sample and focused by a series of electromagnetic lenses in the beam path. The resolution and depth of field for the instrument are determined by the beam current and the size of the electron beam as it contacts the sample. The beam is focused by a series of condenser lenses followed by probe-forming objective lenses. In addition to focusing on the sample, the lenses also help to minimize the effects of spherical aberration, diffraction and astigmatism [136]. After the incident electrons interact with the surface, secondary or backscattered electrons are emitted. The SEM image is formed by detecting the intensity of the secondary

electrons at each x, y point of the surface during the rastering of the electron beam across the sample.

In addition to the sample morphology, the SEM is capable of investigating the sample composition. This is accomplished through the detection of other emissions from the interaction of the probe beam with the sample. The two most common signals detected for composition are the X-ray and backscattered electrons. The X-ray signal is used to provide elemental analysis through the addition of an electron-dispersive spectrometer (EDS) or wavelength-dispersive spectrometer (WDS) [130, 136]. The backscattered electrons go deeper into the sample due to low-energy loss during its collisions. The percentage of electrons that emerge from the sample in this method have been found to be dependant on the atomic number of the sample material [137, 138]; allowing this signal to be used to investigate sample composition [139].

The instruments discussed in this chapter were vital for the study of the mechanical properties of coiled carbon nanotubes. The AFM was used for the precise control of the compression of the nanocoil. The SEM enabled the measurement of the nanocoil orientation and dimensions. The TEM allowed investigation of the chemical structure of the nanotubes.

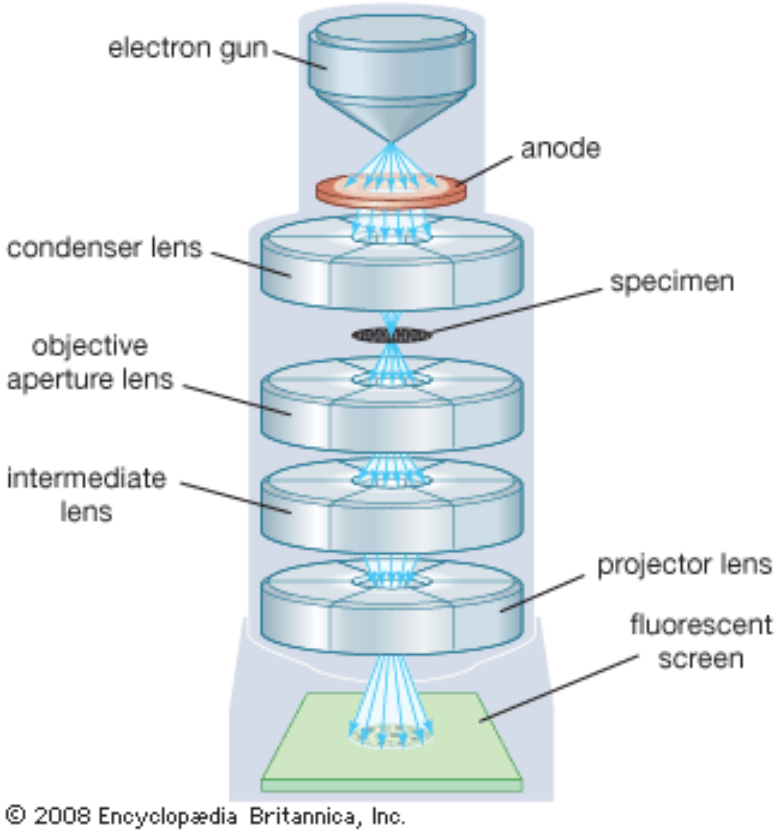

Figure 2.13. Illustration of the primary components of a transmission electron microscope (TEM). (By courtesy of Encyclopaedia Britannica, Inc., copyright 2008; used with permission)

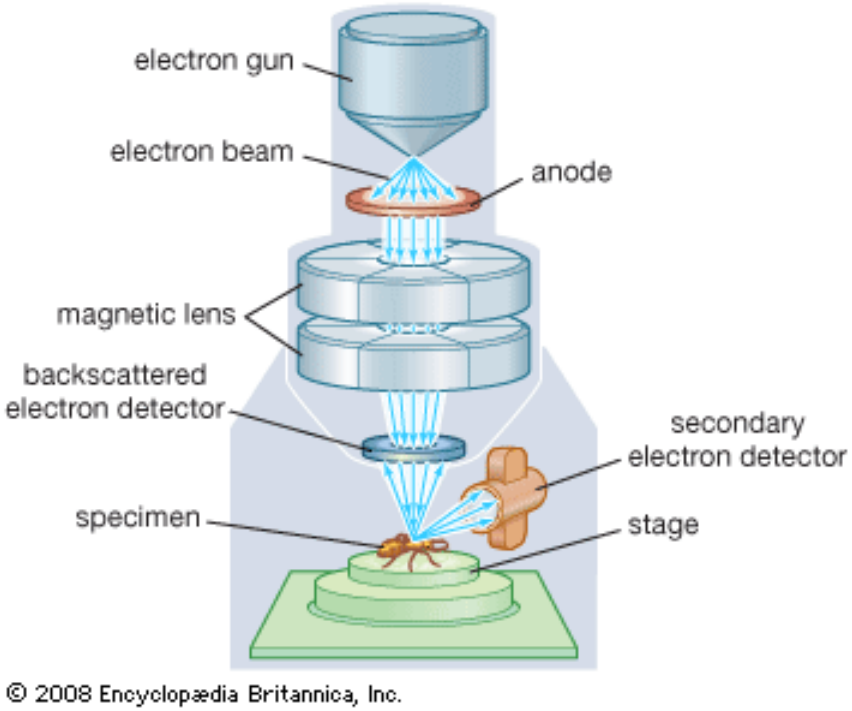

Figure 2.14. Illustration of the primary components of a scanning electron microscope (SEM). (By courtesy of Encyclopaedia Britannica, Inc., copyright 2008; used with permission)

CHAPTER 3

EXPERIMENTAL DESIGN

The atomic force microscope (AFM) was the primary tool for the manipulation of the nanotubes during the study. To enable mechanical compression studies of an individual coiled carbon nanotube, several unique instrument modifications and experimental methodologies were created. Nanotubes were affixed to a commercially available cantilever probe. The AFM hardware was modified to allow the collection of signals not readily available from the manufacturer. Custom software was developed in house, to acquire, process, and analyze these signals during the compression of the nanocoil. To enable determination of the chemical structure of the carbon nanocoils, modifications to conventional specimen holders for SEM and TEM were also required. This chapter describes these instrumental and procedural improvements in detail.

3.1 General Experiment Overview

Compression tests on the CCNT modified tips were conducted using a Veeco (Santa Barbra, CA) Nanoscope IIIa scanning probe microscope under a nitrogen environment (relative humidity below 6%). The microscope was modified to gain access to raw vertical and horizontal deflection signals for use in multi parameter force spectroscopy (MPFS). General operation of the microscope was done through the use of Nanoscope 5R31 software. Calibration of the x,y and z motion of AFM piezoelectric scanner was conducted using NIST certified calibration gratings (MikroMasch) and the instrument software.

Each compression test commenced with cycling the piezoscanner in the z-direction for ~2hours using an unmodified cantilever probe to allow the scanner to reach thermal equilibrium. This ‘warm up’ period would reduce scanner drift during the

compression of the nanocoils. After the warm up period, the modified cantilever was loaded into the cantilever holder and the instrument was set to Tapping Mode™ operation. In Tapping Mode™ operation, the oscillation amplitude is used to determine the point of contact between the cantilever and the substrate. By monitoring the oscillation of the cantilever, approach to the surface occurs with less risk of tip damage. Next, the fundamental beam vibration frequency is identified and the amplitude of the secondary piezoelectric actuator is set to achieve a user defined oscillation. Typically, the oscillation is set between 0.5 and 1.5V depending on the cantilever stiffness. After tuning, the extension of the scanner begins and continues until the coil contacts the surface. The contact set-point is determined by a user defined oscillation damping factor that occurs as the oscillation amplitude decreases as the tip approached the substrate. To protect the nanocoil from damage, the instrument is set to false engage the surface with an oscillation amplitude damping factor set to 1.4.

When the set-point is triggered, the microscope is immediately toggled from image acquisition mode to force curve operations. In this mode, the cantilever deflection is monitored as a function of scanner vertical motion. Both the force distance data and oscillation amplitude data for the system can be displayed in this mode. The user is then able to manually adjust the piezoscanner position to bring the nanocoil into contact with the substrate. All compression studies were conducted with a scan velocity of 50 nm/s with a scan size of 2.5μm and scan rate of 0.02Hz. Force curves and oscillation amplitude plots were captured using these settings with and without external excitation to the cantilever beam. For frequency capture, the external excitation was turned off allowing only thermal vibration of the cantilever to be measured. The DAQ was also used to acquire the time-dependent deflection data, piezo drive voltage signal, and the horizontal deflection signal. The settings for the cantilever resonance frequency capture by the LabView software were set at a window size of 7000 FFT points, 400 kHz frequency range, and 400 waterfall points recorded. An ensemble average was taken for

every 15 of the Fourier transforms to increase the signal to noise ratio of power spectral density (PSD) traces. These settings allowed approximately 2 cycles to be monitored during data capture with sufficient resolution within the ensemble to detail the compression event. The data was processed using custom software described below.

Following the compression tests, the nanocoils were imaged using both SEM and TEM. The SEM imaging was to determine if any damage was incurred during the compression tests. In almost all cases, the nanocoils exhibited no deformations from the study. The TEM was used determine the chemical structure, number of walls, for the nanocoils. This information is used to model the compression of these structures. TEM imaging was not conducted prior to compression tests to avoid any beam induced damage that may occur on the nanocoils. The last operation performed on the nanocoils was to determine the optical lever sensitivity (OLS) of the beams. This value is used in the several frequency calculations, as well as in relating beam deflection to applied force. Ideally, the OLS would be measured for each beam prior to the attachment of the nanocoils; as the method to determine OLS requires tip contact with a rigid surface. To preserve the nanocoils, a custom stage was designed to deflect the cantilever beams under standard AFM operation without making contact to the CCNT. Through the use of this stage the OLS for the beams were measured.

3.2 Nanotube Modified Scanning Probe Tips

Due to their unique geometry and mechanical properties, carbon nanotube modified tips are ideal scanning probe structures. Carbon nanotube modified tips can be fabricated in a number of ways. Cheung et al. [98] have grown individual single-walled carbon nanotubes (SWCNTs) directly on the cantilever probe tip using the CVD method, described previously. The catalyst material and growth conditions can be changed for either SWCNT or MWCNT growth. This approach provides little control over the

nanotube orientation. The carbon nanotube tip can be shortened, increasing its resistance to bending or buckling, and sharpened to improve its lateral resolution using current induced oxidation [140]. While this approach enables batch fabrication of nanotube-modified tips, characterization of tip orientation and tip shortening must be done on a tip-by-tip basis. A second approach for preparing CNT-modified tips involves picking up individual nanotubes from a surface and securing it to the cantilever or the probe. The nanotubes can be either clamped, via electron beam induced deposition [8], or welded, via arc discharge [97], to the cantilever probe. The coiled carbon nanotube (CCNT) modified cantilever probe tips used in this study were fabricated in this manner [97].

Coiled carbon nanotube modified cantilever probe tip fabrication was completed at NASA Ames Research Center (ARC) under the tutelage of C.V. Nguyen and R.M. Stevens. The fabrication was completed through the following changes to the arc discharge method described above. Uncoated silicon cantilevers (NSC-18) purchased from MikroMasch (Wilsonville, OR) were coated with 5 nm of nickel to provide the conductive path for the arc discharge. The nanotube source material was generated from a proprietary CVD catalyst developed at ARC. This catalyst was deposited onto a copper wire and nanotube growth was completed using standard CVD methods. The catalyst material was such that a low yield of multi-walled coiled carbon nanotubes were grown onto the wire. The curvature of the wire, along with the low yield of nanotubes along the surface, allowed individual nanocoils to be addressed. Both the nanotube source and the cantilever were each mounted onto a three-stage micromanipulator. These were mounted on top of a Zeiss Axioskop (Germany) inverted optical microscope. The optics of the microscope included large working distance lenses that created a total magnification of 1000x, along with various polarizing filters to enhance the visualization of the individual CCNTs. A Hewlett Packard 6234A dual output power supply was used to anchor the nanocoil to the tip. The cantilever was connected to the negative electrode and the nanotube source was connected to the positive electrode. Once aligned via the translation

stages, 25V was applied and the current was increased until arc discharge occurred. This technique takes advantage of the alignment of nanotubes with an applied current observed during arc discharge synthesis, first reported by Saito et al. [141]. Figure 3.1 illustrates the precision to which CCNTs can be aligned with the cantilever tip using this approach. A schematic of the attachment apparatus id given in Figure 3.2. A batch of ~50 cantilevers was prepared with a variety of coil geometries and lengths.

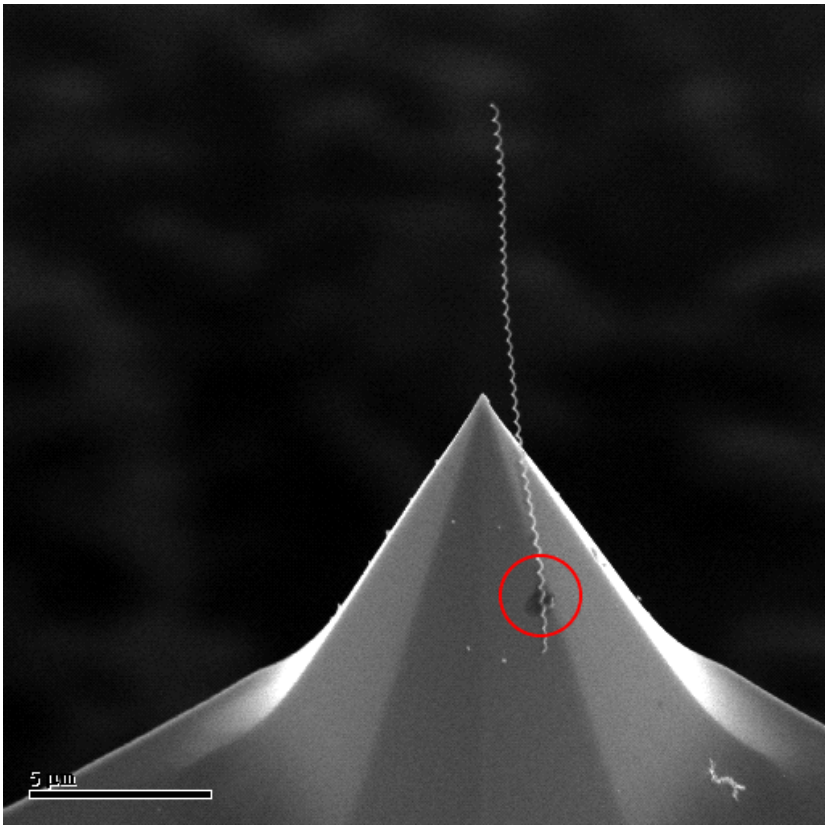

Figure 3.1. SEM image of a coiled carbon nanotube (CCNT) modified cantilever probe tip. The attachment point (red) is believed to be a covalent bond formed during the arc discharge attachment method.

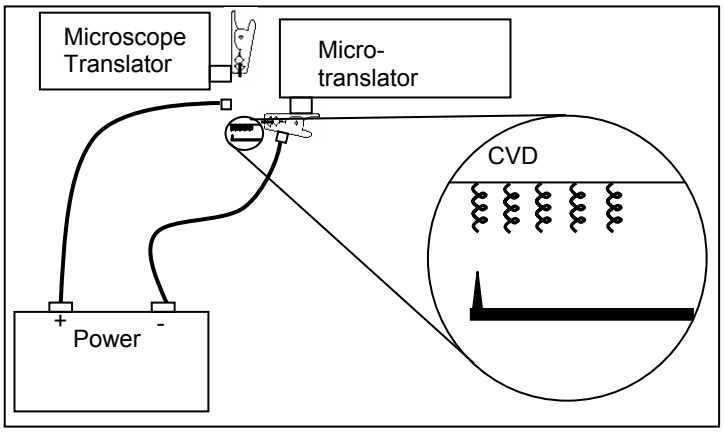

Figure 3.2. Schematic for the cantilever modification apparatus. Silicon cantilever was coated with nickel to provide a conductive surface to facilitate arc discharge. A coiled-MWNT sample and the cantilever were translated within close proximity of each other. A voltage is applied to create an arc discharge attachment of the nanocoil to the cantilever.

3.3 Cantilever Selection Criterion

The primary metric used in determining the cantilever for the CCNT modification was the force (spring) constant of the beam. This constant is often expressed in values of force per unit length and represents the flexural response of the beam to an applied load. Commercial suppliers of cantilevers express the force constant of the cantilever beams in units of Newtons per meter (N/m). The larger the force constant value, the greater the force that must be exerted to the beam to cause it to deflect. Recall that these cantilever probes are primarily used in an AFM, where the instrument measures the displacement of the cantilever beam caused during interactions with sample surface.

At the onset of this investigation, the effective stiffness of the nanocoils was not known. The relative stiffness of both the nanocoil and the cantilever has direct impact on the utility of the AFM for measuring the compression behavior of the carbon nanocoils. Mechanical loading of the nanocoil occurs through the restorative force of the cantilever;

to be measured by the instrument, the compression of the nanocoil must effect a deflection of the cantilever beam. If the cantilever is too pliant, the mechanical load is insufficient to cause compression of the nanocoil. If the cantilever is too rigid, nanocoil compression occurs without any measurable beam deflection.

MikroMasch (Wilsonville, OR) scanning probes were used in this study. This choice was made based on the immediate availability of product supplies and the range of properties expressed in the available cantilever catalog. Two types of chips were used for CCNT modification: NSC-18 and CSC-38. Cantilevers on the former series have a manufacturer's rated force constant averaging 3.5N/m. The CSC-38 has a 3-lever design (Figure 3.3) where each cantilever has a different average force constant value: 0.08 N/m (beam A), 0.03 N/m (beam B), and 0.05 N/m (beam C).

Figure 3.3. SEM image of a three-beam cantilever (CSC-38). During nanocoil attachment, one or more tips will become modified. This is due to limited control of the attraction of nanocoils to the different cantilever beams.

Multi-Parameter Force Spectroscopy (MPFS) was developed to track the change of the thermally excited resonant frequency of the cantilever beam while measuring the

force-distance and oscillation amplitude data [142]. Monitoring the frequency response of the cantilever as it comes into contact with a surface enables measure of the elasticity, stiffness, and compressibility of the substrate as well as material places between it and the tip.

Limited information in the force-distance curve acquired using rigid beam compression is illustrated in Figure 3.4. At the point of contact with the substrate, no measurable deflection of the cantilever beam was observed. A frequency shift was observed indicating a compression event had occurred in the system. The force-distance response from the compression of nanocoil modified CSC-38 cantilevers given in Figure 3.5. With the pliant beam, linear compression of the nanocoil is observed.

3.4 Equipment Setup

3.4.1 AFM Hardware Modifications

MPFS has been developed in the Bottomley group to simultaneously measure several key signals generated during typical AFM measurements [142]. These signals include the vertical cantilever deflection, torsional cantilever deflection, thermal resonance frequency of the cantilever, and piezoelectric scanner position. Conventional AFM software does not provide this information to the user. Hardware and software modifications were made to the instrument to generate MPFS data during the compression of carbon nanocoils.

All force measurements and compression studies were conducted using a Nanoscope IIIa (Veeco, Santa Barbra, CA) atomic force microscope with extender electronics. The microscope was equipped with a signal access module (SAM) allowing access to signals used in the function of the instrument. The microscope was controlled

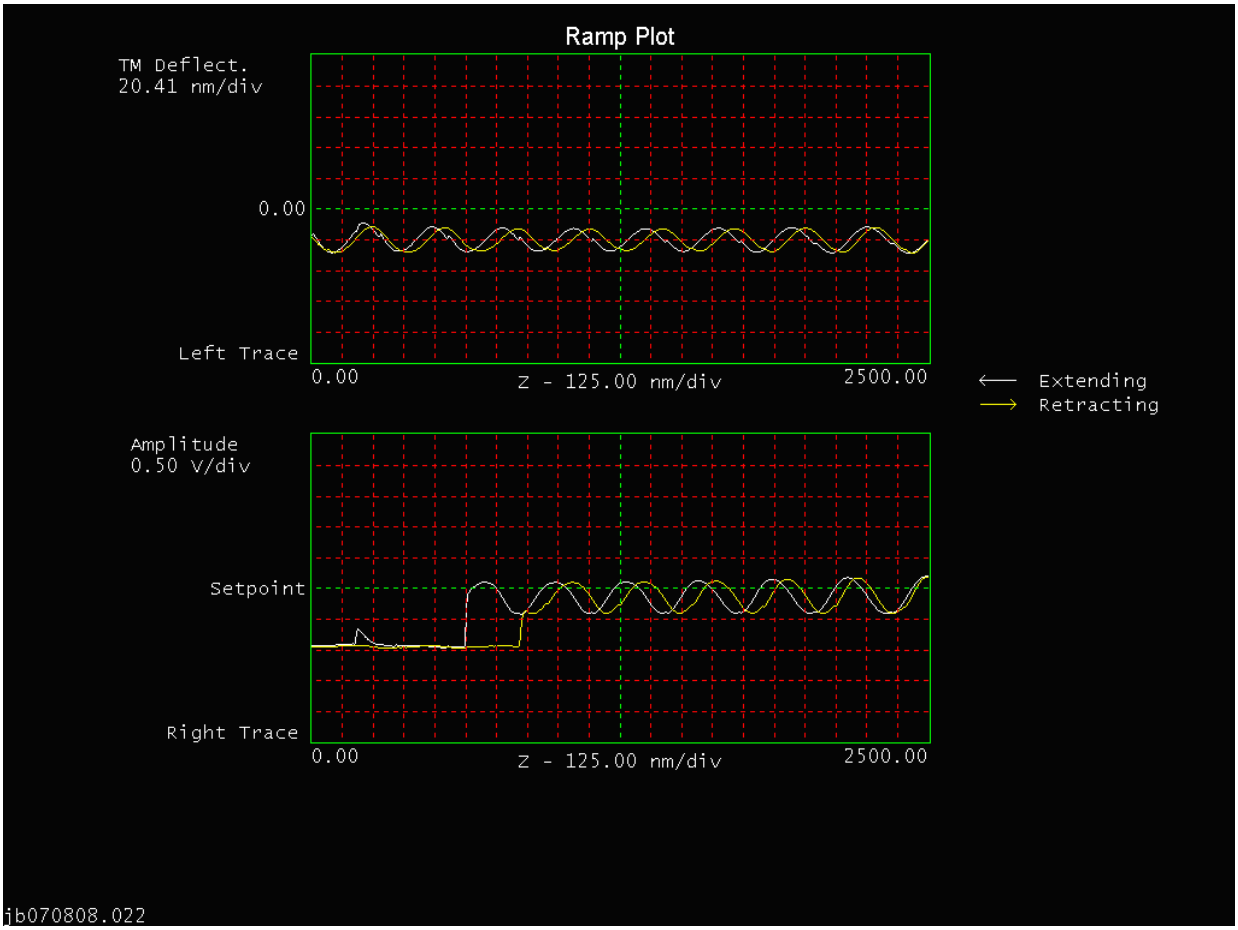

Figure 3.4. Force distance (top) and oscillation amplitude(bottom) plot of a coiled carbon under 625 nm compression. The cantilever has a 'rigid' beam with stiffness of ~3.5N/m (NSC-18). There is no discernable beam deflection occurring in the force distance curve. The oscillation amplitude plot displays the tip contact with the substrate. Approach curve in white. Retract curve presented in yellow.

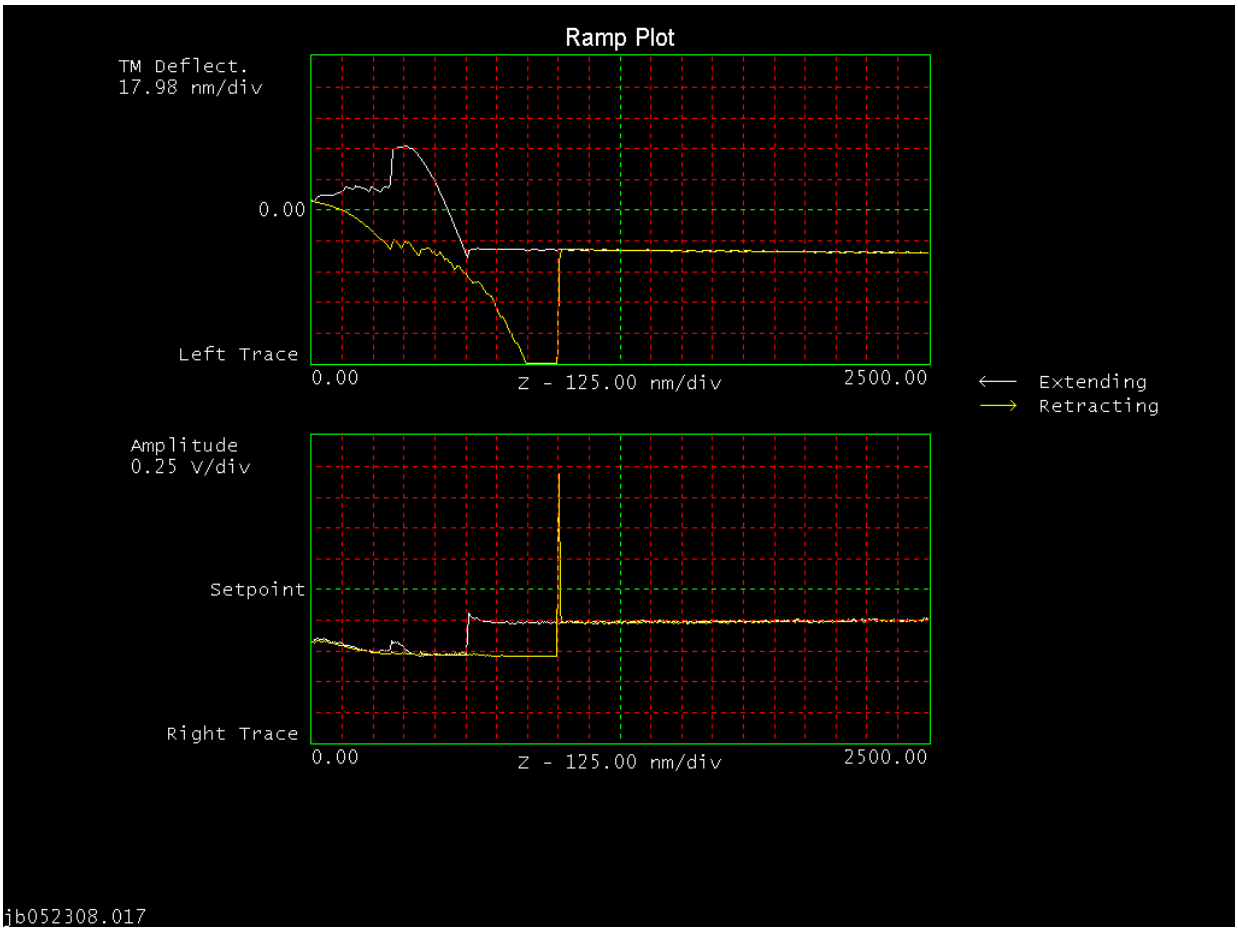

Figure 3.5. Force distance (top) and oscillation amplitude(bottom) plot of a coiled carbon under 625 nm compression. The cantilever has a 'pliant' beam with stiffness of ~0.03N/m (CSC-38, beam B). Both the force distance and oscillation amplitude plots show a response during the compression of the nanocoil.

using standard software supplied by the manufacturer. The SAM uses standard BNC cable connections to allow access to a variety of instrument signals.

During initial MPFS studies, the SAM was used as a source for the piezoscanner voltage, vertical and horizontal deflection signals. These signals were routed to a SRS 785 Dynamic Signal Analyzer (DSA) (Stanford Research System, Sunnyvale, CA) where the time-dependant deflection data was converted into the frequency domain using a BMH window to create power spectral density (PSD) plots. The DSA had a frequency range of 102.4 kHz. It was found that the deflection signals coming from the SAM were transformed with a low-pass filter. This would prevent the MPFS measurements of pliant cantilevers, as their resonant frequencies are often below the filter; with values between 10 and 20 kHz. After communication with the AFM manufacturer, it was determined that the true deflection signals were accessible through contacts on the instruments printed circuit board (Figure 3.6). Components U1, U5, and U6 contained the signals necessary for MPFS measurements. Using test probe and a multimeter, the following signals were identified on these components: raw vertical deflection signal (U1, pin1), PSD sum signal (U5, pin2), normalized vertical deflection (U5, pin 7), raw horizontal deflection (U6, pin 10). Permanent BNC cable connectors were installed to these components to gain access to the signals.

A National Instruments (NI) (Austin, TX) PCI-6120 data acquisition card (DAQ) was used to monitor and acquire the thermally driven power spectrum of the cantilever during the compression studies. Its bandwidth capability extended up to 400 kHz. The signals from the instrument control board (raw vertical and horizontal deflection) as well as the piezoscanner signal from the SAM were connected to a NI BNC-2110 connection box that fed the signals into the DAQ. All cables were isolated and grounded, preventing cross talk and environmental interference. These signals were analyzed using NI's LabView and MATLAB (Mathworks, Natick, MA) software programs on a secondary processing computer. A schematic of the experimental setup is given in Figure 3.7.

3.4.2 Software Design

The general operation of the AFM was conducted through the use of the manufacturer's software. This included control over features such as operating mode (contact or Tapping Mode^{TM}), scan rate, scan size, drive frequency and amplitude, and many other parameters. During the compression studies, the instrument was set to acquire force-distance and oscillation amplitude plots, while applying no external excitation to the cantilever. The general experimental operating procedure is described in the proceeding section. In addition to these conventional plots, MPFS was used to gather more information from the compression studies.

The signals from the PCI-6120 DAQ were analyzed by custom LabView software written by Jeff Boyles (Georgia Institute of Technology, 2006). This software used the input signals of raw vertical and horizontal deflection and the voltage signal to the piezoelectric scanner from the DAQ. It converts the vertical deflection data into the frequency under a Blackman-Harris window, to reduce side lobe effects during the Fourier transform. The data is then passed through a fast Fourier transform (FFT) to give the resonant spectra of the cantilever. Sequential samples of the resonant spectra are ensemble averaged to improve the signal-to-noise ratios. The average spectra are used to create a 'waterfall' plot when the amplitude-frequency data is plotted as a function of time. This is synchronized to the piezoscanner voltage signal. The user may change the number of points used to perform the fast Fourier transform on the data, the sampling range of the analyzer, and perform various averaging operations on the power spectral density (PSD) signal. This data along with the piezoscanner voltage and raw horizontal deflection signal is recorded using this software. The graphical user interface for this program is displayed in Figure 3.8. Several MATLAB programs were written to enable visualization, manipulation, and analysis of the resonant frequency data obtained during the compression of the carbon nanocoil. The source code for the

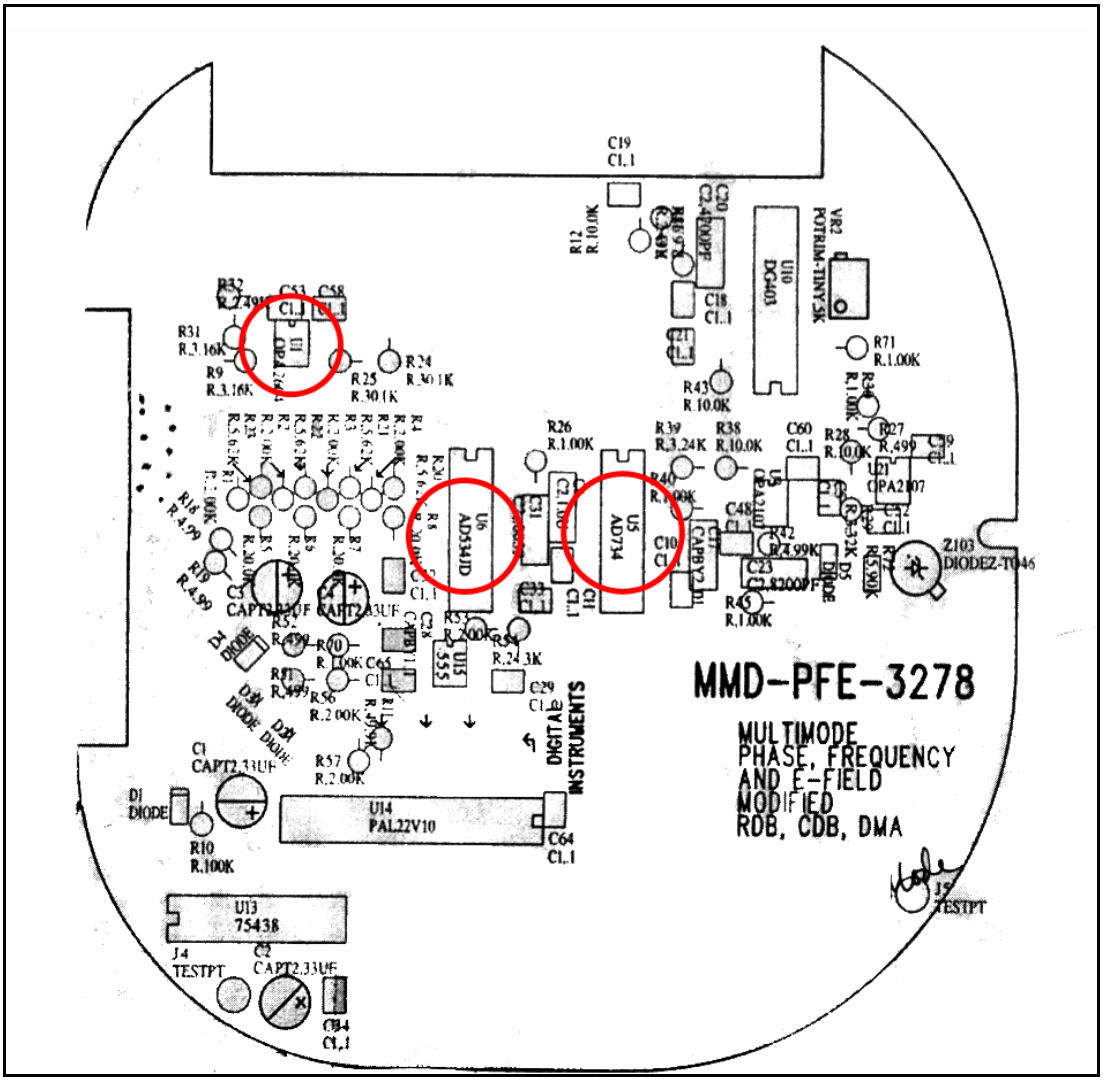

Figure 3.6. Component diagram for Nanoscope 3a control board for Multi-Mode base (MMD-PFE-3278. (courtesy of Jean Jarvais, Veeco, Santa Barbra, CA). Board components U1, U5, and U6 (circled) contained signals needed for MPFS. (Image courtesy of Digital Instruments, Inc.)

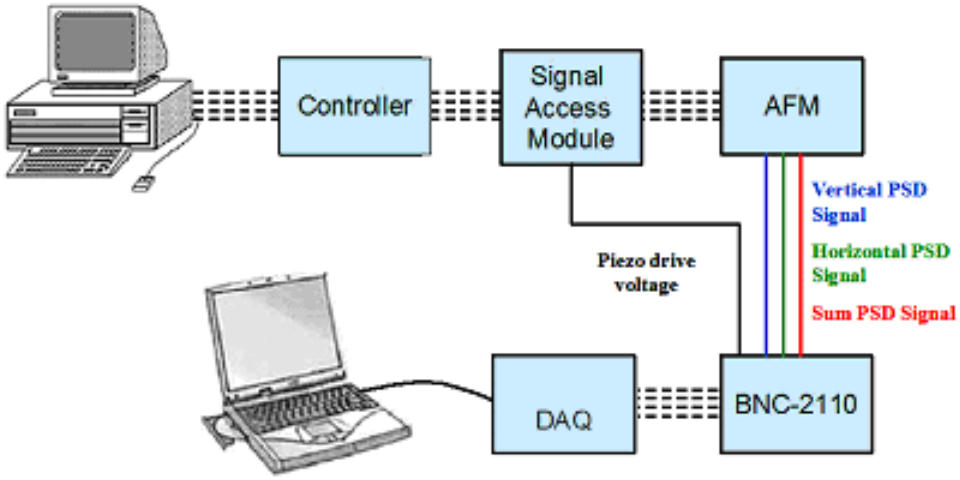

Figure 3.7. Schematic of experimental setup used to simultaneously monitor piezoscanner position, horizontal and vertical cantilever deflection, and thermal resonant spectra.

following programs can be viewed in the Appendix A. The first program developed for MATLAB was made with the purpose of organizing the LabView data into addressable matrices that could be manipulated. The data output format from the LabView software is to store the waterfall data, scanner voltage signal, and horizontal deflection data as separate ASCII text files. These files contain a header section followed by the collected data. The MATLAB programs are designated with a name followed by a *.m* extension.

Program '*jb1b.m*' reads the ASCII files and uses the header to parse the data into several arrays that it saves into a user named matlab.mat file. This data conversion allows MATLAB to load and read the data faster than in the raw ASCII format. The generated m-file contains the saves data into addressable variables that can be accessed through other functions: frequency amplitude data (WF), frequency range (freq), scanner voltage signal (SM), horizontal voltage signal (HM), and the time stamp for each spectra recorded in the waterfall (dtime). Since the conversion process takes a significant amount of time, the .mat data file is often used to access data collected from the compression study.

Program '*jb2b.m*' is used to view the compression data. This program reads the *.mat file and plots the resulting waterfall data. The user inputs upper and lower frequency bounds that are applied to the collected data. This allows the user to view a specific vibration mode or the entire spectrum. Recall that the maximum frequency sampled from the DAQ is 400 kHz. Often multiple vibration modes will occur below this value for pliant beams. Figure 3.9a is the first screen that the user encounters in the program, displaying the frequency-amplitude data of the waterfall plot. In this view, the individual spectra are overlaid, displayed by the different colored plots. Figure 3.9 displays the fundamental and higher order frequency plot for a typical nanocoil compression study. Once the frequency limits are input, the user can either display the waterfall data along with the scanner movement (Figure 3.9b), or by itself (Figure 3.9c).

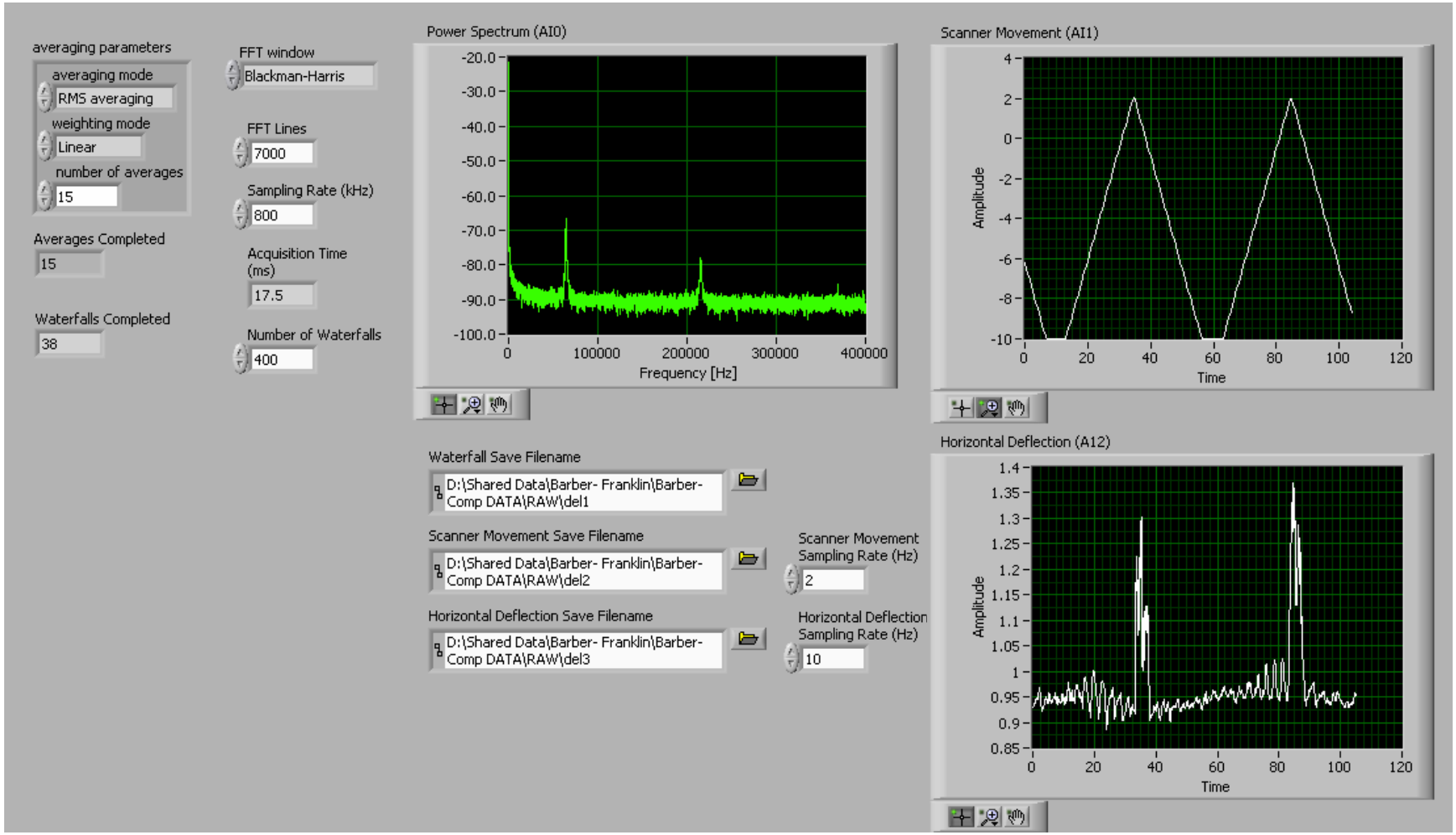

Figure 3.8. Labview™ graphical user interface (GUI). Multi-channel oscilloscope displaying power spectrum density plot of cantilever, scanner displacement, and horizontal deflection signal.

When displaying the waterfall data along with the scanner movement, it is presented in a top view, where the plot given is frequency versus time. The amplitude data is expressed as a change in the plot color in this view.

The user has limited ability to resolve the thermal resonance frequency response from the data given from *jb2b.m*. To better resolve the frequency shifts observed during the compression cycle, 'jbmax.m' was written to perform a peak picking routine on the waterfall data. This program reads the single PSD spectrum and finds the frequency value associated with the highest amplitude value. The user selects a frequency range in which to perform the routine. This is so that the operation can be completed outside of the *1/f* noise influence to prevent false values for the peak picking routine. The data output is a frequency versus time plot with the data points representing the frequencies where the maximum amplitude occurs for each of the waterfall PSD spectrum. Figure 3.10 displays the raw waterfall data (A) and max-amplitude (B) plots for the same data set. Through the use of *jbmax.m,* one removes the background optical interference and other noise signals while retaining frequency response of the cantilever-nanocoil system. One must be careful when interpreting this data. As the amplitude of the frequency data approaches the noise floor (often during initial contact or release events) the ability to resolve the true frequency decreases. This is also the case if an environmental signal (noise) has a large amplitude relative to the resonant frequency. This is given in the circled region of Figure 3.10b, where the peak picking routine assigns data points to an environmental signal rather than the cantilever resonance.

A graphical user interface (GUI) that combines data manipulation and visualization of frequency-amplitude plots functions was developed in *jb2b.m*. This GUI includes a peak picking routine (*jbmax.m*) that is capable of performing analysis on the PSD spectra. The visualization functions are contained in the left-side of the GUI displayed in Figure 3.11. The user can plot the waterfall data in a variety of forms. The

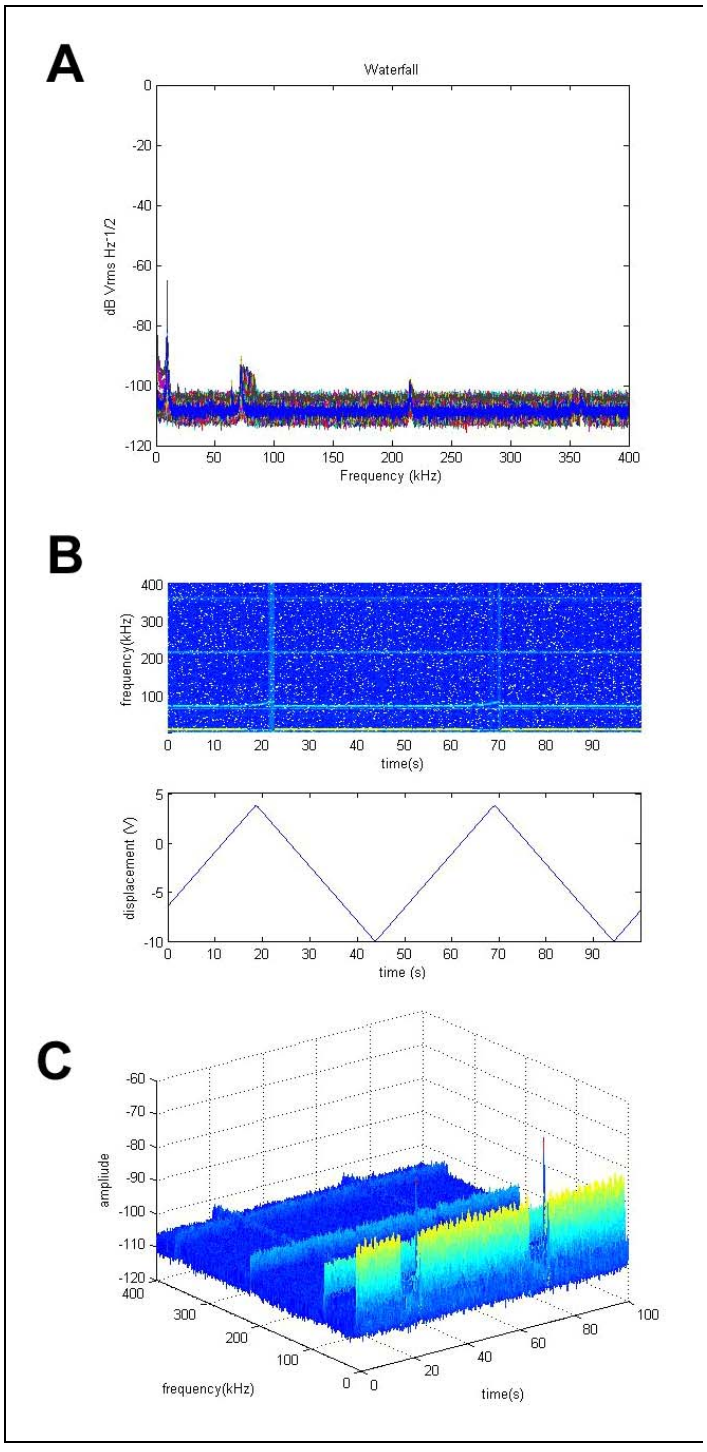

Figure 3.9. Data output from jb2b.m program from compression of carbon nanotube modified cantilever probe tip. A) frequency- amplitude plot of all collected power spectrum density plots captured during the compression cycle. B) frequency response with scanner voltage. C) 3D waterfall plot of collected power spectrum density plots. The scan size was 2500 nm with a rate of 0.02Hz.

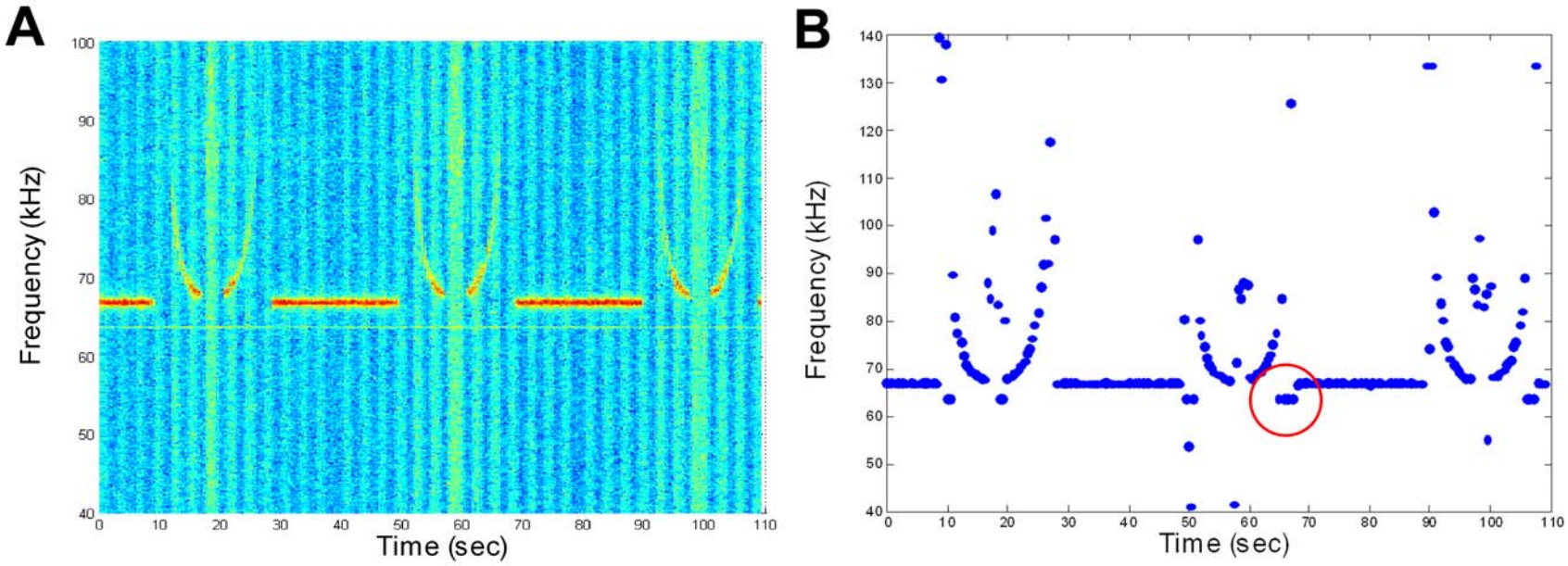

Figure 3.10. Data output from jbmax.m program. The frequency value correlating to the maximum amplitude for each PSD is measured and collected to transform the frequency-amplitude-time waterfall plot (A) into frequency-time plot (B).

analytical functions of the GUI are given in the right-side panels. In this section, the user is able to calculate analyze the curves in one or multiple PSD plots. By fitting a curve to the PSD plot, one can calculate the Q-factor and effective spring constant (k) the system. The GUI can perform this calculation on a single PSD or the entire waterfall ensemble, where it outputs all the values calculated during the data fit into a spreadsheet. This data can be plotted to show the change in k, amplitude, and Q of the system during the compression cycle.

3.4.3 Analytical Calculations

The data processing GUI allows the user to calculate the spring constant of the nanospring-cantilever system through analysis of the power spectra obtained during compression. The user inputs values for the upper and lower bounds of the frequency, initial amplitude, initial Q-factor value, beam sensitivity, and Q-factor tolerance. Using these values, the program then undergoes a recursive calculation to find the best fit curve for the PSD, via the sensitivity method (a.k.a Method of Hutter and Bechhoefer [143]). This method assumes that a microcantilever vibrating in a fluid can be described as a simple harmonic oscillator. This process is automated so that the k-values for all power spectral density plots in a given "waterfall" ensemble are calculated. The output allows the user to track changes in k, oscillation amplitude, or Q-factor to cantilever resonance frequency shifts.

The amplitude versus frequency data can be fit to the following equation assuming the cantilever behaves as a simple harmonic oscillator:

$$A(f) = A_{DC} f_1^2 \left[\left(f_1^2 - f^2 \right)^2 + \frac{f_1^2 f^2}{Q^2} \right]^{-\frac{1}{2}} \qquad \text{Equation 3.1}$$

where $A(f)$ is the amplitude as a function of frequency, A_{DC} is the DC amplitude, f_1 is the fundamental resonance frequency, and Q is the beam quality. The sensitivity method

employs the equipartition theorem to equate the mean value of the harmonic energy to that of the thermal energy of the system (Equation 3.2), allowing a direct calculation of the beam stiffness.

$$\frac{1}{2}K_B T = \frac{1}{2}k\left\langle A^2 \right\rangle \qquad \text{Equation 3.2}$$

where K_B is the Boltzmann constant, T is the absolute temperature, k is the effective beam stiffness, and $<A^2>$ is the mean-square amplitude of the cantilever thermal motion. Calculation of $<A^2>$ is performed by numerical integration. In this study, the acquired thermal spectra is fit to an advanced form of the Hutter-Bechhoeffer equation, including terms for white noise floor and 1/f noise as described in Equation 3.3.

$$A(f) = C_0 + \frac{C_1}{f^{C_2}} + A_{DC} f_1^2 \left[\left(f_1^2 - f^2 \right)^2 + \frac{f_1^2 f^2}{Q^2} \right]^{-\frac{1}{2}} \qquad \text{Equation 3.3}$$

where the fit quantities of C_0, C_1, C_2, A_{DC}, f_1, and Q are determined by a nonlinear least squares optimization algorithm in MATLAB. Figure 3.12 displays the resultant data from the 375 nm compression of a nanocoil using this technique. One drawback of this approach is that the calculated spring constant (k) develops a dependence on the measured amplitude of the curve fitting routine. For optical lever systems, such as the AFM, the measured values for k may be influenced by noise floor amplitude.

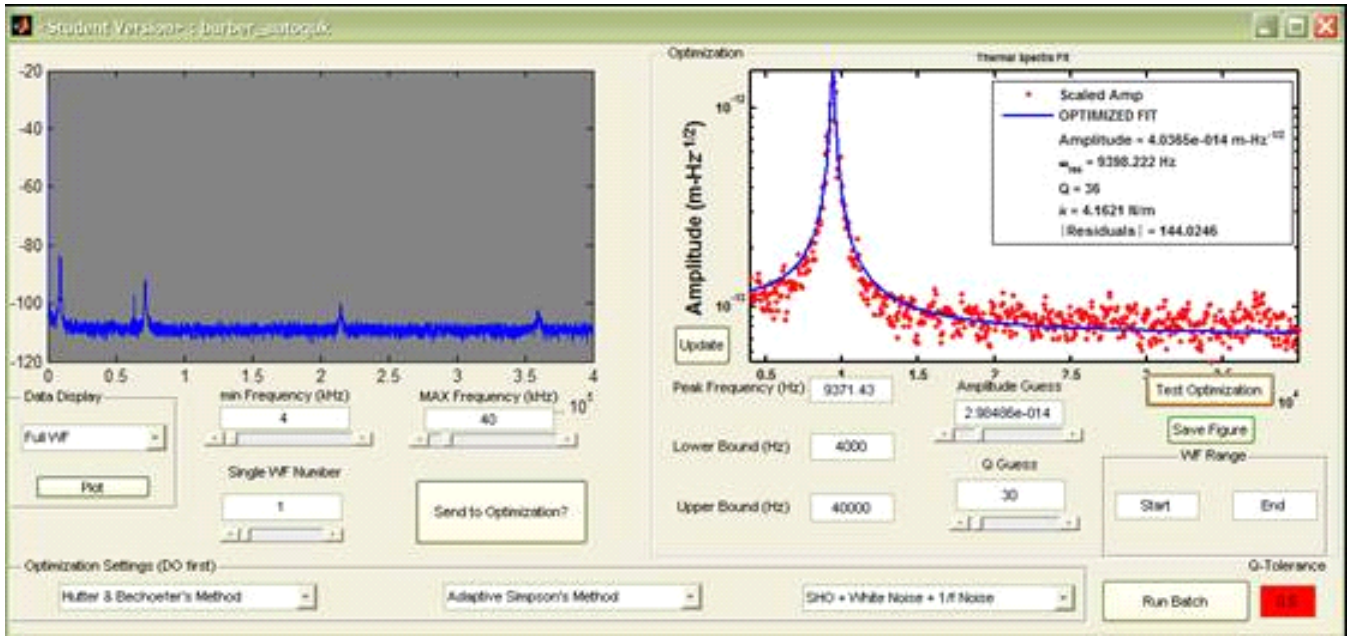

Figure 3.11. Autoquk program graphical user interface (GUI). The user can display the data in as full PSD, single PSD, or peak max (left). The right section of the program allows the user perform quantitative analysis on the selected PSD data.

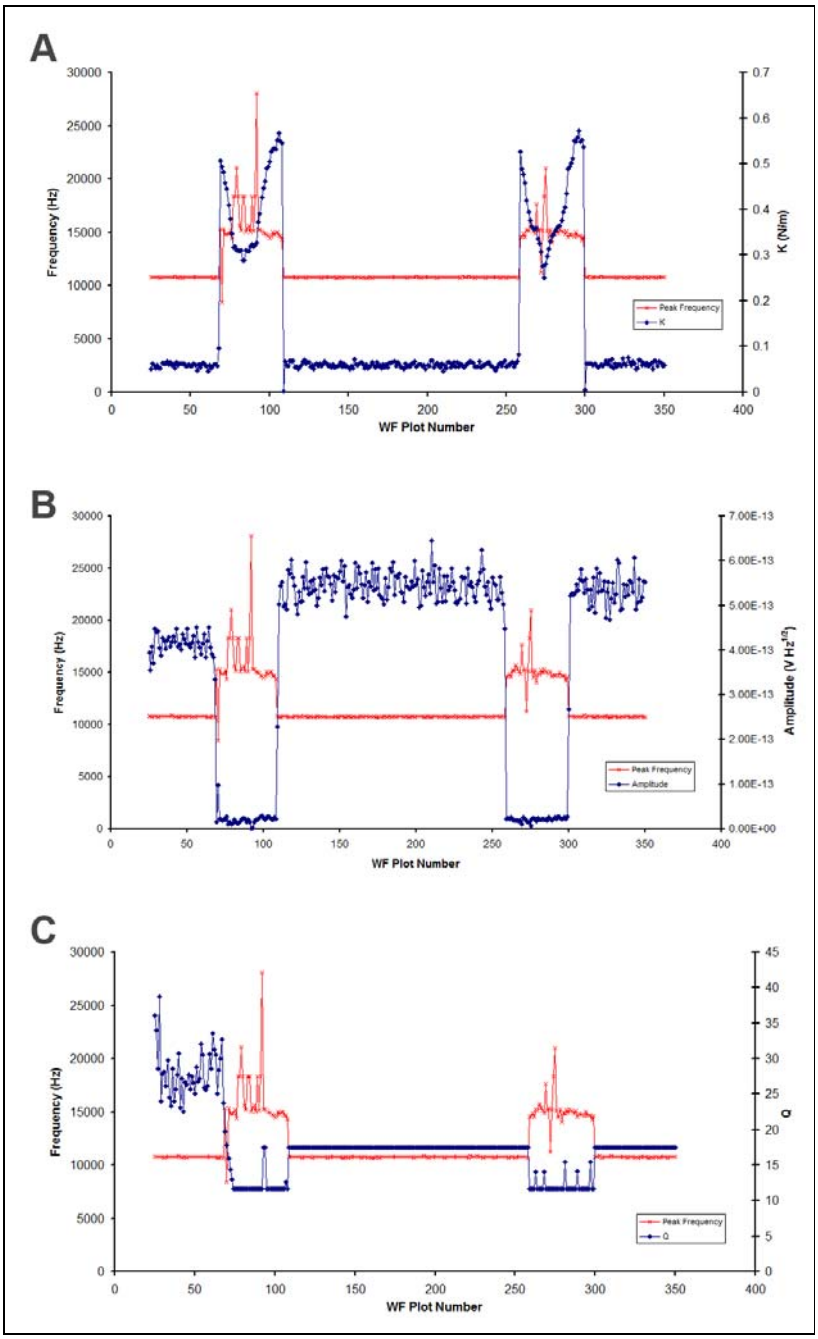

Figure 3.12. Data from the analysis of the power spectrum density plots using the sensitivity method calculated from the Analytical MATHLAB GUI. The nanocoil is under a 375 nm compression cycle. Plots of peak frequency (red) relative to spring constant for cantilever-nanocoil system (A), amplitude (B), and Q (C) is presented.

3.5 Substrate Setup and Shim Modification

Substrates used during the compression tests were thiol-modified template-stripped gold (TSG) surfaces [144]. The TSG substrates were prepared by depositing a gold film (~400 nm) onto a cleaved mica surface via e-beam evaporation. A one-half inch diameter circular disk was punhed from the mica sheet using a punch obtained from Ralmike's Tool-a-Rama (Springfield, NJ). The gold side of this disk was epoxied to a silicon chip. After curing, the mica is removed from the chip leaving an exposed gold surface; the template-stripped gold. Freshly prepared TSG surfaces were treated with 1mm thiolic solutions. After several hours the substrate is removed from the derivatizing solution, subsequently rinsed with filtered ethanol, and stored in a desiccator prior to use in compression tests. Just before use, the thiol-modified TSG substrate is secured to a magnetic AFM shim with the use of a temporary adhesive. The majority of the compression experiments were conducted on substrates consisting of 11-dodecanethiol (Sigma-Aldrich) SAMs due to minimize the adhesion of the nanocoil with the substrate [114, 142]. TSG substrates were mounted onto flat or tapered shims [145] to afford systematic variation in the angle in which the nanocoil contacts the substrate. Tapered magnetic shims with 5° or 10° slopes were manufactured in house by the GTRI Machine Shop personnel.

3.6 TEM Holder Design

A JEOL100CX-2 TEM was used in the structural characterization of the carbon nanocoils. This instrument was chosen because it had a removable sample holder design. A custom TEM holder capable of securing the entire cantilever chip within the beam path was designed and manufactured. This allowed the preservation of the modified cantilever for further studies. Without this holder, the cantilever beam would need to be

removed from the chip and placed onto a standard TEM sample grid, a nontrivial and irreversible procedure. The custom built TEM holder is shown in Figure 3.13.

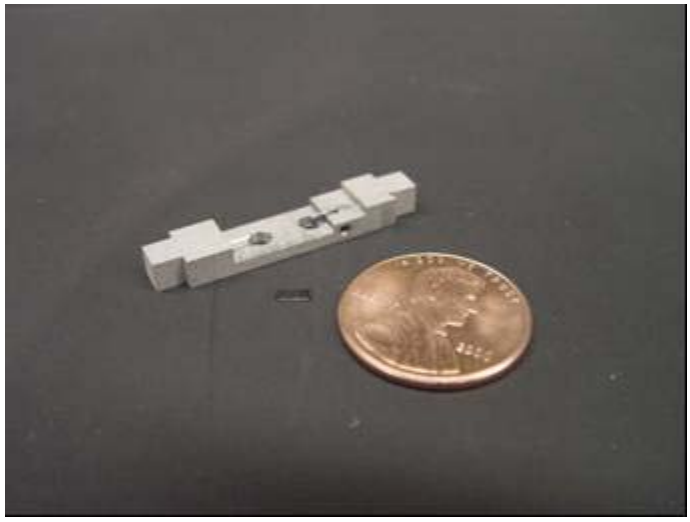

Figure 3.13. Custom TEM holder with cantilever chip and penny also shown for size reference.

Initial TEM imaging of the CCNT modified cantilever tips had unexpected results. Beam induced damage to the nanocoil was observed. The TEM holder design freely suspends the cantilever in the beam path, connecting to the holder at a set screw. Conventional TEM sample holders consist of a porous carbon grid on which samples rest. With the cantilever suspended in vacuum, there is no direct path for heat to dissipate from the sample to the holder. It is believed that the heating of the sample is the cause of the damage observed in Figure 3.14B. To prevent this from occurring during nanocoil characterization, the duration of direct beam contact with the nanocoil was limited. This reduced observable beam damage in subsequent imaging of the nanocoils.

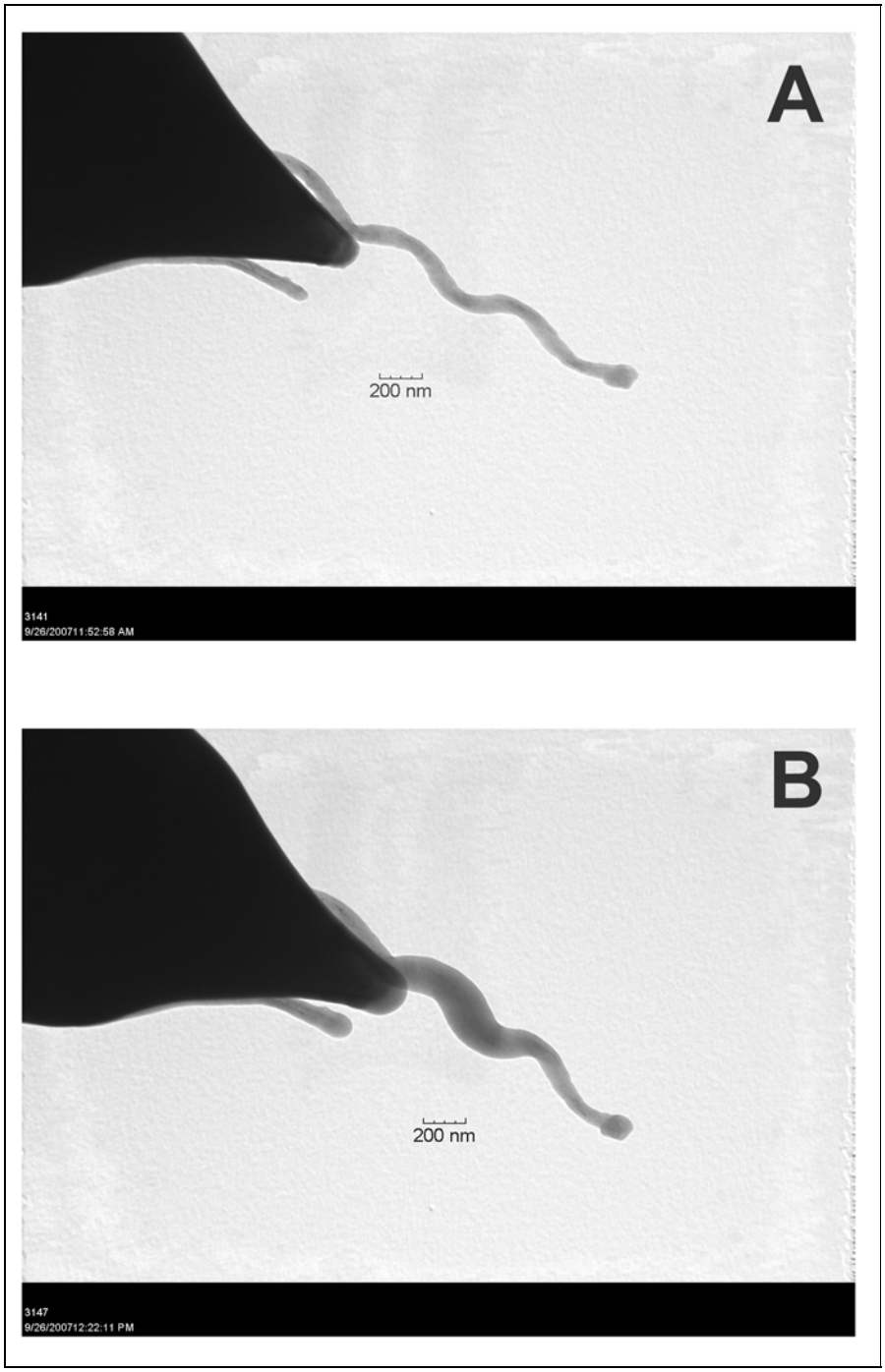

Figure 3.14. (A) TEM of nanocoil modified probe tip. (B) Damage to the nanocoil is observed after several minutes of beam exposure.

CHAPTER 4

MULTI-PARAMETER FORCE SPECTROSCOPY OF COILED CARBON NANOTUBES

In this chapter, the mechanical response of a helical multi-walled carbon nanocoil to axial compression is presented. The text of this chapter is taken, for the most part, from a manuscript in review at ACS Nano. The nanocoil was attached to the apex of a cantilever probe tip; the atomic force microscope was employed to apply a cyclic axial load on the nanocoil. The mechanical response was determined by collecting in real-time the thermal resonance frequency, displacement, and oscillation amplitude of the cantilever-nanotube system. Depending upon compression parameters, the coil undergoes buckling, bending and slip-stick motion. Characteristic features in the thermal spectrum, force and oscillation amplitude curves for each of these responses to induced stress are presented.

4.1 Introduction

Multi-parameter force spectroscopy (MPFS) is a technique developed within the Bottomley group to simultaneously measure the force-distance, oscillation amplitude, and frequency response of a cantilever based atomic force microscope (AFM) during dynamic interactions with a sample. Conventional AFM operational software uses the photosensitive detector (PSD) to measure the cantilever deflection as it rasters across a sample surface [103, 146-148] . During dynamic mode operation the cantilever is externally excited using a piezoelectric actuator to modulating at the cantilever's natural resonant frequency to achieve user defined amplitude [149]. The oscillation amplitude and cantilever deflection can be recorded as the cantilever probe tip interacts with the

substrate. Figure 4.1 displays the frequency response waterfall during the compression of a coiled carbon nanotube.

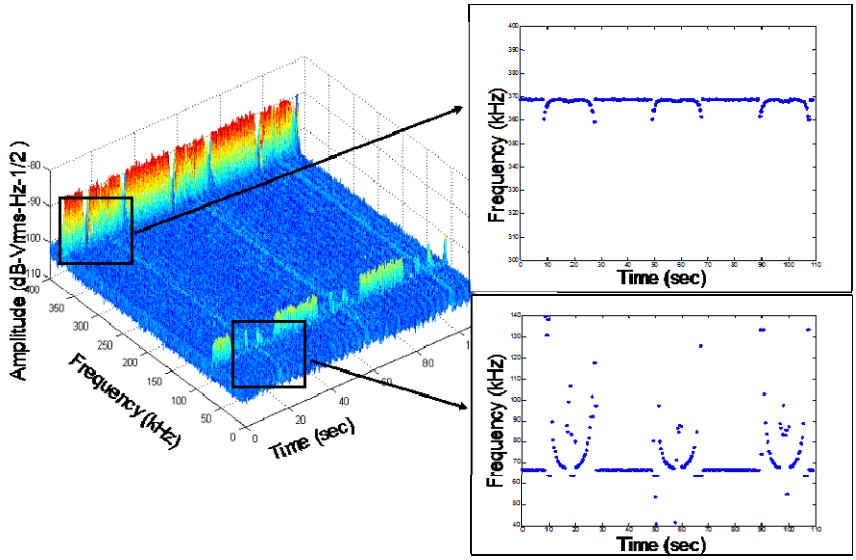

Figure 4.1. Thermal resonant frequency response of coiled carbon nanotube during cyclic compression. The fundamental and second order vibration frequency responses are displayed.

4.2 Background

Since their discovery, carbon nanotubes have attracted great interest in nanoscale applications [150, 151] due to their unique mechanical and electrical properties. Carbon nanotubes can be as long as hundreds of microns yet have diameters of only a few nanometers. The single walled carbon nanotubes (SWNT) are straight, whereas the multi-walled carbon nanotubes (MWNT) can have straight as well as coiled morphology. These materials are lightweight, have an extremely large elastic modulus, and exhibit high thermal and electrical conductivity. For example, carbon nanotubes have been used as the sensing element in chemical sensors [152] to improve the mechanical integrity of polymer composites [153-156] and as devices in nanoelectronics [157-162].

A considerable amount of effort has been extended in characterizing carbon nanotubes. Electrical and mechanical properties have been investigated on bulk nanotube samples [26] as well as single nanotube samples [102, 111, 163]. The scanning tunneling and atomic force microscopes have been invaluable tools in this endeavor, particularly for measuring properties on individual nanotube samples, since these instruments facilitate nanoscale positioning, control, and measurement [47]. Scientists have investigated the tensile strength [8, 59] and bending properties of SWNTs and MWNTs [52, 57, 164, 165]. Chen and co-workers stretched a carbon nanocoil anchored at each end to a AFM cantilever and measured its tensile response [46]. Recently researchers have begun to investigate the application of helical MWNTs in composite materials [166], or as mechanical sensors [167, 168]. Mechanical entanglement between the coil and the matrix enhances the fracture toughness and mechanical strength of the composite.

Initial studies of the mechanical properties of an individual coiled nanotube attached to an atomic force microscope probe tip were previously investigated within the Bottomley group. A shift in resonance frequency of during compression of the nanocoil was found to be associated with the compression and buckling of the nanocoil between the probe tip and the substrate surface [142].

4.3 Mechanical Response of a Coiled Carbon Nanotube to Axial Compression

An AFM was used to compress a multi-walled coiled carbon nanotube (CCNT) that was attached to a probe tip. Figure 4.2 displays a scanning electron micrograph of the nanocoil used in this study; the nanocoil was mounted onto a cantilever beam with a spring constant of 0.037 N/m. Extension of the z-piezo scanner supplies mechanical loading to the CCNT. The magnitude of applied load is a function of the magnitude of scanner extension following contact of the nanocoil with the substrate and the spring

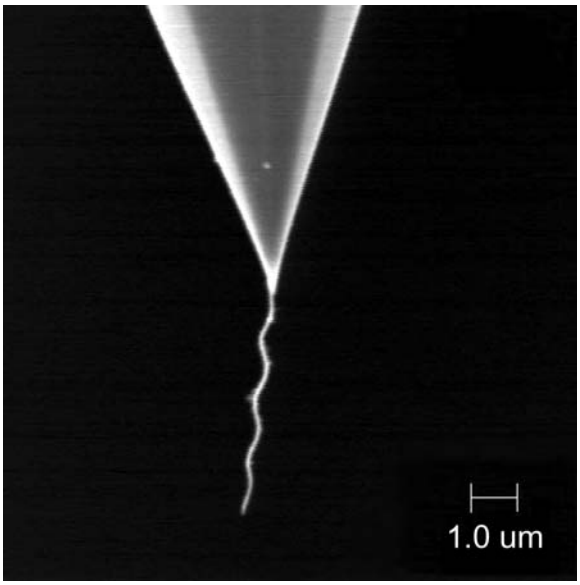

Figure 4.2. SEM image of a CCNT-modified AFM probe tip. The CCNT was mounted on a low-stiffness AFM cantilever beam (MikroMasch CSC-38) with a measured spring force constant of 0.037 N/m. The CCNT extends 4.7μm beyond the Si tip with a helical pitch of 1.16 μm.

constant of the cantilever to which the nanocoil is attached. In this study, to systematically vary the applied load, the scanner start position was varied; the range and speed of scanner extension was kept constant at 2500 nm and 0.02 Hz, respectively. To reduce the probability of mechanically-induced damage and/or detachment of the nanocoil, compression/decompression studies were performed without contacting the silicon probe tip to the surface. This constraint coupled with the desire to precisely control the magnitude of applied load necessitated the following protocol. Prior to approaching the surface, the microscope was placed in tapping mode and the cantilever is driven at its fundamental vibrational frequency. After false engagement, the microscope was switched to force curve mode. Cantilever oscillation amplitude was used to determine the point of contact between the nanocoil and the surface; contact being

characterized by a sharp decrease in the oscillation amplitude. With contact established, setting the oscillation drive amplitude to zero enabled monitoring of the thermal resonance of the cantilever continuously during cyclic movement of the scanner. Thus, at each compression increment, force curves, oscillation amplitude plots, and thermal resonance spectra were acquired.

4.3.1 Reproducibility

Figure 4.3 presents the thermal resonance frequency as a function of time over four cycles of scanner extension and retraction as the CCNT was brought into and out of contact with an 11-dodecanethiol-modified template-stripped gold substrate surface anchored onto a flat shim. In this figure, the CCNT was in contact with the substrate only during the last 250 nm of scanner extension. Two thermal resonance frequencies are observed over the frequency band of 0 to 400 kHz. Prior to contact, the fundamental cantilever resonance frequency (orange) is found at 9.4 kHz and the secondary vibrational mode (blue) is observed at 71.7 kHz. At the point of contact, the fundamental resonance increases to a value that cannot be determined due to its amplitude falling below the noise floor. The CCNT begins buckling shortly after contact with the surface; during buckling the resonance frequency drops from 30 kHz to 12 kHz at full extension of the scanner. During the retract portion of the scan cycle, the resonance frequency increases until the point of release of the nanocoil from the surface. At this point, the resonance frequency returns to its fundamental resonance value in free space. A similar trend was observed for the secondary vibration of the cantilever. Since the signal-to-noise ratio during compression of the second mode is greater than that observed for the primary mode (data not shown), from this point forward, the secondary vibration mode data will be presented. A salient feature of the data presented in Figure 4.3 is the similarity of the frequency shifts from one scanner cycle to the next. There is an

asymmetry in the frequency response of the system; during retraction higher values are observed. A plausible explanation for this observed hysteresis is increased tension caused by adhesive interactions between the coil and the surface [102].

During initial compression studies, the following factors that might affect the frequency response of the nanocoil-cantilever system were investigated: compression velocity, extent of compression, and substrate treatments. It was found that the compression velocity had little to no effect on the magnitude of the frequency shift of the nanocoil as it contacts the substrate. However, as the rate of compression increased, faster data acquisition rates were required to maintain constant resolution along the frequency axis. Given the maximum slew rate range of the DAQ card and the desire to minimize the time intervals between thermal resonance spectra, a Z-piezo scan rate of 0.02Hz was selected. At this rate, a scanner extension/retraction cycle is completed every 50 seconds. The Labview^{TM} (National Instruments, Austin, TX) software was optimized to the following settings: 800 kHz bandwidth, 7000 point FFT, and 15 power spectrum density (PSD) plots were ensemble averaged per data entry, and 400 PSD plots were collected in each waterfall data set. Along with these settings, a scan size of 2500 nm was chosen to allow the piezoelectric JV scanner (Veeco) to remain in the linear portion of its operation. These experimental conditions were used throughout all compression experiments.

4.3.2 Substrate Effects

The observed frequency response of the nanocoil during compression was dependent upon the identity of the substrate. Compression of carbon nanocoils on highly ordered pyrolytic graphite (HOPG) was investigated using freshly cleaved grade-1 HOPG (SPI Supplies) as a substrate. Because of their similar hexagonal carbon structures and

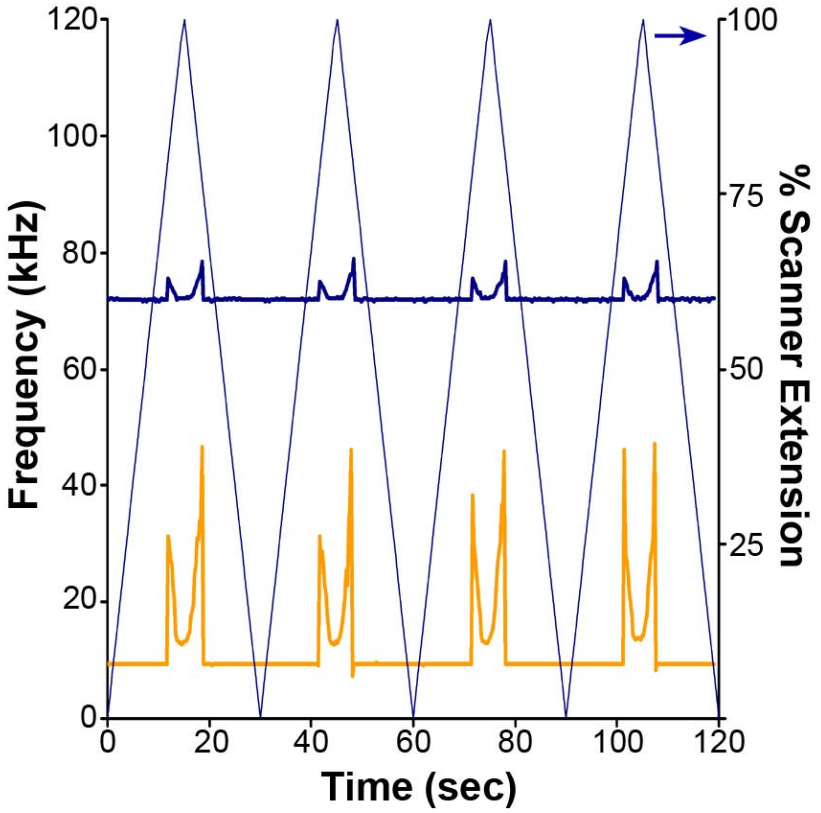

Figure 4.3. Thermal resonance frequency of the primary (orange) and secondary (blue) vibration modes of the CCNT-modified cantilever during cyclic compressions applied via AFM. The nanocoil is compressed to a distance of 250 nm during each scanner cycle as the z-piezo scanner (light-blue) moves the substrate toward the cantilever probe tip creating a mechanical load on the nanocoil. The z-piezo scanner had a scan size of 2500 nm.

potential π-π interactions, it was anticipated that their interaction forces would be greater that that observed for interaction of the nanocoil with a methyl-terminated thiol-modified TSG substrate [169]. Figure 4.4 compares the frequency response from the nanocoil undergoing 350nm of compression on HOPG and on a 1-dodecanethiolated TSG

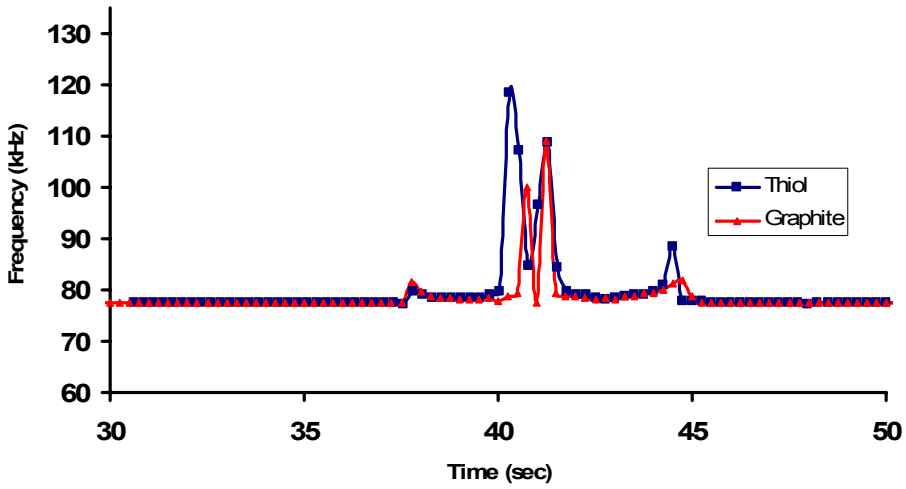

Figure 4.4. 350 nm compression of a coiled carbon nanotube on 1-dodecanethiol modified TSG and HOPG substrates.

substrate. The approach portion is identical on both substrates indicating similar compression conditions occurring during both experiments. The retract portion of the compression cycle exhibits a higher frequency shift on the TSG substrate, indicating increased adhesion of the nanocoil to this surface. This result suggests that the nanocoil surface may not have the same graphitic structure as straight carbon nanotubes or that

compliance of the thiol superlattice is increasing the contact area (relative to HOPG) and thus increasing the strength of adhesion.

Figure 4.5 displays the compression results from 375 and 750 nm compression on substrates with methyl and carboxyl-terminated thiol monolayers. Comparing the frequency response of the nanocoil during compression on the functionalized substrates reveals several trends. Firstly, the magnitude of the frequency shift occurring during compression on the methyl functionalized substrate is greater that that of the carboxyl group. The frequency shift is used to calculate the stiffness of the nanocoil-cantilever system during compression. Because the cantilever is a fixed material, silicon, with a constant geometry, its stiffness is constant throughout the compression experiments. The cause of the observed frequency shift is due to changes in the mechanical properties of the carbon nanocoil. As the frequency shift increases in value, the effective stiffness of the nanocoil is increasing.

It was expect that at initial contact between the nanocoil and the substrate would result in the same values for the frequency response. One explanation of this phenomenon is that the rigidity of thiol monolayers are not equivalent [104]. As the nanocoil is compressed against a pliant monolayer, the force exerted on the nanocoil would be dampened, thus reducing the observed frequency response [170, 171]. The second observed trend is that the carboxyl-terminated has a greater attraction (adhesion) to the nanocoils. This is evidenced as the nanocoil remains in contact with the substrate for a greater period during the retract portion of the frequency response. Figure 4.5A demonstrates this phenomenon between ~79 and 81 seconds. This region of the plot is at the end of compression cycle where the piezomotor is in retract motion. The frequency response for the carboxyl thiol continues for ~150 nm of scanner motion past

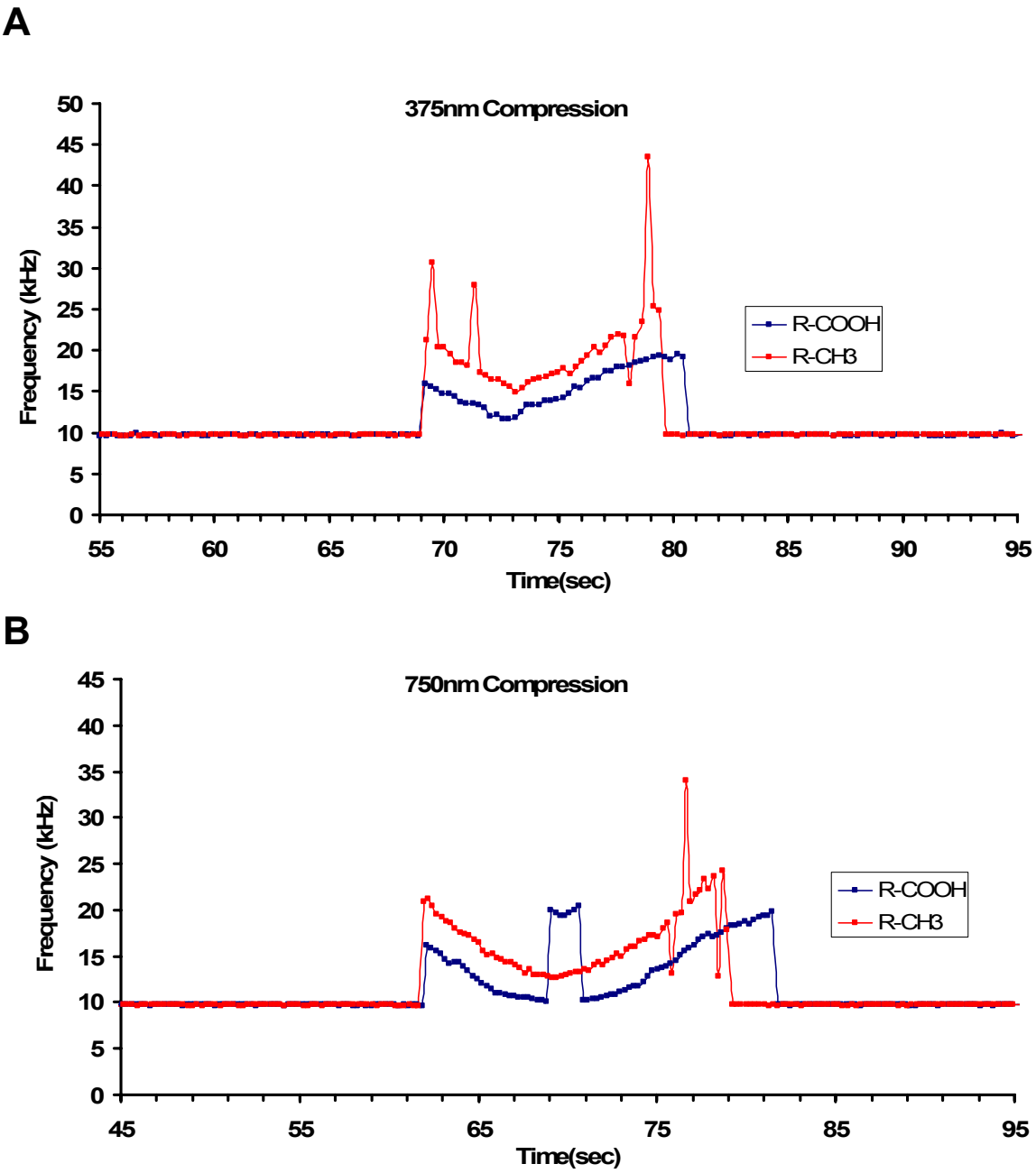

Figure 4.5. Frequency response of nanocoil under 375(A) and 750 nm(B) compression on substrates treated with 1-dodecanethiol (red) and 11-mecaptoundecanoic acid (blue).

the release observed in the methyl-terminated thiol. This event is observed in Figure 4.5B between ~79 and 82 seconds. The last phenomenon observed is that the carboxyl-functionalized substrate causes a second frequency shift to occur during the compression. This second buckling event could be caused by defects in the coil structure exhibiting failure under the applied load or slip-stick motion of the nanocoil on the substrate.

4.3.3 Force-Distance Curve Response

Figure 4.6a displays the corresponding force curve acquired by the AFM during one scanner cycle. The point of contact on the approach portion of the force curve occurred at the same time point as the jump in frequency presented in Figure 4.5. Similarly, the return of the frequency to 9.4 kHz occurred at precisely the same time as the release event in the retract portion of the force curve. The downward deflection of the cantilever on scanner retraction is consistent with a small amount of adhesion between the nanocoil and the chemically-modified surface.

Figure 4.6 also presents force curves acquired as the distance of scanner extension with the CCNT in contact with the substrate increased from 125 to 875 nm. Salient features in the approach curves over this distance interval include two regions of increasing cantilever deflection with scanner extension and an intermediate region where no deflection is occurring despite upward movement of the substrate. Note that the second linear region is not due to contact with the probe since the nominal length of the nanocoil is 4.7μm (helical pitch of 1.16 um) is more than thrice the distance the scanner extends following contact.

The response in Figure 4.7 is comparable in shape to those reported previously for a nanocoil affixed to a stiff cantilever. Traces d-f exhibit a second shift in thermal resonance frequency that was not previously observed. The time point on the upward

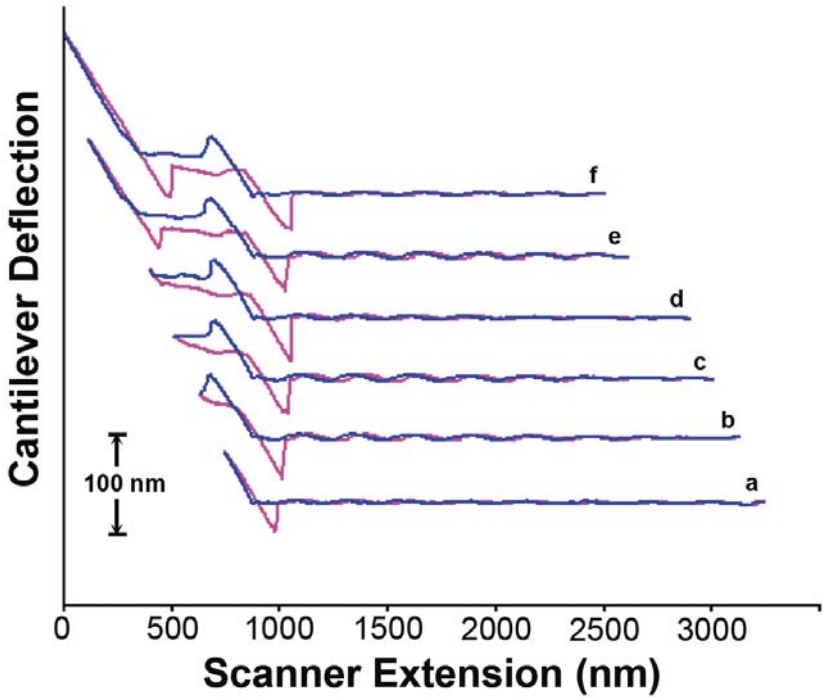

Figure 4.6. Force-curve data collected during compression of the CCNT at an approach angle of 7º to the surface. The total z-piezo scanner size was held constant at 2500 nm. The compression amounts on the nanocoil were increased by changing the start position of the scanner cycle. The force-curves are collected at 125 (a), 250 (b), 375 (c), 500 (d), 750 (e), and 875 nm (f) compression distance. The data are offset so that the jump to contact in the approach curves (blue) are aligned for comparison.

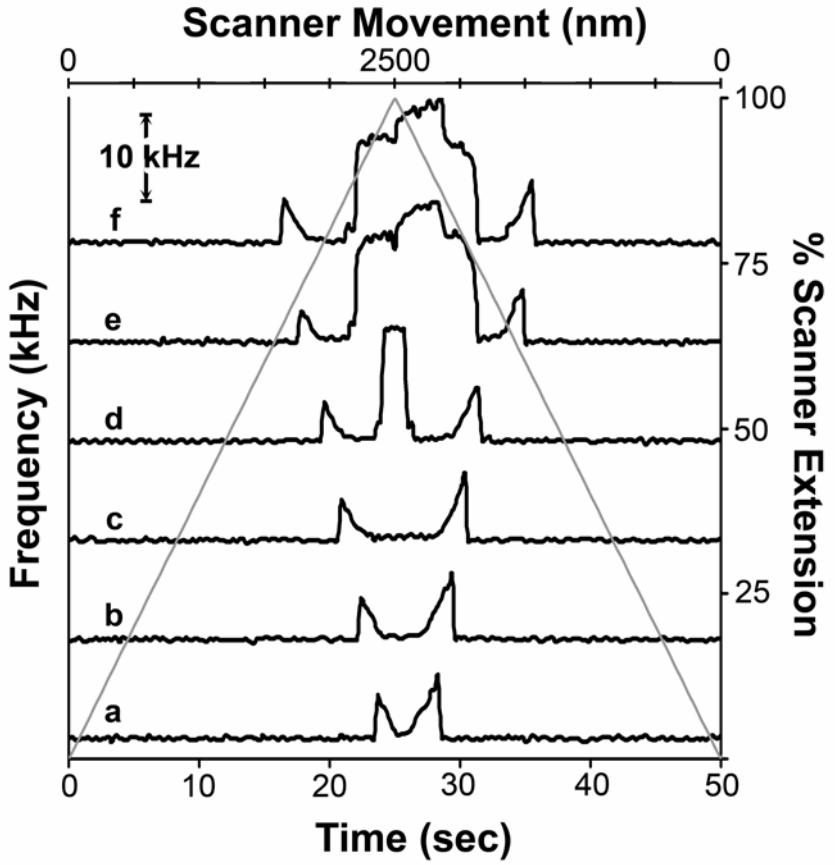

Figure 4.7 Thermal resonance frequency response of the CCNT at varying compression conditions. The z-piexo scan size was set at 2500 nm. The nanocoil was compressed on an angled substrate to give an approach angle of 7º to the surface. Compression amounts of 125 (a), 250 (b), 375 (c), 500 (d), 750 (e), and 875 nm (f) are presented. The occurrence of slip-stick is observed beginning at a compression distance of approximately 457 nm, and can be observed at larger compression distances. The displayed frequency data is from the second vibration mode, due to increased S/N response.

movement of the scanner at which the second rise in frequency occurs corresponds to the time at which the cantilever bends upward for the second time.

4.3.4 MPFS Analysis

Figure 4.8 displays the frequency response (A), force curve (B), and oscillation amplitude (C) data collected during a single scanner cycle for a contact distance of 875 nm and stacked in a manner to aid comparison. Note that in this figure, the frequency data is plotted as a function of scanner movement. The cantilever-CCNT system remains in free space vibration until the scanner extends to the point of contact between the nanocoil and the substrate; the initial contact (designated with arrow #1 in all three panels) occurs at ~1620 nm into the scan cycle and is marked by a decrease in cantilever oscillation amplitude when the cantilever is driven and by upward deflection of the cantilever and an increase in its resonant frequency with driven by only thermal motion. As the scanner continues to extend, there is a non-linear drop in frequency simultaneously with a linear upward deflection of the cantilever (designated with arrow #2). This combined behavior is consistent with CCNT buckling.

At ~1815 nm of scanner extension, the cantilever begins to deflect downward, towards the substrate. Beginning at ~1865 nm of scanner extension (designated with arrow #3), cantilever deflection and resonant frequency remain constant even though the scanner is continuing to extend towards the cantilever. Constant deflection and resonant frequency is observed until the scanner has extended to ~2150 nm (designated with arrow #4). At this point, the cantilever bends upward in a linear fashion and its resonant frequency increases with scanner extension until the point at which the scanner begins to retract. As the scanner retracts, the expected decrease in cantilever deflection and resonant frequency is observed. At ~495 nm of scanner retraction, a sudden upward motion of the cantilever is observed typical of sudden release of the tip from the substrate

surface (designated with arrow #5). The resonant frequency and deflection remains constant until the scanner has retracted by ~1050 nm. Then, the nanocoil detaches from the surface (designated with arrow #6) and the frequency of the cantilever-nanocoil system returns to its free space value.

Three possible explanations for this behavior are that the CCNT undergoes: 1) post buckling – a deformation of the wall structure of the nanotube [172], 2) higher order buckling that deforms the helical structure of the nanocoil, or 3) movement across the substrate by slip-stick motion [173, 174]. The observation of two "ringing" events during retract motion of the scanner in the oscillation amplitude plot (Figure 4.8) supports the slick-hypothesis. These are indicated by arrows #5 and #6. During scanner retraction, tension increases until the restorative forces acting on the cantilever overcome the adhesive interaction. A sudden release from contact causes a short-lived oscillation of the cantilever, i.e. "ringing". The observation of two "ringing" events in the oscillation amplitude plot is also supportive of the slip-stick hypothesis. It is postulated that slip-stick motion results in a larger portion of the nanocoil coming into contact with the substrate. The tension imposed by scanner retraction and the increased contact area should result in a larger resistance to the restorative force of the cantilever. Release of a portion of the CCNT from the surface results in ringing as the coil adopts a new geometry.

4.3.5 Slip-Stick Validation

To test the slip-stick hypothesis, the nanocoil angle at point of contact was systematically varied. The geometry and orientation of the CCNT, relative to the cantilever, was determined by analysis of a set of scanning electron micrographic images acquired at various angles. When brought into contact, the angle at the point of contact of

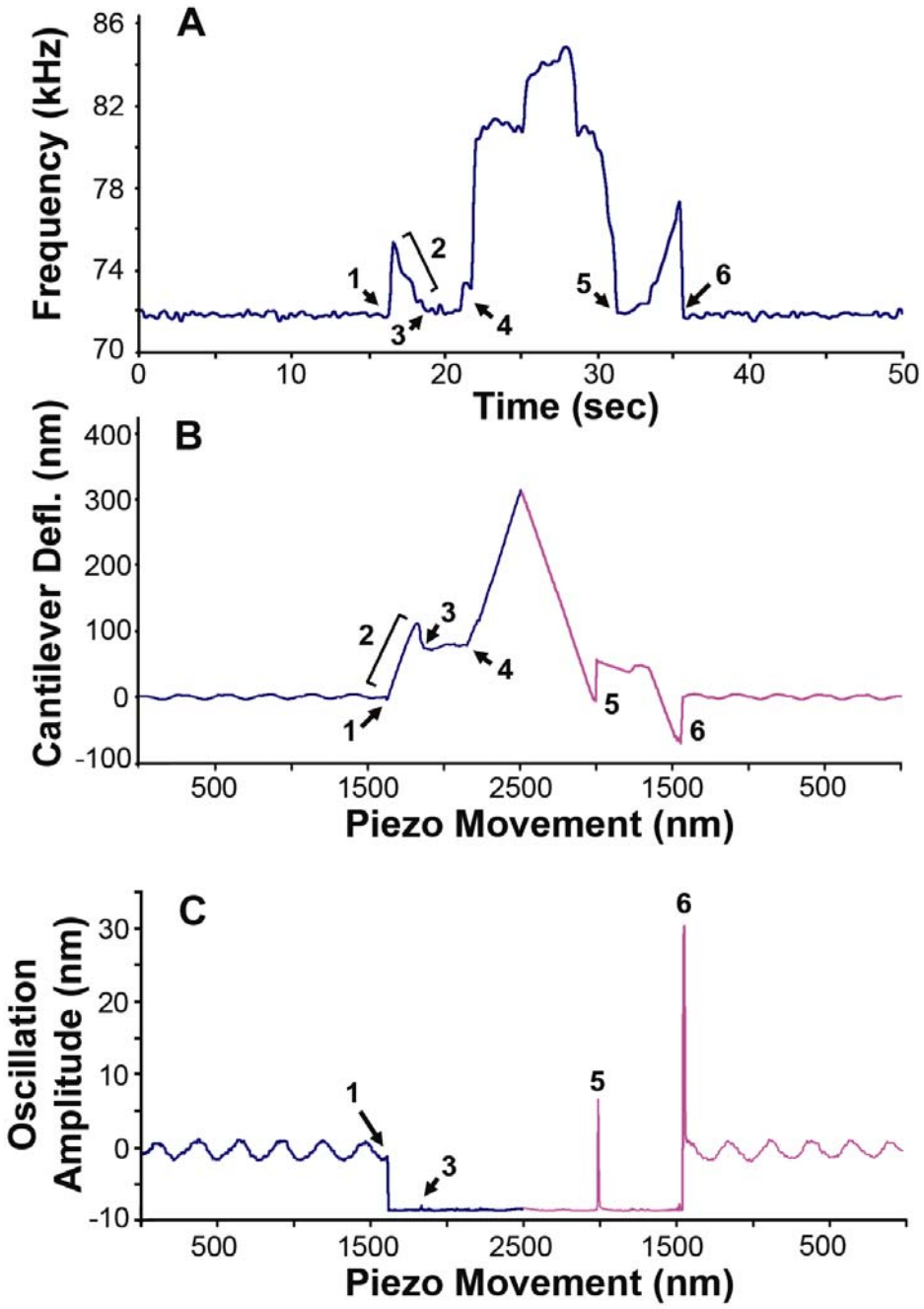

Figure 4.8. Thermal resonance frequency response (A), force-distance (B) and oscillation amplitude (C) responses of the cantilever-CCNT system under 875 nm compression with an approach angle of 7°. The displayed frequency data is from the second vibration mode, due to increased S/N response. In the several phenomena are observed occurring during the scanner extension: the initial contact with the substrate (1), buckling response of the nanocoil (2), slip(3)-stick(4) motion. During scanner retract motion several ringing events are observed in the oscillation amplitude that correlate to the return to the buckling geometry of the coil (5) and release from the surface (6).

the CCNT is ~7° relative to the surface normal. To change the angle, beveled shims were used in place of standard mounting shims. Wedge-shaped shims [145] were manufactured with a 5° grade and scribed to mark the reference position. As illustrated in Figure 4.9, a simple 180° rotation of the wedge-shaped shim afforded the acquisition of data sets at nanocoil point of contact angles of 2° and 12°.

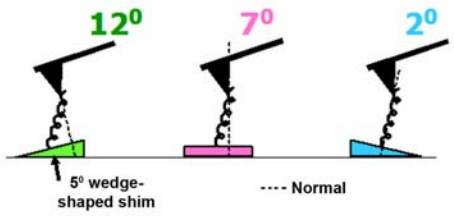

Figure 4.9. Illustration representing the use of an angled shim to change the effective approach angle of the CCNT to the substrate surface.

Experiments were conducted using the wedge-shaped shim in the same manner as with a flat shim. If the onset of the second jump in resonant frequency was due to a stick event following slip, then our expectation was that this event would occur at lower scanner extension values with increasing point of contact angle. Figure 4.10 is a compilation of the frequency shifts observed during nanocoil compression at the following point of contact angles: 2° (blue), 7° (red), and 12° (green). Figure 4.10a shows no discernible differences in the frequency response at the three angles when the CCNT was in contact with the substrate for a scanner extension distance of only 250 nm. At an in-contact distance of 375 nm (Figure 4.10b), the frequency response on the 2° and 7° substrates are the same, however the occurrence of a second frequency shift is

observed on the 12° substrate. At greater in-contact distances (Figure 4.10c & 4.10d), the second frequency shift event occurs at all three angles. It is interesting to note that as the contact angle is increased, the frequency response of the system during the approach and retract segments is asymmetric and correlates with point of contact angle. On the 2° substrate at 875 nm of extension, the first and second frequency shifts have a strong symmetry with the cyclic motion of the piezo scanner. As the angle is increased to 7° or 12°, this symmetry is lost and is indicative of increased areas of contact between the CCNT and the substrate facilitated by the slip-stick event.

Figure 4.11A presents force curve and frequency response data when the CCNT was brought in and out of contact with the substrate angled at 2° for a contact distance of 375 nm. Note that over the time interval of 23.5 - 25 s, the scanner is extending without a significant change in either cantilever deflection or resonant frequency. Similarly, over the time interval 25.5 – 27 s, the scanner is retracting with no significant change in cantilever deflection or resonant frequency. During each of these periods, the CCNT is sliding across the surface into a new geometry. Figure 4.11B compares the resonant frequency response to the apparent spring constant of the cantilever-nanocoil system calculated from the thermal spectra acquired at each data point in the frequency plot. Note that over the time interval of where the frequency response is constant, the spring constant of the system increases, indicating a mechanical stiffening of the nanocoil. As the nanocoil undergoes the 'slip' portion of slip-stick across the surface it is under a constant force from the cantilever, rather than a progressive force observed during buckling. As the contact area of the nanocoil increases, the frictional forces acting on the coil increase; causing the measured stiffness

to increase. The point at which the CCNT sticks to the substrate, the frequency response again increases as a new region of the nanocoil undergoes buckling.

At its onset, the objective of this investigation was the determination of CCNT's stiffness to axial compression. As delineated above, this stiffness is not directly

measurable when it is mounted onto a soft cantilever or when the nanocoil undergoes bending, buckling, or slip-stick motion. The bending/buckling phenomenon is facilitated by open end spring geometry [175]. The compression stiffness of the CCNT can be estimated, however, from the resonant frequency of the cantilever at the point of contact with the substrate surface. At this point, the spring constant of the coil is computed from the effective spring constant of the system using a springs in series model. A k_{CCNT} of 0.051 ± 0.004 Nm^{-1} was computed using this approach. No significant difference in the calculated value of k_{CCNT} with respect to the angle at the point of contact was observed

.

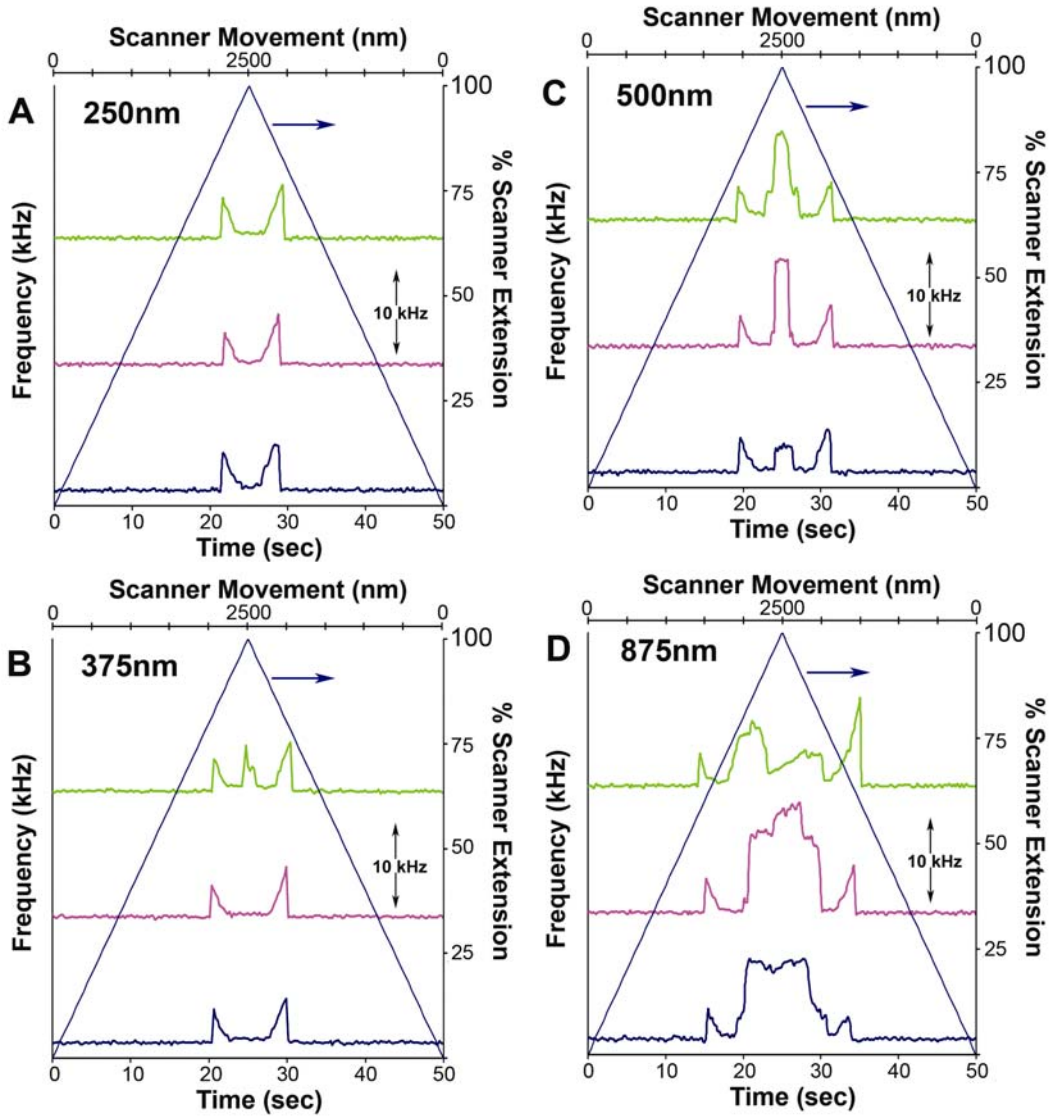

Figure 4.10. The thermal resonance frequency response of the CCNT at different approach angles are displayed at compression distances of 250(A), 375(B), 500(C), and 875 nm (D). The approach angle was changed from 12° (green), 7° (magenta), and 2° (blue) through the use of an angled substrate. The z-piezo scan size was 2500 nm with a scan rate of 0.02Hz. The displayed frequency data is from the second vibration mode, due to increased S/N response.

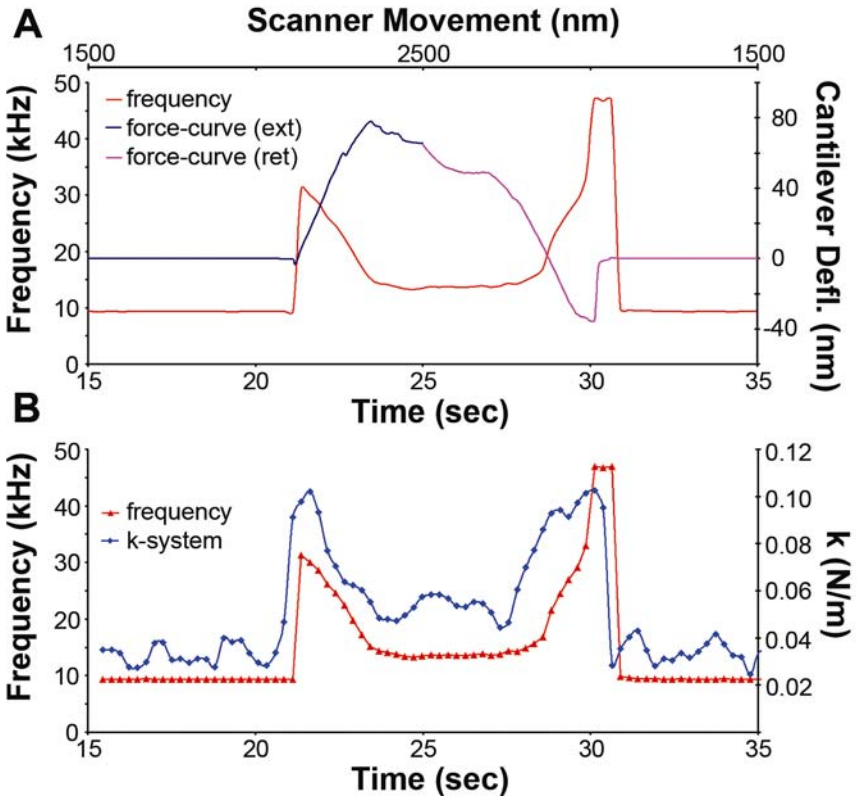

Figure 4.11 . Thermal resonance frequency response with force-distance (A) and calculated system stiffness (B). The data is displayed for the CCNT under a compression distance of 375 nm and approach angle of 2° to the surface.

CHAPTER 5

LARGE ANGLE COMPRESSION OF A CCNT

5.1 Background

In order for the CCNT to behave as an ideal compression spring in NEMS systems, the axial compression needs to be at the surface normal (an compression angle of 0°). In addition to this requirement, the nanocoils need to have closed ends, preventing torque during compression [175-177]. However, the current fabrication technique [96, 97] of the arc discharge method for carbon nanocoil modified probe tips generates an open-ended spring system on the probe. Compounding this with the varying angles of contact during compression, these systems rarely approach ideal compression spring behavior, as found in their macroscale analogs.

In the previous chapter, the compression of a nanocoil system with small but varying angles of compression with respect to the substrate was examined. The initial contact of the coil with the substrate was observed with a characteristic drop in oscillation amplitude, jump to contact in the force-distance plot, and an increase in the thermal resonance frequency [34, 38, 142]. This event is followed with a decrease in the thermal resonance frequency associated with the buckling of the nanocoil. The importance of surface-tip geometry during compression of a carbon nanocoil was discussed. In particular, the occurrence of slip-stick motion can be inhibited or enhanced through changing the angle of compression of the nanocoil to the surface. This was achieved through the use of substrates with a tapered angle.

In this chapter, the compression of an as-fabricated carbon nanocoil modified probe tip exhibiting a 35° compression angle (Figure 5.1) is presented. Due to the large

compression angle of this system, a significant buckling response during the compression study was anticipated. To our surprise, the MPFS response of this system exhibited unique behaviors in both the force-distance and oscillation amplitude plots.

5.2 Results and Discussion

A series of compression studies were conducted on the CCNT modified AFM cantilever probe (see Figure 5.1). The experimental parameters used were identical to those used on the coil presented in Chapter 4. A characteristic drop was observed in the oscillation amplitude curve was used to monitor the point of initial contact between the nanocoil and the substrate. After the initial point of contact was established, the piezo scanner start position was adjusted so that the net compression of the nanocoil increased in multiples of 125 nm. During compression, the nanocoil cantilever system changes from a pinned-open spring system (free-vibrating system) to a pinned-pinned spring (surface-coil-tip system) [175, 176, 178]; due to the geometry of the coil relative to the probe and substrate. During this change, lateral compressive forces are applied to the nanocoil from both the tip and the substrate. Because the nanocoil has an open coil face in contact with the substrate, the nanocoil enters into a buckled state (non-axial compression) once a mechanical load is applied. If the nanocoil had a closed face and appropriate orientation, the system would undergo axial compression of the spring system, behaving as an ideal macro-scale compression spring. After capturing the frequency data, the substrate is retracted form the cantilever returning the system to the free-vibrating state.

During compression studies, several phenomena believed to be influenced by the large compression angle (35°) of the system were observed. These phenomena have not been observed during previous compression, experiments performed on CCNT-modified

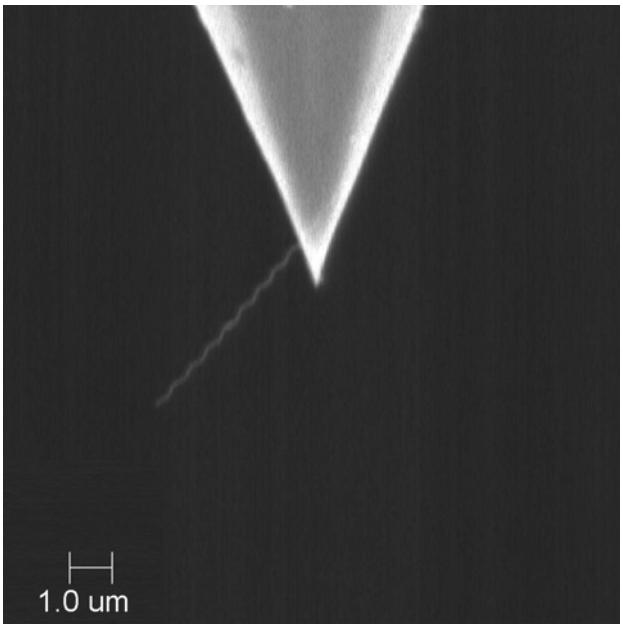

Figure 5.1. SEM image of nanocoil modified scanning probe tip with a compression angle of 35°, relative to the substrate surface.

tips. A zero-load approach to the surface slip-stick motion, and distinct adhesion events are observed during the 'compression' experiments performed on this nanocoil. These were measured using MPFS where the force-distance, oscillation plot, and frequency response were recorded during the compression experiments.

Figure 5.2 displays the acquired force-distance (A) and oscillation amplitude (B) plots for the nanocoil at the initial point of contact with the substrate. The conventional definition of initial contact is the point where either a negative deflection is observed in the force-distance plot due to the van der Waals interactions, or a decrease in the oscillation amplitude approach curve. Although captured at this 'initial' contact point, a significant portion of the nanocoil (~750 nm) is observed having already interacted with the substrate. This figure describes compression events where the nanocoil is able to contact and interact with the substrate without an observable deflecting the cantilever.

The relevant data in the force-distance and oscillation amplitude plots are the significant nanocoil-substrate interactions occurring during the retract potion of the curves. In the oscillation amplitude plot (Figure 5.2B), the occurrence of several amplitude spikes ('ringing' events) in the retract portion of the plot is observed. These have previously been associated with release events between the nanocoil and substrate during slip-stick motion.

The ringing occurs when the surface retracts from the cantilever, putting the coil in tension. During slip-stick motion, the lateral motion of the nanocoil overcomes the friction force of the substrate and ruptures, resulting in low friction movement of the coil across the substrate the slip-portion of the phenomena. This lateral motion is translated into a vertical oscillation observed in the cantilever beam via the nanocoil coupling. The large adhesion interactions occurring in the force-distance plot and slip-stick ringing observed in the oscillation amplitude plot, give evidence that a significant portion of the nanocoil is in contact with the substrate prior to the initial drop in oscillation amplitude associated with the initial contact of the nanocoil to the substrate. This is contradictory to the traditional metrics that associate surface contact with a drop in the oscillation amplitude. Thus with a 35° compression angle, the nanocoil-cantilever system undergoes buckling and slip-stick events prior to conventional detection techniques. In addition to this, no measurable force is applied to the nanocoil (as determined by the force-distance plot) to initiate the buckling. The slip-stick events observed in Figure 5.2 exhibit a phenomena described as zero-load engagement.

The second unique phenomena observed in the large compression angle experiment was that distinct adhesion events observed in the retract portion of both the force-distance and amplitude plots. These events indicate a repeated "tension and release" of the nanocoil modified cantilever probe tip during the retract motion of the substrate. Since only the nanocoil is in contact with the substrate during these studies,

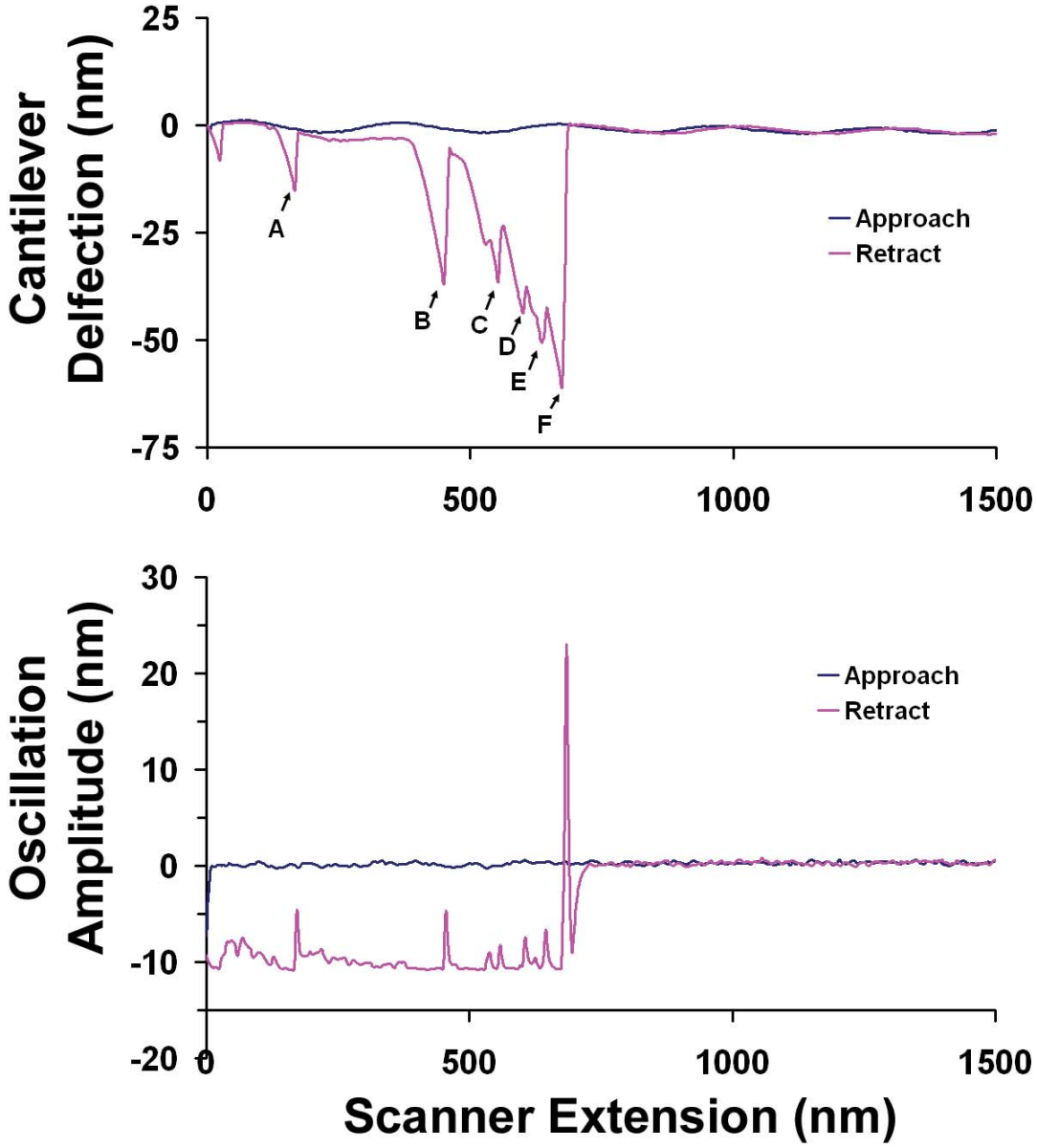

Figure 5.2. Force-distance (A) and oscillation amplitude plot (B) of large compression angle nanocoil at initial contact with surface (0 nm compression). Points A-F represent regions where release events may be occurring between the nanocoil and the substrate.

the adhesion events observed in the force-distance plot are due solely to nanocoil-substrate interactions. These features also correlate to the ringing events occurring in the oscillation amplitude plot with spacing measured at 47.07, 100.37, 137.09, and 274.17 nm from the initial surface contact (as determined from oscillation amplitude drop).

Figure 5.3 is the force-distance and oscillation amplitude plots taken at a compression distance of 125 nm past the initial point of contact. The same features are observed in this plot as those observed in Figure 5.2. In addition to the ringing events from the nanocoil-substrate interactions, a cantilever deflection response associated with compression of the nanocoil is observed. This is similar to the compression of other nanocoils where the applied load forces causes buckling to occur in the nanocoil. Figure 5.3 displays similar spacing of the adhesion events; measured at 55.7, 125, 148.09, and 288.04 nm. These values were similar to those measured in Figure 5.2, suggesting that they are caused by physical features of the nanocoil, rather than random interactions between the nanocoil and the substrate during slip-stick motion. To confirm this, an SEM image of the nanocoil was taken at different angles to better determine its geometry. Through comparing the values of the adhesion events to the physical geometry of the nanocoil (Figure 5.4), a direct correlation between the observed "tension and release" or ringing events with the structure of the nanocoil is confirmed.

5.3 Frequency Response

Under normal AFM operation, a linear response is observed in the force-distance curve as the nanocoil contacts the substrate. In the case of a nanocoil with a large compression angle, this relationship is not observed. However during the retract portion of the plot, significant adhesion occurs for approximately ~750 nm of scanner retract motion in the force-distance and oscillation amplitude plots (Figure 5.2). Initial interpretations of the force-distance and oscillation amplitude plots suggest that there is

no mechanical coupling of the nanocoil-substrate interactions with the cantilever motion during the initial contact with the substrate. Using conventional techniques, the true initial contact between nanocoil and substrate cannot be established. Buckling and slip-stick motion of the nanocoil has already occurred by the time the jump-to-contact in the force-distance and oscillation amplitude plots is observed. The conventional techniques to establish surface contact are unable to determine the true initial point of contact of the nanocoil to the substrate under the extreme orientation of the nanocoil with respect to the substrate, where zero-load engagement occurs. However these techniques are useful in describing events occurring during the retract motion of the scanner, as the nanocoil is observed to have significant adhesive interactions with substrate resulting in observable 'tension and release' events. Although these techniques have been shown to describe events during retract in great detail, their insensitivity to the initial loading of the nanocoil is problematic. By monitoring changes in the thermal resonance frequency of the nanocoil-cantilever system, the points of initial contact, buckling and compression of the nanocoil are easily discerned.

The thermal resonance frequency of the nanocoil-cantilever system was measured during the acquisition of force-distance data a given compression distance. The frequency response for the 125 nm compression is displayed in Figure 5.5. Unlike the force-distance and oscillation amplitude plots, the features observed in the thermal resonant frequency plot are similar to those encountered during the previous compression experiments with small compression angle nanocoils. At the initial contact with the substrate, there is an increase in the measured frequency is associated with system change from a clamped-free to a clamped-clamped state. This frequency increase also indicates an increase in the stiffness of nanocoil-cantilever system. Since the cantilever stiffness is constant, any change in the observed stiffness of the system is attributed to the

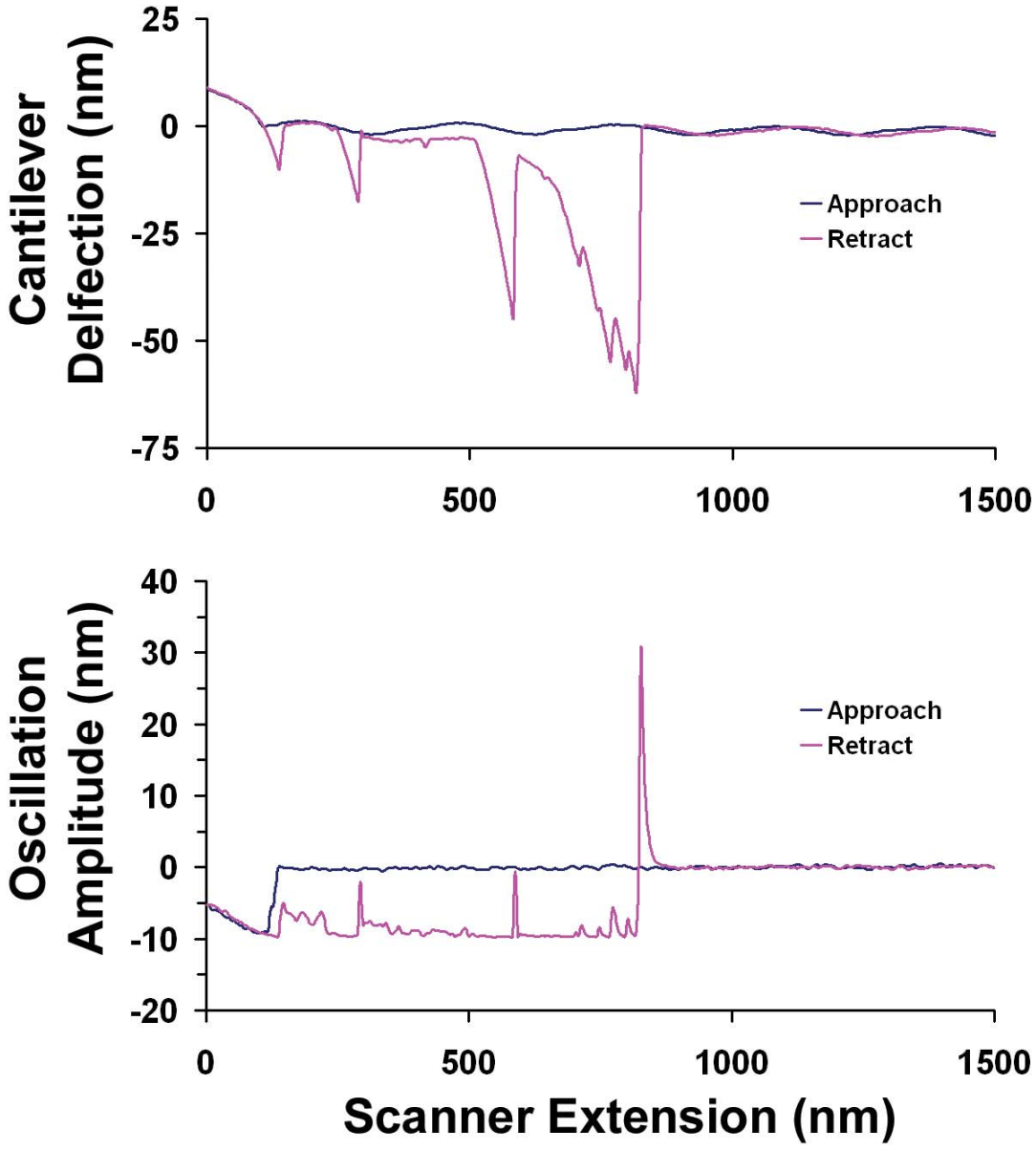

Figure 5.3. Force-distance (A) and oscillation amplitude plot (B) of large compression angle nanocoil after 125 nm compression.

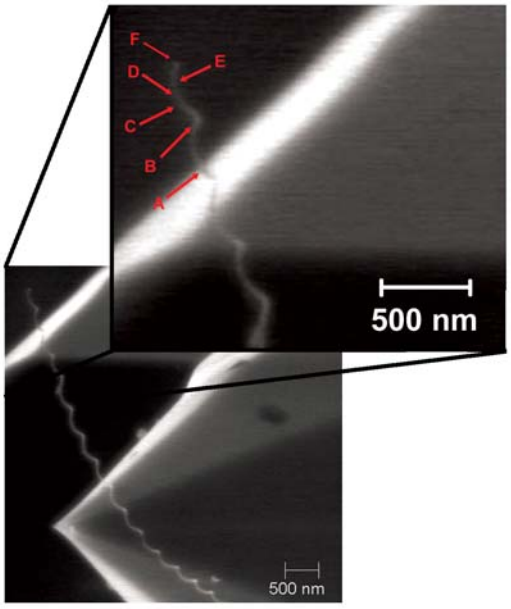

Figure 5.4. SEM image of large compression nanocoil estimating locations where observed slip-stick events A-F may occur. These distances were measured from the free end of the nanocoil.

mechanical properties of the nanocoil. As the compression increases, the nanocoil undergoes mechanical buckling; a phenomenon commensurate with a decrease in the resonant frequency. The frequency response differs significantly during the retract portion of the compression cycle as multiple release events occur.

The retract portion of the frequency plot supports the argument for increased adhesive interactions between the nanocoil and the substrate. The "tension and release" events observed in the force-distance plots are observed in the thermal resonant frequency plot (Figure 5.5: 25-32 seconds) as an increase in the frequency followed by a ringing event. The frequency increase is attributed to the tension that nanocoil experiences as the substrate is retracted. The frequency shift associated with tension has values greater than the initial frequency shift observed during the initial contact between the nanocoil and the substrate. As the coil is put into tension, the stiffness increases to a value greater than that of the nanocoil when put into compression; a phenomena similar

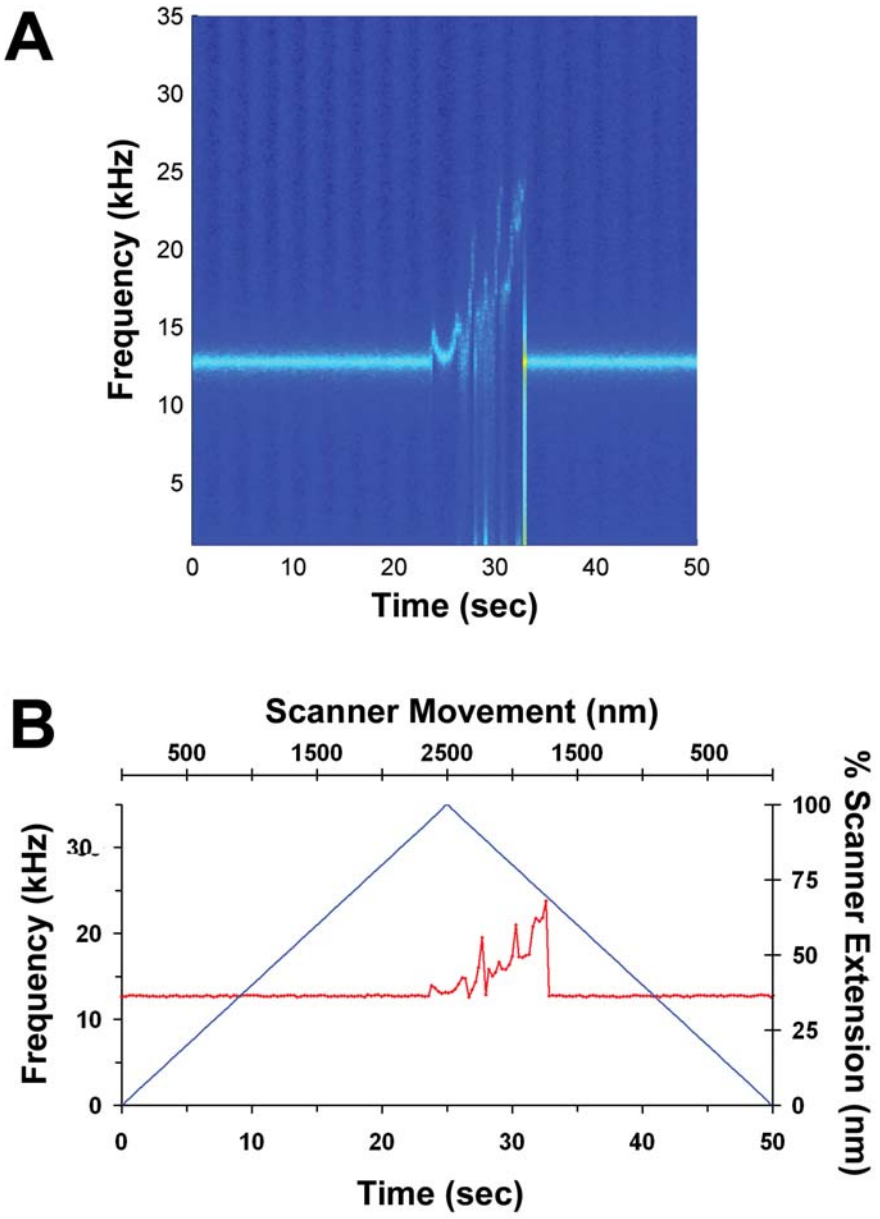

Figure 5.5. Thermal resonant frequency response of large compression angle nanocoil at 125 nm compression. The frequency-amplitude plot displays ringing events occurring (~25-32 seconds) during the retract portion of the scanner movement (A). The frequency response is displayed with the piezoelectric scanner motion (B).

to a macroscale spring [44, 46]. Furthermore, the ringing event is most noticeable as a large amplitude, broad band event in the frequency that does not correlate to any specific mode of the nanocoil-cantilever system. Multiple ringing events in the frequency plot (Figure 5.5A) are observed as there are multiple release events occurring.

5.4 Nanocoil Contamination

Following this above series of compression experiments, a second study was conducted on the nanocoil on a new template stripped gold substrate. The conditions of the second compression experiment were identical to those of the initial compression experiment. In this subsequent set of compression experiments, the force-distance, oscillation amplitude and thermal resonant frequency data were recorded using the MPFS technique.

Figure 5.6 displays the force-distance and oscillation amplitude plots from the second set of experiments at 0 nm (A) and 375 nm (B) compression. Both of these plots display significant nanocoil-substrate interactions, as evidenced by the hysteresis in the retract portion of the curves, where the nanocoil maintains contact with the surface beyond jump to contact point during the retract motion of the scanner. A significant difference between these plots and those initially obtained for the compression of the nanocoil is the absence of the "tension-release" features in the force-distance curve and slip-stick induced "ringing" observed in the oscillation amplitude plots during the first compression study (Figure 5.2). Because the cantilever holder positions the cantilever probe tip in a specific orientation, the same regions of the nanocoil should be in contact with the substrate during both experiments. Given that the contact geometry and the

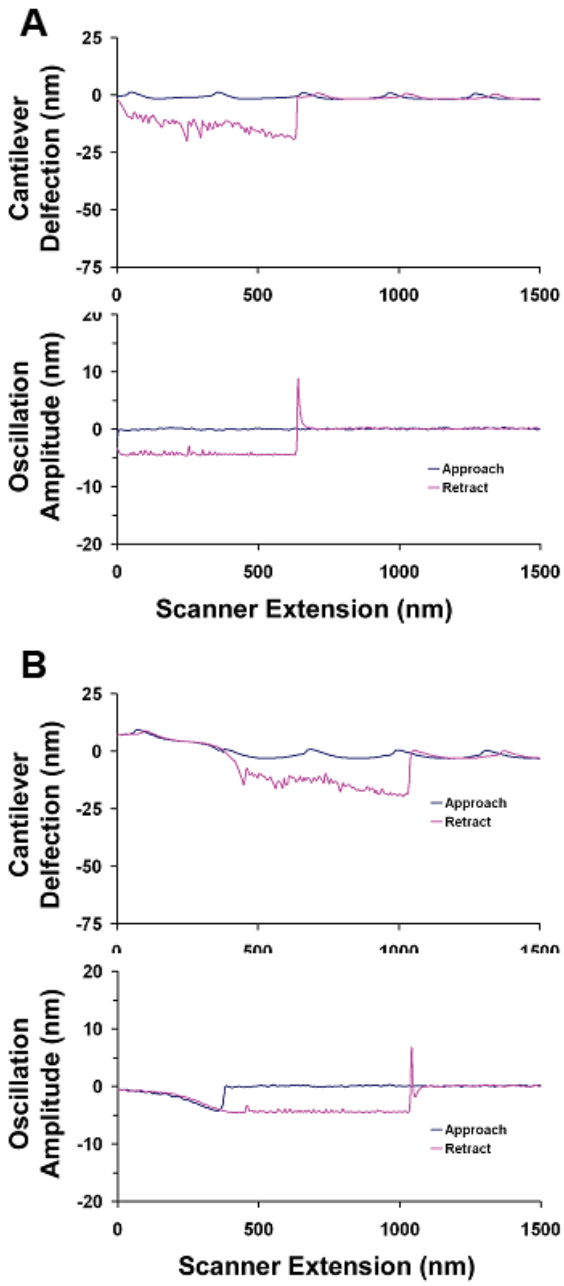

Figure 5.6. Large compression angle tip exhibiting different interactions with a second, freshly prepared 1-dodecanethiol modified gold substrate. Force-distance and oscillation amplitude plots are given for 0 nm (A) and 125 nm (B) compression.

substrate chemistry is identical in both experiments, the loss of these features indicates that a change in the surface chemistry of the nanocoil may have occurred.

5.6 Adhesion Force Measurement

The adhesive forces at each of the unique tension and release events occurring during the compression study of the nanocoil was calculated. These were calculated from the release events occurring in compression experiments conducted at 0, 125, 250, and 350 nm from the point of contact. The force at each release event was calculated by multiplying the cantilever spring constant (0.08 N/m) with the measured displacement from the force distance curve at each event. Table 5.1 displays the calculated forces and their averaged values.

Table 5.1. Summary of experimental rupture forces observed during slip-stick motion of large compression angle coiled nanotube (values given in nN).

Feature	0 nm	125 nm	250 nm	375 nm	Avg.
A	1.2416	1.392	1.6784	1.2264	1.3846
B	2.7848	3.3656	3.0776	2.8664	3.0236
C	2.3648	2.0288	1.624	3.716	2.4334
D	1.624	2.1088	2.0648	----	1.932533
E	1.0296	0.9616	1.5832	1.2488	1.2058
F	1.4616	0.7464	1.9624	1.0624	1.3082

In chapter 4, the mechanical response of a single nanocoil to compression was investigated as a function of substrate surface composition and angle. The important findings from this chapter were: the sensitivity of MPFS measurements to substrate composition, the identification of the second bucking event as slip-stick motion of the nanocoil, and the calculation of the effective spring constant of the nanocoil-cantilever system.. In the present chapter, the mechanical response of an improperly oriented nanocoil was examined. The important findings were that the MPFS technique is very

sensitive to the point of contact on approach and to the physical structure of the nanocoil upon retract. In the following chapter, the compression of several CCNTs will be carried out using the MPFS protocol described above. The structure of these nanocoils will be determined with transmission electron microscopy. Coupling the results of these two investigations, a correlation between the mechanical properties of the CCNTs with their structure will be presented.

CHAPTER 6

CARBON NANOCOIL COMPRESSION MODELING

6.1 Modeling Mechanical Properties of Nanotubes

Nanotubes are either single or nested molecules that have distinct material behavior at the nanometer level. Many of its applications however, involve macro-scale ensembles of nanotubes, e.g. bundles of tubes woven into fibers. Different modeling techniques must be applied to investigate phenomenon occurring over specific dimensional ranges; the results must be reconciled. Some examples of different modeling techniques include molecular simulations, coarse grain simulations, continuum mechanics, micro-scale composite mechanics, and component level structural mechanics (listed in increasing size domain applications) [62, 64, 65, 179]. The dissertation is focused on the behavior of an individual carbon nanotube, rather than its applications; this chapter will focus on modeling applicable to the nanotube itself.

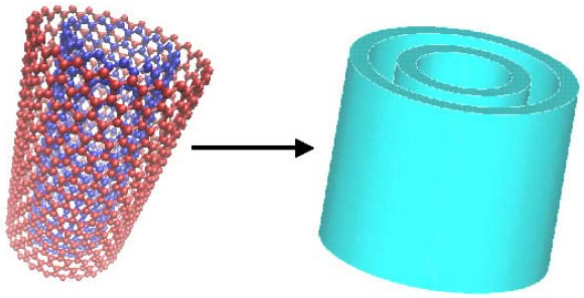

Figure 6.1. Illustration of a double-walled carbon nanotube (left) and its continuum mechanics structure equivalent (right).

6.1.1 Continuum Method

The continuum model is based on traditional engineering models such as beams, shells or membranes. When applied to nanotubes, this model treats the molecules as a continuous material with a definite geometry and isotropic material properties (e.g. Young's modulus) as depicted in Figure 6.1. This is in contrast to molecular dyamics (MD) simulations, where each atom of the molecule is modeled and the interactions with other atoms are mathematically defined.

Yakobson found "a remarkable synergism between the methods of MD and those of macroscopic structural mechanics… [and] with properly chosen parameters, this analytical model predicts nanotube behavior not only at small deformations but also beyond the linear response" [62]. His conclusion was reached during a study in which a molecular dynamic model of nanotubes under axial compression, bending, and torsional deformations was studied. By comparing the observed behavior of the MD system to that of a continuum models, confidence was given to researchers modeling nanotubes by a continuum model based on a simple rod.

Govinjee and Sackman modeled MWCNTs using the Euler beam theorem [180]. In particular, they investigated the use of Euler-Bernoulli beam bending theory (discussed in section 6.1.4) to infer the Young's modulus of the nanotubes. They showed that at the nanoscale, a size dependency exists on the material properties when the continuum cross-section assumption is used. This phenomenon does not exist in classical continuum mechanics. They demonstrated that the use of the continuum cross-section assumption in calculating the nanotube modulus is valid only when the nanotube contains a large number of atomic layers (walls). Using this assumption for nanotubes with a small number of walls yields a greater modulus than that observed experimentally. The continuum-beam assumption was further explored by Harik [181, 182].

Harik addressed the specific applicability of the continuum-beam model to the determination of mechanical properties of carbon nanotubes [181, 182]. This work explains several criteria for the application of the Euler beam model to carbon nanotubes and other nano-rod structures. These criteria assess homogenization, aspect ratio, and linearity of strain of the nanostructures. The homogenization criterion states that $L_{NT}/a_1>10$, where L_{NT} is the length of the nanotube and a_1 is the width of the carbon ring. This criterion asserts that any consideration of homogenization requires a minimum number of graphene cells along the length of the nanotube before the material averaging can be considered unique. The aspect ratio criterion states that $L_{NT}/d_{NT}>10$, where d_{NT} is the diameter of the nanotube. The strain criterion states $(L_{NT}-L_{NT0})/L_{NT0}\ll 1$, where the axial strain of the nanotube is infinitesimal [182]. This work asserts that nanotube, or nanorod, structures will undergo Euler buckling provided that their geometry satisfies the above criterion as described in an applicability map (Figure 6.2). For most nanotube studies, the nanotube is of sufficient length to allow the continuum-beam model to be applied to the system. In cases of small aspect ratio geometries for the nanotube, this model may not be applicable.

Ru used a shell model to determine the effects of interlayer forces in the axial buckling and bending of carbon nanotubes [49]. The shell model is a continuum mechanical model of MWCNTs as tubes within tubes. He found that the van der Walls forces between layers of a double or multi-walled nanotube cause an inward force to act on some of the tubes in the molecule. This causes the critical axial strain of MWCNTs to be lower than that of SWCNTs of the same outer diameter [50, 183, 184]. Although the axial strain for the MWCNT may be reduced compared to the SWCNT, the axial force applied to it may be increased due to the larger cross-sectional area. When nanotubes are embedded in an elastic matrix, the relationship between strain and interlayer forces is again observed [184, 185]. This again demonstrates the significant relationship between

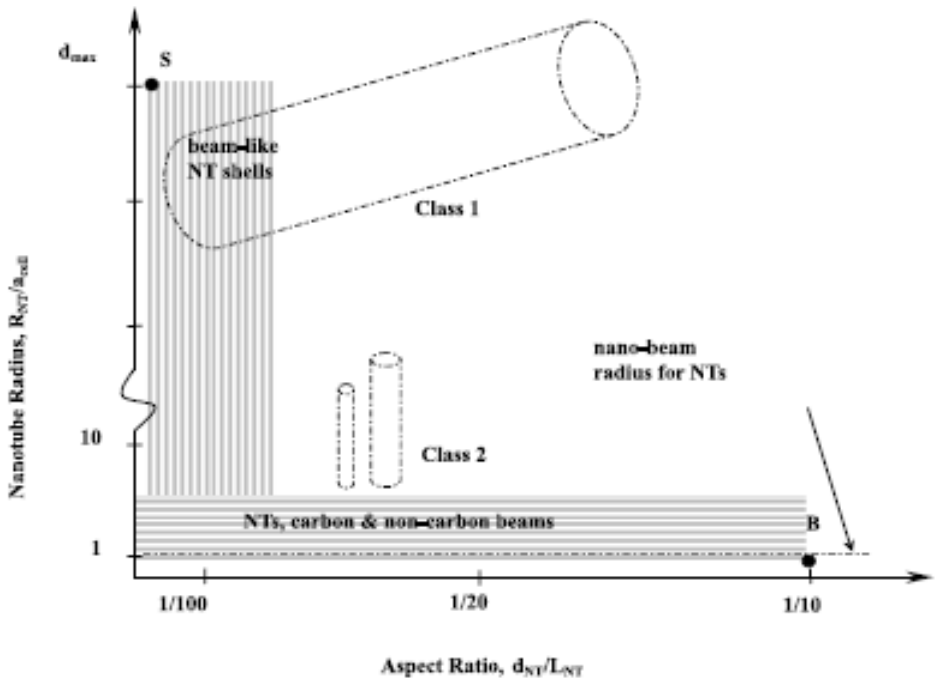

Figure 6.2. Applicability map for the continuum beam model depending on non-dimensional ratios of geometric parameters found by the scaling analysis of the consecutive behavior of carbon nanotubes. (Reprinted from [182]. Copyright 2002, with permission from Elsevier)

the observed geometry and composition (number of walls) with the material properties of the nanotube.

6.1.2 Material Properties of SWCNTs

In the macroscale analysis of mechanical systems, one of the more important quantities is the Young's Modulus, E, a constant material property. When investigating the Young's Modulus of carbon nanotubes, the value is expected to change with the diameter of the tube, since the change in curvature of the tube modifies the C-C bond hybridization [186], thus changing the stiffness of the molecule. When determining the properties of single and multi-walled carbon nanotubes, some groups treat the nanotube as an isotropic structure, with a fixed shell thickness, according to the continuum mechanics model. In modeling a single walled carbon nanotube (SWCNT), the continuous shell approximation has been found to be a sufficient approximation with the calculated values of E and the shell thickness (t) for the nanotube having similar values to that of a single graphene sheet. The Young's modulus of multi-walled carbon nanotubes (MWCNTs) was found to be similar to that of bulk graphite.

Differing reports have been presented on the calculated modulus of the single-walled nanotube. Yakobson and Zhong Chan have reported values of $E \approx 5TPa$ with an associated shell thickness $t \approx 0.07$ nm [62, 69, 187], where the wall thickness value is defined by the pi-bond thickness. Many other groups have reported values comparable to that of bulk graphite, $E \approx 1TPa$ with $t \approx 0.34$ nm [53, 64] for the SWCNT. Treating the nanotube as a homogenous isotropic continuous shell of thickness t, the elastic deformations can be calculated from the Young's modulus and the Poisson's ratio, ν. If one neglects the curvature of the nanotube, assuming it to be a graphene sheet of width $2\pi R$, E and t can be determined from the bending rigidity (D(t)) and in-plane stiffness (C(t)) of graphene [188]

$$D(t) = \frac{Et^3}{12(1-\nu^2)}$$ Equation 6.1

$$C(t) = Et$$ Equation 6.2

where D(t), C(t), and ν are values intrinsic to the graphene determined from the C-C bond rigidity and can be calculated without assuming a value for t.

The bending rigidity (*D*) of graphene has been determined from a number of different techniques including molecular dynamics [189] and first principle calculations [61, 179], neutron scattering from the out-of-plane vibrational frequency of graphite [190]. In these cases the bending rigidity is determined by inversion configuration of the C-C bonds [191]. The values of the *D* varied from 0.85cV to 1.5cV depending on the method by which it was determined. The in-plane stiffness (*C*) is found to have a value of ~60eV/atom and depends on bond stretching and the angle variation in the molecular force field framework [188]. The value for graphene Poisson's ratio (ν) is also calculated from a variety of methods, giving a broad range of values between 0.16 and 0.34 [65, 187, 189, 192]. Using these values in (Equation 6.1) and (Equation 6.2) the modulus and thickness are given as $E \approx$ 5TPa and $t \approx 0.07$ nm. Some groups continue to use $E \approx$ 1TPa and $t \approx 0.34$ nm (values comparable to graphite) when describing single walled nanotube properties, despite the evidence that the thickness of the shell should be less than 0.1 nm when using the isotropic continuous shell approximation, assuming the nanotube similar to graphene. This disagreement stems from the treatment of the thickness of the graphene sheet in their respective theoretical models, as the values are equivalent when determining axial stiffness. The value of *E* however, becomes important in determining the flexural properties of the nanotube.

The moment of inertia for a single-walled nanotube is greater than that of a graphene sheet. This conclusion follows from the calculation of the effective flexural rigidity (*EI*) of a SWCNT [188]

$$EI = E\frac{\pi D_0^4}{64}\left(1-\left(\frac{D_i}{D_0}\right)^4\right) = E\frac{\pi D_0^4}{64}\left(1-\left(1-\left(\frac{2t}{D_0}\right)\right)^4\right) \quad \text{Equation 6.3}$$

if $2t \ll D_0$, then $(1-(2t/D_0))^4 \approx 1-4(2t/D_0)$. Thus, the flexural rigidity (Equation 6.3) can be written as

$$EI = \frac{\pi}{8}D_0^3 Et = \frac{\pi}{8}D_0^3 C \quad \text{Equation 6.4}$$

this relationship describes that the in-plane stiffness of graphene, *C,* governs the bending rigidity of a large diameter SWCNT. Thus, the shell thickness of graphite ($E \approx 1$TPa, $t \approx$ 0.34 nm) can be used to approximate the properties of a SWCNT.

6.1.3 Material Properties of MWCNTs

The multi-walled carbon nanotube can be described as concentric graphene sheets rolled on top of each other. The system can also be approximated a system of graphene stacks laying on each other. A two-layer graphene tube is considered as an anisotropic shell with a thickness of $t_D = t + d_i$, where d_i is the interlayer distance (0.34 nm for graphite). If van der Waals forces are assumed to prevent the sliding of the layers, then the neutral plane is between the layers and the bending stiffness is determined by the in-plane C-C bonds instead of the out-of-plane stiffness of a single graphene sheet [190]. The properties of the two-layered graphene stack is described as a shell with $E \approx 1$ TPa and $t \approx 0.34$ nm. When determining the Young's modulus of nanotubes with a larger number of shells, N, the following is used

$$E_N = \frac{N_W}{N_W - 1 + (t/d_i)}\frac{t}{d_i}E \quad \text{Equation 6.5}$$

where E = 4.7Tpa and t = 0.074 nm [187].

6.1.4 Beam Theory

The above sections described the application of the continuum mechanical model to carbon nanotubes. Many groups have modeled the carbon nanotube as an elastic beam. There are different mathematical models describing the transverse vibration of beams taking into account different effects that one may experience in the real world behavior of the beam. Bress-Timoshenko [193] and Love theories model the beam with bending, shear deformation, and rotary inertia. The Rayleigh theory [194] models only bending and shear effects on the beam elements. The Euler-Bernoulli beam theory [194], often referred to a simply beam theory, models only the transverse bending of a beam.

Euler-Bernoulli beam theory describes the relationship between beam deflection and an applied load. The beam was originally modeled as a one-dimensional object with a distributed load. The simplicity of beam theory has led to its adoption as an important tool in science and engineering. The following is differential expression for the transverse vibration of a thin beam from Euler-Bernoulli theory

$$\frac{\partial^2}{\partial x^2}\left[EI(x)\frac{\partial^2 y}{\partial x^2}\right]+\rho A\frac{\partial y^2}{\partial t^2}=0 \qquad \text{Equation 6.6}$$

where y is the deflection of the beam, EI is the bending modulus of the beam, ρ is the density of the beam material, A the cross-sectional area, and t is time. The successive derivatives of y along with terms in Equation 6.6 give quantities that describe the slope of the beam deflection (θ), bending moment (M), and shear force (V) [194, 195]

$$\theta=\frac{\partial y}{\partial x}, \qquad M=EI(x)\frac{\partial^2 y}{\partial x^2}, \qquad \mathrm{V}=-\frac{\partial}{\partial x}\left(EI(x)\frac{\partial^2 y}{\partial x^2}\right) \qquad \text{Equation 6.7}$$

making the Euler-Bernoulli model a widely used and versatile model for engineers and scientists. As the beam becomes more complicated with specific conditions such being on an elastic foundation, under an axial force, etc, then additional terms can be added to

the differential form of beam theory. Equations for such conditions are listed in Table 6.1. By combining these, the differential equations used to describe different beam behaviors can be generated. The distributed load on a basic beam is given by

$$q(x) = \rho A \frac{\partial^2 y}{\partial t^2} + EI \frac{\partial^4 y}{\partial x^4} \qquad \text{Equation 6.8}$$

where $q(x)$ is the distributed applied load, y is the displacement, ρ is the density, A is the cross-sectional area. The stiffness of the beam, k, is also derived from beam theory from the second moment of the cross-sectional area to give

$$k = \frac{3EI}{l^3} \qquad \text{Equation 6.9}$$

where l is the beam length. The critical buckling load (P_{crit}) is the axial load where the compressive stresses of the beam can lead to failure. This is calculated as

$$P_{crit} = \frac{\pi^2 EI}{l^2} \qquad \text{Equation 6.10}$$

for a beam with both ends pinned. The pinned-pinned boundary condition describes the cantilever probe under compressive load. This expression changes with the variety of boundary conditions that can exist for the beam.

The vibration of the cantilever can occur at several modes. The fundamental mode (natural) vibration of the beam is of great importance to researchers. The natural frequency of the ith mode of vibration for the beam is

$$\omega_i = \frac{\beta_i^2}{l^2} \sqrt{\frac{EI}{\rho A}} \qquad \text{Equation 6.11}$$

where β_{i} is the solution for an equation that is dictated by the boundary conditions of the beam system. For approximating a nanotube beam freely vibrating, a clamped-free boundary condition is assumed. The clamped end has zero displacement and zero slope, while the free end has zero reaction forces during the displacement. The boundary equation for a clamped free system is given as

Table 6.1. Mathematical models of transverse vibration of non-uniform Euler-Bernoulli beams [195]

Conditions	Differential equation of transverse vibration (Euler-Bernoulli model, EI is not constant)	Comments
End is shifted; axial force is compressive	$\frac{\partial^2}{\partial x^2}\left[EI(x)\frac{\partial^2 y}{\partial x^2}\right]+N\frac{\partial y^2}{\partial x^2}+\rho A\frac{\partial y^2}{\partial t^2}=0$	Force N is constant or not, but does not depend on *y(x,t)* ; system is linear
End is shifted; axial force is tensile	$\frac{\partial^2}{\partial x^2}\left[EI(x)\frac{\partial^2 y}{\partial x^2}\right]-N\frac{\partial y^2}{\partial x^2}+\rho A\frac{\partial y^2}{\partial t^2}=0$	Force N is constant or not, but does not depend on *y(x,t)* ; system is linear
Winkler foundation. One stiffness characterization	$\frac{\partial^2}{\partial x^2}\left[EI(x)\frac{\partial^2 y}{\partial x^2}\right]+k_{tr}y+\rho A\frac{\partial y^2}{\partial t^2}=0$	Reaction of the foundation: $R(x)=k_{tr}y$ k_{tr} is translational stiffness coefficient
Pasternak foundation. Two Stiffness characterization	$\frac{\partial^2}{\partial x^2}\left[EI(x)\frac{\partial^2 y}{\partial x^2}\right]+k_{tr}y-k_{rot}\frac{\partial^2 y}{\partial x^2}+\rho A\frac{\partial y^2}{\partial t^2}=0$	Reaction of the foundation: $R(x)=k_{tr}y-k_{rot}\frac{\partial^2 y}{\partial x^2}$ k_{rot} is the rotational stiffness

$$\cos\beta_i \cosh\beta_i + 1 = 0 \qquad \text{Equation 6.12}$$

The solutions for Equation 6.12 give values used in determining the *i*th-mode frequencies of a clamped-free beam. These values are calculated as $\beta_1 \approx 1.875$, $\beta_2 \approx 4.694$, and $\beta_3 \approx 7.855$. Higher order modes can be calculated, but are not often experimentally observed in nanotube vibration. The amplitude of vibration for a nanotube is given by

$$\sigma^2 = \frac{16L^3kT}{\pi E(a^4 - b^4)} \sum_n \beta_n^{-4} \approx 0.4243 \frac{L^3kT}{E(a^4 - b^4)} \qquad \text{Equation 6.13}$$

where σ is the amplitude at the free end of the beam, L is the beam length, k is the Boltzman constant, T is the temperature, a is the outer radius and b is the inner radius of the nanotube.

6.2 Nanocoil Compression Model: Data Acquisition

A group of 18 carbon nanocoil modified cantilever probe tips were chosen to determine the relationship between nanocoil structure and its mechanical properties. For each nanocoil, the geometry was measured through SEM imaging, and the chemical structure was measured through TEM imaging. Multi-parameter force spectroscopy (MPFS) was used to measure the mechanical response of each individual nanocoil under a compressive load.

This study sets the ambitious goal of developing a predictive model from MPFS and TEM data to predict the structure of carbon nanocoils from mechanical properties measured from the collected compression data; consisting of thermal resonance frequency response, force-distance and oscillation amplitude plots. Some groups have developed theoretical models relating the structure of a straight MWCNT to its mechanical properties [187]. Other groups have experimentally observed that the geometry of the MWCNT can impact the mechanical response [140]. Specific research into coiled carbon nanotubes and their mechanical properties is limited. Chen et al. [46]

have measured the mechanical response of a single nanocoil under tensile load; finding it to behave as elastic coils with minimal deformation. The majority of the publications focusing on coiled carbon nanotubes are focused on their fabrication rather than their properties.

6.2.1 Cantilever Selection

Two sets of carbon nanocoil modified cantilever probe tips were fabricated according to methods described in Chapter 3. The scanning probes used in this investigation were MikroMasch Series 18 and CSC-38 cantilever probe chips; chosen for their broad range of cantilever beam spring constants. Table 6.2 contains the manufacturer specifications for the selected cantilevers in this study. The Series-18 probes contained a single beam with an average stiffness of 3.5N/m. The CSC-38 chip had three beams, hereby designated as beam-a, beam-b or beam-c, with average beam stiffness values of 0.08(a), 0.03(b) and 0.05(c) N/m. Carbon nanocoils were attached to these probe tips using the arc discharge attachment method [97]. The coiled carbon nanotube source was created using the CVD method with a proprietary catalyst formulation designed to preferentially grow coiled nanotubes over straight tubes.

Although the CSC-38 cantilever chips have three beams, only one was modified per chip. This decision was based on the following facts. Firstly, the tips are aligned under an optical microscope whose field of view is small. Only one beam could be observed and properly modified at a time. Secondly, even though several probes per chip can be prepared, only one nanocoil can be monitored at a time as it interacts with the substrate. Compression studies carried out on the nanocoils attached to shorter, stiffer beams would be performed with nanocoils attached to longer beams experiencing such high compressive loads that mechanical damage to the nanocoils is highly likely. To avoid this problem, the decision was made to only modify one of the three beams on the

CSC-38 chip. In the CSC-38 fabrication process, the majority of the modified cantilevers were beam-B; having the lowest rigidity and being the longest of the three cantilever beams. The beam length also allowed for improved alignment between the tip and the CCNT sample.

6.2.2 Nanocoil Characterization

Following the fabrication process, the quality of the cantilever tip alignment was investigated by scanning electron microscope imaging (SEM). The SEM used in this investigation was a LEO 1550 model with a resolution of 2 nm. SEM imaging provides two functions; verification of the condition of the nanotube (alignment and geometry) and measuring the beam dimensions. The nanotube alignment and geometry is used to classify the large scale structural characteristics of the nanocoil. SEM imaging is able to

Table 6.2. MikroMasch manufacturer specifications for Series-18 and CSC-38 cantilever beams.

			Cantilever Thickness (μm)			Resonant Frequency (kHz)			Force Constant (N/m)		
Cantilever Type	Cantilever Length (±5 μm)	Cantilever Width (±3 μm)	min	typical	max	min	typical	max	min	typical	max
Series 18	230	40	2.5	3	3.5	60.0	75.0	90.0	2.0	3.5	5.5
CSC38											
lever A	250	35	0.7	1.0	1.3	14.0	20.0	28.0	0.02	0.08	0.2
lever B	350	35	0.7	1.0	1.3	7.0	10.0	14.0	0.01	0.03	0.08
lever C	300	35	0.7	1.0	1.3	9.5	14.0	19.0	0.01	0.05	0.1

provide information about the nanocoil geometry used in the analysis of the compression study: compression angle, coil (spring) diameter (D), bar diameter (d) (width of the nanotube), free length (l_0), and number of active coils (n). An illustration describing

these dimensions is given in Figure 6.3. Beam dimensions from SEM images can be used to determine the cantilever stiffness and resonance frequencies using the Sader [196, 197] or Cleveland [198, 199] method. These treat the beam as a simple harmonic oscillator, calculating the resonance behavior from the material properties and geometry of the beam. In this study, the frequency of the beam is directly measured from two sources, the Nanoscope™ tuning software and from the Fourier transform performed on the beam deflection signal. During batch imaging of the nanocoils, it was soon discovered that a range of nanocoil geometries and alignments were made during the tip fabrication process. A complete catalog of the carbon nanocoil-modified cantilever portfolio is provided in Appendix B.

Prior to the compression of a nanocoil, SEM images of the nanocoil were captured in three different orientations to determine the coil alignment with respect to the probe tip. The images were collected with the tip directly in front of the cantilever beam (down-beam), the left or right side view of the tip and beam (side-beam), and the view from the apex of the tip (top). These view points are demonstrated in Figure 6.4. Collectively, these images provide a three dimensional approximation of the nanocoil structure. The relative angle between the nanocoil and the cantilever probe tip allows us to determine the contact angle that the coil will experience when in contact with a flat substrate. Orthogonal view points were used to measure α1 and α2, the relative angle of the nanocoil to the probe tip. These values were used in Equation 6.14 to calculate the compression angle of the nanocoil (α_{comp}).

$$\alpha_{comp} = \frac{\pi}{2} - \arctan\left[\frac{2}{\sqrt{(\tan\alpha_1)^2 - (\tan\alpha_2)^2}}\right] \qquad \text{Equation 6.14}$$

A group of nanocoils were selected for the compression study based on several factors. Because the compression angle can impact the onset of buckling and slip-stick motion of the nanocoil, those with small compression angles (<10°) were selected. With the use of

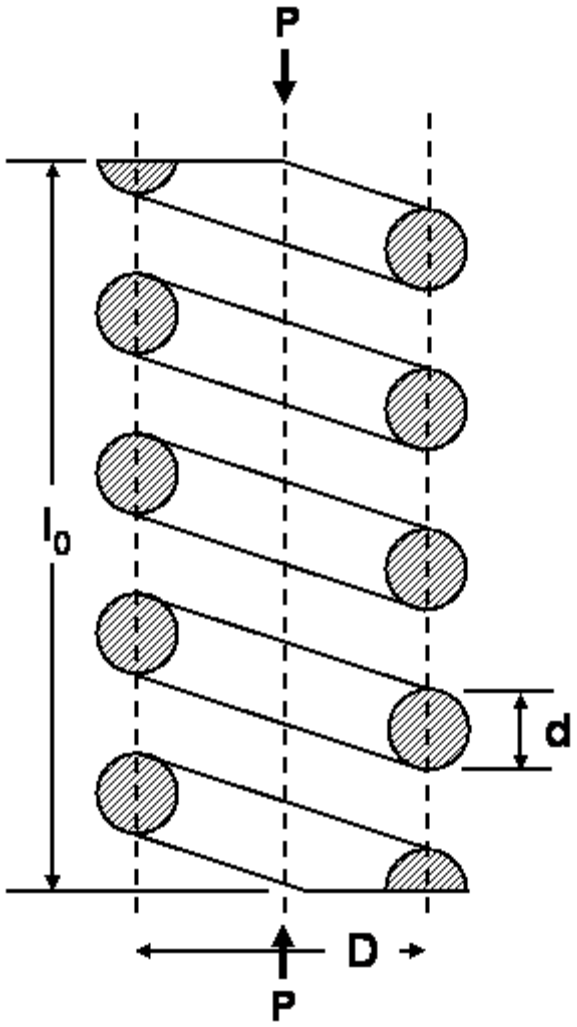

Figure 6.3. Illustration of coil (D) and bar (d) diameter of helical compression coil

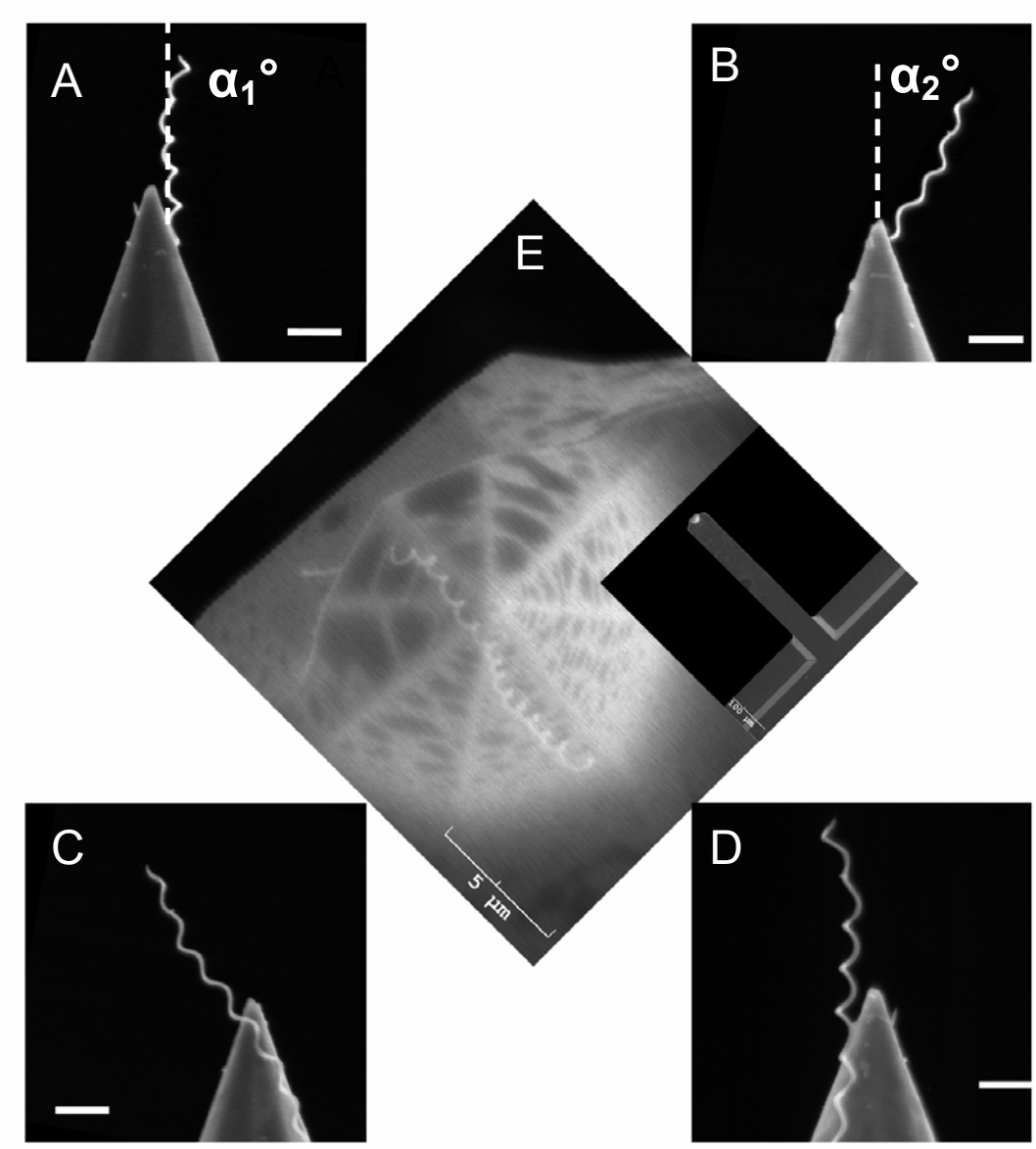

Figure 6.4. SEM images of nanocoil displaying different captured viewpoints: down-beam (A), right side (B), left side (C), up-beam (D), and top (E). Orthogonal view points are used to measure the angle of the nanocoil relative to the tip. α1 and α2 are used to calculate the effective compression angle of the nanocoil using Equation 6.14. Scale bars represent 2µm, unless otherwise stated.

angled substrate shims, the compression angle of the nanocoil was corrected to achieve values nearing the ideal conditions of axial compression of the nanocoil, a compression angle of zero degrees. The compression angles of the selected nanocoils are presented in Table 6.3. The nanocoils were also selected based on the helical structure of active nanocoil. During the attachment process using the arc discharge method, the free end of the nanocoil attaches to the scanning probe tip. It is detached from the source material as the applied current induces resistive heating at a defect site along the length of the coil. Because of this, the carbon nanocoils in the present study have varying number of active coils, helical angle, free length, and thickness. Currently there is no known method to control the length of the nanocoils during the arc discharge attachment method. There are several published techniques that can be used to shorten the nanocoils length after attachment [140, 200], however this was not performed on the nanocoils studied herein. The geometry of the nanocoils is intrinsic to the fabrication process. Table 6.3 gives the measured geometries from SEM images of the nanocoils used in this study.

6.2.3 Compression Experiments

After SEM imaging, each nanocoil subjected to the compression studies: identical conditions and instrumental parameters were used throughout this study. All nanocoils were compressed against flat TSG substrate treated with a 1-dodecanethiol. In some cases, compressions were performed with an angled shim.

After the substrate and the cantilever chip were placed in the AFM, the system would be enclosed in a dry nitrogen box to minimize the humidity during the compression study. The extent of nanocoil compression was controlled through the AFM software operating in both force-distance and oscillation amplitude capture modes. The 'jump-to-contact' observed in the oscillation amplitude plot was used to reference the starting point for the compression. The piezoscanner would then travel past this set point

Table 6.3. Summary of carbon nanocoil geometry measurements from scanning electron microscope imaging.

	CSC-38													Series-18				
Tip Number	**1**	**2**	**3**	**4**	**5**	**6**	**7**	**8**	**9**	**10**	**11**	**12**	**13**	**14**	**15**	**16**	**17**	**18**
Lever	C	B	B	B	B	B	B	C	C	C	C	C	C					
number of coils (n)	2	9	6	4	4.5	3	4	2.5	12	3.75	2.75	13	2	2.5	11	1	3.5	5
free length (l_0)	1.40	4.01	6.00	5.17	11.26	9.04	5.08	7.93	11.95	6.72	3.47	7.07	6.60		12.866	3.691	4509.7	
coil diameter (D)	0.200	0.095	0.282	0.322	0.355	0.596	0.258	0.428	0.289	0.276	0.289	0.166	0.326	0.2424	0.2509	0.5183		
bar diameter (d)	0.146	0.039	0.137	0.119	0.121	0.097	0.107	0.082	0.102	0.107	0.090	0.061	0.118	0.100	0.119	0.134		
Angle From Tip Normal	16.8	5.9	7.3	19	7.58	5.57	24.11	4.37	11.96	6.11	10.54	40.7	20.68	12.26	6.628	7.34	18.52	
Compression Angle	4.8	6.1	4.7	7	4.42	6.43	12.11	7.63	0.04	5.89	1.46	28.7	8.68	0.26	5.372	4.66	6.52	

*all units in μm

to the following values: 125, 250, 375, 500, 625, 825, and 925 nm. The scan size for the piezomotor cycle was held constant at 2500 nm with a scan rate of 0.02Hz. For each compression experiment, the force-distance, oscillation amplitude plot, and the frequency response of the nanocoil-cantilever system were recorded. These are used in the quantitative analysis of the compression of the individual nanocoils. In some cases, such as with nanocoils of large length, additional compression experiments were conducted at higher compression values. The frequency capture software (Labview) were a 7000 point FFT of the deflection signal, with 15 averages of conducted on each recorded power spectrum data set. To capture the waterfall plot, 400 of the averaged PSDs were captured. These compression conditions were optimized so that two complete scan cycles could be recorded by the software. In addition to these conditions, additional frequency data was collected at a scan rate of 0.01Hz to better resolve the frequency response of the system during compression.

6.2.4 Transmission Electron Microscopy

Following the compression experiments, transmission electron microscope images of the nanocoils were obtained. This was completed with the use of a custom holder designed specifically for the JEOL100CX-2 TEM. Conventional TEM sample holders are less than are designed to hold a circular sample grid less than a few hundred microns thick. To image the nanocoils on the conventional sample grid, it would need to be removed from the cantilever, preventing any further studies from being conducted with the imaged coil. In addition to this limitation, locating the nanocoil on the grid would further complicate capture of the TEM of the nanocoil. With the custom holder (Figure 3.13) both of these problems are solved. The whole cantilever can be placed in the holder, preserving the modified tip. In addition to this, the holder is designed to suspend the probe tip near the center of the beam path, enabling the user to locate the nanocoil

with relative ease. The TEM images are used to determine the number of wall that make up the carbon nanocoils. Chapter 3 discusses the equipment setup and the collection of the compression data in greater detail. Table 6.4 displays the TEM measurements of the nanocoils in this study.

6.3 Nanocoil Modeling and Theory

The material properties of the carbon nanocoils are calculated using several different methods. In each method, the goal is to measure or calculate the Young's modulus of the carbon nanocoil while it is attached to the cantilever probe tip. Because of the helical nature of the carbon nanocoil, the following calculations assume that it has spring-like behavior and can be modeled as a compression spring. With this assumption, the nanocoil-cantilever system is simplified into a mechanical system composed of two springs. Figure 6.5 describes the different configurations for two mechanical springs with an applied load: series and parallel.

Working under the assumption that carbon nanocoils possess compression spring behavior, the spring constant of the coil can be used to determine its elastic modulus. The spring constant for a coil (k) is related to the shear modulus of the spring material through geometric relationship given in the following equation

$$k = \frac{Gd^4}{8D^3n} \qquad \text{Equation 6.15}$$

where G is the shear modulus of the spring material, d is the bar diameter, D the coil diameter and n the number of active coils [175]. Re-writing the equation to incorporate a hollow spring bar or tube, and putting it in terms of shear modulus giving

$$G = \frac{8kD^3n}{(d_0^4 - d_i^4)} \qquad \text{Equation 6.16}$$

Table 6.4. Summary of carbon nanocoil geometry and internal structure by transmission electron microscopy.

	CSC-38													Series 18				
Tip Number	**1**	**2**	**3**	**4**	**5**	**6**	**7**	**8**	**9**	**10**	**11**	**12**	**13**	**14**	**15**	**16**	**17**	**18**
free length (l_0)	1596.8	3246.9	5748		8324.1		4755.9	7542.3	11360		3141.6	5420.2	4370	1650.6	17.567	2831.3	5491	9.241
coil diameter (D)	225.7	58.65	268.9	175.14	142.1	576.51	180.62	415.4	120.24	276.2	228.28	126.63	216.58	180.2	121.26	440.24	292.53	230.45
bar diameter (d)	49.557	32.32	90.418	71.799	55.292	83.97	58.337	67.522	63.587	59.81	61.7	32.84	52.595	72.651	72.3	84.398	87.162	88.679
wall thickness (t)	11.443	7.89	37.98	16.655	25.406	31.71	20.421	17.234	20.824	8.143	15.832	13.341	21.572	29.52	30.453	22.405	37.829	40.889
inner radius (r_i)	13.336	8.27	7.229	19.245	2.2401	10.275	8.7475	16.527	10.969	21.762	15.018	3.079	4.7255	6.8055	5.697	19.794	5.7518	3.4505
outer radius (r_0)	24.779	16.16	45.209	35.9	27.646	41.985	29.169	33.761	31.793	29.905	30.85	16.42	26.298	36.326	36.15	42.199	43.581	44.34
number of walls (N)	33.7	23.2	111.7	49.0	74.7	93.3	60.1	50.7	61.2	24.0	46.6	39.2	63.4	86.8	89.6	65.9	111.3	120.3

Springs in Series

$$\frac{1}{k_{eq}} = \frac{1}{k_1} + \frac{1}{k_2}$$

Springs in Parallel

$$k_{eq} = k_1 + k_2$$

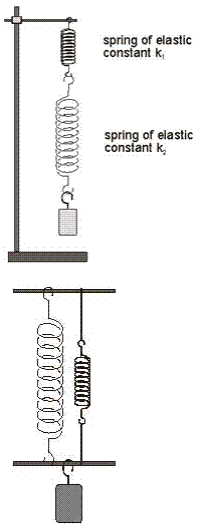

Figure 6.5. Equations for the calculation of the effective spring constant k_{eq} for two springs in series (top) and parallel (bottom).

where d_0 and d_i are the outer and inner bar diameters, respectively. For elastic materials, the shear modulus is related to the elastic (Young's Modulus) by the following expression: $G=E/2(1+v)$, where ν is the Poisons ratio. Assuming ν = 0.3, one can write the expression in terms of the elastic modulus to give

$$E = 2.6G = \frac{20.8kD^3n}{(d_0^4 - d_i^4)} \qquad \text{Equation 6.17}$$

Two approaches were explored to calculate the spring constant of the coil. The first uses the linear response of the nanocoil-cantilever system measured in the force-distance curve to determine the spring constant of the nanocoil. The second method calculates the spring constant of the coil from the frequency response of the nanocoil-cantilever system through fitting the power spectrum density plot (PSD) of the fundamental vibration of the cantilever-nanocoil system during compression. Force-distance data was also used to calculate the shear modulus of the nanocoil-cantilever system, without measuring the spring constant of the nanocoil or the cantilever beam. In some cases, the force-distance plot demonstrates bucking and slip-stick motion of the system. The shear modulus can be

calculated by measuring the force (load) acting on the nanocoil as it buckles. For a helical spring, the following expression describes the critical buckling C_B , the ratio of the deflection at critical load (σ_{CR}) to the free length of the spring (l_0)

$$C_B = \delta_{CR} / l_0 = 0.812\left[1 \pm \sqrt{1 - 6.87\left(\frac{D}{l_0}\right)^2}\right] \qquad \text{Equation 6.18}$$

this expression is derived in detail in Wahl's Mechanical Springs Book [175]. The critical load (P_{CR}) is related to the critical buckling through the compressive rigidity (α_0) of the coil

$$P_{CR} = \frac{\delta_{CR}\alpha_0}{l_0} = C_B\alpha_0 \text{ where } \alpha_0 = \frac{Gd^4 l_0}{64r^3 n} \qquad \text{Equation 6.19}$$

solving for shear modulus (G)

$$G = \frac{64P_{CR}r^3 n}{0.812(d_0^4 - d_i^4)l_0\left(1 \pm \sqrt{1 - 6.87\left(\frac{D}{l_0}\right)^2}\right)} \qquad \text{Equation 6.20}$$

where r is the mean coil diameter. The D/l_0 term describes the conditions of the coil ends. D/l_0 is for fixed-guided spring ends. $2D/l_0$ is used for fixed-fixed spring ends, and $D/2l_0$ is used for clamped-free spring ends. Using $G=E/2.6$ one can calculate the Young's modulus as

$$E = 2.6G = \frac{204.92P_{CR}r^3 n}{(d_0^4 - d_i^4)l_0\left(1 \pm \sqrt{1 - 6.87\left(\frac{D}{l_0}\right)^2}\right)} \qquad \text{Equation 6.21}$$

Although one would assume that the nanocoil follows the fixed-guided end conditions, all three end conditions are calculated to determine the effect on these conditions on the calculated modulus of the coil. The values for P_{CR} were measured directly from force-distance curves of the nanocoil compression from the AFM software. Figure 6.6 is an illustration of the force-distance curve obtained during compression of the nanocoil

describing three points where the critical buckling load is measured: divergence from linear response (A), observed slip induced load (B), the extrapolated force of slip-load from system stiffness(C).

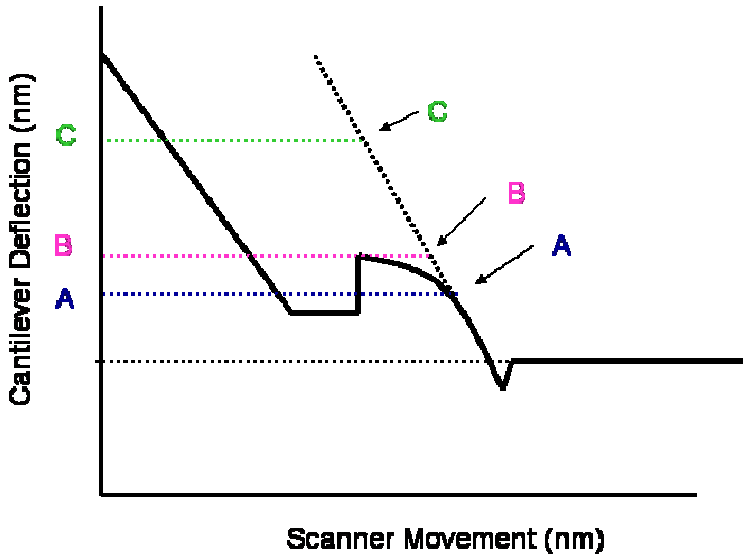

Figure 6.6. Illustration of force-distance response of nanocoil during compression showing points of divergence from linear response (A), slip induced load (B), the extrapolated force of slip-load from system stiffness(C).

6.4 Results

The following section will present the data collection and analysis performed on selected nanocoil modified tips used in developing the compression model. These tips were chosen because they describe representative trends observed during the data collection process. The data collected from the remaining tips used the study are presented in Appendix B.

6.4.1 Tip #5 Characterization

6.4.1.1 Scanning Electron Microscopy Imaging: Tip #5

Figure 6.7 displays SEM images collected for Tip #5 in several orientations. Measuring the orientation of the nanocoil relative to the probe tip, it was found that this nanocoil has an alignment of 7.6° from the tip normal. This is calculated through the use of Equation 6.14, using values of $\alpha_1 = 11.7°$ measured from the side-view orientation (A) and $\alpha_2 = 9.4°$ from the down-beam viewpoint (B) SEMs. The effective compression angle for Tip #5 is 4.4°, as the cantilever is held at a 12° pitch in the AFM holder. Nanocoil dimensions were also obtained from SEM images. The free length of the nanocoil (l_0) is 11.257μm, measured from the coil apex to the cantilever tip, where the point of attachment is established (Figure 6.7A). The number of active coils (n) for this tip is 4.5. In this case, four full helical coils are counted from the free-end of the nanocoil towards the attachment point, where a partial coil (1/2) is counted. The average coil diameter (D) from images of the side-view and down beam orientation is 354.6 nm. The tube diameter(d_0) is measured as 121.3 nm. These measurements are performed using Adobe Photoshop™ (San Jose, CA) image processing software. Each measurement has an error of 2.4 nm, as determined from the minimum pixel width distinguishable by the software.

6.4.1.2 Force-Distance and Oscillation Amplitude Plots: Tip #5

During compression experiments, the nanocoil is exposed to increasing compression distances controlled by the piezoelectric scanner. Figure 6.8 displays the force-distance curves acquired during these experiments. As the scanner cycles, the compression distance is measured from the initial point of contact between the nanocoil and the substrate (jump-to-contact). In this series, the compression distances used are 125 nm(a), 250 nm(b), 375 nm(c), 500 nm(d), 625 nm(e) and 750 nm(f). The force-distance

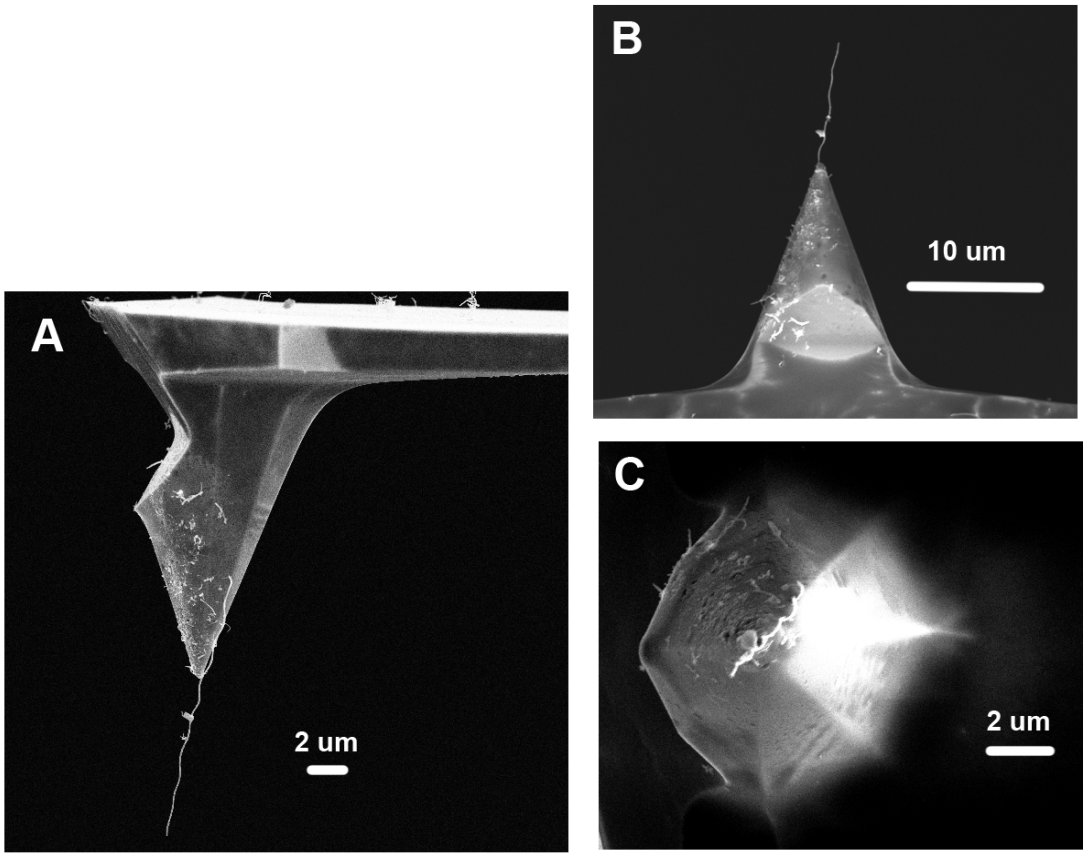

Figure 6.7. SEM images of Tip#5 presented in side-view (A), down-beam (B), and top view (C) orientations. This tip has a calculated compression angle of 4.4°.

data is artificially offset in the x-axis (scanner movement) to align the curves with each other at the jump-to-contact. The data is also offset in the y-axis (cantilever deflection) by 40 nm each cycle, to better resolve the features of the approach (blue) and retract (magenta) portions of the cycle.

Figure 6.9 displays the force-curve plots superimposed on one another, with the jump-to-contact point used to align the data sets. Following the jump-to-contact, the nanocoil-cantilever system displays a linear response to the scanner motion (Figure 6.9A). This has a slope measured as 0.190±0.002. As the nanocoil compresses or buckles under the load there is a non-linear response (Figure 6.9B). As the load force acting on the nanocoil increases, the nanocoil buckles followed by the onset of slip-stick motion. The occurrence of slip-stick motion is observed in the approach portion of the scan cycle. This occurs as the compressive or buckling force exerted on the nanocoil from the restorative force of the cantilever exceeds the friction forces between the nanocoil tip and the substrate. The characteristic response in the force-curve as slip-stick occurs is the negative deflection response in the approach curve of the force-distance plot. This is displayed in Figure 6.9, where the force required to induce slip-stick can be measured by extrapolating the cantilever deflection at B (42.07 nm) and multiplying it by the stiffness of the cantilever beam (0.0172 N/m); this force is calculated as $7.23(\pm 0.03)\text{x}10^{-10}$N.

The data from the force-distance curve in (Figure 6.9) is used in the calculation of the critical buckling load for the nanocoil as expressed in Equation 6.6. Because both the nanocoil and the cantilever are in motion as the scanner cycles, the force (load) at several events is measured. Point **A** represents the load on the nanocoil-cantilever system as it no longer responds linearly to scanner motion. Point **B** represents the system load as the nanocoil undergoes slip-stick motion. Point **C**, is the extrapolated load at the point of slip-stick relative to the system stiffness, the extrapolated slope of linear response region of the nanocoil-cantilever system.

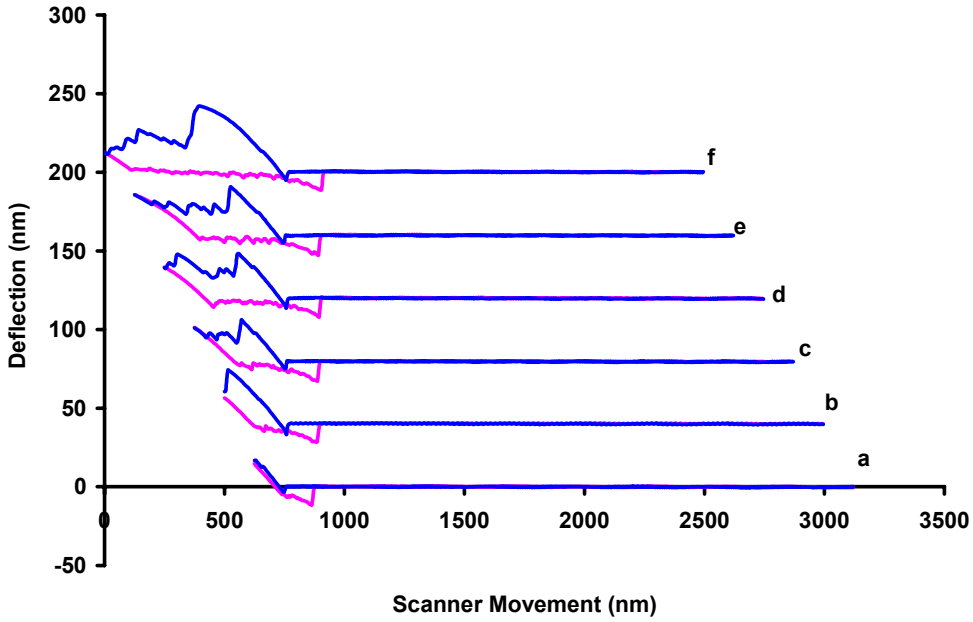

Figure 6.8. Force-distance curve of Tip #5 undergoing 125(a), 250(b), 375(c), 500(d), 625(e) and 750 nm(f) compression. The plots are artificially offset by 40 nm in the cantilever deflection axis and aligned at the jump to contact. The approach data is in blue, retract data is in magenta.

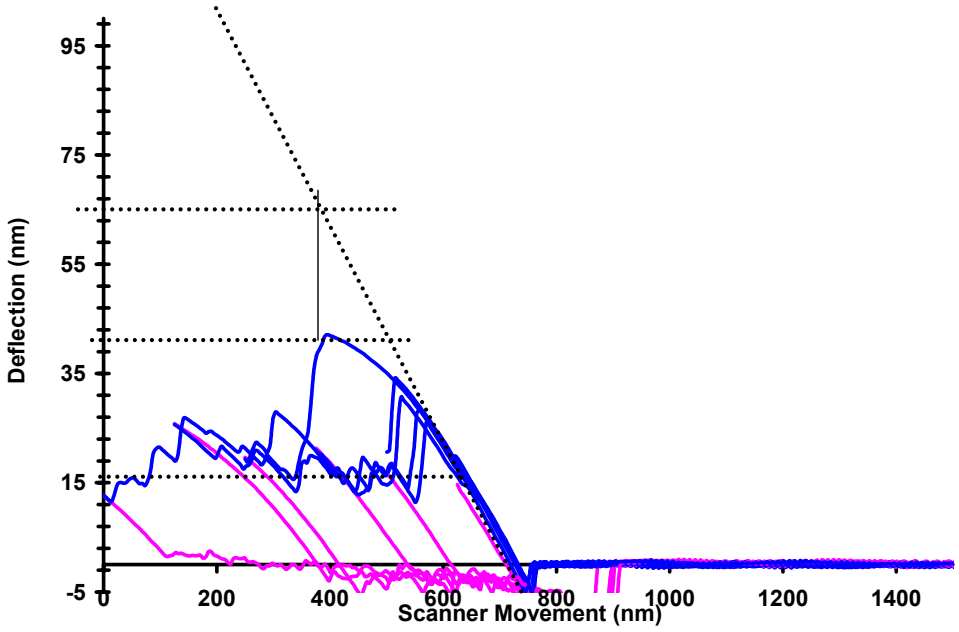

Figure 6.9. Superimposed force-distance curve data for Tip #5; artificially offset to align the contact point of the compression cycle. The force at the divergence from linearity (A), onset of slip-stick motion (B), and extrapolated load at slip-stick (C) are calculated from the plot.

The oscillation amplitude plot of the compression experiments performed on Tip #5 is presented in Figure 6.10. These plots are superimposed onto each other aligned to the jump-to-contact of the tip. In oscillation amplitude plots, the jump to contact is determined by the signal drop in the oscillation signal. There is a high degree of reproducibility in both the approach (blue) and retract (magenta) portions of the plots. While the tip is in contact with the substrate, the oscillation amplitude drops to a minimum value. However, during slip-stick motion of the tip a response is observed (~250-600 nm scanner motion). These events correlate to the fine structure observed in the force-distance curves during the occurrence of slip-stick motion.

The force-distance data is used to calculate the effective spring constant of the nanocoil. This is done through the measured slope of the approach curve (m) at the linear response region of nanocoil-cantilever system. This region of the plot describes the motion of two-springs in series. Figure 6.11 illustrates the displacement of the system (z) as determined from the motion of the piezo scanner, and the deflection of the cantilever (x). Since the nanocoil is undergoing compression as the cantilever deflects, nanocoil displacement is given by (z-x). Equating the compressive force of the cantilever ($\mathbf{F_{beam}=k_{beam}x}$) and the restoring force from the nanocoil ($\mathbf{F_{coil}=k_{coil}(z-x)}$), fields an expression for the relationship between scanner displacement, and cantilever deflection.

$$k_{beam}x = k_{coil}(z-x), \text{ where } x = \frac{k_{coil}}{k_{beam}+k_{coil}}z \qquad \text{Equation 6.22}$$

The slope from the linear region of the approach portion of the force-distance plot is

$$m = \frac{k_{coil}}{k_{beam}+k_{coil}}$$

writing this expression in terms of the nanocoil stiffness (k_{coil}) giving

$$k_{coil} = \frac{m * k_{beam}}{(1-m)} \qquad \text{Equation 6.23}$$

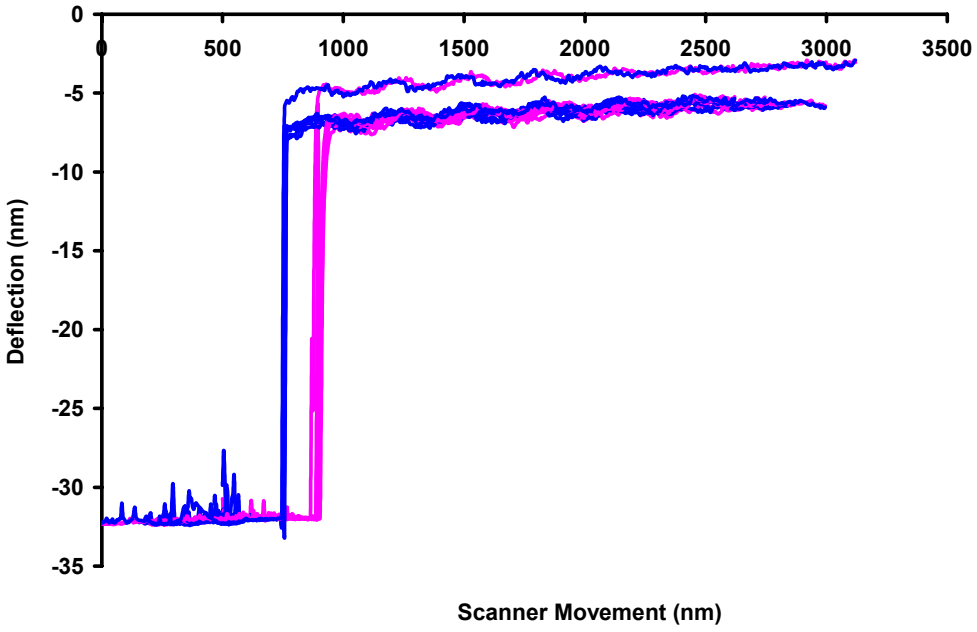

Figure 6.10. Oscillation amplitude plot of the compression of Tip #5; artificially aligned at the point of contact. Slip-stick response is observed in the amplitude plot between ~250-600 nm of scan motion.

With knowledge of the spring constant of the beam, and given the linear response of the nanocoil-modified tip measured from force-distance data, the effective nanocoil stiffness can be calculated. This method assumes that the nanocoil behaves as an ideal spring as the load from the cantilever is applied. In addition to this assumption, this derivation can be used for nanocoil modifications on either a pliant or stiff cantilever beam. Using this method, the nanocoil stiffness for Tip #5 is calculated as 0.004 N/m with an uncertainty of 6% based on a propagation of error calculation.

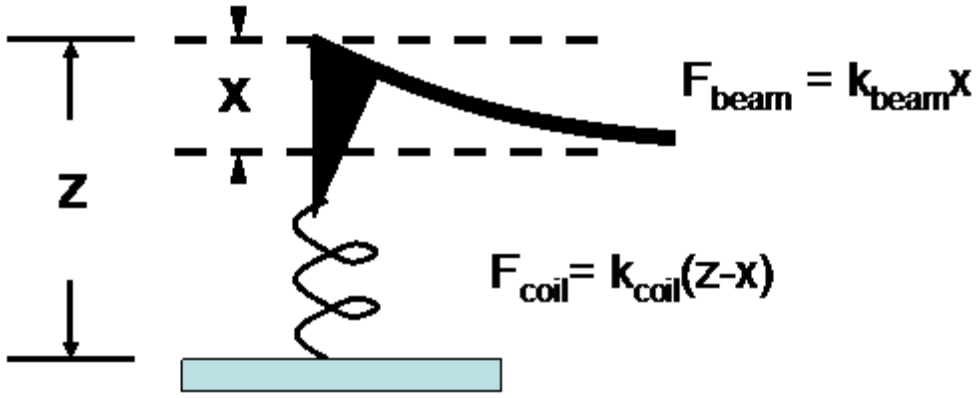

Figure 6.11. Illustration of nanocoil-cantilever system under static deflection.

6.4.1.3 Frequency Response: Tip#5

The frequency response of the nanocoil-cantilever system was recorded at several compression amounts. Figure 6.12 presents the collected PSD plots during the 375 nm compression. This data is presented with a frequency range of 1-400 kHz; below 1 kHz,

the *1/f* noise signal dominates the cantilever frequency signal. The frequency-amplitude plot of the nanocoil-cantilever system is given in **A**. In this plot, all 400 PSDs are plotted simultaneously. Notice that the significant range in the baseline amplitude of these frequency plots is due to optical lever effects. As the cantilever approaches the substrate (thiol-modified TSG) some of the laser spills over the beam and reflects from the substrate surface. This surface reflection undergoes optical interference with the reflected laser from the cantilever beam, causing regions of constructed and destructed signal. A diagram of this effect is presented in Figure 6.13. The frequency response of the waterfall plot is

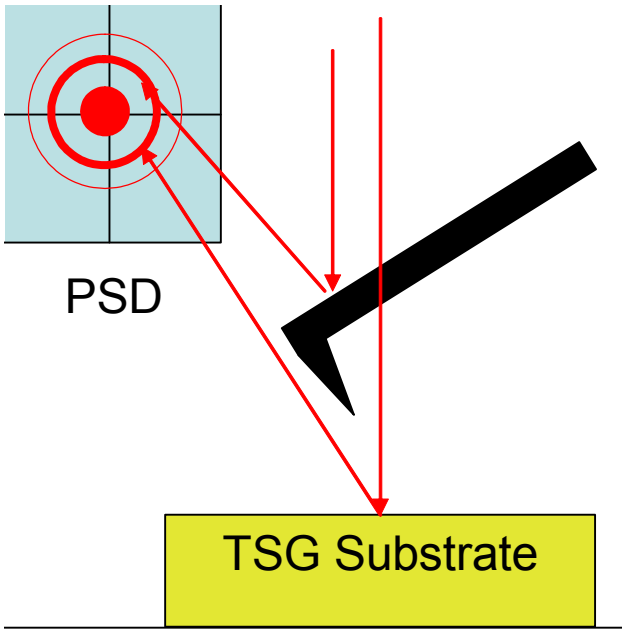

Figure 6.13. Illustration of laser spillover from cantilever to substrate. The resulting interference pattern is measured by the PSD. The result of the optical interference are the observed fluctuations of signal amplitude in the PSD plots.

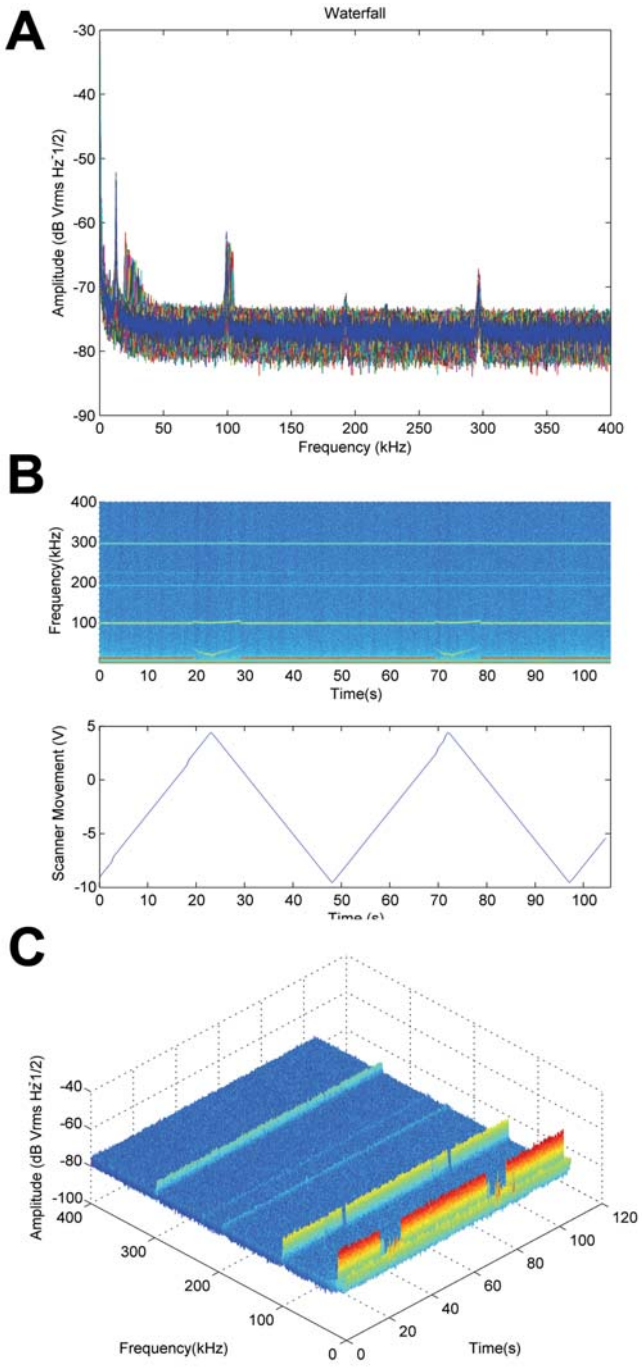

Figure 6.12. Frequency response of Tip #5 during compression distance of 375 nm. A) frequency- amplitude plot of all collected power spectrum density plots captured during the compression cycle. B) frequency response with scanner voltage. C) 3D waterfall plot used to extrapolate the stiffness of the coil. This occurs at the first measurable frequency of collected power spectrum density plots. The scan size was 2500 nm with a rate of 0.02Hz.

given along with the piezoscanner voltage in Figure 6.12B. The fundamental frequency of the nanocoil-cantilever system is observed at ~12.7 kHz. In this view, the frequency response during the compression of the coil is observed occurring between ~20-30 seconds and ~70-80 seconds in consecutive compression cycles. Higher vibration modes are also observed in this plot. The second-order vibration mode is observed at ~100 kHz, where the compression response can be observed. In addition to the cantilever frequency response, environmental noise signals were also detected in the PSD waterfall plots. These are observed at 65 kHz and 220 kHz. Figure 6.12C gives a 3D representation of the waterfall data for the compression.

Quantitative information from the frequency response of the nanocoil-cantilever system is acquired through the analysis of individual PSD plots. This is accomplished through the use of custom MATLAB software using the method of Hutter and Bechhoefer to fit the data acquired from MPFS. The results of this analysis are the spring constant (k) or stiffness for the system, Q-factor, and baseline amplitude. The software completes this analysis for each PSD collected during the compression experiment. Figure 6.14 displays the frequency response of the nanocoil during the compression experiment, given in blue, along with the calculated k-system (A) and amplitude (B) in red. The frequency plot is the frequency value at maximum amplitude from a single PSD plot. The k for the coil-cantilever system is derived from Equation 3.2. The amplitude value represents the baseline amplitude of the PSD signal approaching infinite frequency, not the amplitude measured at the peak frequency.

The calculated values of k-system displayed in Figure 6.14A are used to determine the effective stiffness of the cantilever beam (k_{beam}) and the effective stiffness of the coil-cantilever system (k_{sys}). The stiffness of the coil-cantilever while in free space is assumed to be equivalent to the stiffness of the unmodified beam. This is due to the negligible mass that the nanocoil adds to the cantilever beam. By averaging the values of k_{sys} outside of the compression region, the value for the beam stiffness is given; measured as

0.017(±0.001) N/m. The value of k_{sys} at the initial contact of the coil to the substrate is used to extrapolate the stiffness of the coil. This occurs at the first measurable frequency increase in the cycle (at waterfall number 75). At this point there is assumed to be no guided or clamped-clamped mechanical system. As the scanner motion continues, a load from the restoring force of the cantilever is applied onto the nanocoil. The value of k_{sys} at the initial coil contact is 0.0367±0.0006 N/m. In this dynamic system, the nanocoil and cantilever behaves as two springs in parallel. To calculate the effective spring constant of the nanocoil, the values for k_{sys} at the contact point for all compression experiments are measured and averaged. The resulting value for the spring constant of this nanocoil (k_{coil}) is 1.95(±.003)x10^2 N/m, using the frequency method.

6.4.1.4 Transmission Electron Imaging: Tip #5

Figure 6.15 displays transmission electron microscope images of Tip #5. These images display the internal structure of the nanocoil. Because the carbon nanocoils were made using CVD growth method the presence of defects along the nanocoil is expected. This may also be the reason for the MWCNT to grow into a helix rather than a tube-like structure. Figure 6.15A displays the region of the nanocoil near the point of attachment with the cantilever probe tip. At this joining point, there is no observable MWNT character. The coil appears to be amorphous or fibrous at this point. Outside of the attachment point (red), a crystalline structure (dark) similar to what is expected from multi-walled nanotubes is observed. The exterior of the nanocoil appears to consist of amorphous residue (light contrast). These amorphous regions of the nanocoil, may be created during the arc discharge attachment process, or may be generated during the CVD growth of the nanocoils.

Figure 6.15B displays a TEM image taken in the middle of the nanocoil. The crystalline structure of concentric graphitic planes in the image are observed

A

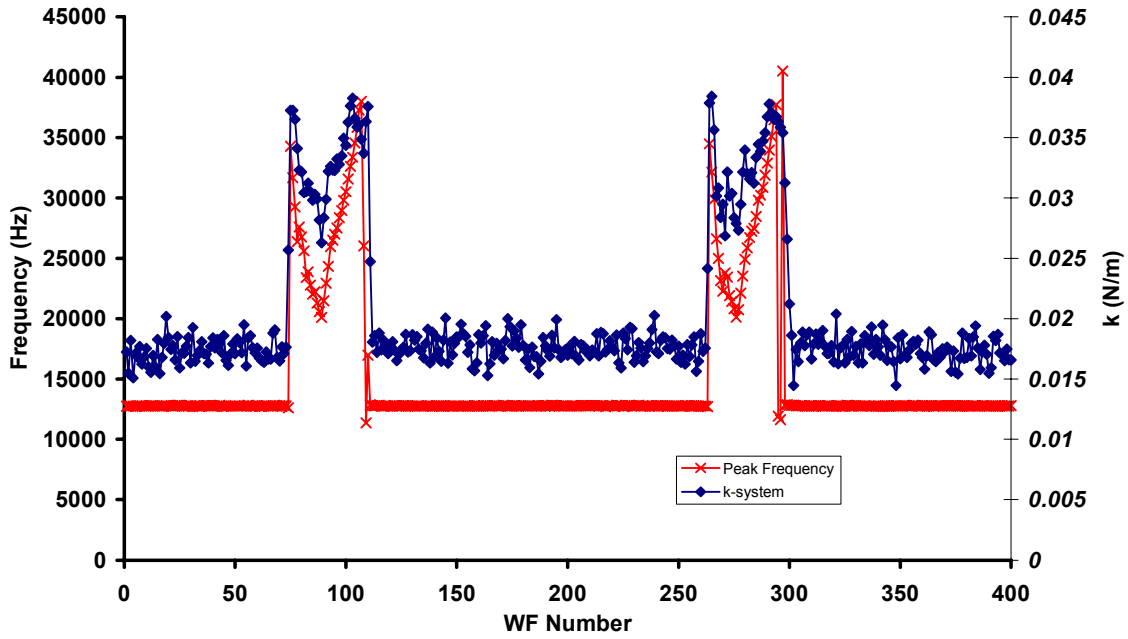

B

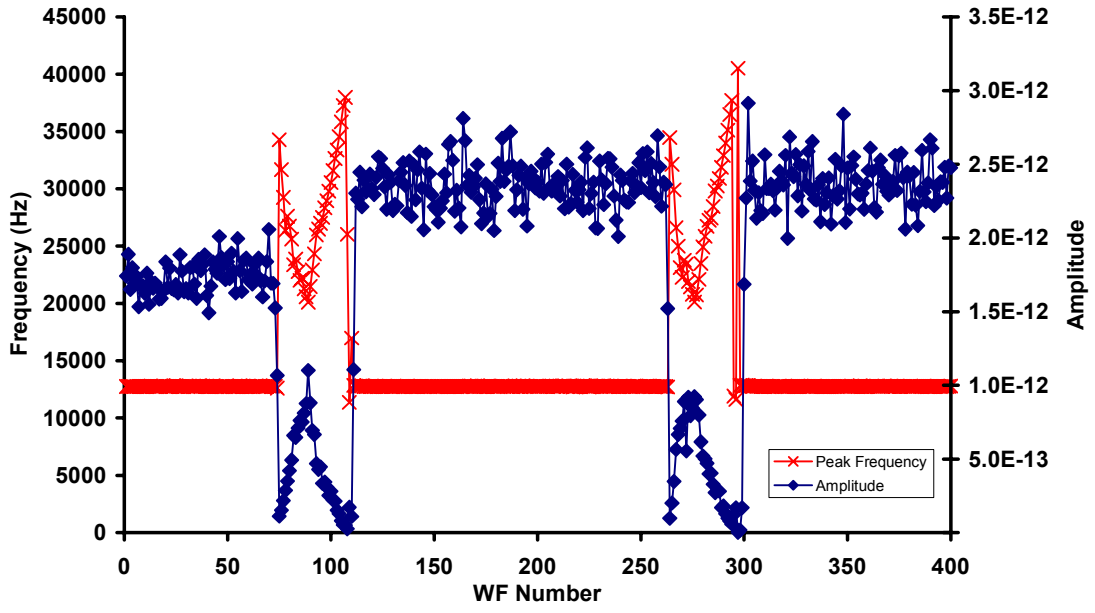

Figure 6.14. Calculated spring constant (A) and amplitude (B) for the nanocoil-cantilever system of Tip #5 at a compression amount of 375 nm. Amplitude units are dB-V_{RMS}-$Hz^{-1/2}$.

A

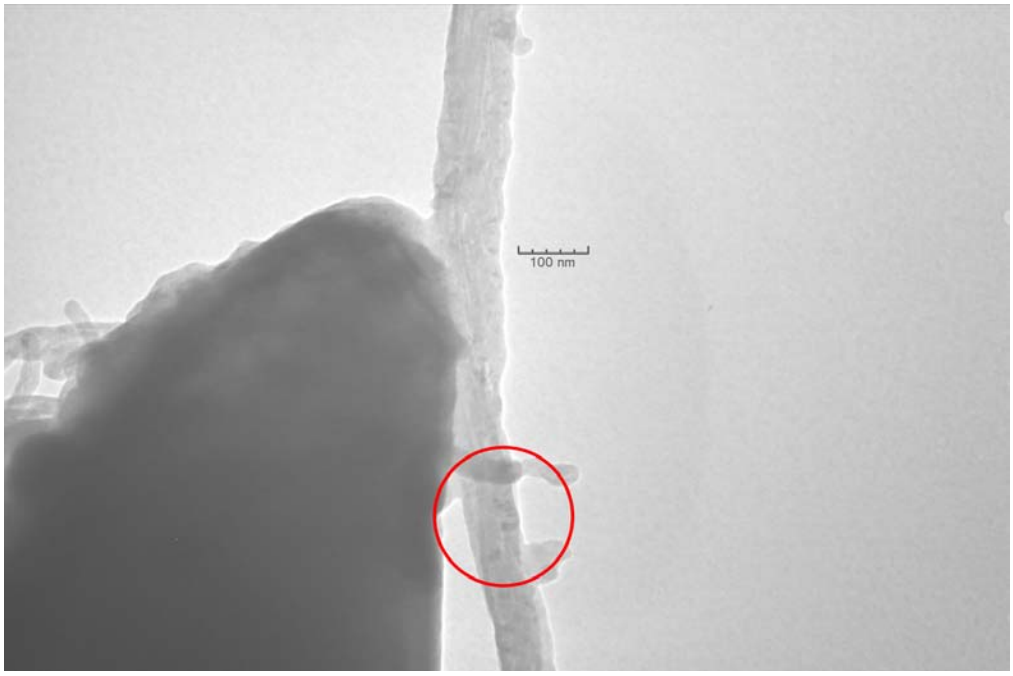

B

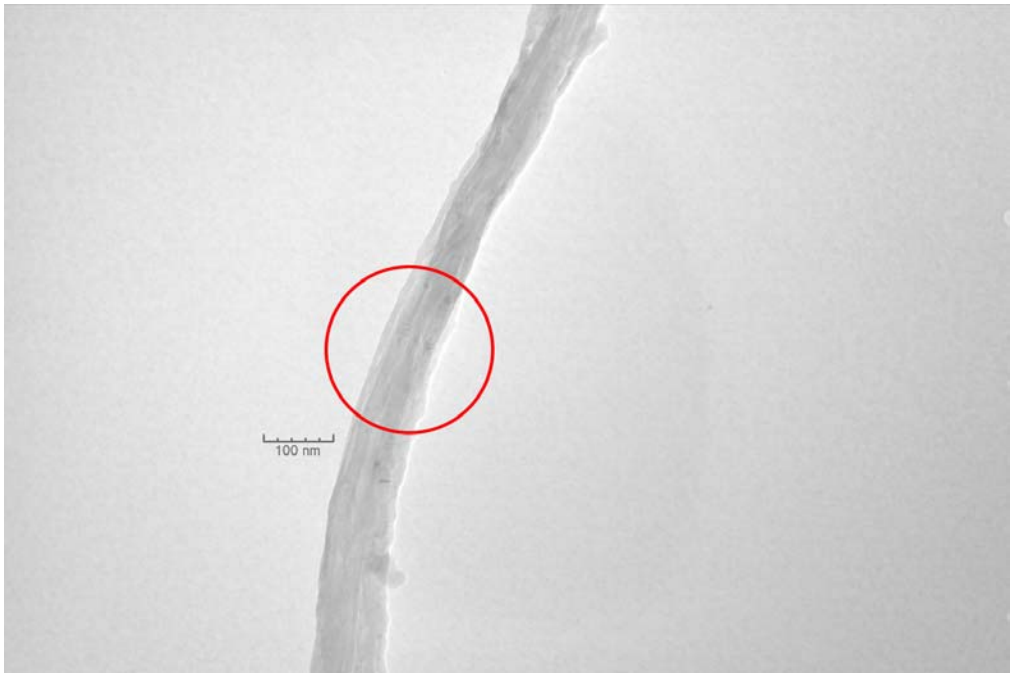

Figure 6.15. TEM images of Tip #5 near the attachment point (A) and in the middle of the coil (B).

(focused in red). In this region a MWCNT with crystalline material filling its void space is observed. Several other nanocoils in this study demonstrated similar structures, prompting the classification of "filled-tube" nanocoils. In terms of modeling the tubular region of the nanocoil, it is assumed that the filling material and the amorphous coating of the nanocoil do not significantly contribute to the mechanical properties of the nanocoil. From the TEM images, the thickness of the crystalline segments of the MWCNT in addition other parts of the nanocoil geometry is apparent and measurable. The coil diameter (D) is measured as 142 nm, outer diameter of the nanotube (d_o) is 55.3 nm, inner diameter of nanotube is 4.5 nm. These values are measured with a resolution of ~1.1 nm from the pixel size of the images. Using these values, the number of walls in the nanocoil structure is calculated to be 75(±7). TEM values are used to calculate tube geometry.

6.4.2 Tip #6 Characterization

6.4.2.1 Scanning Electron Microscopy Imaging: Tip #6

Figure 6.16 displays SEM images collected for Tip #6 in several orientations. Measuring the orientation of the nanocoil relative to the probe tip, it was found that this nanocoil has an alignment of 5.6° from the tip normal. This is calculated through the use of Equation 6.14, using values of $\alpha_1 = 37.8°$ measured from the side-view orientation (A) and $\alpha_2 = 17.7°$ from the down-beam viewpoint (B) SEMs. The effective compression angle (α_{comp}) for Tip #6 is 6.4°, as the cantilever is held at a 12° pitch in the AFM holder. The free length of the nanocoil (l_0) is measured at 9.035μm. This is measured from the coil apex to the attachment point on the probe tip. The number of active coils (n) for this tip is three. The average coil diameter (D) from images of the side-view and down beam orientation is 596.3 nm. The tube diameter(d_0) is measured as ~97 nm. Each

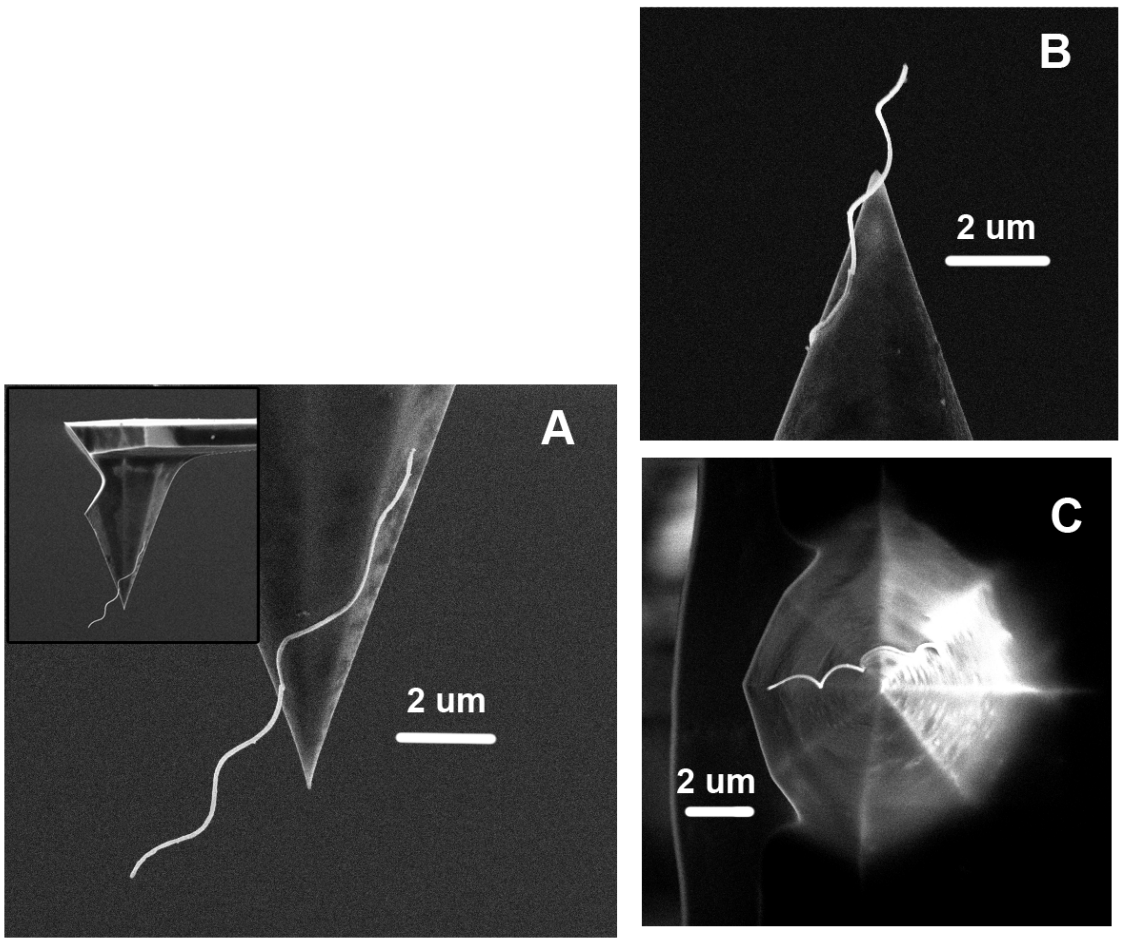

Figure 6.16. SEM images of Tip#6 presented in side-view (A), down-beam (B), and top view (C) orientations. This tip has a calculated compression angle of 6.4°.

measurement has an implicit error of 2.4 nm, as determined from the minimum pixel width.

6.4.2.2 Force-Distance and Oscillation Amplitude Plots: Tip #6

Figure 6.17 displays the force-distance curves acquired during the compression experiments of Tip #6. As the scanner cycles, the compression distance is measured from the initial point of contact between the nanocoil and the substrate (jump-to-contact). The force-distance data is artificially offset in the x-axis (scanner movement) to align the curves with each other at the jump-to-contact. The data is also offset in the y-axis (cantilever deflection) by 75 nm each cycle. The approach curve is displayed in blue, the retract curve is shown in magenta.

Figure 6.18 displays the force-curve plots superimposed on one another, with the jump-to-contact point used to align the data sets. Following the jump-to-contact, the nanocoil-cantilever system displays a linear response to the scanner motion (dashed line). This has a slope measured as 0.375±0.003. As the substrate and nanocoil apply a compressive load to the nanocoil, it undergoes buckling. Tip #6 does not however undergo slip-stick motion, as observed in the compression of Tip #5 (Figure 6.9). As the compressive load is applied to this nanocoil, the system continues to buckle. There is no characteristic response in the force-curve to describe slip-stick motion, the negative deflection response in the approach curve of the force-distance plot.

Figure 6.18 is still used to calculate the critical buckling load for the nanocoil. This is because the force-distance curve of the nanocoil exhibits a clear linear compression region. The force acting on the system to cause the system to undergo non-linear response (onset buckling) to the applied load is measured as $9.41(\pm 0.3)\text{x}10^{-10}$ N. The forces as the nanocoil undergoes slip-stick motion or its extrapolated load at the point of slip-stick relative to the system stiffness cannot be determined. The slope of the linear region of

Figure 6.18 is measured to be 0.190±0.002, Equation 6.23 the spring constant for the nanocoil is found to be 0.027N/m with an uncertainty of 10%.

The oscillation amplitude plot of the compression experiments performed on Tip #6 is presented in Figure 6.19. These plots are superimposed onto each other aligned to the jump-to-contact of the tip. In oscillation amplitude plots, the jump to contact is determined by the signal drop in the oscillation signal. There is a high degree of reproducibility in both the approach (blue) and retract (magenta) portions of the plots. While the tip is in contact with the substrate, the oscillation amplitude drops to a minimum value. Since this nanocoil does not undergo slip-stick motion, no other relevant information is gained from the oscillation amplitude plot.

6.4.2.3 Frequency Response: Tip#6

Figure 6.20 presents the collected power spectrum density (PSD) plots during the 375 nm compression of Tip #5. This data is presented with a frequency range of 1-400 kHz; below 1 kHz, the amplitude of the *1/f* noise prevents accurate imaging of the cantilever frequency signal. The frequency-amplitude plot of the nanocoil-cantilever system is given in Figure 6.20A for all 400 PSD. The frequency response of the waterfall plot is given along with the piezoscanner voltage in Figure 6.20B. The fundamental frequency of the nanocoil-cantilever system is observed at ~9.7 kHz. The compression of the nanocoil is observed occurring between ~14-23 seconds and again at ~65-75; these are displayed in consecutive compression cycles. Higher vibration modes are also observed in this plot. The second-order vibration mode is observed at ~78 kHz, where the compression response can be observed. In addition to the cantilever frequency response, environmental noise signals were also detected in the PSD waterfall plots. These are observed at 65 kHz and 220 kHz.. Figure 6.20C gives a 3D representation of the waterfall

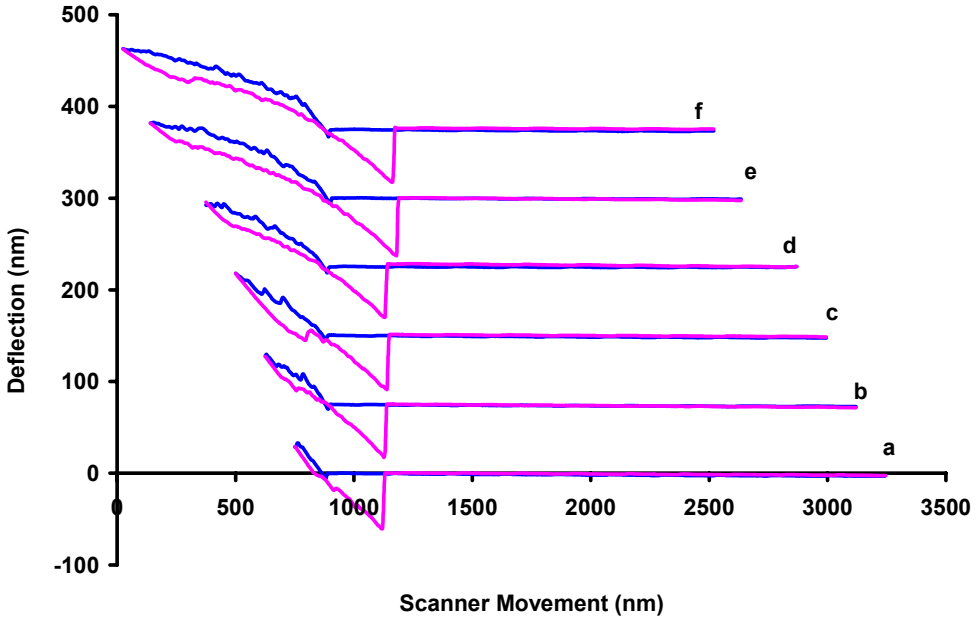

Figure 6.17. Force-distance curve of Tip #6 undergoing 125(a), 250(b), 375(c), 500(d), 625(e) and 750 nm(f) compression. The plots are artificially offset by 75 nm in the cantilever deflection axis and aligned at the jump to contact. The approach data is in blue, retract data is in magenta.

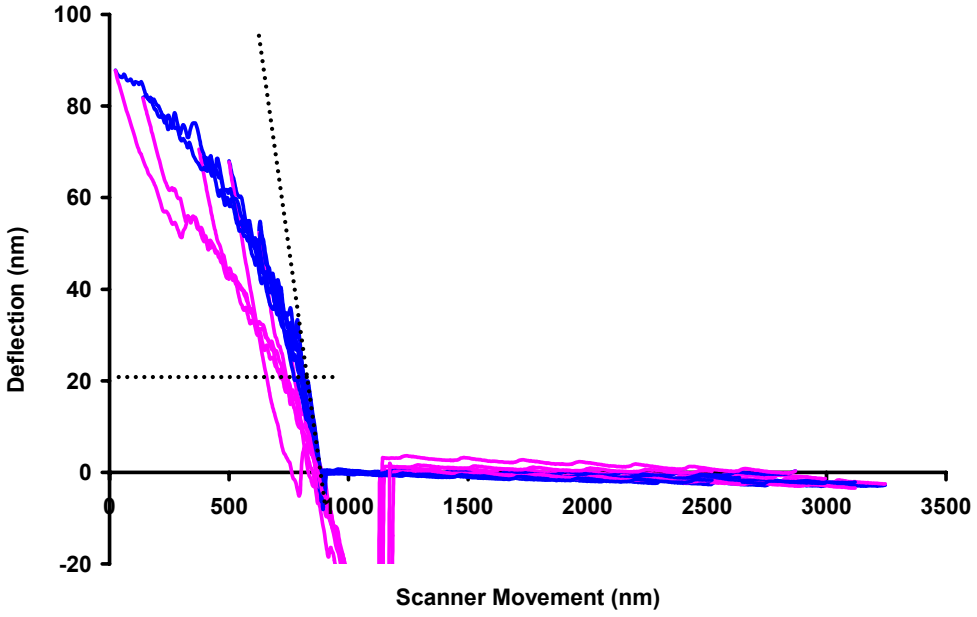

Figure 6.18. Superimposed force-distance curve data for Tip #6; artificially offset to align the contact point of the compression cycle. The force at the divergence from linearity (dashed line) is calculated from the plot to be measured as $9.41 \times 10^{-10} \pm 3 \times 10^{-11}$ N.

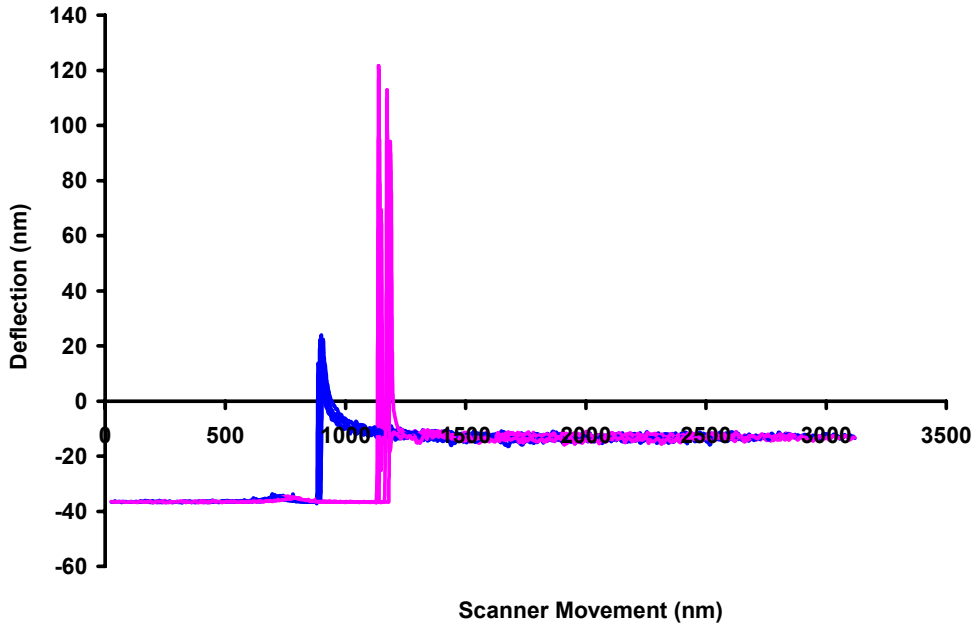

Figure 6.19. Oscillation amplitude plot of the compression of Tip #6; artificially aligned at the point of contact. No slip-stick response is observed in the amplitude plot.

data for the compression. Quantitative information from the frequency response of the Tip#6 is given in Figure 6.21. The results of the PSD analysis are the spring constant (k) or stiffness for the system, Q-factor, and baseline amplitude. This analysis technique is presented in Chapter 3 in greater detail. Figure 6.21 displays the frequency response of the nanocoil during the compression experiment, given in blue, along with the calculated k-system (A) and amplitude (B) in red.

The calculated values of k-system displayed in Figure 6.21A are used to determine the effective stiffness of the cantilever beam (k_{beam}) and the effective stiffness of the coil-cantilever system (k_{sys}). By averaging the values of k_{sys} outside of the compression region, a value for the beam stiffness is measured as 0.045±0.003 N/m. The value of k_{sys} at the initial contact of the coil to the substrate is used to extrapolate the stiffness of the coil; this occurs at the first measurable frequency increase in the cycle (waterfall number 75). At this point there is assumed to be no load on the nanocoil. As the scanner motion continues, a load from the restoring force of the cantilever is applied onto the nanocoil. The value of k_{sys} at the initial coil contact is 0.1144±0.0035 N/m. Assuming the nanocoil and cantilever behave as two springs in parallel, the calculated value of the spring constant for the nanocoil (k_{coil}) is 0.069±0.0004 N/m, using the frequency method.

6.4.2.4 Transmission Electron Microscopy Imaging: Tip #6

Figure 6.22 displays transmission electron microscope images of Tip #6. These images display the internal structure of the nanocoil. Figure 6.22A displays the region of the nanocoil near the point of attachment with the cantilever probe tip. This image displays the transition from amorphous carbon or damaged MWCNT into the defined tubular structure of the nanocoil (red). Regions of the nanocoil closest to the contact point and the free end nanocoil exhibit little or no MWNT characteristics. The nanocoil is

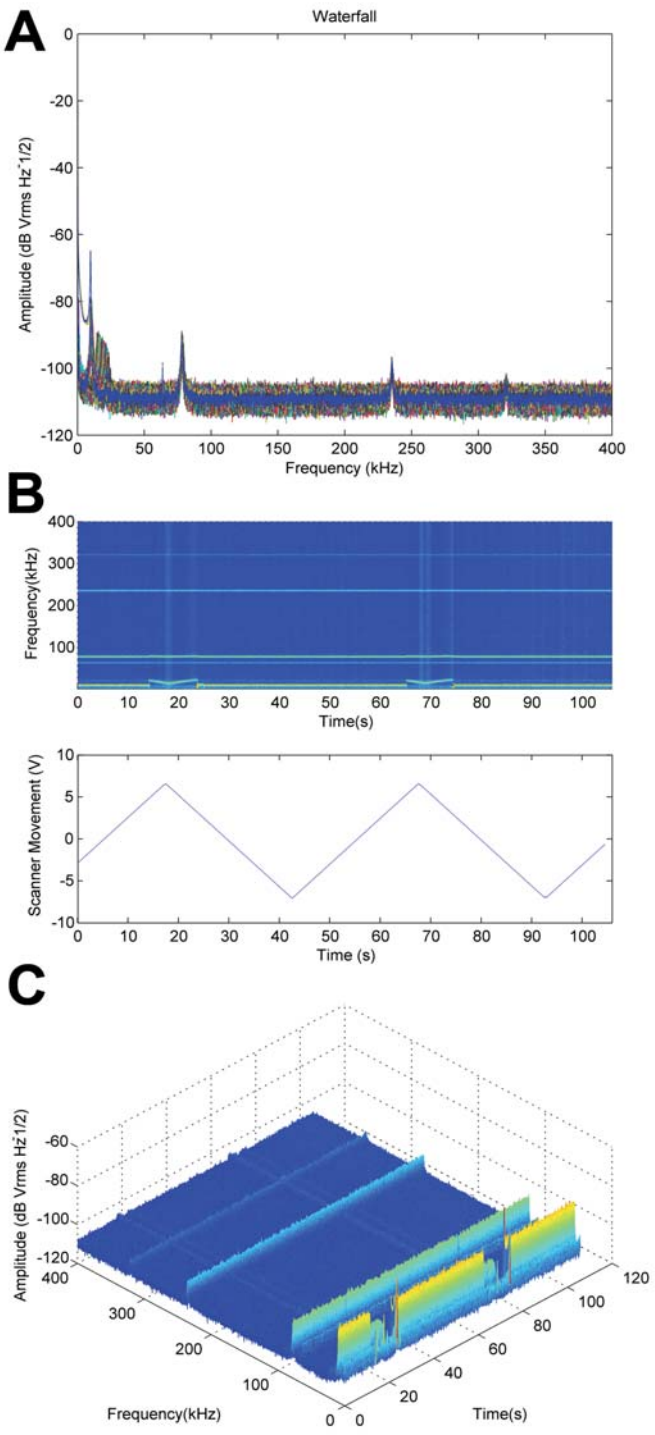

Figure 6.20. Frequency response of Tip #6 during compression distance of 375 nm. A) frequency- amplitude plot of all collected power spectrum density plots captured during the compression cycle. B) frequency response with scanner voltage. C) 3D waterfall plot of collected power spectrum density plots. The scan size was 2500 nm with a rate of 0.02Hz.

A

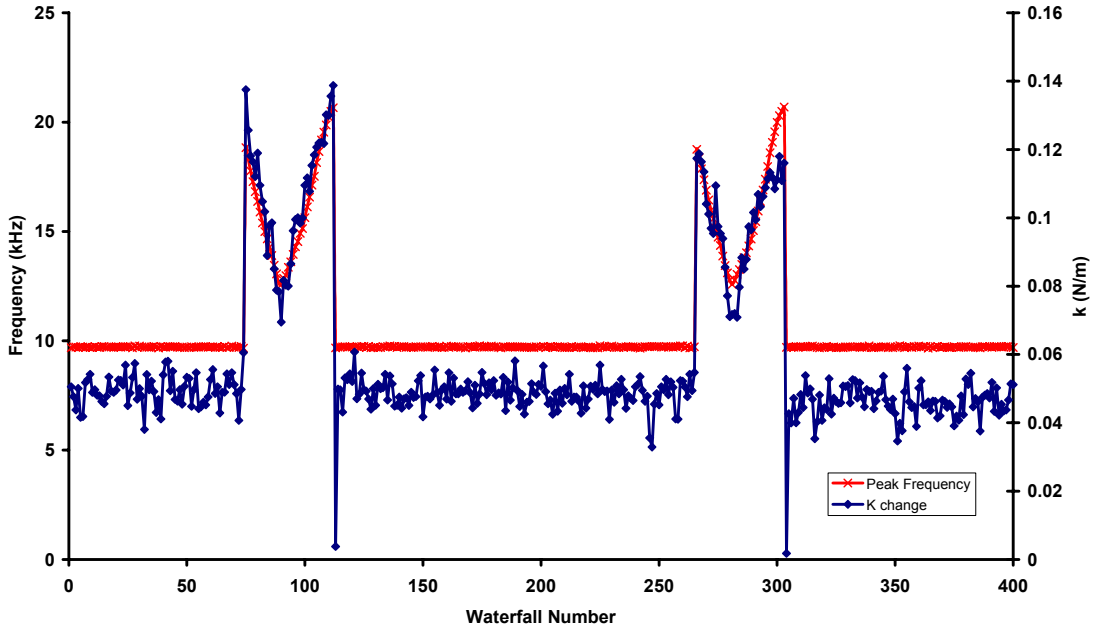

B

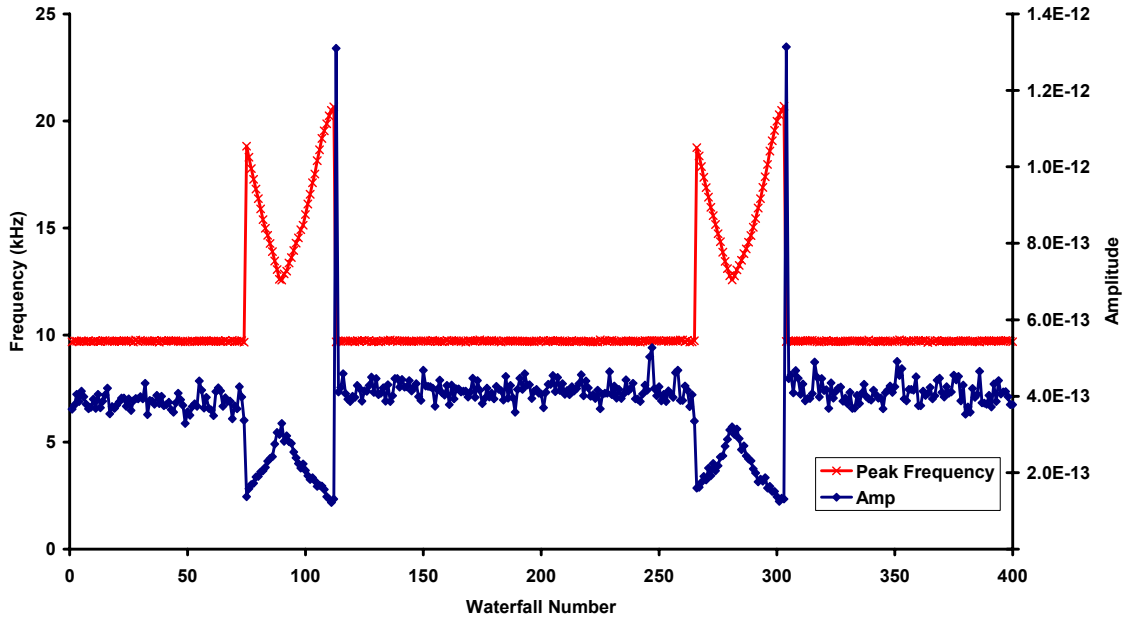

Figure 6.21. Calculated spring constant (A) and amplitude (B) for the nanocoil-cantilever system of Tip #6 at a compression amount of 375 nm. Amplitude units are dB-V_{RMS}-$Hz^{-1/2}$.

A

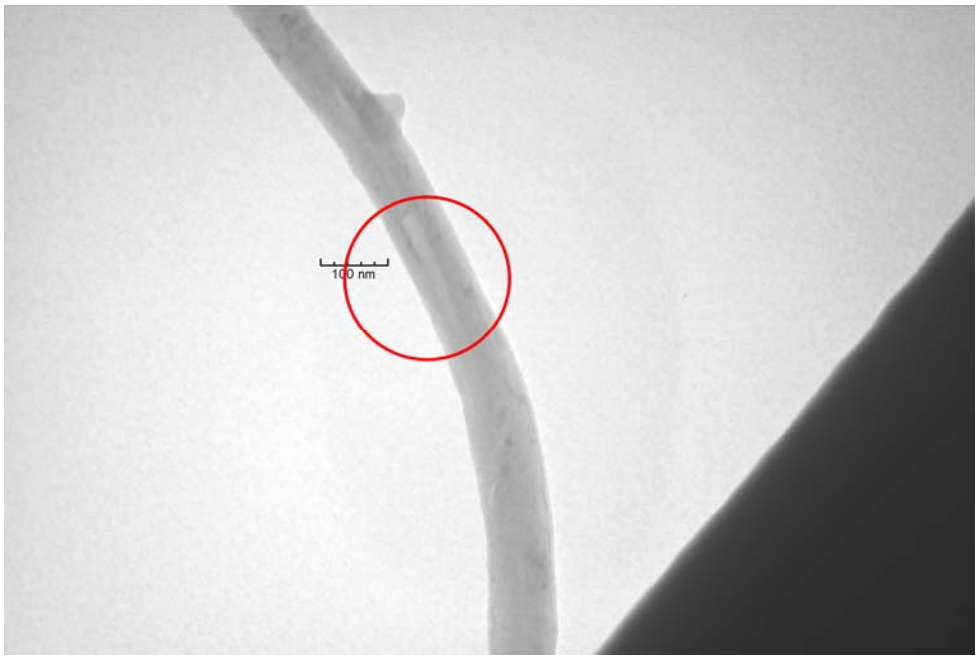

B

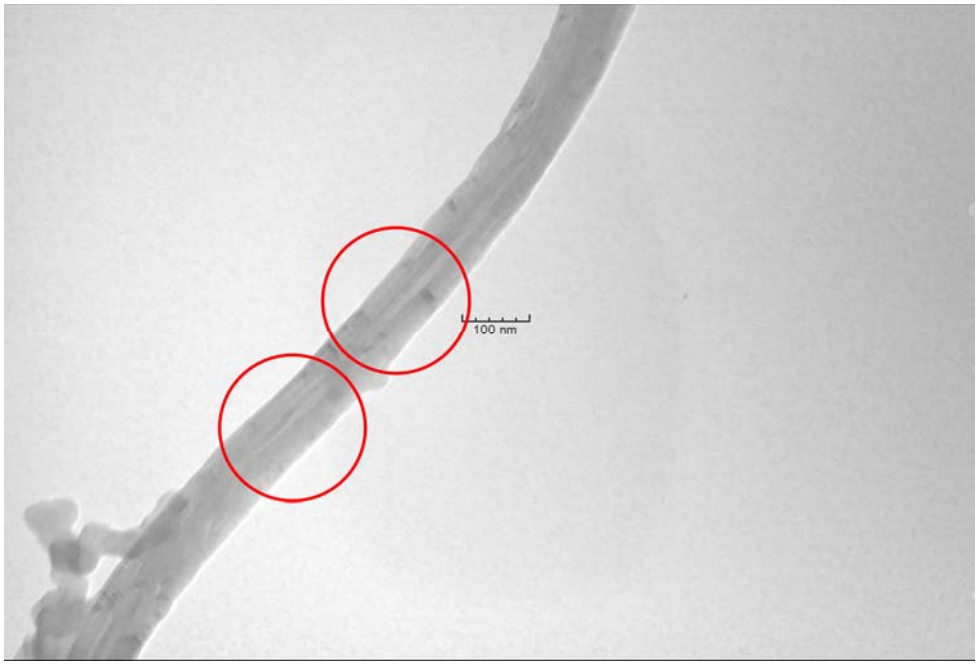

Figure 6.22. TEM images of Tip #6 near the attachment point (A) and in the middle of the coil (B). Regions of amorphous carbon may be created during the arc discharge attachment process, or may be generated during the CVD growth of the nanocoils.

coated in an amorphous material, assumed to be amorphous carbon. Figure 6.22B displays a TEM image taken near the middle portion of the nanocoil. The crystalline structure of concentric graphitic planes can be clearly observed in the image (focused in red). A MWCNT with no material trapped in its core is presented. From the TEM images, the thickness of the crystalline segments of the MWCNT is measured, in addition to other parts of the nanocoil geometry. The coil diameter (D) is measured as 576.5 nm, outer diameter of the nanotube (d_o) is 83.9 nm, inner diameter of nanotube is 20.5 nm. These values are measured with a resolution of ~1.1 nm from the pixel size of the images. Using these values, the number of walls in the nanocoil structure is calculated to be 93±7.

6.4.3 Tip #13 Characterization

6.4.3.1 Scanning Electron Microscopy Imaging: Tip #13

Figure 6.23 displays SEM images collected for Tip #13 in several orientations. The effective compression angle (α_{comp}) for Tip #13 is 8.7°, as the cantilever is held at a 12° pitch in the AFM holder. The free length of the nanocoil (l_0) is measured at 6.598μm. This is measured from the coil apex to the probe tip. The number of active coils (n) for this tip is two. The average coil diameter (D) is measured from images of the side-view and down beam orientation as 325.8 nm. The tube diameter(d_0) is measured as 118.4 nm. These measurements are performed using Adobe Photoshop™ (San Jose, CA) image processing software. Each measurement has an error of 2.4 nm, as determined from the minimum pixel width distinguishable by the software.

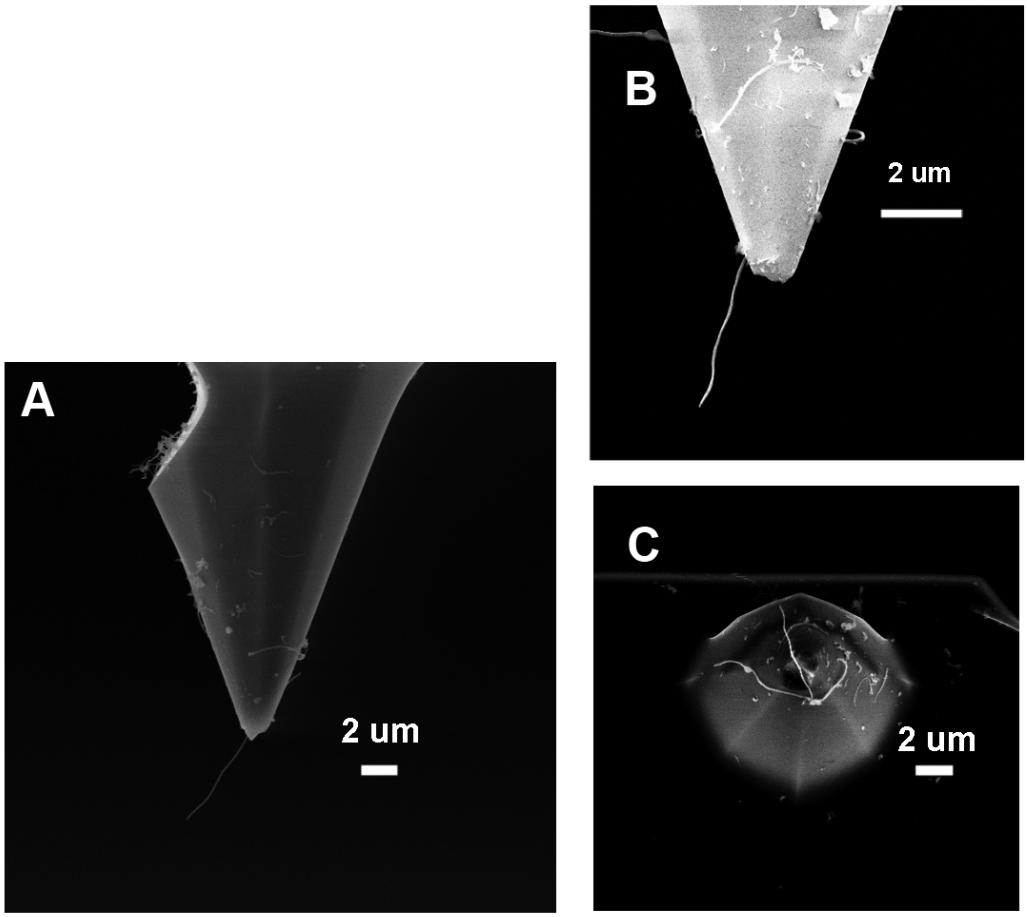

Figure 6.23 SEM images of Tip#13 presented in side-view (A), down-beam (B), and top view (C) orientations. This tip has a calculated compression angle of 8.7°.

Force-Distance and Oscillation Amplitude Plots: Tip #13

Figure 6.24 displays the force-curve plots of the compression of Tip #13 superimposed on one another, with the jump-to-contact point used to align the data sets. Following the jump-to-contact there is no observable linear region of the approach curve. Without the linear response region, the force-distance data can not be used to calculate the nanocoil stiffness. There is a noticeable region where slip-stick may be occurring (~600 nm scanner movement). This is marked in Figure 6.25 with a dashed line. The force measured at this value is $216(\pm 7.6)x10^{-11}$N. No oscillation amplitude plot was captured for this data set.

6.4.3.3 Frequency Response: Tip#13

Figure 6.26 presents the collected power spectrum density (PSD) plots during the 375 nm compression of Tip #13. The fundamental frequency of the nanocoil-cantilever system is ~15.4 kHz. A single compression cycle is displayed showing the compression of the nanocoil occurring between ~43-60 seconds. In addition to the cantilever frequency response, environmental noise signals were also detected in the PSD waterfall plots (Figure 6.26B). These are observed at 65 kHz and 220 kHz. Figure 6.26C gives a 3D representation of the waterfall data for the compression. The scan size was 2500 nm, the scan rate was reduced to 0.01Hz to capture a single compression cycle.

The calculated values of k-system are displayed in Figure 6.27. These are used to determine the effective stiffness of the cantilever beam (k_{beam}) and the effective stiffness of the coil-cantilever system (k_{sys}). By averaging the values of k_{sys} outside of the compression region, the value for the beam stiffness is given as 0.132±0.007 N/m. The value of k_{sys} at the initial contact of the coil to the substrate is used to extrapolate the stiffness of

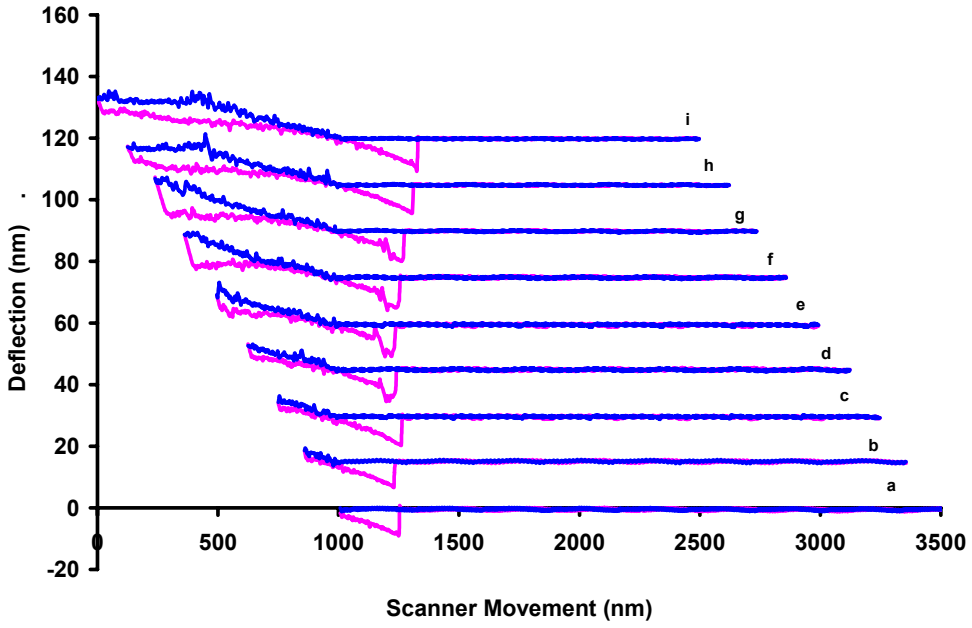

Figure 6.24. Force-distance curve of Tip #13 undergoing 125(a), 250(b), 375(c), 500(d), 625(e), 750 (f), 875(g), 1000(h), and 1125 nm (i) compression. The plots are artificially offset by 15 nm in the cantilever deflection axis and aligned at the jump to contact. The approach data is in blue, retract data is in magenta.

f

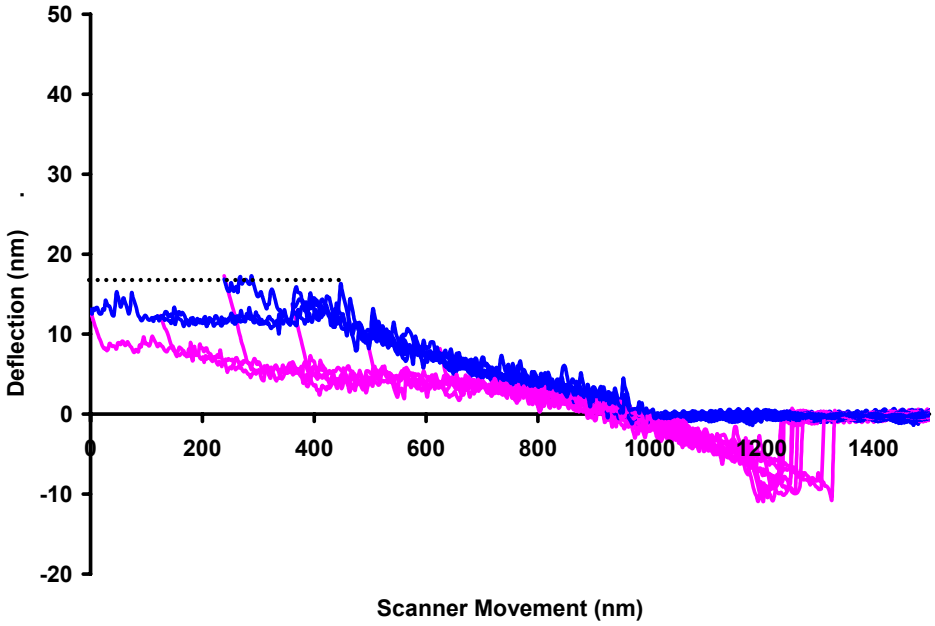

Figure 6.25. Superimposed force-distance curve data for Tip #13; artificially offset to align the contact point of the compression cycle. There is no distinguishable linear response in this data set. The force at the onset of slip-stick motion (dashed line) calculated from the plot is $2.16 \times 10^{-9} \pm 7.6 \times 10^{-11}$N.

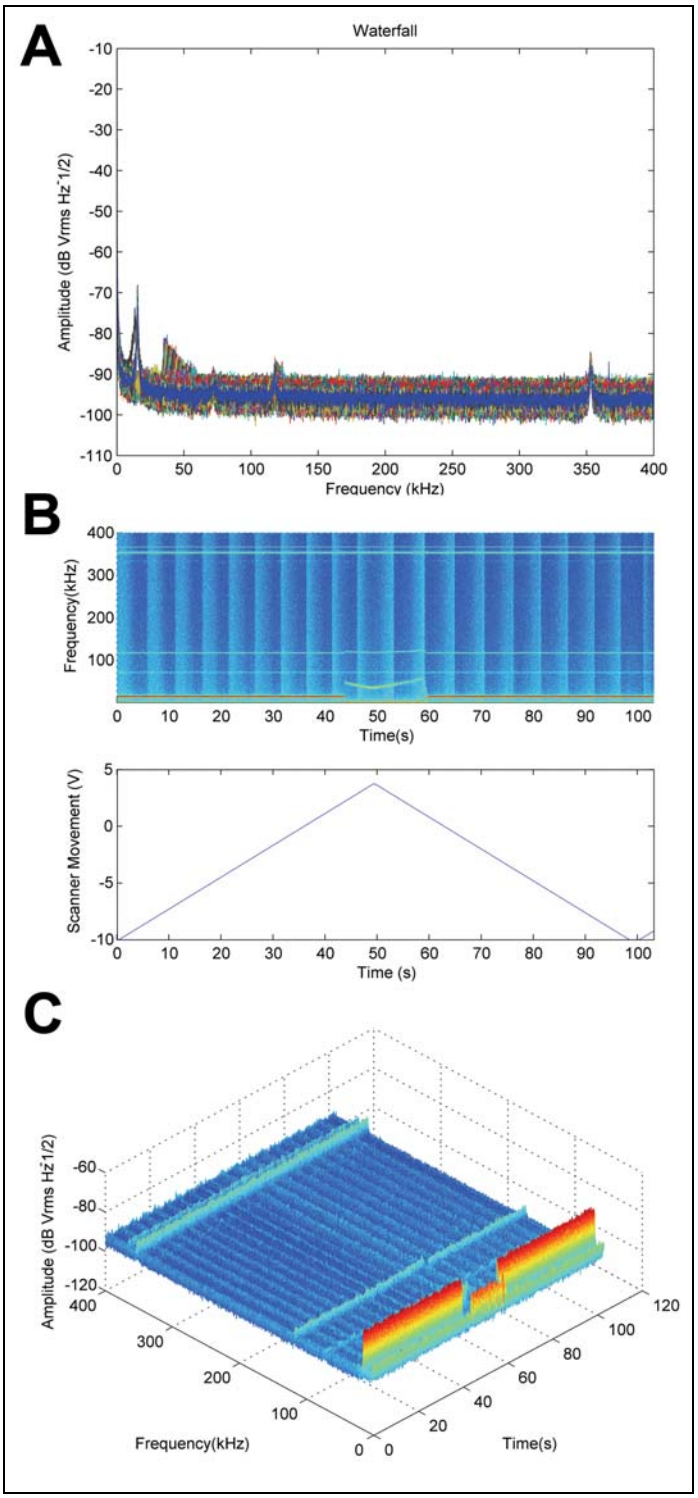

Figure 6.26. Frequency response of Tip #13 during compression distance of 375 nm. A) frequency- amplitude plot of all collected power spectrum density plots captured during the compression cycle. B) frequency response with scanner voltage. C) 3D waterfall plot of collected power spectrum density plots. The scan size was 2500 nm with a rate of 0.02Hz.

the coil; this occurs at the first measurable frequency increase in the cycle (waterfall number 86). At this point, there is assumed to be no load on the nanocoil. As the scanner motion continues, a load from the restoring force of the cantilever is applied onto the nanocoil. The value of k_{sys} at the initial coil contact is 0.346±0.02 N/m. Assuming the nanocoil and cantilever behave as two springs in parallel, the calculated value of the spring constant for the nanocoil (k_{coil}) is 0.214±0.0007 N/m, using the frequency method.

6.4.3.4 Transmission Electron Microscopy Imaging: Tip #13

Figure 6.28 displays transmission electron microscope images of Tip #13. These images display the internal structure of the nanocoil to have regions of tube-like crystalline structure and regions of fibrous structures. Figure 6.28A displays the region of the nanocoil near the point of attachment with the cantilever probe tip. Immediately at the cantilever probe tip, a crystalline nanotube structure can be observed. However the diameter of this structure is far less than the rest of the nanocoil. It is believed that at this region of the nanocoil the amorphous carbon was removed during the arc discharge attachment. Approximately 700 nm away from the probe tip, a fibrous structure that makes up the bulk of the nanocoil is presented. This is different from the 'filled-tube' structure observed in Tip #5. An outermost layer of graphitic material is found within the fibrous sections of the nanocoil. This layer is used to calculate the effective wall thickness for the nanocoil system.

Figure 6.28B displays the free tip of the nanocoil. Some regions of the nanocoil exhibits very regular nanotube-like structure (red), while the remaining parts of the nanocoil are amorphous or fibrous in nature. The coil diameter (D) is measured as 216.6 nm, outer diameter of the nanotube (d_o) is 52.6 nm, the inner diameter of nanotube

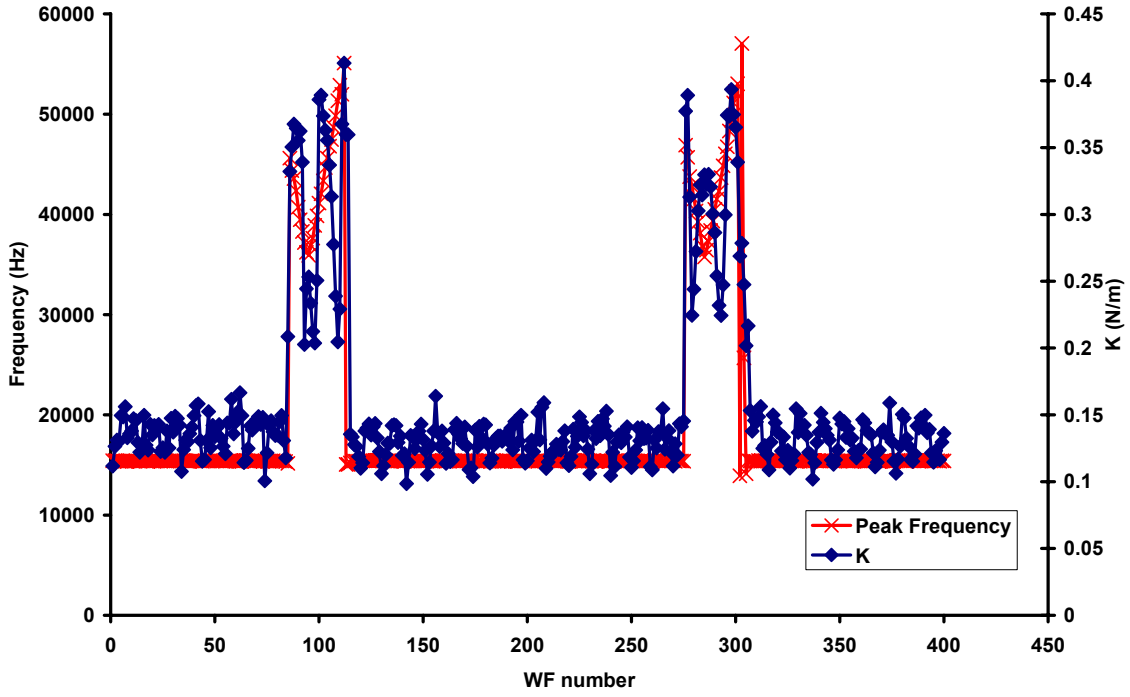

Figure 6.27. Calculated spring constant and frequency response for the nanocoil-cantilever system of Tip #13 at a compression amount of 375 nm.

A

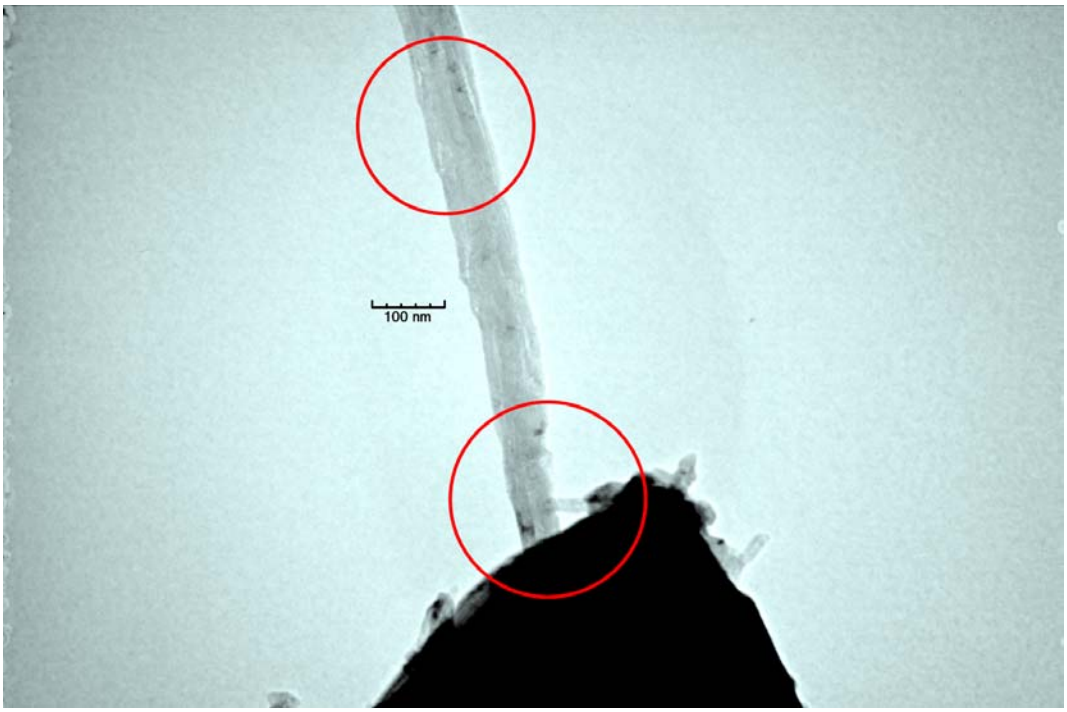

B

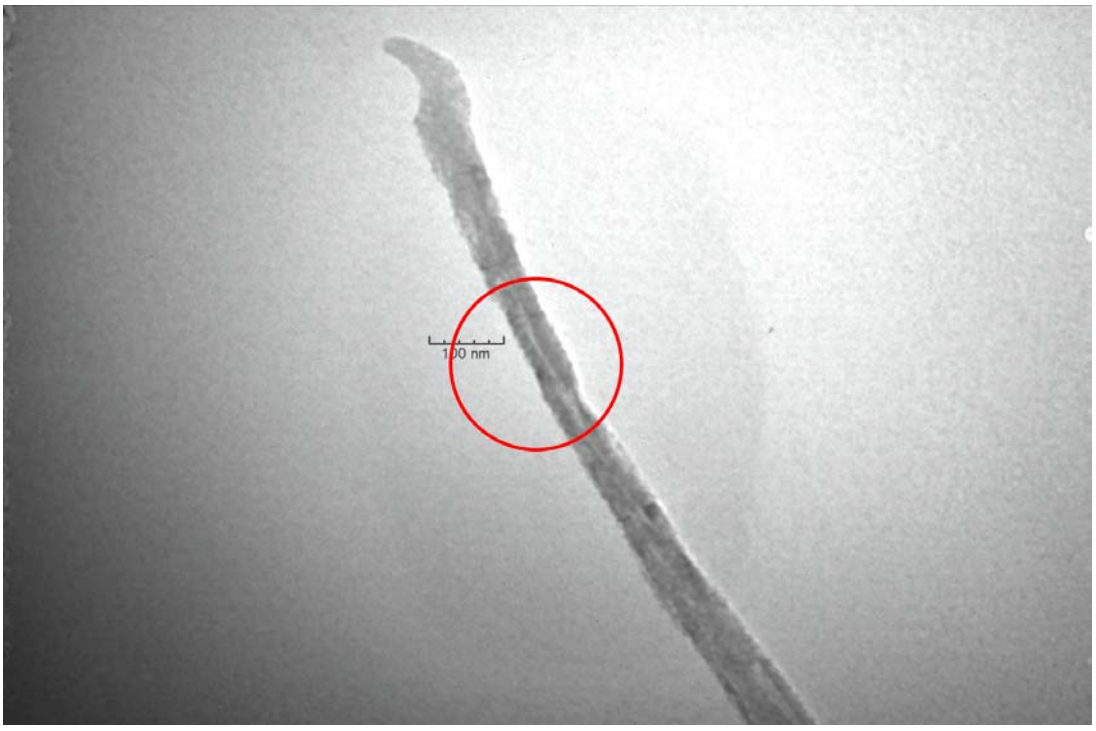

Figure 6.28. TEM images of Tip #13 near the attachment point (A) and in the free end of the coil (B).

is 9.5 nm. Using these values, the number of walls in the nanocoil structure is calculated to be 63±7.

6.4.4 Series-18 Tip Analysis

Tip characterization was completed on the Series-18 modified cantilevers. The analysis of Tips #14-18 was completed in parallel to the study of the CSC-38 cantilevers. SEM and TEM image characterization and compression analysis were competed along analysis of the frequency response collected from MPFS. The large difference between the cantilever beam stiffness and the nanocoil stiffness prevented accurate calculation of the nanocoil properties. The stiffness of the nanocoil-cantilever system could not be accurately determined using either the force-distance or frequency techniques. Figure 6.29 displays the force-distance plot for Tip #14. There is no measurable cantilever deflection through 875 nm compression of the nanocoil. Figure 6.30 displays the calculated stiffness from the frequency response of the nanocoil-cantilever system during a 375 nm compression cycle. Although a measurable frequency response occurs in the scan, there is no discernable change in the stiffness of the system during the compression of the nanocoil. This confirms the assumption that the nanocoil-cantilever system behaves as springs in parallel, as the effective spring constant of the nanocoil is negligible compared to that of the cantilever. Because of these limitations, the techniques used to calculate the effective stiffness of the nanocoil cannot be applied to modified Series-18 cantilevers.

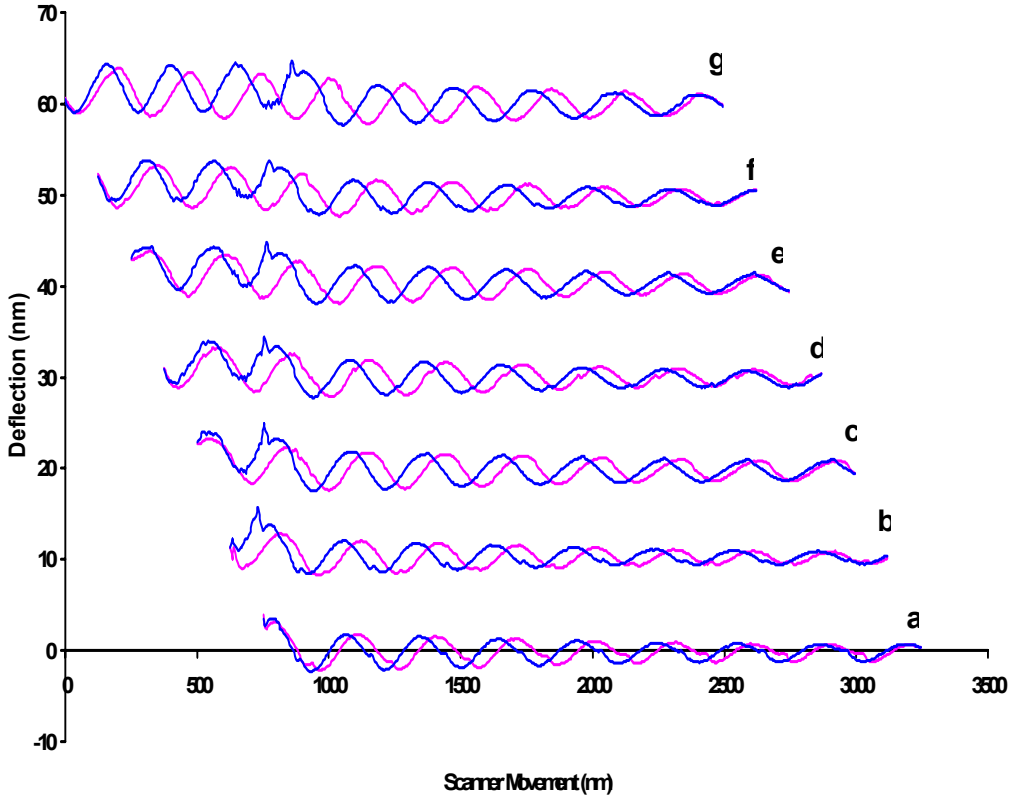

Figure 6.29. Force-distance curve of Tip #14 undergoing 125(a), 250(b), 375(c), 500(d), 625(e), 750 (f), and 875(g) compression. The plots are artificially offset by 40 nm in the cantilever deflection axis and aligned at the jump to contact. The approach data is in blue, retract data is in magenta. No measurable deflection of the cantilever is observed.

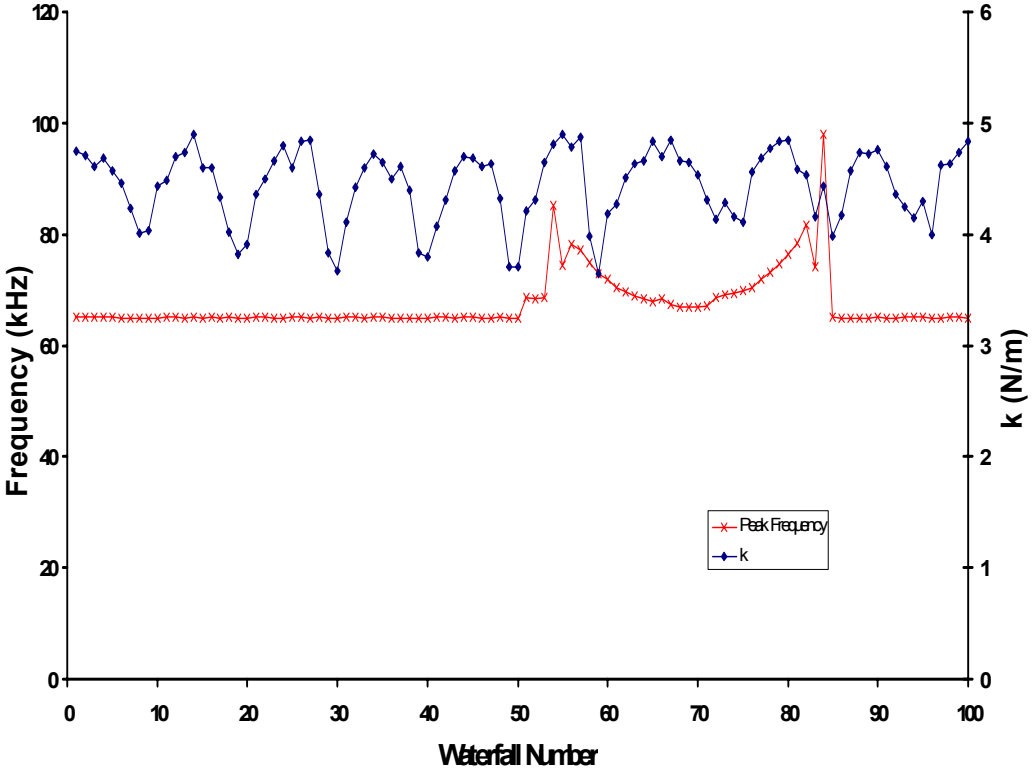

Figure 6.30. Calculated spring constant and frequency response for the nanocoil-cantilever system of Tip #14 at a compression amount of 375 nm.

6.5 Correlation of Mechanical Properties With Structure

Using the coil geometries measured from the SEM and TEM images along with the data from MPFS analysis, the material properties of the nanocoils were calculated using the frequency response, linear force-distance response, and critical buckling response. Table 6.5 displays the calculated values for the elastic moduli of the carbon nanocoil tips. The frequency method and force-curve method calculated the elastic modulus of the nanocoil from its effective spring constant using Equation 6.17. The critical force method measured the force at the point where the nanocoil-cantilever system diverges from a linear region. This force is used in Equation 6.21 to calculate the nanocoil modulus. Both boundary conditions of fixed-guided and fixed-fixed were investigated for the nanocoil in this method. The properties of Tip #13 cannot be calculated using the linear force or critical force methods due to the force-distance plot lacking a discernable linear region.

The calculated moduli are plotted against the number of walls for the nanocoils in Figure 6.31 to determine if a relationship exists between the structure and mechanical properties of the carbon nanocoil. A clear differentiation between nanocoils classified as fibrous from those of regular tube and filled-tube structures is observed in the plot of the frequency method results (Figure 6.31A). The linear force method (Figure 6.31B) does not demonstrate any trends to differentiate the nanocoils by structure. Neither does the critical force method (Figure 6.31C,D) differentiate fibrous and filled-nanocoils from tube-like nanocoils. From these results, one can conclude that the structure of carbon nanocoils can be determined from using their mechanical properties using either their frequency response (MPFS method), but not from measuring information from the force-distance response.

Table 6.5. Summary of calculated elastic moduli for coiled carbon nanotubes measured using the frequency method, force-curve method, and critical force method.

	Structure	Filled	Fiber	Tube	Fiber	Fiber	Tube	Tube	Filled	Fiber	Filled	Tube	Tube	Tube
	Walls	**34**	**23**	**112**	**49**	**75**	**93**	**60**	**51**	**61**	**24**	**47**	**39**	**63**
Frequency Method	k coil (N/m)	0.115	0.073	0.336	0.107	0.020	0.054	0.146	0.094	0.016	0.176	0.461	0.020	0.214
	k error (%)	5.8	4.1	5.6	2.5	0.2	0.8	4.0	1.4	0.7	3.1	24.1	2.9	3.3
	E(TPa)	0.0100	0.0027	0.0122	0.0020	0.0006	0.0130	0.0062	0.0178	0.0004	0.0314	0.0229	0.0093	0.0118
	E error (%)	19.4	30.0	31.7	13.2	100.1	21.9	26.2	14.5	20.9	15.2	35.4	73.0	47.6
Force-Curve Method	k coil (N/m)	0.0375	6.967	0.8072	0.0486	0.0040	0.0270	0.0742	0.0495	1.658	1.304	3.922	0.1504	
	k error (%)	17.4	19.8	10.1	30.2	6.4	10.1	111.7	12.3	13.9	9.6	15.7	10.8	
	E(TPa)	0.0032	0.2589	0.0293	0.0009	0.0001	0.0065	0.0032	0.0094	0.0446	0.2327	0.1951	0.0042	
	E error (%)	20.3	27.4	11.5	31.3	11.4	11.5	112.0	14.4	16.6	15.0	18.0	16.6	
Critical Force Method	E(TPa) fixed-guided	0.0558	0.3883	0.1319	0.0197	0.0125	0.0280	0.3230	0.0211	0.0490	0.4106	0.0454	0.0699	
	E(TPa) fixed-fixed	0.0138	0.0971	0.0329	0.0049	0.0031	0.0070	0.0807	0.0053	0.0122	0.1026	0.0113	0.0175	
	E error (%)	10.8	19.1	5.9	8.5	10.7	6.6	10.9	7.3	10.9	11.5	8.8	25.0	

A

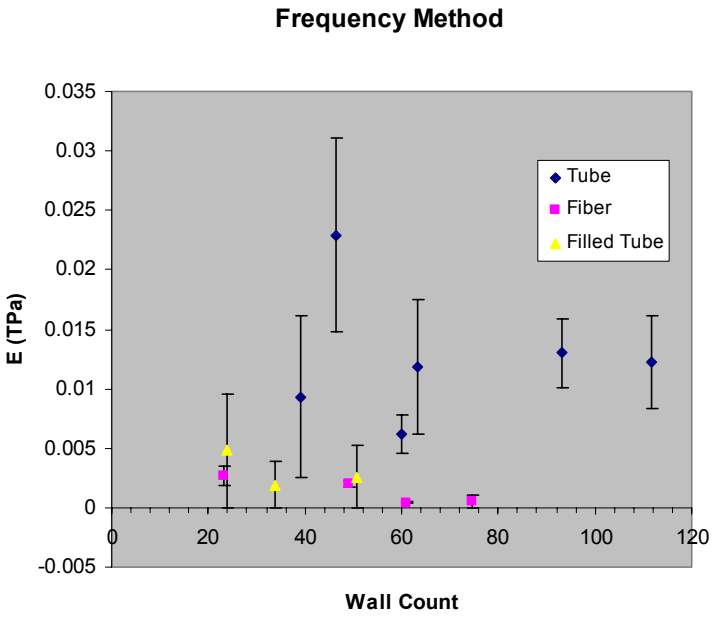

B

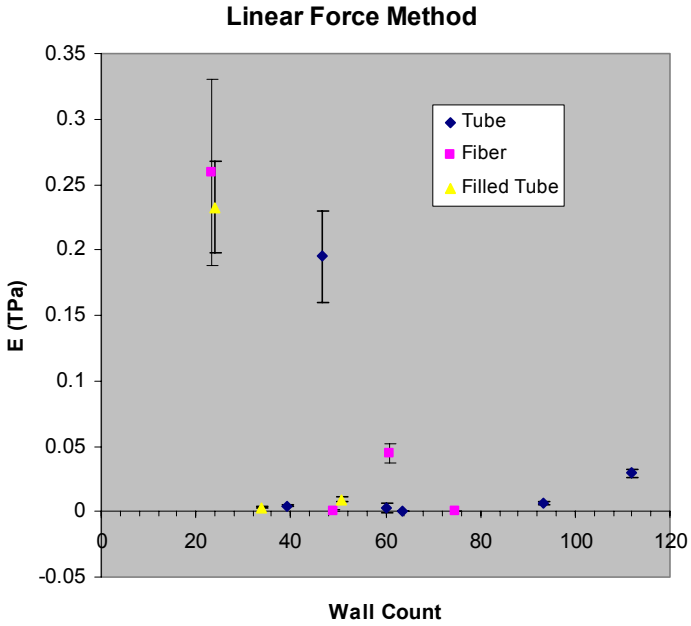

Figure 6.31. Calculated elastic moduli of coiled carbon nanotubes using the frequency method (A), linear force method (B), critical force method (C,D). Moduli are plotted against graphitic wall number as measured by TEM imaging.

C

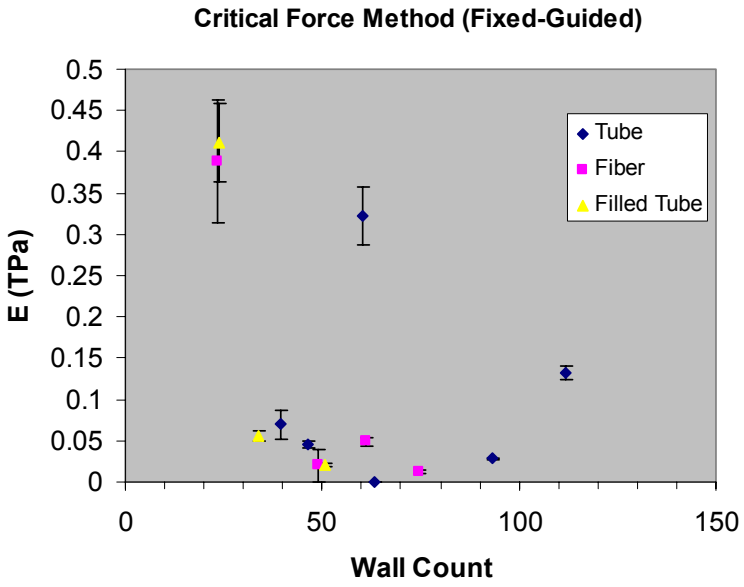

D

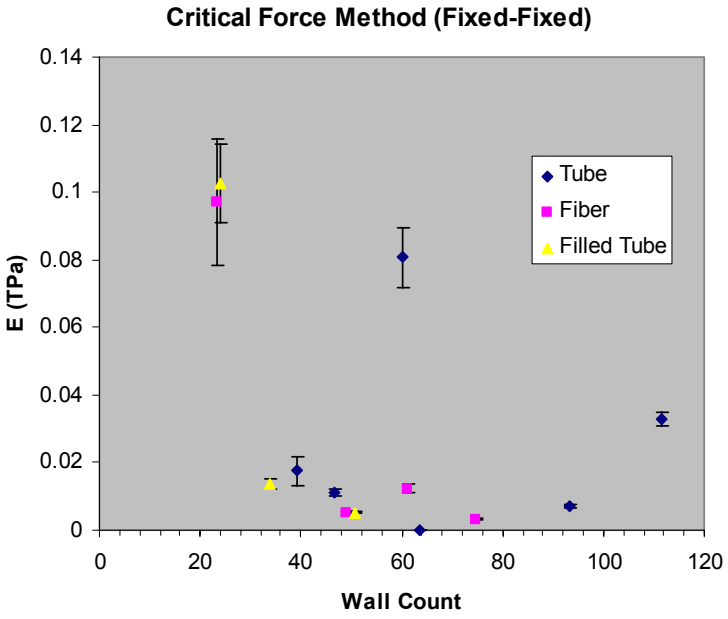

Figure 6.31 (continued). Calculated elastic moduli of coiled carbon nanotubes using the frequency method (A), linear force method (B), critical force method (C,D). Moduli are plotted against graphitic wall number as measured by TEM imaging.

CHAPTER 7

FUTURE DIRECTIONS OF RESEARCH

The research goals set forth for this study were accomplished. First and foremost, the mechanical compression of as-fabricated carbon nanocoils has been vigorously investigated and a relationship has been established with the structure of the carbon nanostructures. The term nanocoils is more appropriate than coiled carbon nanotubes in describing the nanostructures encountered in this study which included conventional hollow nanotubes, filled nanotubes, and nanofibers.

In previous reports [102], the sensitivity of MPFS to substrate composition was proposed. From the results presented in Chapter 4, this was demonstrated to be true; as the surface functionality chosen for the compression studies affected the resultant frequency response of the nanocoil. A significant difference in the frequency response was observed as the nanocoil was compressed on 1-dodecanethiol and 11-mercaptanoic acid functionalized gold substrates (Figure 4.5). The frequency response measured by MPFS relates to a change in the stiffness of the moiety attached to the probe tip under load. It would be expected that MPFS can be used to investigate the properties of any number of different material anchored to the probe tip or substrate, such as the nanocoils or thiol monolayers described in this dissertation. This result suggests that MPFS may be sensitive the mechanical properties of small molecules. Based on these results, several questions remain unanswered as to the applicability of MPFS to measure small molecule properties. Experiments could be conducted to determine what impact, if any, the probe tip modification plays on the sensitivity of MPFS.

During the compression experiments conducted on carbon nanocoils, several phenomena occurring in the measured frequency response, which were not previously understood, were observed. Through the use of improved hardware modifications (Chapter 3), including direct access to PSD signals and the use of data acquisition hardware capable

of sample rates up to 800 kHz, these phenomena were investigated. The first improvement on previous compression techniques came directly from the hardware modifications. The capture and analysis of higher vibration modes for the nanocoil-cantilever system was achieved. Unfortunately, only first and second order vibration modes for the Series-18 cantilever were observed; while up to four vibration modes for the CSC-38 cantilevers were observed in some cases. Because of the significant decrease in energy at higher modes, only the primary and secondary vibration modes had high enough signal-to-noise ratios to be used in the characterization of the mechanical behavior of the nanocoils. Another improvement on previous techniques was the increase of compression amount from <100 nm to greater than 1200 nm during some experiments. This enabled the investigation and identification of buckling and slip-stick motion of the nanocoil under compressive load. The impact of compression angle was also demonstrated to be significant to the mechanical response of the nanostructures.

Despite these improvements, the experimental techniques presented in the dissertation are limited in the ability to accurately measure the true frequency response of the nanocoil as makes the initial contact with the substrate. In the calculations presented in Chapters 5 and 6, the first observed shifted frequency value was used. This value is the result of averaging several power spectrum density plots to improve the S/N of the primary vibration mode of the system. In addition to this limitation the acquisition rate of the card used in this study does not capture the frequencies relating to the torsional vibration modes of the cantilevers, estimated to be in the megahertz range. The accuracy of these calculations can be significantly improved through the reduction of the noise floor of the power spectrum density plot and improved capture rate of the PSD data. This can be accomplished through the use of a data acquisition card with significantly greater sampling rate than the PCI-6120 used in the presented experiments. Similar compression studies could also be performed using a non-optical AFM system, such as strain gauge or

magnetically monitored cantilevers, in efforts to reduce the interference patterns observed during data acquisition.

Despite the uncertainties in the calculated moduli of the nanocoils, the application of MPFS in the analysis of nanostructure mechanics and material properties was demonstrated. Chapter 6 describes in great detail the methodology used to measure the large scale and chemical structures and the mechanical response of a batch of carbon nanocoils to a compressive load. The fabrication and use of a custom TEM holder allowed the investigation of the fine structure of the nanocoils, without requiring their removal for imaging; allowing further experiments to be conducted on the nanocoils. Because of the high occurrence of defects, carbon nanocoils created through CVD methods were not optimal for the creation of a predictive behavioral model. However, the use of multi parameter force spectroscopy (MPFS) to determine the elastic and shear modulus of the nanocoils was found to distinguish the fibrous structures from those with tube-like properties. This result alone warrants the use of MPFS as a screening tool for nanomaterial properties. MPFS, even with the presented limitations, can still be used to screen nanomaterials based on their measured mechanical properties. Additional research can also be performed on more ordered crystalline structures, to improve upon the predictive modeling capabilities of MPFS.

One potential application of the MPFS analysis method would be to incorporate the mechanical properties with the electrical properties of nanomaterials. Carbon nanotubes and nanocoils present ideal materials, on which these studies can be performed. Recently, the electrical properties of novel nanotube morphologies have been investigated [201]. The electrical properties of Y-shaped nanotube structures produced by arc-discharge synthesis methods have demonstrated non-linear I-V characteristics. These have been proposed to be used as an electrical gate in NEMS applications [202]. Carbon nanocoils may also present unique electronic behaviors due to inclusion of defects in the graphite matrix (Figure 1.5). These experiments can be conducted on the the carbon nanocoil modified cantilever tips

used within this dissertation. The inclusion of a nickel layer for the arc discharge attachment method provides a convenient conductive path to the nanocoils from the cantilever base.

The mechanical-electric behavior of nanostructures can be investigated [203, 204]. In such studies, MPFS analysis of the material can be used instead of, or in conjunction with TEM; where the nanostructure would need to be removed from the tip in order to be imaged. If a relationship exists between the electrical properties and the mechanical deformation (compression/ extension) of these materials, applications may exist as tactile sensors [205, 206] or as electrical components in NEMS/ MEMS systems.

APPENDIX A:

jb1b.m

program written for the conversion of frequency data from DAQ and Labview™ formats into array format for use in MATLAB™ programs.

```
clear;
loc1=input('location of Waterfall file? ','s');
loc2=input('location of Horizontal Movement? ','s');
loc3=input('location of Scan Mvmt file? ','s');
[col_wf1,col_wf2]=textread(loc1,'%s%s');
[col_hm1,col_hm2]=textread(loc2,'%s%s');
[col_cmp1,col_cmp2]=textread(loc3,'%s%s');

%Counting Data Generic
ss=col_wf2(13,1);%size of data set
s=size (col_wf1);
s0=s(1,1)-20;
size1=str2double(ss);%Equal to the numerical value of FFT
sr=size1+9;  %Number of data points +9
n=ceil(s0/sr);
n1=n/2;
wf1=str2double(col_wf1);
wf2=str2double(col_wf2);

%Waterfall matrix creation
WF1=zeros(size1,1:n1);%First col rep freq, others represent dB response
WF2=zeros(size1,1:n1);%First col rep freq, others represent dB response
WF=[WF1 WF2];

wft=cell(n,1);%WF time data
freq=wf1(21:21+str2double(ss)-1);
for i=1:n
    k=i-1;
    start=21+str2double(ss)*k+9*k;
    fend=21+str2double(ss)*i+9*k-1;
    c=wf2(start:fend);%change to wf2
    WF(:,i)=c;
    tend=15+str2double(ss)*k+9*k;
    wft(i,1)=col_wf2(tend,1);
end

bdwth=wf2(13,1);

temp=char(wft);
temp2=temp(:,7:12);
%some time data lost after 10th character.  Time will sensitive only to
%tenths-place
dtime=str2num(temp2);

hm1=str2double(col_hm1);
hm2=str2double(col_hm2);
cmp1=str2double(col_cmp1);
cmp2=str2double(col_cmp2);

s2=size(hm1);
s3=size(cmp1);
HM=[hm1(21:s2) hm2(21:s2)];
SM=[cmp1(21:s3) cmp2(21:s3)];

plot(freq,WF);
%axis([0 4.5e5 -120 -60]);
%plot(hm1,hm2);
%plot(cmp1,cmp2);

%a=col_1(21:40020,:)  For extracting interior data
save1=input('save converted data to? ','s');%will save in default matlab folder
save (save1,'freq','WF','HM','SM','dtime','wft','bdwth');
%macro saves freq,WF, HM, SM data
```

APPENDIX A:

jb2b.m

program written for visualization of frequency data; used after data conversion from jb1b.m

```
%Use on condensed matlab file created from jb1b
%HM (horizontal deflection)  time vs value
%SM (scanner movement)time vs value

hold off;
fkhz=freq/1000;
plot(fkhz,WF);
xlabel('Frequency (kHz)');
title('Waterfall');
ylabel('dB Vrms Hz^-1/2');
clc;
'For Waterfall Data'
q1=input('what is the lower frequency limit? (kHz) ');
q2=input('what is upper limit of freq range? (kHz) ');
verify=input('are these correct? (y/n)?  ','s');
if verify~='y'
    clc;
    'For Waterfall Data'
    q1=input('what is the lower frequency limit? (kHz) ');
    q2=input('what is upper frequency limit? (kHz) ');
    verify=input('are these correct? (y/n)?  ','s');
end
s=size(WF);
fstelem=fkhz(2,1);
l1=(q1-rem(q1,fstelem))/fstelem+1;
l2=(q2-rem(q2,fstelem))/fstelem+1;
Nfreq=fkhz(l1:l2,:);
NWF=WF(l1:l2,:);
plot(Nfreq,NWF);
xlabel('Frequency (kHz)');
ylabel('Amplitude (dB?)');
title('Waterfall');

dt1=dtime(2,1)-dtime(1,1);
dt2=dtime(4,1)-dtime(3,1);
stime=size(dtime);
times=(0:stime(1,1)-1);
time=times'*(dt1+dt2)/2;
%save0=input('do you want to save new freq data? (y/n)?  ','s');
%if save0=='y'
%    save1=input('save converted data to?  ','s');%will save in default matlab folder
%    save (save1,'Nfreq','NWF','time');
%end
%time stuff

%'For Deflection /Scanner Movement'
%verify2=input('Check Horiz Movement/Scanner movement data? (y/n)  ','s');
%if verify2=='y'
%   x=HM(:,1);
%    y1=HM(:,2);%Horiz Mov data
%    y2=SM(:,2);%SM data
%  [AX,H1,H2] = plotyy(x,y1,x,y2,'plot');
   %**** Touches of Nice
%    set(get(AX(1),'Ylabel'),'String','HM Units
(volt)');set(get(AX(2),'Ylabel'),'String','Scanner Movement');
%    xlabel('Time (sec)');
%    title('Horz Mov/Scanner Movement');
    %set(H1,'linestyle','.');
    %set(H2,'linestyle','.');
    %else
    %verify2=input('Check Horz Mov/Scanner movement data? (y/n)  ','s');
%end

%For 3d plot must manipulate the frequency data to allow for axis fit
f3d=zeros(size(Nfreq),stime(1,1));
n=stime(1,1);
for i=1:n
   f3d(:,i)=[Nfreq];
```

```
end
hold off;
mesh(time,f3d,NWF);
xlabel('time(s)'),ylabel('frequency(kHz)'),zlabel('ampliude');
%hold on;
%plot(SM(:,1),SM(:,2))
%

verify3=input('Check Offset? (y/n)  ','s');
if verify3=='y'
    subplot(2,1,1);
    mesh(time,f3d,NWF);
    xlabel('time(s)'),ylabel('frequency(kHz)'),zlabel('ampliude');
    nwsize=size(NWF);
    a=nwsize(1,2);
    axis([0 time(a,1) q1 q2]);
    view(0,90);
    %hold off
    subplot(2,1,2);
    plot(SM(:,1), SM(:,2));
    xlabel('time (s)'), ylabel('displacement (V)');
    xlim([0 time(a,1)]);
end
view(0,90)
```

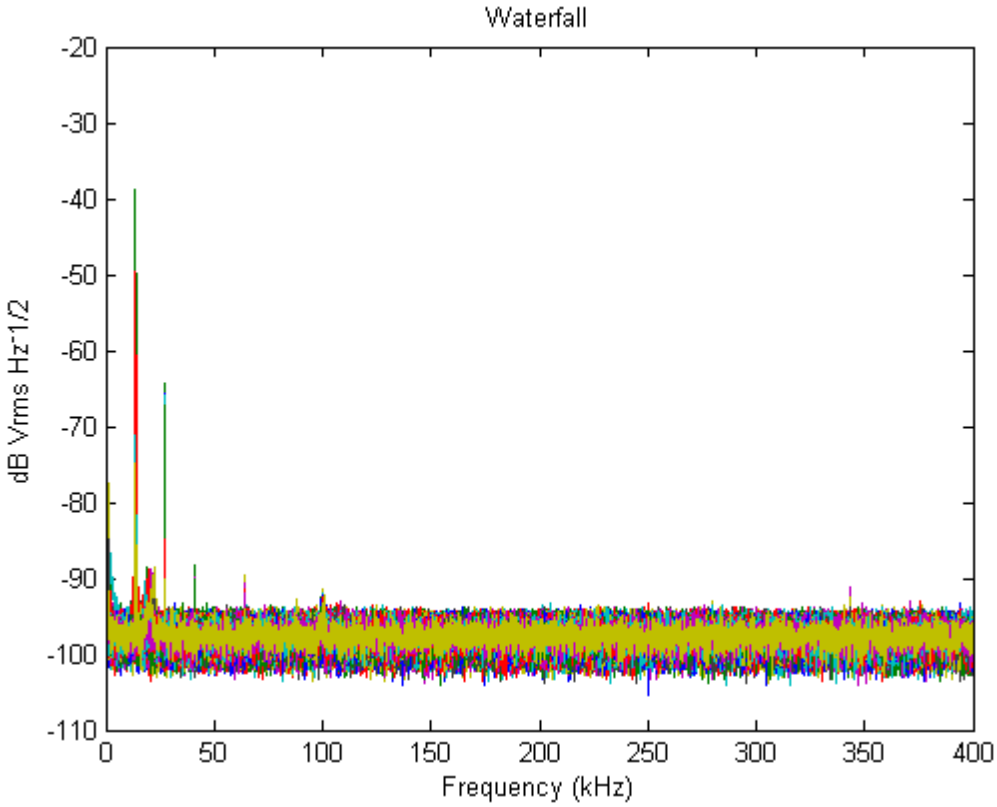

Initial plot generated in jb2b.m; the user can define frequency range to display the data in 2D or 3D plots. Note the units of amplitude.

APPENDIX A:

jbmax.m

Peak-picking routine used to find the frequency values that correlate to largest amplitude signal in power spectrum density plot of data.

```
%Use on condensed matlab file created from jb1b.m
%HM (horizontal deflection)  time vs value
%SM (scanner movement)time vs value

hold off;
fkhz=freq/1000;
plot(fkhz,WF);
xlabel('Frequency (kHz)');
title('Waterfall');
ylabel('dB?');
clc;
'Peak max'
q1=input('what is the lower frequency limit? (kHz)  ');
q2=input('what is upper limit of freq range? (kHz) ');
verify=input('are these correct? (y/n)?  ','s');
if verify~='y'
    clc;
    'For Waterfall Data'
    q1=input('what is the lower frequency limit? (kHz) ');
    q2=input('what is upper frequency limit? (kHz) ');
    verify=input('are these correct? (y/n)?  ','s');
end
s=size(WF);
fstelem=fkhz(2,1);
l1=(q1-rem(q1,fstelem))/fstelem+1;
l2=(q2-rem(q2,fstelem))/fstelem+1;
Nfreq=fkhz(l1:l2,:);
NWF=WF(l1:l2,:);
%plot(Nfreq,NWF);
xlabel('Frequency (Hz)');
ylabel('Amplitude (dB?)');
title('Waterfall');
%dt1=dtime(2,1)-dtime(1,1);
%dt2=dtime(4,1)-dtime(3,1);
%stime=size(dtime);
%times=(0:stime(1,1)-1);
%time=times'*(dt1+dt2)/2;
smsize=size(SM);
stime=size(dtime);
totaltime=SM(smsize(1,1),1);
timeavg=totaltime/stime(1,1);
times=(0:stime(1,1)-1);
time=times'*timeavg;

a=size(NWF);
for i=1:a(2)
  ind=find(NWF(:,i)==max(NWF(:,i)));
  res_freq(i)=Nfreq(ind);
end
plot(res_freq,'.')
xlabel('WF count');
ylabel('Frequency (kHz)');
axis([0 a(1,2) q1 q2]);
x=res_freq';
```

APPENDIX B: CANTILEVER PORTFOLIO

The following are select images and MPFS data collected from the nanocoils used in Chapter 5. The notebook designations are listed along with the tip designation. Tip #4 was described in detail in Chapter 4. Tip# 5, 6, 13 were discussed in Chapter 6.

Each page contains an SEM and TEM image, frequency response plot, and force-distance plot. The frequency response plot presented represents 125nm compression, unless otherwise stated. The force-distance plots are offset to align the jump-to-contact for the compression. All force-distance plots present data for compression amounts of 125, 250, 375, 500, 750, and 875 nm.

Tip #1 (a2s)

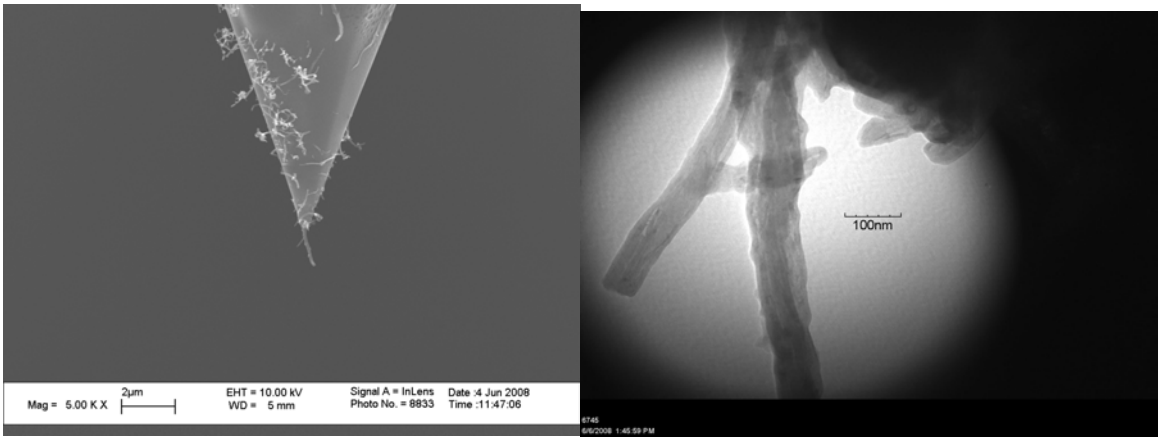
Mag = 5.00 K X
2µm
EHT = 10.00 kV
WD = 5 mm
Signal A = InLens
Photo No. = 8833
Date :4 Jun 2008
Time :11:47:06
100nm

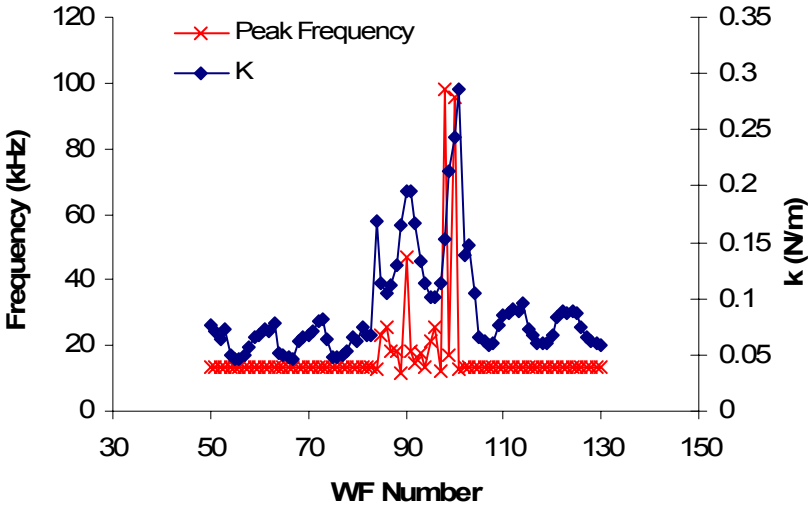
Peak Frequency
K
Frequency (kHz)
k (N/m)
WF Number
120
100
80
60
40
20
0
0.35
0.3
0.25
0.2
0.15
0.1
0.05
0
30
50
70
90
110
130
150

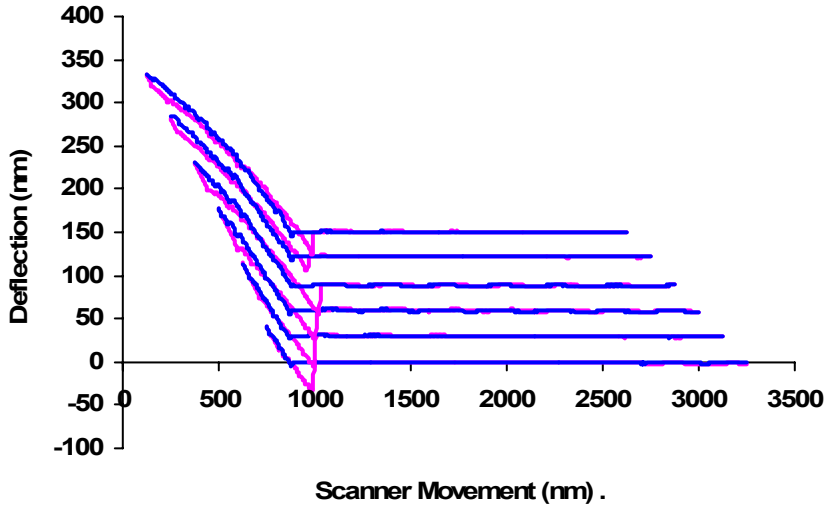
Deflection (nm)
Scanner Movement (nm) .
400
350
300
250
200
150
100
50
0
-50
-100
0
500
1000
1500
2000
2500
3000
3500

Tip #2 (a7s)

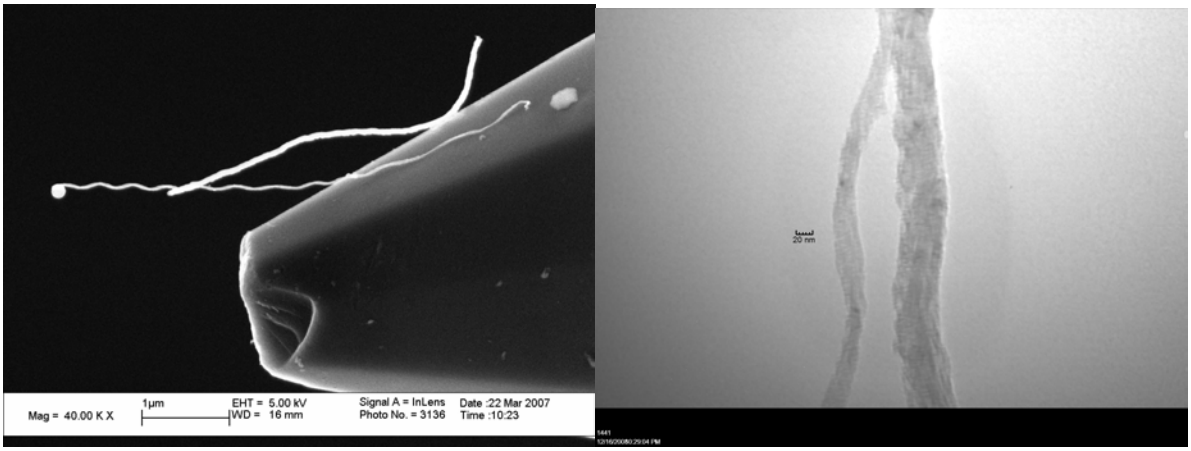
Mag = 40.00 K X
1µm
EHT = 5.00 kV
WD = 16 mm
Signal A = InLens
Photo No. = 3136
Date :22 Mar 2007
Time :10:23

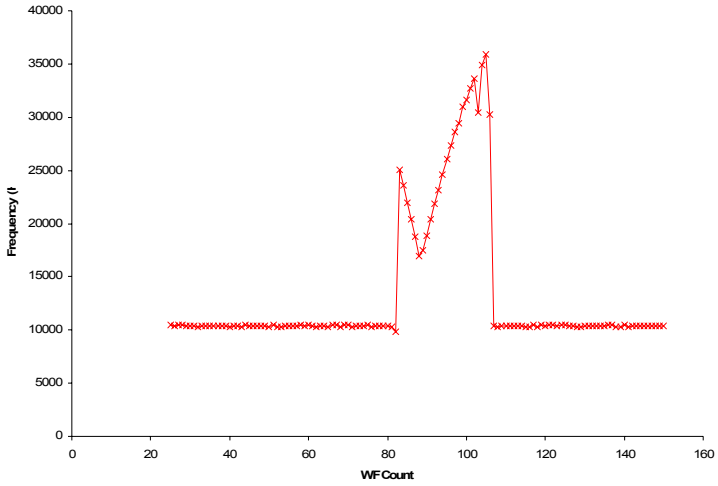
Frequency (
WF Count
0
5000
10000
15000
20000
25000
30000
35000
40000
0
20
40
60
80
100
120
140
160

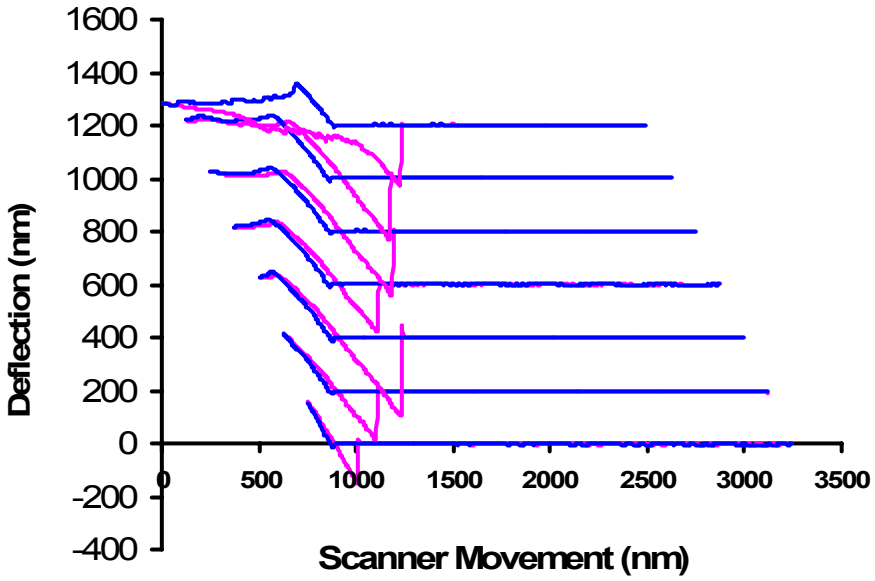
Deflection (nm)
Scanner Movement (nm)
1600
1400
1200
1000
800
600
400
200
0
-200
-400
0
500
1000
1500
2000
2500
3000
3500

Tip #3 (b1s)


Mag = 5.00 K X
2µm
EHT = 5.00 kV
WD = 4 mm
Signal A = InLens
Photo No. = 2020
Date :25 Apr 2008
Time :12:50:39

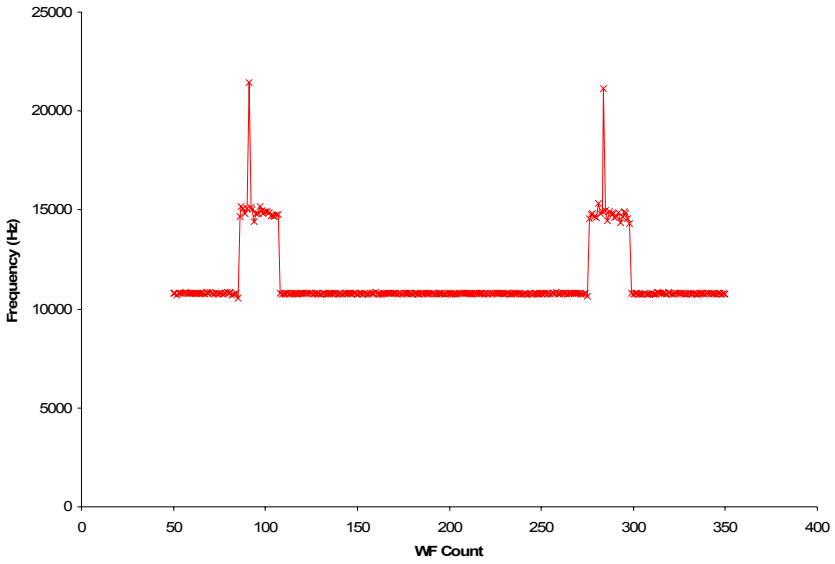
Frequency (Hz)
WF Count
25000
20000
15000
10000
5000
0
0
50
100
150
200
250
300
350
400

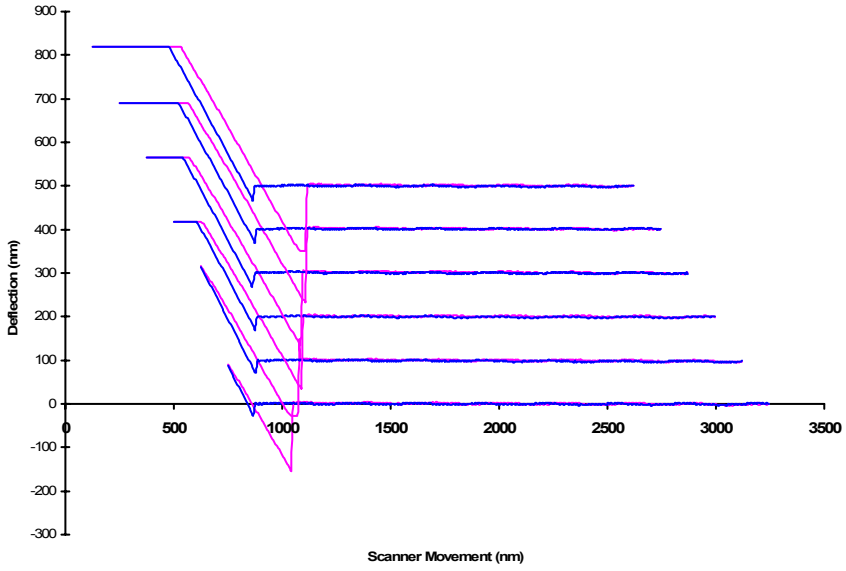
Deflection (nm)
Scanner Movement (nm)
900
800
700
600
500
400
300
200
100
0
-100
-200
-300
0
500
1000
1500
2000
2500
3000
3500

Tip #7 (b9s)

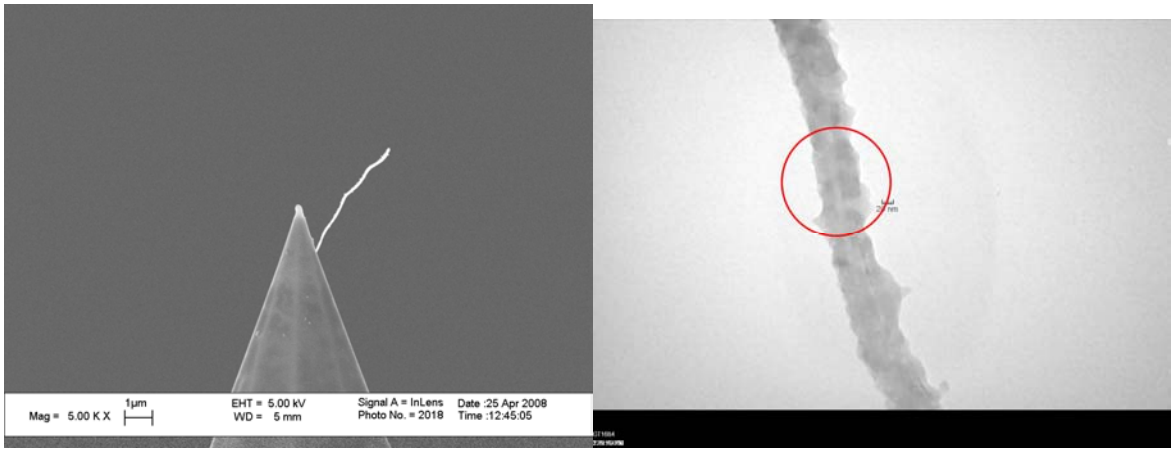
Mag = 5.00 K X
1µm
EHT = 5.00 kV
WD = 5 mm
Signal A = InLens
Photo No. = 2018
Date :25 Apr 2008
Time :12:45:05

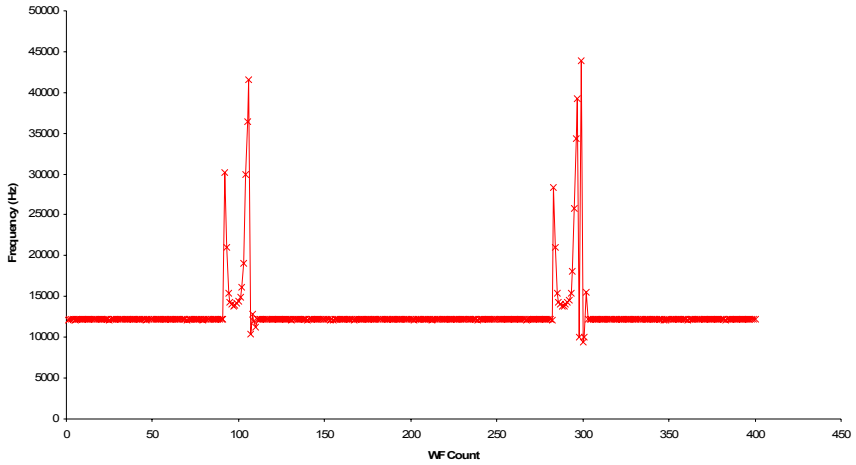
Frequency (Hz)
WF Count
50000
45000
40000
35000
30000
25000
20000
15000
10000
5000
0
0
50
100
150
200
250
300
350
400
450

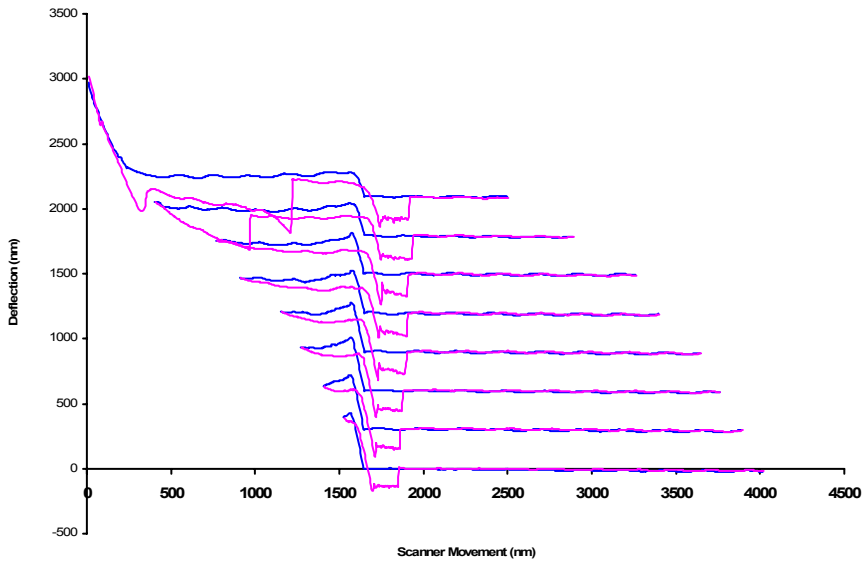
Deflection (nm)
Scanner Movement (nm)
3500
3000
2500
2000
1500
1000
500
0
-500
0
500
1000
1500
2000
2500
3000
3500
4000
4500

Tip #8 (c2s)

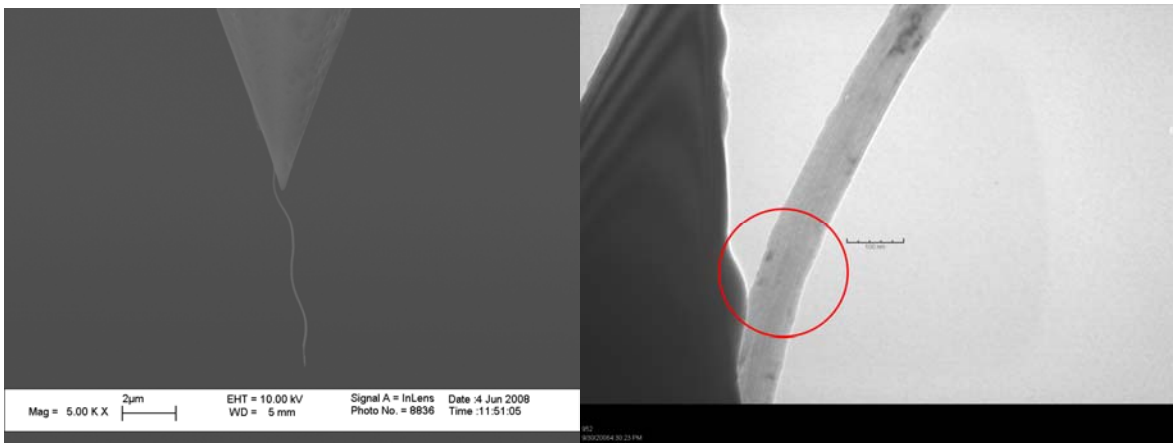
Mag = 5.00 K X
2µm
EHT = 10.00 kV
WD = 5 mm
Signal A = InLens
Photo No. = 8836
Date :4 Jun 2008
Time :11:51:05

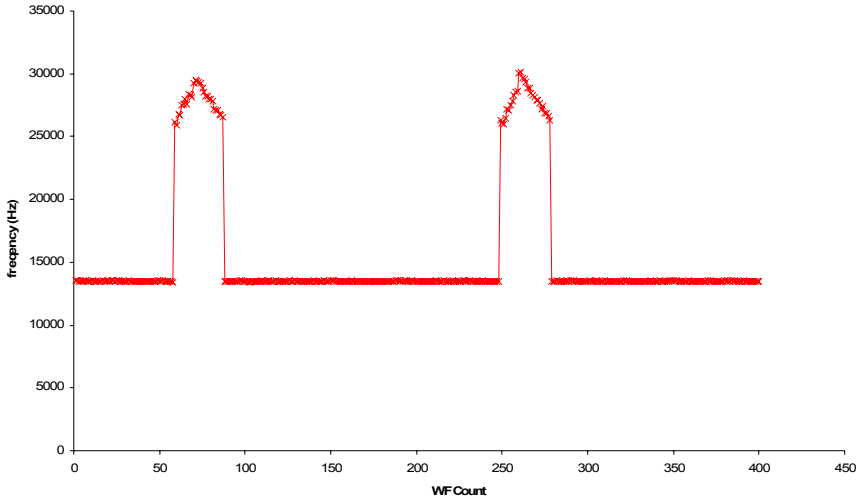
freqency (Hz)
WF Count
35000
30000
25000
20000
15000
10000
5000
0
0
50
100
150
200
250
300
350
400
450

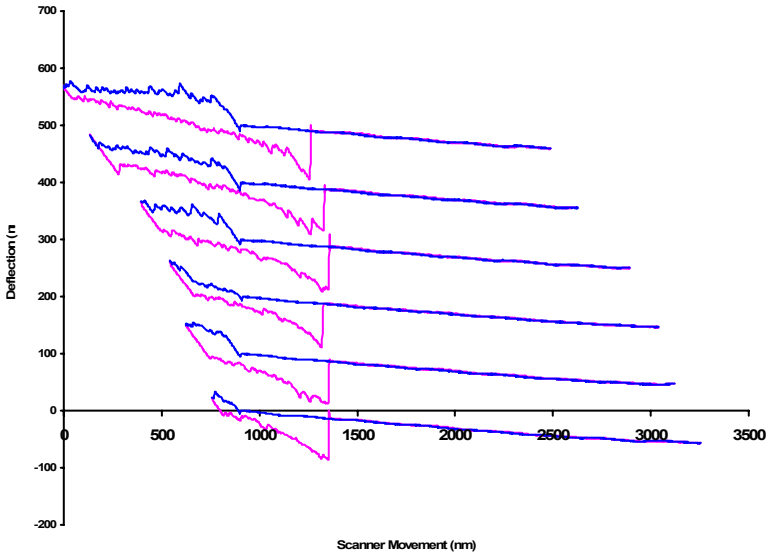
Deflection (n
Scanner Movement (nm)
700
600
500
400
300
200
100
0
-100
-200
0
500
1000
1500
2000
2500
3000
3500

Tip #9 (c3s)

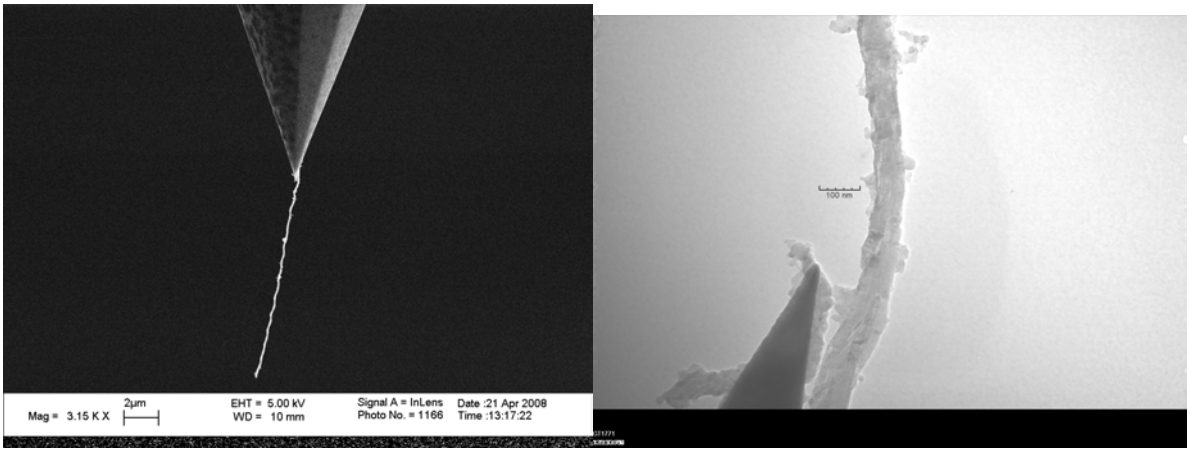
Mag = 3.15 K X
2µm
EHT = 5.00 kV
WD = 10 mm
Signal A = InLens
Photo No. = 1166
Date :21 Apr 2008
Time :13:17:22
100 nm

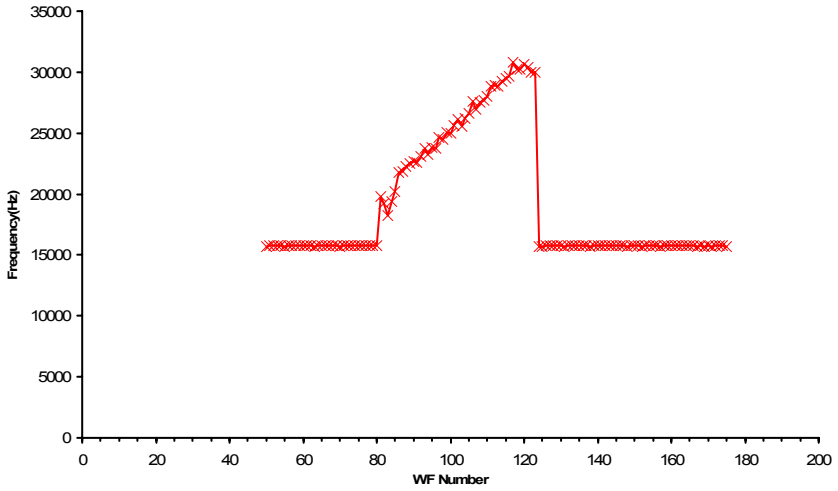
Frequency(Hz)
WF Number
35000
30000
25000
20000
15000
10000
5000
0
0
20
40
60
80
100
120
140
160
180
200

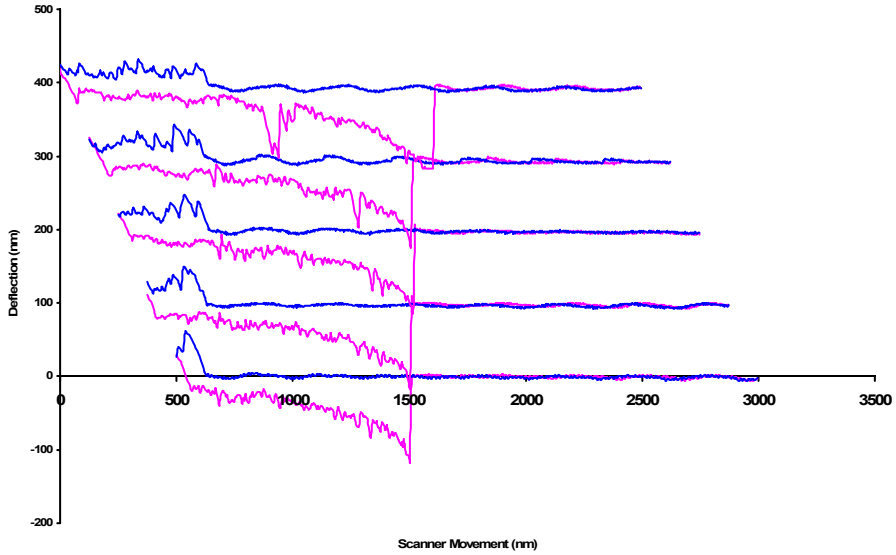
Deflection (nm)
Scanner Movement (nm)
500
400
300
200
100
0
-100
-200
0
500
1000
1500
2000
2500
3000
3500

Tip #10 (c6s)

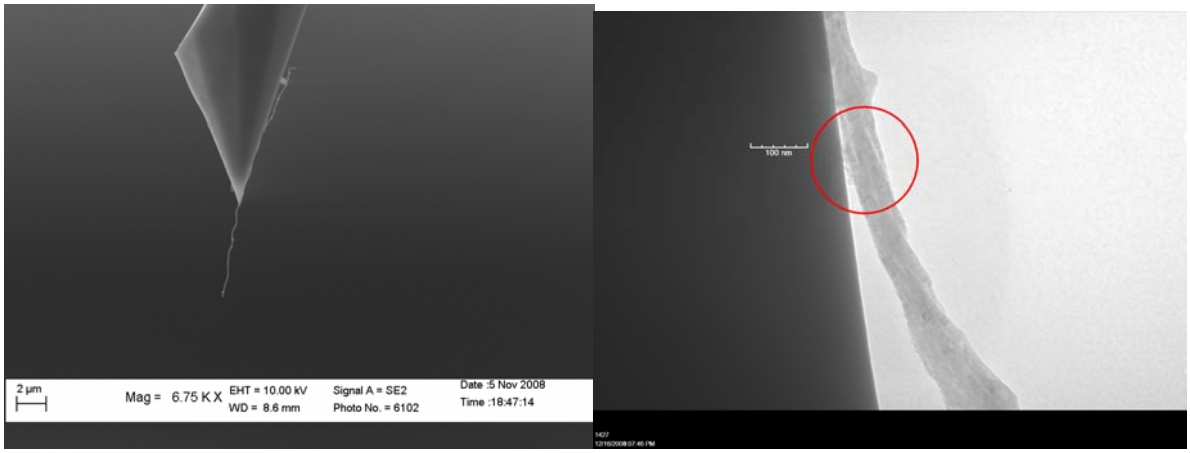
2 µm
Mag = 6.75 K X
EHT = 10.00 kV
WD = 8.6 mm
Signal A = SE2
Photo No. = 6102
Date :5 Nov 2008
Time :18:47:14
100 nm

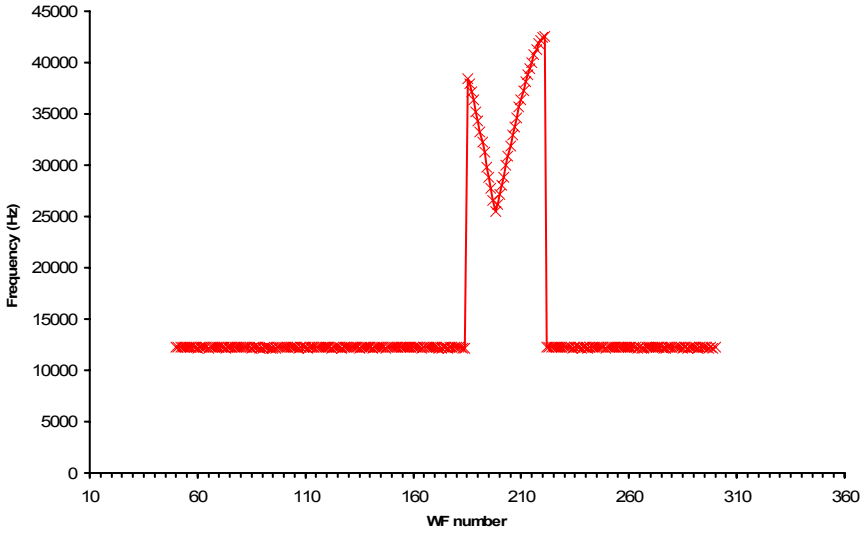
Frequency (Hz)
45000
40000
35000
30000
25000
20000
15000
10000
5000
0
10
60
110
160
210
260
310
360
WF number

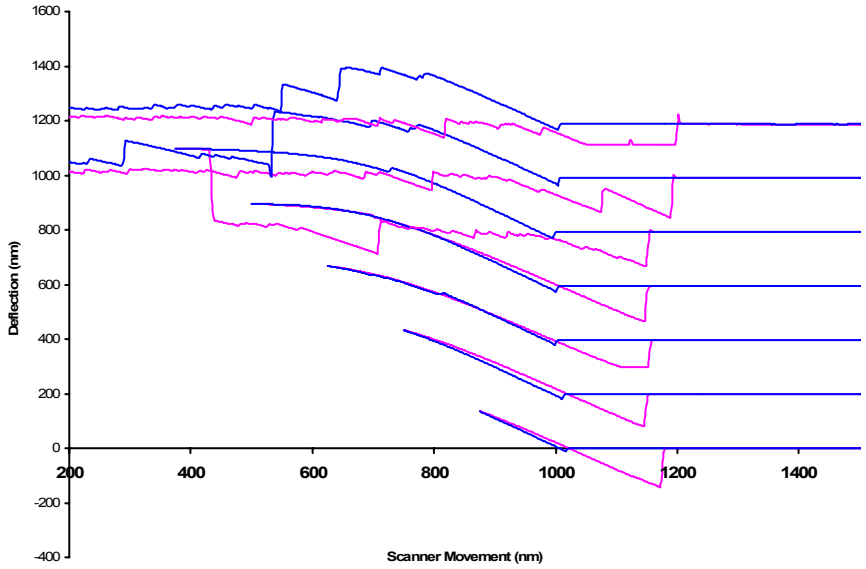
Deflection (nm)
1600
1400
1200
1000
800
600
400
200
0
-200
-400
200
400
600
800
1000
1200
1400
Scanner Movement (nm)

Tip #11 (c7s)

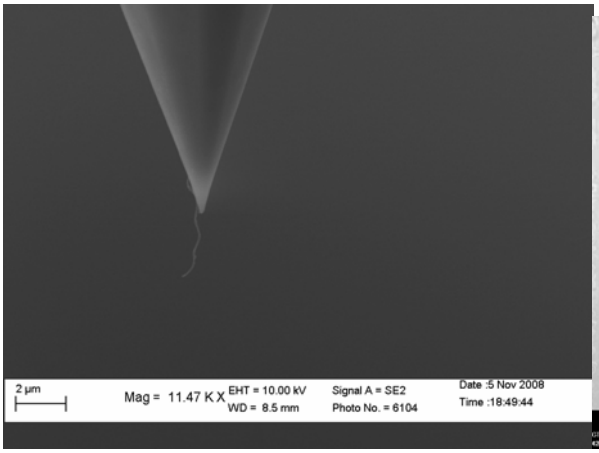
2 µm
Mag = 11.47 K X
EHT = 10.00 kV
WD = 8.5 mm
Signal A = SE2
Photo No. = 6104
Date :5 Nov 2008
Time :18:49:44

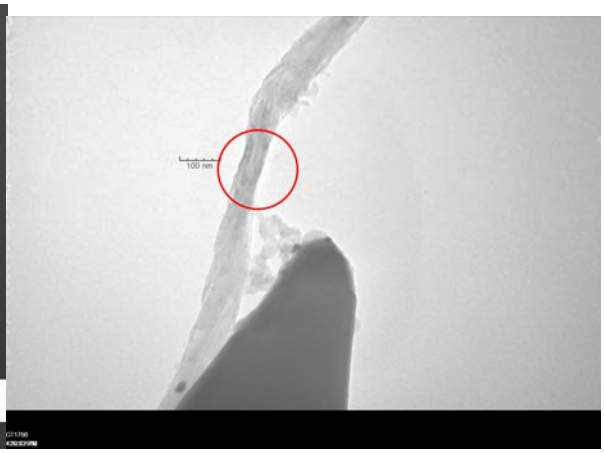
100 nm

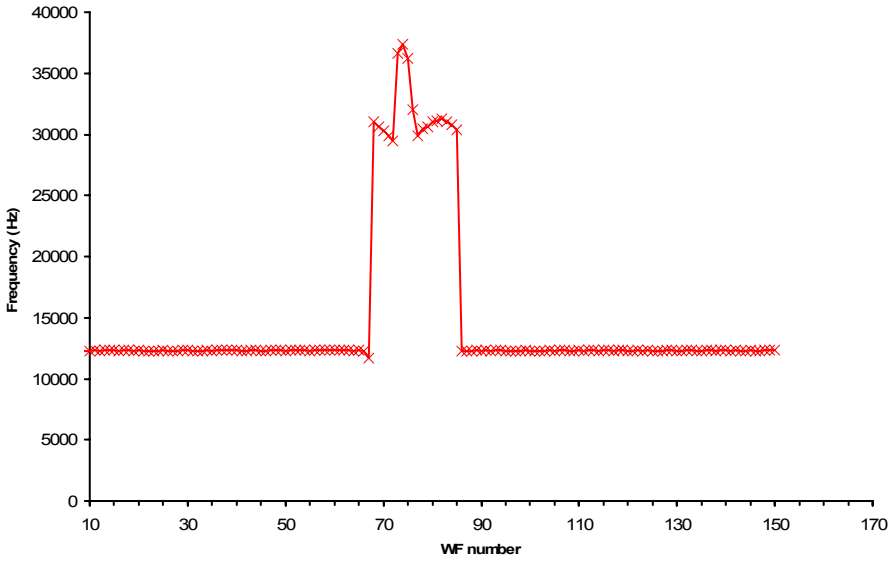
Frequency (Hz)
40000
35000
30000
25000
20000
15000
10000
5000
0
10
30
50
70
90
110
130
150
170
WF number

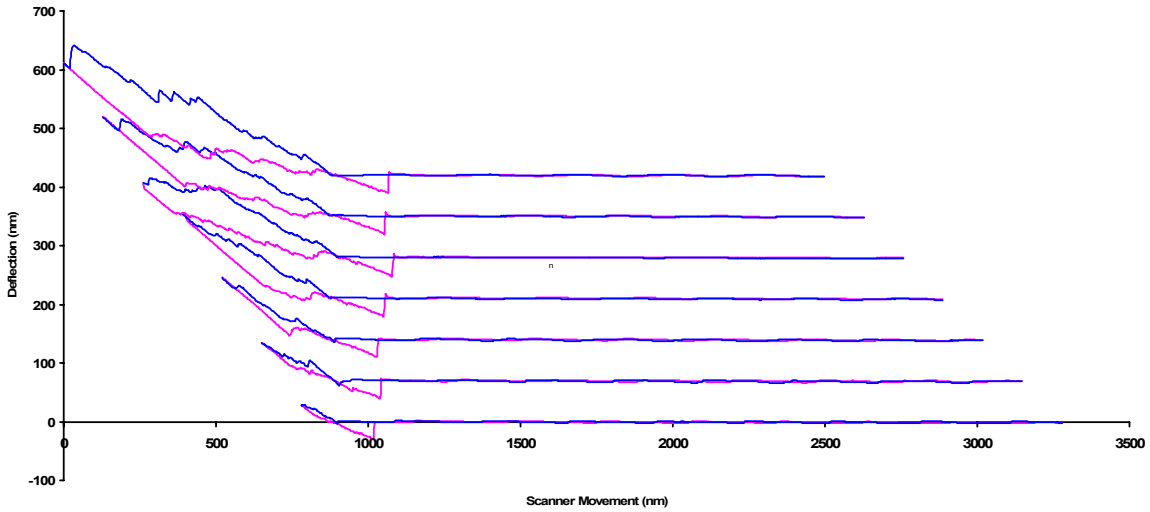
Deflection (nm)
700
600
500
400
300
200
100
0
-100
0
500
1000
1500
2000
2500
3000
3500
Scanner Movement (nm)

Tip #12 (c8s)

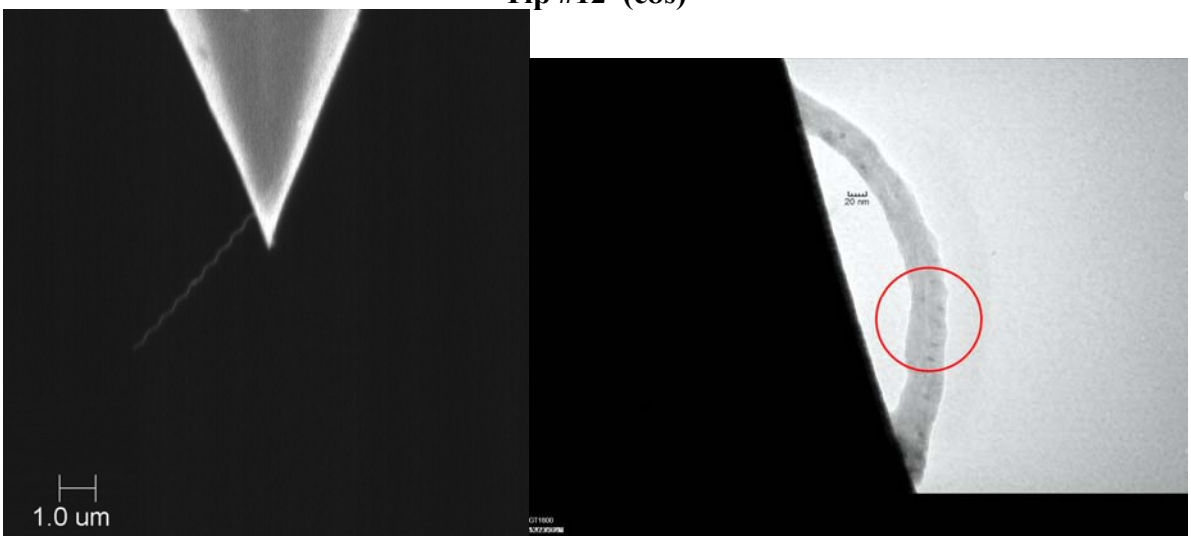
1.0 um

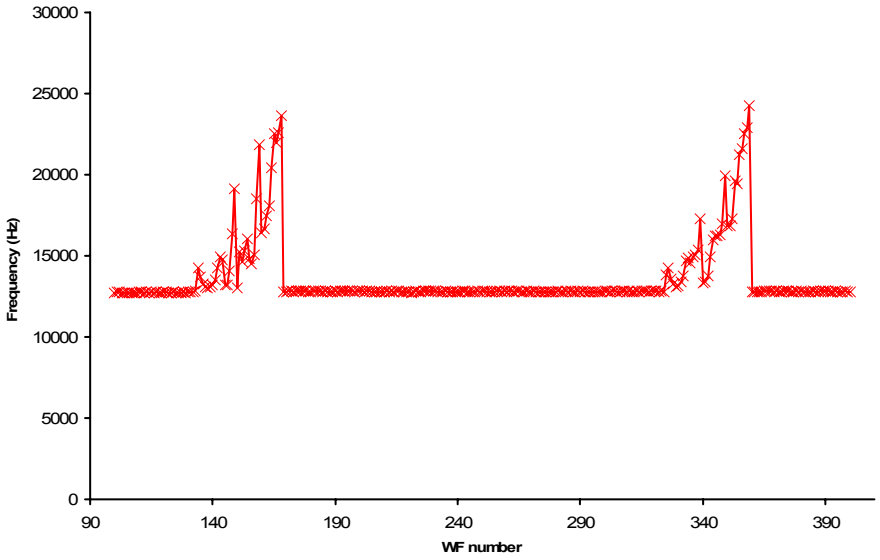
Frequency (Hz)
30000
25000
20000
15000
10000
5000
0
90
140
190
240
290
340
390
WF number

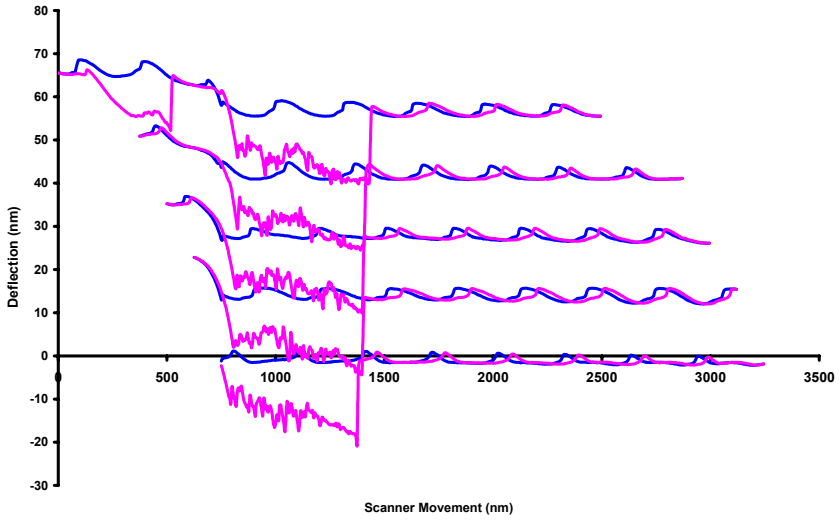
Deflection (nm)
80
70
60
50
40
30
20
10
0
-10
-20
-30
500
1000
1500
2000
2500
3000
3500
Scanner Movement (nm)

Tip #14 (A2H)

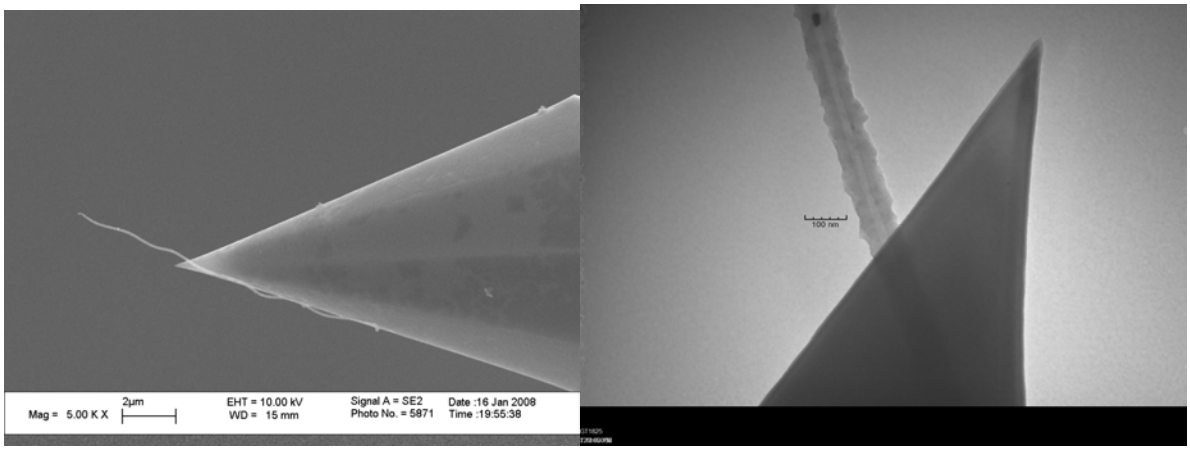

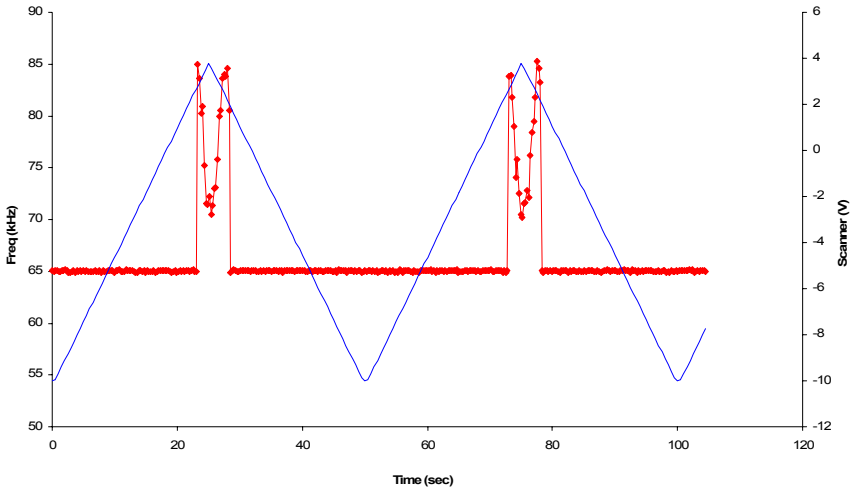

Force Distance Plot

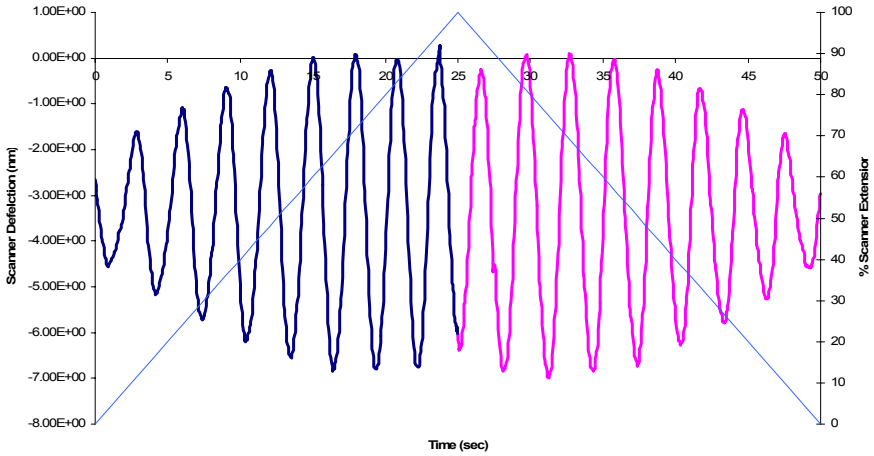

Tip #15 (A3H)

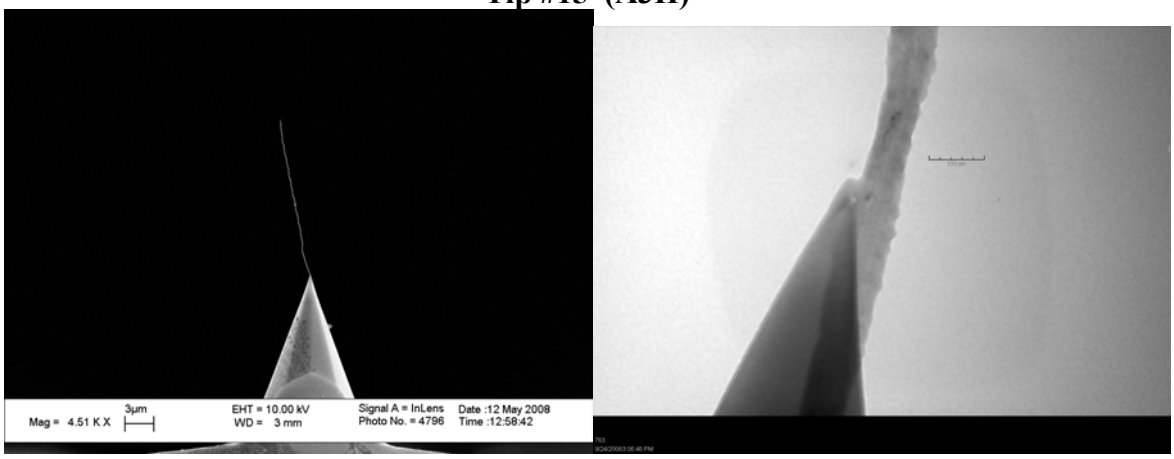

Full Frequency Response

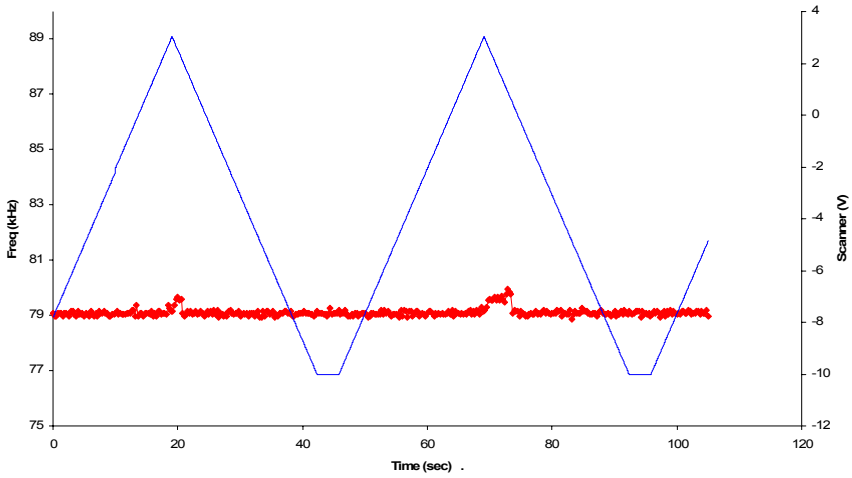

Force Distance Plot

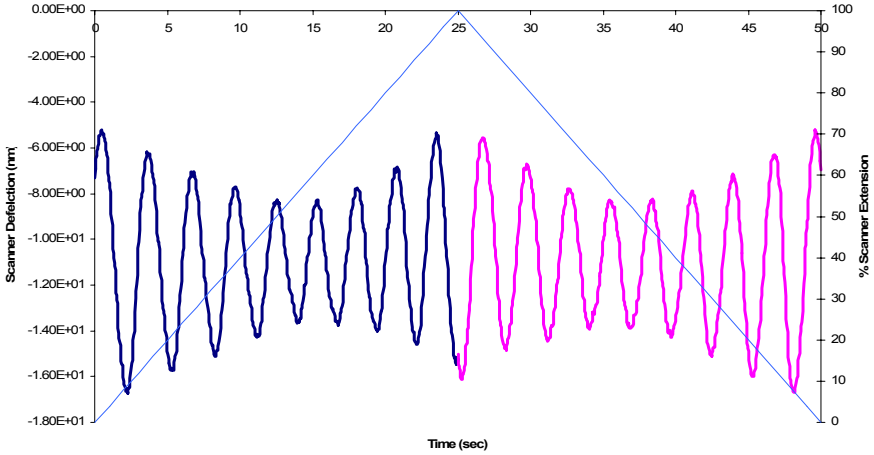

Tip #16 (A4H)

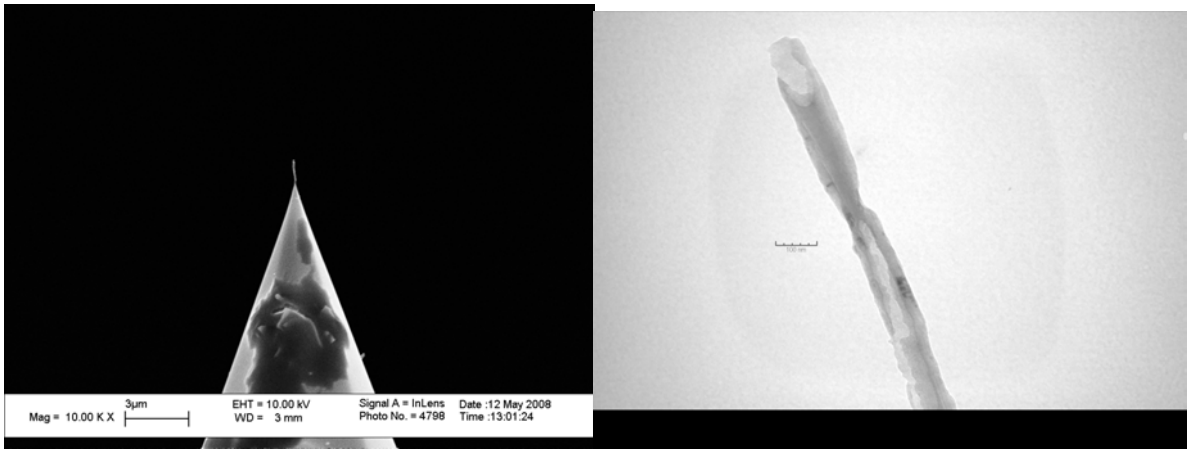

Full Frequency Response

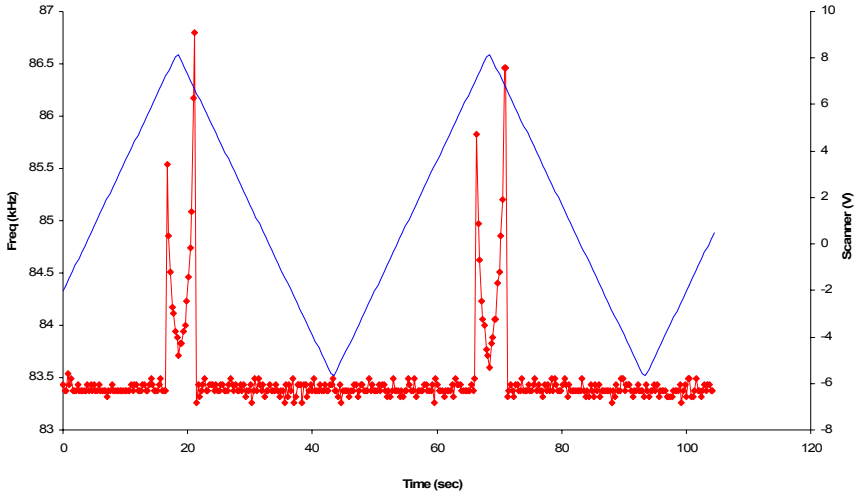

Force Distance Plot

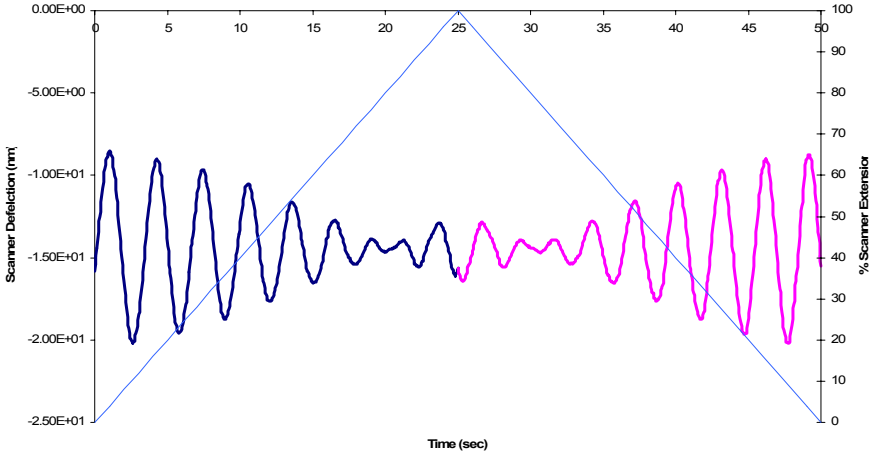

Tip #17 (C3H)

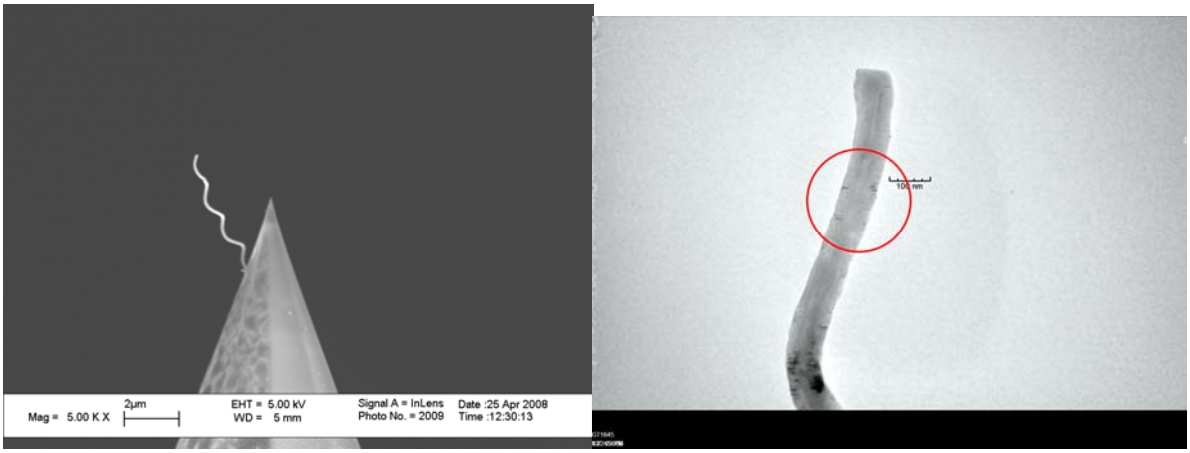

Full Frequency Response

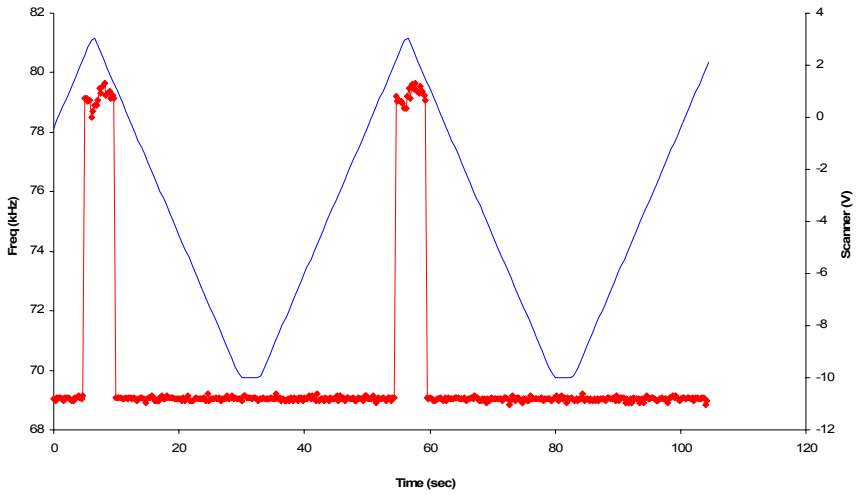

Force Distance Plot

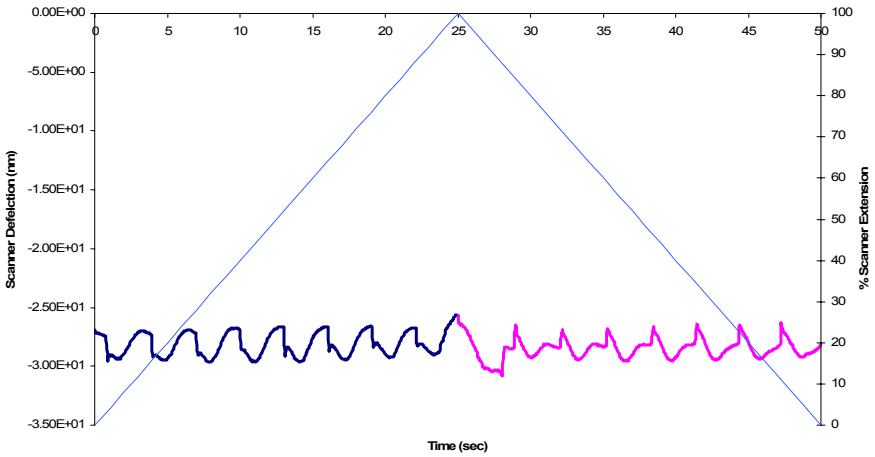

Tip #18 (E2H)

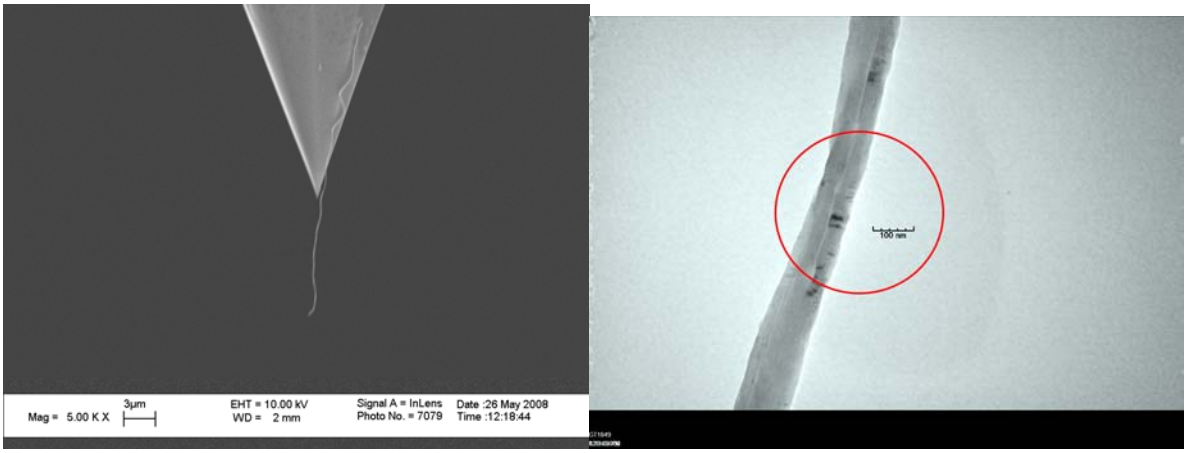

Full Frequency Response

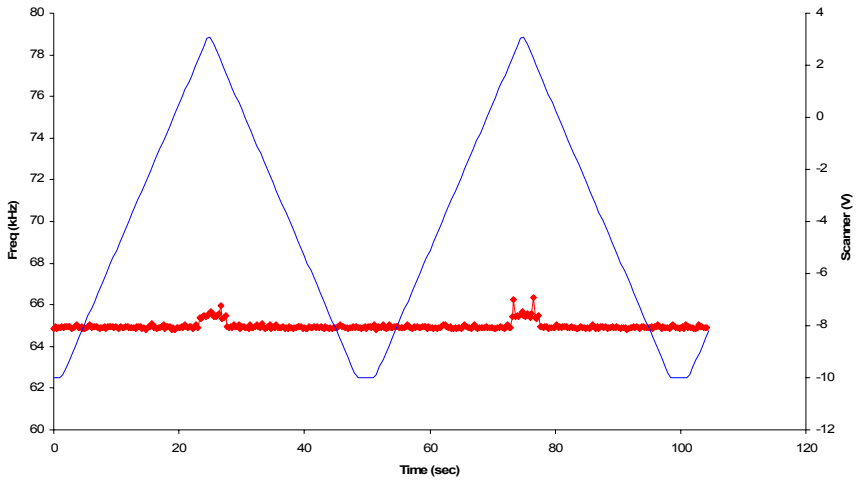

Force Distance Plot

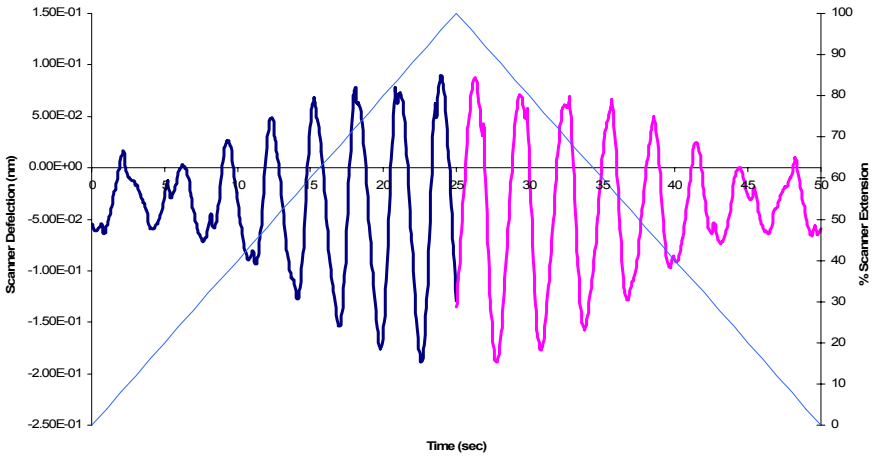

REFERENCES

1. Dresselhaus, M. S.; Dresselhaus, G.; Eklund, P. C.; Editors, *Science of Fullerenes and Carbon Nanotubes*. 1996; p 965 pp.
2. Zhou, O.; Shimoda, H.; Gao, B.; Oh, S.; Fleming, L.; Yue, G., Materials Science of Carbon Nanotubes: Fabrication, Integration, and Properties of Macroscopic Structures of Carbon Nanotubes. In 2002; Vol. 35, pp 1045-1053.
3. Jensen, K.; Weldon, J.; Garcia, H.; Zettl, A., Nanotube Radio. In 2007; Vol. 7, pp 3508-3511.
4. Iijima, S., Carbon nanotubes. *Kotai Butsuri* **1992,** 27, (6), 441-7.
5. Smalley, R. E.; Yakobson, B. I., The future of the fullerenes. *Solid State Commun.* **1998,** 107, (11), 597-606.
6. Dresselhaus, M. S.; Dresselhaus, G.; Charlier, J. C.; Hernandez, E., Electronic, thermal and mechanical properties of carbon nanotubes. *Philos Transact A Math Phys Eng Sci* **2004,** 362, (1823), 2065-98.
7. Barber, A. H.; Kaplan-Ashiri, I.; Cohen, S. R.; Tenne, R.; Wagner, H. D., Stochastic strength of nanotubes: An appraisal of available data. *Compos. Sci. Technol.* **2005,** 65, (15-16), 2380-2384.
8. Yu, M.-F.; Lourie, O.; Dyer, M. J.; Moloni, K.; Kelly, T. F.; Ruoff, R. S., Strength and breaking mechanism of multiwalled carbon nanotubes under tensile load. *Science* **2000,** 287, (5453), 637-640.
9. Falvo, M. R.; Clary, G. J.; Taylor, R. M., 2nd; Chi, V.; Brooks, F. P., Jr.; Washburn, S.; Superfine, R., Bending and buckling of carbon nanotubes under large strain. *Nature* **1997,** 389, (6651), 582-4.
10. White, C. T.; Robertson, D. H.; Mintmire, J. W., Helical and rotational symmetries of nanoscale graphitic tubules. *Phys. Rev. B: Condens. Matter* **1993,** 47, (9), 5485-8.
11. Gao, R.; Wang, Z. L.; Fan, S., Kinetically Controlled Growth of Helical and Zigzag Shapes of Carbon Nanotubes. *J. Phys. Chem. B* **2000,** 104, (6), 1227-1234.
12. Fonseca, A.; Hernadi, K.; Nagy, J. B.; Lambin, P.; Lucas, A. A., Growth mechanism of coiled carbon nanotubes. *Synth. Met.* **1996,** 77, (1-3), 235-42.
13. Zhong-can, O.-Y.; Su, Z.-B.; Wang, C.-L., Coil formation in multishell carbon nanotubes: competition between curvature elasticity and interlayer adhesion. *Phys. Rev. Lett.* **1997,** 78, (21), 4055-4058.
14. Hernadi, K.; Thien-Nga, L.; Forro, L., Growth and microstructure of catalytically produced coiled carbon nanotubes. *J. Phys.Chem. B* **2001,** 105, (50), 12464-12468.
15. Biro, L. P.; Mark, G. I.; Koos, A. A.; Nagy, J. B.; Lambin, P., Coiled carbon nanotube structures with supraunitary nonhexagonal to hexagonal ring ratio. *Phys. Rev. B: Condens. Mat. Mater. Phys.* **2002,** 66, (16), 165405/1-165405/6.
16. Varadan, V. K.; Xie, J., Synthesis of carbon nanocoils by microwave CVD. *Smart Mater. Struct.* **2002,** 11, (5), 728-734.
17. Lu, M.; Lau, K.-T.; Xu, J.-C.; Li, H.-L., Coiled carbon nanotubes growth and DSC study in epoxy-based composites. *Coll. Surf., A: Physicochem. Engin. Aspects* **2005,** 257-258, 339-343.
18. Luo, T.; Liu, J.; Chen, L.; Zeng, S.; Qian, Y., Synthesis of helically coiled carbon nanotubes by reducing ethyl ether with metallic zinc. *Carbon* **2005,** 43, (4), 755-759.

19. Szabo, A.; Fonseca, A.; Nagy, J. B.; Lambin, P.; Biro, L. P., Structural origin of coiling in coiled carbon nanotubes. *Carbon* **2005,** 43, (8), 1628-1633.
20. Jiang, J.; Feng, T.; Cheng, X. H.; Dai, L. J.; Cao, G. B.; Zhang, J. H.; Jiang, B. Y.; Wang, X.; Liu, X. H.; Zou, S. C., Growth and field emission of coiled carbon nanotubes by plasma-enhanced chemical vapor deposition. *Mater. Lett.* **2006,** 60, (8), 1085-1088.
21. Ajayan, P. M.; Ebbesen, T. W., Nanometer-size tubes of carbon. *Rep. Prog. Phys.* **1997,** 60, (10), 1025-1062.
22. Ebbesen, T. W.; Ajayan, P. M., Large-scale synthesis of carbon nanotubes. *Nature* **1992,** 358, (6383), 220-2.
23. Delzeit, L.; Nguyen, C. V.; Stevens, R. M.; Han, J.; Meyyappan, M., Growth of carbon nanotubes by thermal and plasma chemical vapour deposition processes and applications in microscopy. *Nanotechnology* **2002,** 13, (3), 280-284.
24. Delzeit, L.; Nguyen, C. V.; Chen, B.; Stevens, R.; Cassell, A.; Han, J.; Meyyappan, M., Multiwalled Carbon Nanotubes by Chemical Vapor Deposition Using Multilayered Metal Catalysts. *J. Phys.Chem. B* **2002,** 106, (22), 5629-5635.
25. Qin, L.-C.; Iijima, S., Structure and formation of raft-like bundles of single-walled helical carbon nanotubes produced by laser evaporation. *Chem. Phys. Lett.* **1997,** 269, (1,2), 65-71.
26. Kumar, S.; Dang, T. D.; Arnold, F. E.; Bhattacharyya, A. R.; Min, B. G.; Zhang, X.; Vaia, R. A.; Park, C.; Adams, W. W.; Hauge, R. H.; Smalley, R. E.; Ramesh, S.; Willis, P. A., Synthesis, Structure, and Properties of PBO/SWNT Composites. *Macromolecules* **2002,** 35, (24), 9039-9043.
27. Hayashi, T.; Kim Yoong, A.; Natsuki, T.; Endo, M., Mechanical properties of carbon nanomaterials. *Chemphyschem* **2007,** 8, (7), 999-1004.
28. Lau, K. T.; Gu, C.; Hui, D., A critical review on nanotube and nanotube/nanoclay related polymer composite materials. *Composites: B* **2006,** 37, 425-436.
29. Lau, K.-t.; Lu, M.; Liao, K., Improved mechanical properties of coiled carbon nanotubes reinforced epoxy nanocomposites. *Composites, Part A: Appl. Sci. Manufact.* **2006,** 37A, (10), 1837-1840.
30. Tuzun, R. E.; Noid, D. W.; Sumpter, B. G., The dynamics of molecular bearings. *Nanotechnology* **1995,** 6, (2), 64-74.
31. Han, J.; Globus, A.; Jaffe, R.; Deardorff, G., Molecular dynamics simulations of carbon nanotube-based gears. *Nanotechnology* **1997,** 8, (3), 95-102.
32. Liu, C.; Fan, Y. Y.; Liu, M.; Cong, H. T.; Cheng, H. M.; Dresselhaus, M. S., Hydrogen storage in single-walled carbon nanotubes at room temperature. *Science (Washington, D. C.)* **1999,** 286, (5442), 1127-1129.
33. Kam, N. W. S.; Dai, H., Single walled carbon nanotubes for transport and delivery of biological cargos. *Phys. Status Solidi B* **2006,** 243, (13), 3561-3566.
34. Kuang, Y. D.; He, X. Q.; Chen, C. Y.; Li, G. Q., Buckling of functionalized single-walled nanotubes under axial compression. *Carbon* **2009,** 47, (1), 279-285.
35. Wang, Q.; Han, Q. K.; Wen, B. C., Length dependent material properties of carbon nanotubes. *J. Comput. Theor. Nanosci.* **2008,** 5, (7), 1454-1457.
36. Sun, C. Q.; Liu, K. X., Torsional buckling of multi-walled carbon nanotubes under combined axial and radial loadings. *J. Phys. D: Appl. Phys.* **2008,** 41, (20), 205404/1-205404/6.

37. Li, X.-F.; Lau, K.-T.; Yin, Y.-S., Mechanical properties of epoxy-based composites using coiled carbon nanotubes. *Compos. Sci. Technol.* **2008,** 68, (14), 2876-2881.
38. Hao, X.; Qiang, H.; Yao, X., Buckling of defective single-walled and double-walled carbon nanotubes under axial compression by molecular dynamics simulation. *Compos. Sci. Technol.* **2008,** 68, (7-8), 1809-1814.
39. Yap, H. W.; Lakes, R. S.; Carpick, R. W., Mechanical instabilities of individual multiwalled carbon nanotubes under cyclic axial compression. *Nano Lett.* **2007,** 7, (5), 1149-1154.
40. Sun, C.; Liu, K., Vibration of multi-walled carbon nanotubes with initial axial loading. *Solid State Commun.* **2007,** 143, (4-5), 202-207.
41. Li, X.-F.; Lau, K.-T.; Yin, Y.-s., Nano-mechanical properties of coiled carbon nanotube reinforced epoxy composites. *Key Eng. Mater.* **2007,** 334-335, (Pt. 2, Advances in Composite Materials and Structures), 673-676.
42. Salvetat, J. P.; Desarmot, G.; Gauthier, C.; Poulin, P., Mechanical properties of individual nanotubes and composites. *Lect. Notes Phys.* **2006,** 677, (Understanding Carbon Nanotubes), 439-493.
43. Miyagawa, H.; Misra, M.; Mohanty Amar, K., Mechanical properties of carbon nanotubes and their polymer nanocomposites. *J Nanosci Nanotechnol* **2005,** 5, (10), 1593-615.
44. Huang, W. M., Mechanics of coiled nanotubes in uniaxial tension. *Mater. Sci. Eng., A: Struct. Mater.: Prop., Microstruct. Process.* **2005,** A408, (1-2), 136-140.
45. Hui, D.; Chipara, M.; Sankar, J.; Lau, K. T., Mechanical Properties of Carbon Nanotubes Composites. *J. Comput. Theor. Nanosci.* **2004,** 1, (204-215), 204.
46. Chen, X.; Zhang, S.; Dikin, D. A.; Ding, W.; Ruoff, R. S.; Pan, L.; Nakayama, Y., Mechanics of a Carbon Nanocoil. *Nano Lett.* **2003,** 3, (9), 1299-1304.
47. Qian, D.; Wagner, G. J.; Liu, W. K.; Yu, M.-F.; Ruoff, R. S., Mechanics of carbon nanotubes. *Applied Mechanics Reviews* **2002,** 55, (6), 495-533.
48. Wang, Z. L.; Poncharal, P.; De Heer, W. A., Measuring physical and mechanical properties of individual carbon nanotubes by in situ TEM. *J. Phys. Chem. Solids* **2000,** 61, (7), 1025-1030.
49. Ru, C. Q., Effective bending stiffness of carbon nanotubes. *Phys. Rev. B: Condens. Matter Mater. Phys.* **2000,** 62, (15), 9973-9976.
50. Ru, C. Q., Elastic buckling of single-walled carbon nanotube ropes under high pressure. *Phys. Rev. B: Condens. Matter Mater. Phys.* **2000,** 62, (15), 10405-10408.
51. Ru, C. Q., Column buckling of multiwalled carbon nanotubes with interlayer radial displacements. *Phys. Rev. B: Condens. Matter Mater. Phys.* **2000,** 62, (24), 16962-16967.
52. Salvetat, J. P.; Bonard, J. M.; Thomson, N. H.; Kulik, A. J.; Forro, L.; Benoit, W.; Zuppiroli, L., Mechanical properties of carbon nanotubes. *Appl. Phys. A: Mater. Sci. Process.* **1999,** 69, (3), 255-260.
53. Ruoff, R. S.; Lorents, D. C., Mechanical and thermal properties of carbon nanotubes. *Carbon* **1995,** 33, (7), 925-30.
54. Treacy, M. M. J.; Ebbesen, T. W.; Gibson, J. M., Exceptionally high Young's modulus observed for individual carbon nanotubes. *Nature (London)* **1996,** 381, (6584), 678-680.

55. Krishnan, A.; Dujardin, E.; Ebbesen, T. W.; Yianilos, P. N.; Treacy, M. M. J., Young's modulus of single-walled nanotubes. *Phys. Rev. B: Condens. Matter Mater. Phys.* **1998,** 58, (20), 14013-14019.
56. Poncharal, P.; Wang, L.; Ugarte, D.; de Heer, W. A., Electrostatic deflections and electromechanical resonances of carbon nanotubes. *Science (Washington, D. C.)* **1999,** 283, (5407), 1513-1516.
57. Wong, E. W.; Sheehan, P. E.; Lieber, C. M., Nanobeam mechanics: elasticity, strength, and toughness of nanorods and nanotubes. *Science* **1997,** 277, (5334), 1971-1975.
58. Salvetat, J.-P.; Briggs, G. A. D.; Bonard, J.-M.; Bacsa, R. R.; Kulik, A. J.; Stockli, T.; Burnham, N. A.; Forro, L., Elastic and Shear Moduli of Single-Walled Carbon Nanotube Ropes. *Phys. Rev. Lett.* **1999,** 82, (5), 944-947.
59. Yu, M.-F.; Files, B. S.; Arepalli, S.; Ruoff, R. S., Tensile loading of ropes of single wall carbon nanotubes and their mechanical properties. *Phys. Rev. Lett.* **2000,** 84, (24), 5552-5555.
60. Chen, X.; Yang, S.; Takeuchi, K.; Hashishin, T.; Iwanaga, H.; Motojiima, S., Conformation and growth mechanism of the carbon nanocoils with twisting form in comparison with that of carbon microcoils. *Diamond & Related Mater.* **2003,** 12, (10-11), 1836-1840.
61. Robertson, D. H.; Brenner, D. W.; Mintmire, J. W., Energetics of nanoscale graphitic tubules. *phys. Rev. B: Condens. Matter Mater. Phys.* **1992,** 45, (21), 45-48.
62. Yakobson, B. I.; Brabec, C. J.; Bernholc, J., Nanomechanics of carbon tubes: instabilities beyond linear response. *Phys. Rev. Lett.* **1996,** 76, (14), 2511-14.
63. Cornwell, C. F.; Wille, L. T., Elastic properties of single-walled carbon nanotubes in compression. *Solid State Commun.* **1997,** 101, (8), 555-558.
64. Lu, J. P., Elastic Properties of Carbon Nanotubes and Nanoropes. *Phys. Rev. Lett.* **1997,** 79, (7), 1297-1300.
65. Hernandez, E.; Goze, C.; Bernier, P.; Rubio, A., Elastic Properties of C and BxCyNz Composite Nanotubes. *Phys. Rev. Lett.* **1998,** 80, (20), 4502-4505.
66. Yao, N.; Lordi, V., Young's modulus of single-walled carbon nanotubes. *J. Appl. Phys.* **1998,** 84, (4), 1939-1943.
67. Ozaki, T.; Iwasa, Y.; Mitani, T., Stiffness of Single-Walled Carbon Nanotubes under Large Strain. *Phys. Rev. Lett.* **2000,** 84, (8), 1712-1715.
68. Van Lier, G.; Van Alsenoy, C.; Van Doren, V.; Geerlings, P., Ab initio study of the elastic properties of single-walled carbon nanotubes and graphene. *Chem. Phys. Lett.* **2000,** 326, (1,2), 181-185.
69. Xin, Z.; Jianjun, Z.; Zhong-can, O.-Y., Strain energy and Young's modulus of single-wall carbon nanotubes calculated from electronic energy-band theory. *Phys. Rev. B: Condens. Matter Mater. Phys.* **2000,** 62, (20), 13692-13696.
70. Belytschko, T.; Xiao, S. P.; Schatz, G. C.; Ruoff, R. S., Atomistic simulations of nanotube fracture. *Phys. Rev. B: Condens. Matter Mater. Phys.* **2002,** 65, (23), 235430/1-235430/8.
71. Troya, D.; Mielke, S. L.; Schatz, G. C., Carbon nanotube fracture - differences between quantum mechanical mechanisms and those of empirical potentials. *Chem. Phys. Lett.* **2003,** 382, (1,2), 133-141.

72. Binning, G.; Rohrer, H.; Gerber, C.; Weibel, E., Surface studies by scanning tunneling microscopy. *Phys. Rev. Lett.* **1982,** 49, (1), 57-61.
73. Binnig, G.; Quate, C. F.; Gerber, C., Atomic Force Microscope. *Physical Review Letters* **1986,** 56, (9), 930.
74. Manne, S.; Hansma, P. K.; Massie, J.; Elings, V. B.; Gewirth, A. A., Atomic-resolution electrochemistry with the atomic force microscope: copper deposition on gold. *Science* **1991,** 251, (4990), 183-6.
75. Green, C. P.; Sader, J. E., Torsional frequency response of cantilever beams immersed in viscous fluids with applications to the atomic force microscope. *J. Appl. Phys.* **2002,** 92, (10), 6262-6274.
76. Green, C. P.; Sader, J. E., Frequency response of cantilever beams immersed in viscous fluids near a solid surface with applications to the atomic force microscope. *J. Appl. Phys.* **2005,** 98, (11), 114913/1-114913/12.
77. Van Eysden, C. A.; Sader, J. E., Frequency response of cantilever beams immersed in viscous fluids with applications to the atomic force microscope: Arbitrary mode order. *J. Appl. Phys.* **2007,** 101, (4), 044908/1-044908/11.
78. Lillehei, P. T.; Bottomley, L. A., Scanning force microscopy of nucleic acid complexes. *Methods Enzymol.* **2001,** 340, (Drug-Nucleic Acid Interactions), 234-251.
79. Salmeron, M.; Ogletree, D. F.; Neubauer, G.; Murray, M. N.; Wilson, T. E.; Bednarski, M. D.; Kolbe, W.; Folch, A., Imaging of biological material with STM/AFM. *Proc. SPIE-Int. Soc. Opt. Eng.* **1992,** 1556, (Scanning Microsc. Instrum.), 40-54.
80. Haggerty, L.; Lenhoff, A. M., STM and AFM in biotechnology. *Biotechnol Prog* **1993,** 9, (1), 1-11.
81. Firtel, M.; Beveridge, T. J., Scanning probe microscopy in microbiology. *Micron* **1995,** 26, (4), 347-62.
82. Hobbs, J. K.; McMaster, T. J.; Miles, M. J.; Barham, P. J., Direct observations of the growth of spherulites of poly(hydroxybutyrate-co-valerate) using atomic force microscopy. *Polymer* **1998,** 39, (12), 2437-2446.
83. Numata, K.; Hirota, T.; Kikkawa, Y.; Tsuge, T.; Iwata, T.; Abe, H.; Doi, Y., Enzymatic degradation processes of lamellar crystals in thin films for poly[(R)-3-hydroxybutyric acid] and its copolymers revealed by real-time atomic force microscopy. *Biomacromolecules* **2004,** 5, (6), 2186-94.
84. Fesenmaier, C. C.; Li, X. S.; To, B.; Levi, D. H., Real-time spectroscopic ellipsometry studies of zinc oxide deposition. *Mater. Res. Soc. Symp. Proc.* **2008,** 1074E, (Synthesis and Metrology of Nanoscale Oxides and Thin Films), No pp given, Paper #: 1074-I07-11.
85. Hansma, P. K.; Elings, V. B.; Marti, O.; Bracker, C. E., Scanning tunneling microscopy and atomic force microscopy: application to biology and technology. *Science* **1988,** 242, (4876), 209-16.
86. Burnham, N. A.; Colton, R. J., Measuring the nanomechanical properties and surface forces of materials using an atomic force microscope. *J. Vac. Sci. Technol., A* **1989,** 7, (4), 2906-13.
87. Bhushan, B.; Koinkar, V. N., Nanoindentation hardness measurements using atomic force microscopy. *Appl. Phys. Lett.* **1994,** 64, (13), 1653-5.

88. Hengsberger, S.; Kulik, A.; Zysset, P., A combined atomic force microscopy and nanoindentation technique to investigate the elastic properties of bone structural units. *Eur Cell Mater* **2001,** 1, 12-7.
89. Falvo, M. R.; Clary, G.; Helser, A.; Paulson, S.; Taylor, R. M., II; Chi, V.; Brooks, F. P., Jr.; Washburn, S.; Superfine, R., Nanomanipulation experiments exploring frictional and mechanical properties of carbon nanotubes. *Microsc. Microanal.* **1998,** 4, (5), 504-512.
90. Tang, Q.; Shi, S.-Q.; Zhou, L., Nanofabrication with atomic force microscopy. *J Nanosci Nanotechnol* **2004,** 4, (8), 948-63.
91. Eigler, D. M.; Schweizer, E. K., Positioning single atoms with scanning tunnelling microscope. *Nature* **1990,** 344, (6266), 524-6.
92. Onaran, A. G.; Balantekin, M.; Lee, W.; Hughes, W. L.; Buchine, B. A.; Guldiken, R. O.; Parlak, Z.; Quate, C. F.; Degertekin, F. L., A new atomic force microscope probe with force sensing integrated readout and active tip. *Rev. Sci. Instrum.* **2006,** 77, (2), 023501/1-023501/7.
93. Sarid, D., *Scanning Force Microscopy: With Applications to Electric, Magnetic and Atomic Forces, Revised Edition. [In: Oxford Ser. Opt. Imaging Sci., 1994; 5]*. 1994; p 263 pp.
94. Weisenberger, M. C.; Grulke, E. A.; Jacques, D.; Rantell, T.; Andrews, R., Enhanced mechanical properties of polyacrylonitrile/multiwall carbon nanotube composite fibers. *J Nanosci Nanotechnol* **2003,** 3, (6), 535-9.
95. Madou, M., Si micromachining: the newest precision engineering tool. *Proc. - Electrochem. Soc.* **1996,** 95-18, (Magnetic Materials, Processes, and Devices), 236-252.
96. Nguyen, C. V.; Stevens, R. M. D.; Barber, J.; Han, J.; Meyyappan, M.; Sanchez, M. I.; Larson, C.; Hinsberg, W. D., Carbon nanotube scanning probe for profiling of deep-ultraviolet and 193 nm photoresist patterns. *Appl. Phys. Lett.* **2002,** 81, (5), 901-903.
97. Stevens, R. M. D.; Frederick, N. A.; Smith, B. L.; Morse, D. E.; Stucky, G. D.; Hansma, P. K., Carbon nanotubes as probes for atomic force microscopy. *Nanotechnology* **2000,** 11, (1), 1-5.
98. Cheung, C. L.; Hafner, J. H.; Lieber, C. M., Carbon nanotube atomic force microscopy tips: direct growth by chemical vapor deposition and application to high-resolution imaging. *Proc Natl Acad Sci U S A* **2000,** 97, (8), 3809-13.
99. Ternes, M.; Lutz, C. P.; Hirjibehedin, C. F.; Giessibl, F. J.; Heinrich, A. J., The Force Needed to Move an Atom on a Surface. *Science* **2008,** 319, (5866), 1066-1069.
100. Turner Ya Tsz, A.; Roberts Clive, J.; Davies Martyn, C., Scanning probe microscopy in the field of drug delivery. *Adv Drug Deliv Rev* **2007,** 59, (14), 1453-73.
101. Takai, O.; Hayashi, K., Micro/nanolithography using self-assembled monolayers (SAMs). *Interface Sci. Technol.* **2007,** 14, (Advanced Chemistry of Monolayers at Interfaces), 141-175.
102. Poggi, M. A.; Bottomley, L. A.; Lillehei, P. T., Measuring the Adhesion Forces between Alkanethiol-Modified AFM Cantilevers and Single Walled Carbon Nanotubes. *Nano Lett.* **2004,** 4, (1), 61-64.

103. Breakspear, S.; Smith, J. R.; Campbell, S. A., AFM in surface finishing: part III. Lateral force microscopy and friction measurements. *Trans. Inst. Met. Finish.* **2003,** 81, (4), B68-B70.
104. Serry, F. M.; Strausser, Y. E.; Elings, J.; Magonov, S.; Thornton, J.; Ge, L., Surface characterization with multiple techniques using the atomic force microscope (AFM). *Surf. Modif. Technol. XII, Proc. Int. Conf., 12th* **1998**, 123-133.
105. Rogers, B.; Manning, L.; Sulchek, T.; Adams, J. D., Improving tapping mode atomic force microscopy with piezoelectric cantilevers. *Ultramicroscopy* **2004,** 100, (3-4), 267-276.
106. Satoh, N.; Tsunemi, E.; Miyato, Y.; Kobayashi, K.; Watanabe, S.; Fuji, T.; Matsushige, K.; Yamada, H., Multi-probe atomic force microscopy using piezoelectric cantilevers. *Japanese Journal of Applied Physics Part 1-Regular Papers Brief Communications & Review Papers* **2007,** 46, (8B), 5543-5547.
107. Kusterer, J.; Luker, A.; Herfurth, P.; Men, Y.; Ebert, W.; Kirby, P.; O'Keefe, M.; Kohn, E., Piezo-actuated nanodiamond cantilever technology for high-speed applications. *Diamond and Related Materials* **2008,** 17, (7-10), 1429-1433.
108. Rogers, B.; York, D.; Whisman, N.; Jones, M.; Murray, K.; Adams, J. D.; Sulchek, T.; Minne, S. C., Tapping mode atomic force microscopy in liquid with an insulated piezoelectric microactuator. *Rev. Sci. Instrum.* **2002,** 73, (9), 3242-3244.
109. Adams, J. D.; Manning, L.; Rogers, B.; Jones, M.; Minne, S. C., Self-sensing tapping mode atomic force microscopy. *Sensors and Actuators a-Physical* **2005,** 121, (1), 262-266.
110. Mortet, V.; Haenen, K.; Potmesil, J.; Vanecek, M.; D'Olieslaeger, M., Diamond - Application to piezoelectric bimorph cantilever sensors. *Physica Status Solidi a-Applications and Materials Science* **2006,** 203, (12), 3185-3190.
111. Poggi, M. A.; Gadsby, E. D.; Bottomley, L. A.; King, W. P.; Oroudjev, E.; Hansma, H., Scanning Probe Microscopy. *Anal. Chem.* **2004,** 76, (12), 3429-3444.
112. Takano, H.; Kenseth, J. R.; Wong, S.-S.; O'Brien, J. C.; Porter, M. D., Chemical and biochemical analysis using scanning force microscopy. *Chem. Rev.* **1999,** 99, (10), 2845-2890.
113. Beake, B. D.; Ling, J. S. G.; Leggett, G. J., Correlation of friction, adhesion, wettability and surface chemistry after argon plasma treatment of poly(ethylene terephthalate). *J. Mater. Chem.* **1998,** 8, (12), 2845-2854.
114. Brewer, N. J.; Beake, B. D.; Leggett, G. J., Friction force microscopy of self-assembled monolayers: Influence of adsorbate alkyl chain length, terminal group chemistry, and scan velocity. *Langmuir* **2001,** 17, (6), 1970-1974.
115. Maivald, P.; Butt, H. J.; Gould, S. A. C.; Prater, C. B.; Drake, B.; Gurley, J. A.; Elings, V. B.; Hansma, P. K., Using force modulation to image surface elasticities with the atomic force microscope. *Nanotechnology* **1991**, (2), 103.
116. Roiter, Y.; Minko, S., AFM Single Molecule Experiments at the Solid−Liquid Interface: In Situ Conformation of Adsorbed Flexible Polyelectrolyte Chains. *Journal of the American Chemical Society* **2005,** 127, (45), 15688-15689.
117. Garcia, R.; Magerle, R.; Perez, R., Nanoscale compositional mapping with gentle forces. *Nat Mater* **2007,** 6, (6), 405-411.

118. Hansma, H. G.; Weisenhorn, A. L.; Edmundson, A. B.; Gaub, H. E.; Hansma, P. K., Atomic force microscopy: seeing molecules of lipid and immunoglobulin. *Clin Chem* **1991,** 37, (9), 1497-501.
119. Suo, Z.; Yang, X.; Avci, R.; Kellerman, L.; Pascual, D. W.; Fries, M.; Steele, A., HEPES-Stabilized Encapsulation of Salmonella typhimurium. In 2007; Vol. 23, pp 1365-1374.
120. Holscher, H.; Langkat, S. M.; Schwarz, A.; Wiesendanger, R., Measurement of three-dimensional force fields with atomic resolution using dynamic force spectroscopy. *Appl. Phys. Lett.* **2002,** 81, (23), 4428-4430.
121. Burnham, N. A.; Colton, R. J., Force microscopy. *Scanning Tunneling Microsc. Spectrosc.* **1993**, 191-49.
122. Burnham, N. A.; Colton, R. J.; Pollock, H. M., Interpretation of force curves in force microscopy. *Nanotechnology* **1993,** 4, (2), 64-80.
123. Castle, J. E.; Zhdan, P. A., Characterization of surface topography by SEM and SFM: problems and solutions. *J. Phys. D: Appl. Phys.* **1997,** 30, (5), 722-740.
124. Lemoine, P.; Lamberton, R. W.; Ogwu, A. A.; Zhao, J. F.; Maguire, P.; McLaughlin, J., Complementary analysis techniques for the morphological study of ultrathin amorphous carbon films. *J. Appl. Phys.* **1999,** 86, (11), 6564-6570.
125. Neves, B. R. A.; Salmon, M. E.; Russell, P. E.; Troughton, E. B., Jr., Comparative study of field emission-scanning electron microscopy and atomic force microscopy to assess self-assembled monolayer coverage on any type of substrate. *Microsc. Microanal.* **1999,** 5, (6), 413-419.
126. de Broglie, L., Waves of Matter. *Nature* **1923,** 112, (2815), 540.
127. Busch, H., Berechnung der Bahn von Kathodenstrahlen im axialsymmetrischen elektromagnetischen Felde. *Annalen der Physik* **1926,** 386, (25), 974-993.
128. Ruska, E., The development of the electron microscope and of electron microscopy. *Reviews of Modern Physics* **1987,** 59, (3), 627.
129. Fultz, B.; Howe, J., Transmission Electron Microscopy and Diffractometry of Materials. In 3rd ed.; Springer: 2008; p 758.
130. Briant, M.; Balloy, D., Combined analysis with WDS/EDS spectrometers in SEM. *Eur. Phys. J.: Appl. Phys.* **2008,** 44, (1), 37-42.
131. Egerton, R. F., *Electron Energy-Loss Spectroscopy in the Electron Microscope*. 2nd ed.; Plenum Press: New York, 1996.
132. K. Iakoubovskii, K. M. Y. N. K. F., Thickness measurements with electron energy loss spectroscopy. *Microscopy Research and Technique* **2008,** 71, (8), 626-631.
133. von Ardenne, M., The limits for the resolution of an electron microscope. *Z. Phys.* **1938,** 108, 338-52.
134. Goldstein, J. I.; Newbury, D. E.; Echlin, P.; Joy, D. C.; Fiori, C.; Lifshin, E., *Scanning Electron Microscopy and X-Ray Microanalysis*. 1981; p 673 pp.
135. Zworykin, V. K.; Hillier, J.; Snyder, R. L., A scanning electron microscope. *Proc. Inst. Radio Engrs.* **1942,** 30, 255.
136. Russell, P.; Batchelor, D.; Thornton, J., Scanning Electron Microscopy (SEM) and Atomic Force Microscopy (AFM). Complementary techniques for high resolution surface investigations. *Surf. Modif. Technol. XV, Proc. Int. Conf., 15th* **2002**, 109-118.

137. Howell, P. G. T.; Davy, K. M. W.; Boyde, A., Mean atomic number and backscattered electron coefficient calculations for some materials with low mean atomic number. *Scanning* **1998,** 20, (1), 35-40.
138. Mityukhlyaev, V. B.; Dyukov, V. G., A new method of compositional image formation by a four-element backscattered electron detector in an SEM. *Scanning* **1994,** 16, (1), 6-10.
139. Wilson, D. J.; Curzon, A. E., Film thickness and composition determination for binary alloys using backscattered electrons. *Thin Solid Films* **1988,** 165, (1), 217-25.
140. Nguyen, C. V.; So, C.; Stevens, R. M.; Li, Y.; Delziet, L.; Sarrazin, P.; Meyyappan, M., High Lateral Resolution Imaging with Sharpened Tip of Multi-Walled Carbon Nanotube Scanning Probe. *J. Phys. Chem. B* **2004,** 108, (9), 2816-2821.
141. Saito, Y.; Yoshikawa, T.; Inagaki, M.; Tomita, M.; Hayashi, T., Growth and structure of graphitic tubules and polyhedral particles in arc-discharge. *Chem. Phys. Lett.* **1993,** 204, (3-4), 277-82.
142. Poggi, M. A.; Boyles, J. S.; Bottomley, L. A.; McFarland, A. W.; Colton, J. S.; Nguyen, C. V.; Stevens, R. M.; Lillehei, P. T., Measuring the Compression of a Carbon Nanospring. *Nano Lett.* **2004,** 4, (6), 1009-1016.
143. Hutter, J. L.; Bechhoefer, J., Calibration of atomic-force microscope tips. *Rev. Sci. Instrum.* **1993,** 64, (7), 1868-73.
144. Hegner, M.; Wagner, P.; Semenza, G., Ultralarge atomically flat template-stripped Au surfaces for scanning probe microscopy. *Surf. Sci.* **1993,** 291, 39-46.
145. D'Amato, M. J.; Marcus, M. S.; Eriksson, M. A.; Carpick, R. W., Phase imaging and the lever-sample tilt angle in dynamic atomic force microscopy. *Appl. Phys. Lett.* **2004,** 85, (20), 4738-4740.
146. Hansma, H. G.; Pietrasanta, L., Atomic force microscopy and other scanning probe microscopies. *Curr Opin Chem Biol* **1998,** 2, (5), 579-84.
147. Frommer, J.; Meyer, E., Atomic force microscopy: a tool for surface science. *J. Phys.: Condens. Matter* **1991,** 3, (Suppl. A), S1-S9.
148. Tran Minh, D., Trends in surface analysis. *Spectra 2000* **1991,** 159, ((Suppl.)), 12-16.
149. Song, Y.; Bhushan, B., Atomic force microscopy dynamic modes: modeling and applications. *J. Phys.: Condens. Matter* **2008,** 20, (22), 225012/1-225012/29.
150. Dai, H.; Wong, E. W.; Lu, Y. Z.; Fan, S.; Lieber, C. M., Synthesis and characterization of carbide nanorods. *Nature* **1995,** 375, (6534), 769-72.
151. Baughman, R. H.; Zakhidov, A. A.; de Heer, W. A., Carbon nanotubes-the route toward applications. *Science (Washington, D. C.)* **2002,** 297, (5582), 787-792.
152. Kong, J.; Franklin, N. R.; Zhou, C.; Chapline, M. G.; Peng, S.; Cho, K.; Dailt, H., Nanotube molecular wires as chemical sensors. *Science* **2000,** 287, (5453), 622-625.
153. Lau, A. K.-T.; Hui, D., The revolutionary creation of new advanced materials-carbon nanotube composites. *Composites, Part B: Engineering* **2002,** 33B, (4), 263-277.
154. Antonucci, V.; Hsiao, K.-T.; Advani, S. G., Review of polymer composites with carbon nanotubes. *Adv. Polymeric Mater.* **2003**, 397-437.
155. Peigney, A., Composite materials: Tougher ceramics with nanotubes. *Nature Materials* **2003,** 2, (1), 15-16.

156. Thostenson, E. T.; Ren, Z.; Chou, T. W., Advances in the science and technology of carbon nanotubes and their composites: a review. *Composites Science and Technology* **2001,** 61, (13), 1899-1912.
157. Lu, J. P.; Han, J., Carbon nanotubes and nanotube-based nanodevices. *International Journal of High Speed Electronics and Systems* **1998,** 9, (1), 101-123.
158. Saito, S., Carbon nanotubes for next-generation electronics devices. *Science* **1997,** 278, (5335), 77-78.
159. Rueckes, T.; Kim, K.; Joselevich, E.; Tseng, G. Y.; Cheung, C.-L.; Lieber, C. M., Carbon nanotube-based nonvolatile random access memory for molecular computing. *Science (Washington, D. C.)* **2000,** 289, (5476), 94-97.
160. Tseng, Y.-C.; Xuan, P.; Javey, A.; Malloy, R.; Wang, Q.; Bokor, J.; Dai, H., Monolithic Integration of Carbon Nanotube Devices with Silicon MOS Technology. *Nano Lett.* **2004,** 4, (1), 123-127.
161. Wang, Q. H.; Yan, M.; Chang, R. P. H., Flat panel display prototype using gated carbon nanotube field emitters. *Appl. Phys. Lett.* **2001,** 78, (9), 1294-1296.
162. Wei, Y.; Wang, J.; Guo, H.; Roland, C., Carbon nanotube parametric electron pump: a molecular device. *Phys. Rev. B: Condens. Matter Mater. Phys.* **2001,** 64, (11), 115321/1-115321/4.
163. Poggi, M. A.; Bottomley, L. A.; Lillehei, P. T., Scanning Probe Microscopy. *Anal. Chem.* **2002,** 74, (12), 2851-2862.
164. Salvetat, J.-P.; Kulik, A. J.; Bonard, J.-M.; Briggs, G. A. D.; Stoeckli, T.; Metenier, K.; Bonnamy, S.; Beguin, F.; Burnham, N. A.; Forro, L., Elastic modulus of ordered and disordered multiwalled carbon nanotubes. *Adv. Mater.* **1999,** 11, (2), 161-165.
165. Williams, P. A.; Papadakis, S. J.; Patel, A. M.; Falvo, M. R.; Washburn, S.; Superfine, R., Torsional Response and Stiffening of Individual Multiwalled Carbon Nanotubes. *Phys. Rev. Lett.* **2002,** 89, (25), 255502/1-255502/4.
166. Lau, K. T.; Lu, M.; Hui, D., Coiled carbon nanotubes: Synthesis and their potential applications in advanced composite structures. *Composites, Part B: Engineering* **2006,** 37B, (6), 437-448.
167. Volodin, A.; Ahlskog, M.; Seynaeve, E.; Van Haesendonck, C.; Fonseca, A.; Nagy, J. B., Imaging the Elastic Properties of Coiled Carbon Nanotubes with Atomic Force Microscopy. *Phys. Rev. Lett.* **2000,** 84, (15), 3342-3345.
168. Volodin, A.; Buntinx, D.; Ahlskog, M.; Fonseca, A.; Nagy, J. B.; Van Haesendonck, C., Coiled Carbon Nanotubes as Self-Sensing Mechanical Resonators. *Nano Lett.* **2004,** 4, (9), 1775-1779.
169. Woodside, M. T.; McEuen, P. L., Scanned probe imaging of single-electron charge states in nanotube quantum dots. *Science* **2002,** 296, (5570), 1098-1101.
170. Behrend, O. P.; Odoni, L.; Loubet, J. L.; Burnham, N. A., Phase imaging: Deep or superficial? *Appl. Phys. Lett.* **1999,** 75, (17), 2551-2553.
171. Ye, J.; Kano, M.; Yasuda, Y., Determination of nanostructures and mechanical properties on the surface of molybdenum dithiocarbamate and zinc dialkyldithiophosphate tribochemically reacted films by using atomic force microscope phase imaging technique. *J. Appl. Phys.* **2003,** 93, (9), 5113-5117.
172. Zhang, X.; Jiang, K.; Feng, C.; Liu, P.; Zhang, L.; Kong, J.; Zhang, T.; Li, Q.; Fan, S., Spinning and processing continuous yarns from 4-inch wafer scale super-aligned carbon nanotube arrays. *Adv. Mater.* **2006,** 18, (12), 1505-1510.

173. Tomlinson, G. A., A molecular theory of friction. *Philos. Mag.* **1929,** 7, 905-39.
174. Braun, O. M.; Peyrard, M.; Bortolani, V.; Franchini, A.; Vanossi, A., Transition from smooth sliding to stick-slip motion in a single frictional contact. *Phys. Rev. E: Stat., Nonlinear, Soft Matter Phys.* **2005,** 72, (5-2), 056116/1-056116/15.
175. Wahl, A. M., *Mechanical springs*. 2nd ed.; , McGraw-Hill: New York, 1963; p 323.
176. Dawson, G., End Effects in Compression Springs. *Wire Industry* **1987,** 54, (637), 36-38.
177. Becker, L. E.; Cleghorn, W. L., On the Buckling of Helical Compression Springs. *Int. J. Mech. Sci.* **1992,** 34, (4), 275-282.
178. McIlroy, D. N.; Zhang, D.; Kranov, Y.; Norton, M. G., Nanosprings. *Appl. Phys. Lett.* **2001,** 79, (10), 1540-1542.
179. Robertson, D. H.; Brenner, D. W.; White, C. T., On the way to fullerenes: molecular dynamics study of the curling and closure of graphitic ribbons. *J. Phys. Chem.* **1992,** 96, (15), 6133-5.
180. Govindjee, S.; Sackman, J. L., On the use of continuum mechanics to estimate the properties of nanotubes. *Solid State Commun.* **1999,** 110, (4), 227-230.
181. Harik, V. M., Ranges of applicability for the continuum beam model in the mechanics of carbon nanotubes and nanorods. *Solid State Commun.* **2001,** 120, (7-8), 331-335.
182. Harik, V. M., Mechanics of carbon nanotubes: applicability of the continuum-beam models. *Comput. Mater. Sci.* **2002,** 24, (3), 328-342.
183. Ru, C. Q., Effect of van der Waals forces on axial buckling of a double-walled carbon nanotube. *J. Appl. Phys.* **2000,** 87, (10), 7227-7231.
184. Ru, C. Q., Degraded axial buckling strain of multiwalled carbon nanotubes due to interlayer slips. *J. Appl. Phys.* **2001,** 89, (6), 3426-3433.
185. Ru, C. Q., Axially compressed buckling of a double-walled carbon nanotube embedded in an elastic medium. *J. Mech. Phys. Solids* **2001,** 49, (6), 1265-1279.
186. Salvetat, J.-P.; Bhattacharyya, S.; Pipes, R. B., Progress on mechanics of carbon nanotubes and derived materials. *J Nanosci Nanotechnol* **2006,** 6, (7), 1857-82.
187. Tu, Z.-c.; Ou-Yang, Z.-c., Single-walled and multiwalled carbon nanotubes viewed as elastic tubes with the effective Young's moduli dependent on layer number. *Phys. Rev. B: Condens. Matter Mater. Phys.* **2002,** 65, (23), 233407/1-233407/4.
188. Landau, L. D.; Lifshitz, E. M., *Theory of Elasticity*. 3 ed.; Pergamon: Moscow, 1986; Vol. 7.
189. Sanchez-Portal, D.; Artacho, E.; Soler, J. M.; Rubio, A.; Ordejon, P., Ab initio structural, elastic, and vibrational properties of carbon nanotubes. *Phys. Rev. B: Condens. Matter Mater. Phys.* **1999,** 59, (19), 12678-12688.
190. Lucas, A. A.; Lambin, P. H.; Smalley, R. E., On the energetics of tubular fullerenes. *J. Phys. Chem. Solids* **1993,** 54, (5), 587-93.
191. Odegard, G. M.; Gates, T. S.; Nicholson, L. M.; Wise, K. E., Equivalent-continuum modeling of nano-structured materials. *Compos. Sci. Technol.* **2002,** 62, (14), 1869-1880.
192. Popov, V. N.; Van Doren, V. E.; Balkanski, M., Elastic properties of single-walled carbon nanotubes. *Phys. Rev. B: Condens. Matter Mater. Phys.* **2000,** 61, (4), 3078-3084.
193. Timoshenko, S., *Theory of Elasticity*. p 415 pp.

194. Karnovsky, I. A.; Lebed, O. I., *Free Vibration of Beams and Frames*. McGraw Hill: New York, 2004.
195. Karnovsky, I. A.; Lebed, O. I., *Non-Classical Vibration of Arches and Beams*. McGraw Hill: New York, 2004.
196. Sader, J. E.; Chon, J. W. M.; Mulvaney, P., Calibration of rectangular atomic force microscope cantilevers. *Rev. Sci. Instrum.* **1999,** 70, (10), 3967-3969.
197. Sader, J. E.; Larson, I.; Mulvaney, P.; White, L. R., Method for the calibration of atomic force microscope cantilevers. *Rev. Sci. Instrum.* **1995,** 66, (7), 3789-98.
198. Cleveland, J. P.; Manne, S.; Bocek, D.; Hansma, P. K., A nondestructive method for determining the spring constant of cantilevers for scanning force microscopy. *Rev. Sci. Instrum.* **1993,** 64, (2), 403-5.
199. Higgins, M. J.; Proksch, R.; Sader, J. E.; Polcik, M.; McEndoo, S.; Cleveland, J. P.; Jarvis, S. P., Noninvasive determination of optical lever sensitivity in atomic force microscopy. *Rev. Sci. Instrum.* **2006,** 77, (1), 013701/1-013701/5.
200. Zettl, A.; Cumings, J., Sharpened nanotubes, nanobearings, and nanosprings. *AIP Conf. Proc.* **2000,** 544, (Electronic Properties of Novel Materials--Molecular Nanostructures), 526-532.
201. Szabo, A.; Fonseca, A.; Volodin, A.; Van Haesendonck, C.; Biro, L. P.; Nagy, J. B., Synthesis, properties and possible applications of helical carbon nanotubes. *AIP Conf. Proc.* **2004,** 723, (Electronic Properties of Synthetic Nanostructures), 40-44.
202. Bandaru, P.; Rao, A., Electrical applications for novel carbon nanotube morphologies: Does function follow shape? *JOM Journal of the Minerals, Metals and Materials Society* **2007,** 59, (3), 33-38.
203. Lu, J.-Q.; Jiang, H., Theoretical modeling on mechanical-electrical coupling of carbon nanotubes. *J. Comput. Theor. Nanosci.* **2008,** 5, (4), 449-463.
204. Hall Adam, R.; Falvo Michael, R.; Superfine, R.; Washburn, S., Electromechanical response of single-walled carbon nanotubes to torsional strain in a self-contained device. *Nat Nanotechnol* **2007,** 2, (7), 413-6.
205. Motojima, S.; Chen, X.; Yang, S.; Hasegawa, M., Properties and potential applications of carbon microcoils/nanocoils. *Diamond & Related Mater.* **2004,** 13, (11-12), 1989-1992.
206. Katsuno, T.; Chen, X.; Yang, S.; Motojima, S., Relationship of a carbon microcoil and carbon microcoil tactile sensor element in electrical properties. *Diamond Relat. Mater.* **2007,** 16, (4-7), 1000-1003.